



Universiteit Gent  
Faculteit Wetenschappen  
Vakgroep Fysica en Sterrenkunde

<sup>2</sup> No title yet

<sup>3</sup> No sub-title neither, obviously...

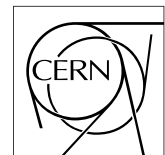
---

<sup>4</sup> Alexis Fagot

5



Thesis to obtain the degree of  
Doctor of Philosophy in Physics  
Academic years 2012-2017







Universiteit Gent  
Faculteit Wetenschappen  
Vakgroep Fysica en Sterrenkunde

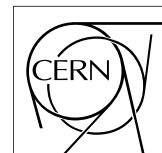
Promotoren: Dr. Michael Tytgat  
Prof. Dr. Dirk Ryckbosch

Universiteit Gent  
Faculteit Wetenschappen  
Vakgroep Fysica en Sterrenkunde  
Proeftuinstraat 86, B-9000 Gent, België  
Tel.: +32 9 264.65.28  
Fax.: +32 9 264.66.97

17



Thesis to obtain the degree of  
Doctor of Philosophy in Physics  
Academic years 2012-2017





## Acknowledgements

<sup>19</sup> Ici on remerciera tous les gens que j'ai pu croiser durant cette aventure et qui m'ont permis de passer  
<sup>20</sup> un bon moment

<sup>21</sup> *Gent, ici la super date de la mort qui tue de la fin d'écriture*  
<sup>22</sup> *Alexis Fagot*



# Table of Contents

23

24	<b>Acknowledgements</b>	i
25	<b>Nederlandse samenvatting</b>	vii
26	<b>English summary</b>	ix
27	<b>1 Introduction</b>	1-1
28	1.1 A story of High Energy Physics . . . . .	1-1
29	1.2 Organisation of this study . . . . .	1-1
30	<b>2 Investigating the TeV scale</b>	2-1
31	2.1 The Standard Model of Particle Physics . . . . .	2-2
32	2.1.1 A history of particle physics . . . . .	2-2
33	2.1.2 Construction and test of the model . . . . .	2-11
34	2.1.3 Investigating the TeV scale . . . . .	2-12
35	2.2 The Large Hadron Collider & the Compact Muon Solenoid . . . . .	2-14
36	2.2.1 LHC, the most powerful particle accelerator . . . . .	2-14
37	2.2.1.1 Particle acceleration . . . . .	2-15
38	2.2.2 CMS, a multipurpose experiment . . . . .	2-18
39	2.2.2.1 The silicon tracker, core of CMS . . . . .	2-20
40	2.2.2.2 The calorimeters, measurement of particle's energy . . . . .	2-20
41	2.2.2.3 The muon system, corner stone of CMS . . . . .	2-22
42	<b>3 Muon Phase-II Upgrade</b>	3-1
43	3.1 High Luminosity LHC and muon system requirements . . . . .	3-2
44	3.2 Necessity for improved electronics . . . . .	3-5
45	3.3 New detectors and increased acceptance . . . . .	3-8
46	3.3.1 Improved forward resistive plate chambers . . . . .	3-9
47	3.3.2 Gas electron multipliers . . . . .	3-12
48	3.3.3 Installation schedule . . . . .	3-19
49	3.4 Implications of the different upgrades on the Level-1 Trigger. Improvement of physics performance. . . . .	3-19
50	3.5 Ecofriendly gas studies . . . . .	3-19
51	3.5.1 Status of the studies and potential candidates . . . . .	3-19
52	3.5.2 Implications in case of no suitable ecofriendly mixture . . . . .	3-19
53		
54	<b>4 Physics of Resistive plate chambers</b>	4-1
55	4.1 Principle . . . . .	4-1
56	4.1.1 Electron drift velocity . . . . .	4-4
57	4.2 Rate capability and time resolution of Resistive Plate Chambers . . . . .	4-4
58	4.2.1 Operation modes . . . . .	4-4

---

59	4.2.2	Detector designs and performance . . . . .	4-6
60	4.2.2.1	Double-gap RPC . . . . .	4-7
61	4.2.2.2	Multigap RPC (MRPC) . . . . .	4-8
62	4.2.2.3	Charge distribution and performance limitations . . . . .	4-9
63	4.3	Signal formation . . . . .	4-12
64	4.4	Gas transport parameters . . . . .	4-12
65	<b>5</b>	<b>Longevity studies and Consolidation of the present CMS RPC subsystem</b>	<b>5-1</b>
66	5.1	Resistive Plate Chambers at CMS . . . . .	5-1
67	5.1.1	Overview . . . . .	5-1
68	5.1.2	The present RPC system . . . . .	5-2
69	5.1.3	Pulse processing of CMS RPCs . . . . .	5-3
70	5.2	Testing detectors under extreme conditions . . . . .	5-4
71	5.2.1	The Gamma Irradiation Facilities . . . . .	5-6
72	5.2.1.1	GIF . . . . .	5-6
73	5.2.1.2	GIF++ . . . . .	5-8
74	5.3	Preliminary tests at GIF . . . . .	5-10
75	5.3.1	Resistive Plate Chamber test setup . . . . .	5-10
76	5.3.2	Data Acquisition . . . . .	5-12
77	5.3.3	Geometrical acceptance of the setup layout to cosmic muons . . . . .	5-12
78	5.3.3.1	Description of the simulation layout . . . . .	5-13
79	5.3.3.2	Simulation procedure . . . . .	5-15
80	5.3.3.3	Results . . . . .	5-16
81	5.3.4	Photon flux at GIF . . . . .	5-16
82	5.3.4.1	Expectations from simulations . . . . .	5-16
83	5.3.4.2	Dose measurements . . . . .	5-21
84	5.3.5	Results and discussions . . . . .	5-22
85	5.4	Longevity tests at GIF++ . . . . .	5-23
86	5.4.1	Description of the Data Acquisition . . . . .	5-26
87	5.4.2	RPC current, environmental and operation parameter monitoring . . . . .	5-27
88	5.4.3	Measurement procedure . . . . .	5-28
89	5.4.4	Longevity studies results . . . . .	5-28
90	<b>6</b>	<b>Investigation on high rate RPCs</b>	<b>6-1</b>
91	6.1	Rate limitations and ageing of RPCs . . . . .	6-1
92	6.1.1	Low resistivity electrodes . . . . .	6-1
93	6.1.2	Low noise front-end electronics . . . . .	6-1
94	6.2	Construction of prototypes . . . . .	6-1
95	6.3	Results and discussions . . . . .	6-1
96	<b>7</b>	<b>Conclusions and outlooks</b>	<b>7-1</b>
97	7.1	Conclusions . . . . .	7-1
98	7.2	Outlooks . . . . .	7-1
99	<b>A</b>	<b>A data acquisition software for CAEN VME TDCs</b>	<b>A-1</b>
100	A.1	GIF++ DAQ file tree . . . . .	A-1
101	A.2	Usage of the DAQ . . . . .	A-2
102	A.3	Description of the readout setup . . . . .	A-3
103	A.4	Data read-out . . . . .	A-3
104	A.4.1	V1190A TDCs . . . . .	A-4

---

105	A.4.2 DataReader . . . . .	A-6
106	A.4.3 Data quality flag . . . . .	A-10
107	<b>A.5 Communications . . . . .</b>	<b>A-12</b>
108	A.5.1 V1718 USB Bridge . . . . .	A-13
109	A.5.2 Configuration file . . . . .	A-13
110	A.5.3 WebDCS/DAQ intercommunication . . . . .	A-17
111	A.5.4 Example of inter-process communication cycle . . . . .	A-18
112	<b>A.6 Software export . . . . .</b>	<b>A-18</b>
113	<b>B Details on the offline analysis package . . . . .</b>	<b>B-1</b>
114	B.1 GIF++ Offline Analysis file tree . . . . .	B-1
115	B.2 Usage of the Offline Analysis . . . . .	B-2
116	B.2.1 Output of the offline tool . . . . .	B-3
117	B.2.1.1 ROOT file . . . . .	B-3
118	B.2.1.2 CSV files . . . . .	B-5
119	B.3 Analysis inputs and information handling . . . . .	B-6
120	B.3.1 Dimensions file and IniFile parser . . . . .	B-6
121	B.3.2 TDC to RPC link file and Mapping . . . . .	B-7
122	B.4 Description of GIF++ setup within the Offline Analysis tool . . . . .	B-9
123	B.4.1 RPC objects . . . . .	B-9
124	B.4.2 Trolley objects . . . . .	B-10
125	B.4.3 Infrastructure object . . . . .	B-11
126	B.5 Handeling of data . . . . .	B-12
127	B.5.1 RPC hits . . . . .	B-13
128	B.5.2 Clusters of hits . . . . .	B-14
129	B.6 DAQ data Analysis . . . . .	B-15
130	B.6.1 Determination of the run type . . . . .	B-16
131	B.6.2 Beam time window calculation for efficiency runs . . . . .	B-17
132	B.6.3 Data loop and histogram filling . . . . .	B-18
133	B.6.4 Results calculation . . . . .	B-19
134	B.6.4.1 Rate normalisation . . . . .	B-19
135	B.6.4.2 Rate and activity . . . . .	B-21
136	B.6.4.3 Strip masking tool . . . . .	B-23
137	B.6.4.4 Output CSV files filling . . . . .	B-25
138	B.7 Current data Analysis . . . . .	B-29



<sup>139</sup>

<sup>140</sup>

## Nederlandse samenvatting –Summary in Dutch–

<sup>141</sup> Le resume en Neerlandais (j'aurais peut-être pu apprendre la langue juste pour ça...).



## English summary

<sup>143</sup> Le meme résume mais en Anglais (on commencera par la hein!).



# List of Figures

144

145	2.1	Through the gold foil experiment Rutherford could show that most of the mass of atoms was contained in a positively charged nucleus and could then propose a more accurate atomic model than that of Thomson. . . . .	2-3
146	2.2	Figure 2.2a: Meson octet. Figure 2.2b: Baryon octet. Figure 2.2c: Baryon decuplet. .	2-8
147	2.3	The elementary particles of the Standard Model are showed along with their names and properties. Their interactions with the strong, weak and electromagnetic forces have been explicated using color squares. In the left column, the scalar higgs boson is depicted, while the central is focused on the matter particles, the fermions, and the right on the force carriers, the gauge bosons. The role of the Higgs boson in electroweak symmetry breaking is highlighted, and the corresponding way properties of the various particles differ in the (high-energy) symmetric phase (top) and the (low-energy) broken-symmetry phase (bottom) are showed. . . . .	2-11
148	2.4	CERN accelerator complex. . . . .	2-15
149	2.5	Pictures of the different accelerators. From top to bottom: first the LINAC 2 and the <i>Pb</i> source of LINAC 3. Then the Booster and the LEIR. Finally, the PS, the SPS and the LHC. . . . .	2-16
150	2.6	Figure 2.6a: schematics of the LHC cryodipoles. 1: Superconducting Coils, 2: Beam pipe, 3: Heat exchanger Pipe, 4: Helium-II Vessel, 5: Superconducting Bus-bar, 6: Iron Yoke, 7: Non-Magnetic Collars, 8: Vacuum Vessel, 9: Radiation Screen, 10: Thermal Shield, 11: Auxiliary Bus-bar Tube, 12: Instrumentation Feed Throughs, 13: Protection Diode, 14: Quadrupole Bus-bars, 15: Spool Piece Bus-bars. Figure 2.6b: magnetic field and resulting motion force applied on the beam particles. . .	2-17
151	2.7	Figure 2.7a: picture of the LHC quadrupoles. Figure 2.7b: magnetic fields and resulting focussing force applied on the beam by 2 consecutive quadrupoles. . . . .	2-18
152	2.8	Picture of the CMS barrel. The red outer layer is the muon system hosted into the red iron return yokes. The calorimeters are the blue cylinder inside in magnet solenoid and the tracker is the inner yellow cylinder built around the beam pipe. . . . .	2-19
153	2.9	View of the CMS apparatus and of its different components. . . . .	2-19
154	2.10	Slice showing CMS sub-detectors and how particles interact with them. . . . .	2-20
155	2.11	CMS tracker. . . . .	2-20
156	2.12	Figure 2.12a: picture of the ECAL. Figure 2.12b: picture of the lead tungstate crystals composing the ECAL. . . . .	2-21
157	2.13	CMS hadron calorimeter barrel. . . . .	2-21
158	2.14	A quadrant of the muon system, showing DTs (yellow), RPCs (blue), and CSCs (green). . . . .	2-22
159	2.15	Figure 2.15a: Barrel wheel with its detector rings and return yokes. Figure 2.15b: CSC endcap disk with the 2 CSC stations. The outer station is made of 10 deg detectors while the inner station is made of 20 deg detectors. Figure 2.15c: RPC endcap disk. The inner station is not equipped and the inner CSC station can be seen.	2-23
160			
161			
162			
163			
164			
165			
166			
167			
168			
169			
170			
171			
172			
173			
174			
175			
176			
177			
178			
179			
180			
181			
182			
183			

- 184    2.16 Figure 2.16a: Cross section of a DT module showing the two superlayers measur-  
 185    ing the  $\phi$  coordinate, perpendicular to the cross section plane, and the superlayer  
 186    measuring the  $\eta$  coordinate, placed in between the two others with honeycomb and  
 187    parallel to the cross section plane. The DT detector is sandwiched in between 2  
 188    RPCs whose readout strips are perpendicular to the cross section plane, measuring  
 189    the  $\phi$  coordinate. Figure 2.16b: A DT cell is shown together with its electric field.  
 190    The path of a muon through a superlayer is shown. . . . . 2-23
- 191    2.17 Figure 2.17a: cathode strips and anode wire layout of a CSC panel. Figure 2.17b  
 192    avalanche development and charge collection by anode wires and induction on cath-  
 193    ode strips inside of a CSC panel. . . . . 2-24
- 194    2.18 Muon track reconstruction through the 6 panels of a CMS CSC using the infor-  
 195    mation of anode wire groups and cathode strip charge distribution combined with  
 196    comparator bits to decide on which half strip the muon is more likely to have passed. 2-24
- 197    2.19 Double gap layout of CMS RPCs. Muons passing through the gas volumes will cre-  
 198    ate electron-ions pairs by ionising the gas. this ionisation will immediately translate  
 199    into a developing avalanche. . . . . 2-25
- 200    3.1 Detailed timeline projection of for LHC and HL-LHC operation until 2039 show-  
 201    ing the evolution of the instantaneous and integrated luminosity as designed (Fig-  
 202    ure 3.1a) and in the ultimate case where the instantaneous luminosity is increased to  
 203     $7.5 \times 10^{34} \text{ cm}^{-2}\text{s}^{-1}$  (Figure 3.1b) [20, 22]. . . . . 3-2
- 204    3.2 Absorbed dose in the CMS cavern after an integrated luminosity of 3000 fb. Using  
 205    the interaction point as reference, R is the transverse distance from the beamline and  
 206    Z is the distance along the beamline. . . . . 3-3
- 207    3.3 A quadrant of the muon system, showing DTs (yellow), RPCs (blue), and CSCs  
 208    (green). The locations of new forward muon detectors for Phase-II are contained  
 209    within the dashed box and indicated in red for GEM stations (ME0, GE1/1, and  
 210    GE2/1) and dark blue for improved RPC (iRPC) stations (RE3/1 and RE4/1). . . . . 3-4
- 211    3.4 Figure 3.4a: Extrapolated fraction of failing channels of the present DT MiC1 elec-  
 212    tronics as a function of the integrated luminosity for different scenari until LS4. Fig-  
 213    ure 3.4b: Comparison of the current (left) and upgraded (right) DT data processing.  
 214    So far, the data is sent to service cavern of CMS facility via copper-to-optical-fiber  
 215    translators (CuOF) by each MiC1. There, data including RPCs and outer hadron  
 216    calorimeter is combined into trigger primitives (TPG) and transmitted by the Twin-  
 217    Mux system to CMS Track Finder. The time-to-digital converter (TDC) data is col-  
 218    lected and sent to the CMS data acquisition system (DAQ) by the micro read-out  
 219    server ( $\mu$ ROS). After the upgrade, the TDC data will be sent via optical links to  
 220    a patch panel inside the experimental cavern by each MiC2, and transferred to the  
 221    back-end, where triggering and event building will be performed. . . . . 3-6
- 222    3.5 Figure 3.5a: The event loss fractions as a function of the instantaneous luminosity is  
 223    compared for CFEBs (Phase-1) and DCFEBs (Phase-II) at different CSC locations.  
 224    HL-LHC luminosity is marked with the dashed brown line. Figure 3.5b: Comparison  
 225    of the current (left) and upgraded (right) CSC data processing. A part of the con-  
 226    nections in between ALCTs and DCFEBs, and the trigger mother boards (TMBs)  
 227    and data acquisition mother boards (DMBs) will be upgraded toward optical data  
 228    transfer. The detector dependent units (DDUs) used as interface in between CSCs'  
 229    front-end electronics and the CMS DAQ will be replaced by new FED boards. . . . . 3-7
- 230    3.6 Comparison of the simulated time residuals in between reconstructed and true muon  
 231    times without (blue) and with (red) the upgraded RPC link system. . . . . 3-8

232	3.7	RMS of the multiple scattering displacement as a function of muon $p_T$ for the proposed forward muon stations. All of the electromagnetic processes such as bremsstrahlung and magnetic field effect are included in the simulation. . . . .	3-9
233			
234			
235	3.8	Simulation of the impact of RPC hit inclusion onto the local trigger primitive efficiency in station 3 (left) and station 4 (right). The contribution of iRPC starts above $ \eta  = 1.8$ . . . . .	3-9
236			
237			
238	3.9	Expected hit rate due to neutrons, photons, electrons and positrons at HL-HLC instantaneous luminosity of $5 \times 10^{34} \text{ cm}^{-2}\text{s}^{-1}$ in RE3/1 and RE4/1 chambers. The sensitivities of iRPCs used in the simulation for each particle are reported and differ from one endcap disk to another as the energies of the considered particles varies with the increasing distance from the interaction point. . . . .	3-10
239			
240			
241			
242			
243	3.10	Measured average charge per avalanche as a function of the effective electric field for different gas gap thickness in double gap RPCs using HPL electrodes. . . . .	3-11
244			
245	3.11	The PETIROC time jitter as a function of the input signal amplitude, measured with and without internal clocks. . . . .	3-12
246			
247	3.12	Schematics of a GEM showing the cathode on top, the GEM foil separating the gas volume into the drift region, in between the cathode and foil, and the induction region, in between the GEM foil and the anode, and the anode on which a 2D readout is installed. A negative voltage is applied on the cathode while the anode is connected to the ground. . . . .	3-13
248			
249			
250			
251			
252	3.13	Left: Picture of a CMS GEM foil provided by a scanning electron microscope. Right: Representation of the electric field lines in a GEM hole and of the amplification that electrons and ions undergo in the hole's volume due to the very intense electric field. . . . .	3-14
253			
254			
255	3.14	Schematic representation of CMS triple GEMs. The gas volume is divided into 4 areas. The drift area is the region where the primary electrons are created before being amplified a first time while passing through the first GEM foil. Then the process of drift and amplification is repeated twice in following two transfer areas and GEM foils. Finally, the charges have been amplified enough to induce current in the read-out strips while in the last drift area. The dimensions, potentials and electric fields are provided. . . . .	3-14
256			
257			
258			
259			
260			
261			
262	3.15	Simulated efficiency and rate of the standalone Level-1 muon trigger using tracks reconstructed in CSCs and all GEM stations compared with Phase-I values in the case where only CSCs are used or CSCs+GE1/1. The zones of inefficiency of the CSC subsystem are compensated by the addition of GEMs during Phase-II and the trigger rates is kept from increasing due to the high luminosity. . . . .	3-15
263			
264			
265			
266			
267	3.16	Figure 3.16a: Simulated resolution of the muon direction measurement $\Delta\phi$ with Phase-II conditions. In the second endcap station, the resolution is compared in the case of CSCs (ME2/1) alone and CSCs+GEMs (GE2/1+ME2/1) while a similar resolution measurement is given in the case of the first station (GE1/1+ME1/1). Figure 3.16b: The addition of GEM detectors on stations 1 and 2 (ME0 is considered to contribute to station station 1) as redundant system to CSCs allows to improve the muon momentum improvement through a more accurate measurement of the local bending angles $\phi_1$ and $\phi_2$ . . . . .	3-16
268			
269			
270			
271			
272			
273			
274			
275	3.17	Schematics of the data communication chain for DAQ of the GEM subsystems. The sending of trigger data via optical links to the CSC OTMBs is only done for GE1/1 and GE2/1 to match the data with ME1/1 and ME2/1. . . . .	3-16
276			
277			



327	4.11	Ratio between total induced and drifting charge have been simulated for single gap, double-gap and multigap layouts [58]. The total induced charge for a double-gap RPC is a factor 2 higher than for a multigap. . . . .	4-10
330	4.12	Charge spectra have been simulated for single gap, double-gap and multigap lay- outs [58]. It appears that when single gap shows a decreasing spectrum, double and multigap layouts exhibit a spectrum whose peak is detached from the origin. The detachment gets stronger as the number of gaps increases. . . . .	4-11
334	4.13	The maximal theoretical efficiency is simulated for single gap, double-gap and multi- gap layouts [58] at a constant gap thickness of 2 mm and using an effective Townsend coefficient of $9 \text{ mm}^{-1}$ . . . . .	4-11
337	5.1	Signals from the RPC strips are shaped by the FEE described on Figure 5.1a. Out- put LVDS signals are then read-out by a TDC module connected to a computer or converted into NIM and sent to scalers. Figure 5.1b describes how these converted signals are put in coincidence with the trigger. . . . .	5-3
341	5.2	Description of the principle of a CFD. A comparison of threshold triggering (left) and constant fraction triggering (right) is shown in Figure 5.2a. Constant fraction triggering is obtained thanks to zero-crossing technique as explained in Figure 5.2b. The signal arriving at the input of the CFD is split into three components. A first one is delayed and connected to the inverting input of a first comparator. A sec- ond component is connected to the noninverting input of this first comparator. A third component is connected to the noninverting input of another comparator along with a threshold value connected to the inverting input. Finally, the output of both comparators is fed through an AND gate. . . . .	5-4
350	5.3	Figure 5.3a: The integrated charge per region (Barrel, Endcap) is extrapolated to HL-LHC integrated luminosity ( $3000 \text{ fb}^{-1}$ ) using the data accumulated in 2016 in every HV channels. Figure 5.3b: The hit rate per region (Barrel, Endcap) is linearly extrapolated to HL-LHC highest instantaneous luminosity ( $5 \times 10^{34} \text{ cm}^{-2}\text{s}^{-1}$ ) using the rate as a function of instantaneous luminosity recorded by RPCs in 2017 showing a linear dependence. . . . .	5-5
356	5.4	Background Fluka simulation compared to 2016 Data at $L = 10^{34} \text{ cm}^{-2}\text{s}^{-1}$ in the fourth endcap disk region. A mismatch in between simulation and data can be observed. <a href="#">[To be understood.]</a> . . . . .	5-6
359	5.5	Layout of the test beam zone called X5c GIF at CERN. Photons from the radioactive source produce a sustained high rate of random hits over the whole area. The zone is surrounded by 8 m high and 80 cm thick concrete walls. Access is possible through three entry points. Two access doors for personnel and one large gate for material. A crane allows installation of heavy equipment in the area. . . . .	5-7
364	5.6	$^{137}\text{Cs}$ decays by $\beta^-$ emission to the ground state of $^{137}\text{Ba}$ (BR = 5.64%) and via the 662 keV isomeric level of $^{137}\text{Ba}$ (BR = 94.36%) whose half-life is 2.55 min. . . . .	5-8
366	5.7	Floor plan of the GIF++ facility. When the facility downstream of the GIF++ takes electron beam, a beam pipe is installed along the beam line (z-axis). The irradiator can be displaced laterally (its center moves from $x = 0.65 \text{ m}$ to $2.15 \text{ m}$ ), to increase the distance to the beam pipe. . . . .	5-8
370	5.8	Simulated unattenuated current of photons in the xz plane (Figure 5.8a) and yz plane (Figure 5.8b) through the source at $x = 0.65 \text{ m}$ and $y = 0 \text{ m}$ . With angular correction filters, the current of 662 keV photons is made uniform in xy planes. . . . .	5-9

373	5.9	Description of the RPC setup. Dimensions are given in mm. A tent containing RPCs is placed at 1720 mm from the source container. The source is situated in the center of the container. RE-4-2-BARC-161 chamber is 160 mm inside the tent. This way, the distance between the source and the chambers plan is 2060 mm. Figure 5.9a provides a side view of the setup in the $xz$ plane while Figure 5.9b shows a top view in the $yz$ plane. . . . .	5-10
374			
375			
376			
377			
378			
379	5.10	RE-4-2-BARC-161 chamber is inside the tent as described in Figure 5.9. In the top right, the two scintillators used as trigger can be seen. This trigger system has an inclination of $10^\circ$ relative to horizontal and is placed above half-partition B2 of the RPCs. PMT electronics are shielded thanks to lead blocks placed in order to protect them without stopping photons from going through the scintillators and the chamber. . . . .	5-11
380			
381			
382			
383			
384	5.11	Hit distributions over all 3 partitions of RE-4-2-BARC-161 chamber is showed on these plots. Top, middle and bottom figures respectively correspond to partitions A, B, and C. These plots show that some events still occur in other half-partitions than B2, which corresponds to strips 49 to 64, in front of which the trigger is placed, contributing to the inefficiency of detection of cosmic muons. In the case of partitions A and C, the very low amount of data can be interpreted as noise. On the other hand, it is clear that a little portion of muons reach the half-partition B1, corresponding to strips 33 to 48. . . . .	5-12
385			
386			
387			
388			
389			
390			
391			
392	5.12	Results are derived from data taken on half-partition B2 only. On the 18 <sup>th</sup> of June 2014, data has been taken on chamber RE-2-BARC-161 at building 904 (Prevessin Site) with cosmic muons providing us a reference efficiency plateau of $(97.54 \pm 0.15)\%$ represented by a black curve. A similar measurement has been done at GIF on the 21 <sup>st</sup> of July with the same chamber giving a plateau of $(78.52 \pm 0.94)\%$ represented by a red curve. . . . .	5-13
393			
394			
395			
396			
397			
398	5.13	Representation of the layout used for the simulations of the test setup. The RPC is represented as a yellow trapezoid while the two scintillators as blue cuboids looking at the sky. A green plane corresponds to the muon generation plane within the simulation. Figure 5.9a shows a global view of the simulated setup. Figure 5.9b shows a zommed view that allows to see the 2 scintillators as well as the full RPC plane. . . . .	5-14
399			
400			
401			
402			
403	5.14	$\gamma$ flux $F(D)$ is plot using values from table 5.1. As expected, the plot shows similar attenuation behaviours with increasing distance for each absorption factors. . . . .	5-17
404			
405	5.15	Figure 5.15a shows the linear approximation fit done via formulae 5.7 on data from table 5.2. Figure 5.15b shows a comparison of this model with the simulated flux using a and b given in figure 5.15a in formulae 5.4 and the reference value $D_0 = 50\text{cm}$ and the associated flux for each absorption factor $F_0^{ABS}$ from table 5.1 . . . . .	5-19
406			
407			
408			
409	5.16	Dose measurements has been done in a plane corresponding to the tents front side. This plan is 1900 mm away from the source. As explained in the first chapter, a lens-shaped lead filter provides a uniform photon flux in the vertical plan orthogonal to the beam direction. If the second line of measured fluxes is not taken into account because of lower values due to experimental equipments in the way between the source and the tent, the uniformity of the flux is well showed by the results. . . . .	5-21
410			
411			
412			
413			
414			
415	5.17	. . . . .	5-22
416	5.18	Evolution of the maximum efficiency for RE2 (5.18a) and RE4 (5.18b) chambers with increasing extrapolated $\gamma$ rate per unit area at working point. Both irradiated (blue) and non irradiated (red) chambers are shown. . . . .	5-24
417			
418			
419	5.19	Evolution of the working point for RE2 (5.19a) and RE4 (5.19b) with increasing extrapolated $\gamma$ rate per unit area at working point. Both irradiated (blue) and non irradiated (red) chambers are shown. . . . .	5-24
420			
421			

422	5.20 Evolution of the maximum efficiency at HL-LHC conditions, i.e. a background hit rate per unit area of 300 Hz/cm <sup>2</sup> , with increasing integrated charge for RE2 (5.20a) and RE4 (5.20b) detectors. Both irradiated (blue) and non irradiated (red) chambers are shown. The integrated charge for non irradiated detectors is recorded during test beam periods and stays small with respect to the charge accumulated in irradiated chambers. . . . .	5-25
428	5.21 Comparison of the efficiency sigmoid before (triangles) and after (circles) irradiation for RE2 (5.21a) and RE4 (5.21b) detectors. Both irradiated (blue) and non irradiated (red) chambers are shown. . . . .	5-25
431	5.22 Evolution of the Bakelite resistivity for RE2 (5.22a) and RE4 (5.22b) detectors. Both irradiated (blue) and non irradiated (red) chambers are shown. . . . .	5-26
433	5.23 Evolution of the noise rate per unit area for the irradiated chamber RE2-2-BARC-9 only. . . . .	5-26
435	A.1 (A.1a) View of the front panel of a V1190A TDC module [64]. (A.1b) View of the front panel of a V1718 Bridge module [65]. (A.1c) View of the front panel of a 6U 6021 VME crate [66]. . . . .	A-3
438	A.2 Module V1190A <i>Trigger Matching Mode</i> timing diagram [64]. . . . .	A-4
439	A.3 Structure of the ROOT output file generated by the DAQ. The 5 branches ( <code>EventNumber</code> , <code>number_of_hits</code> , <code>Quality_flag</code> , <code>TDC_channel</code> and <code>TDC_TimeStamp</code> ) are visible on the left panel of the ROOT browser. On the right panel is visible the histogram corresponding to the variable <code>nHits</code> . In this specific example, there were approximately 50k events recorded to measure the gamma irradiation rate on the detectors. Each event is stored as a single entry in the <code>TTree</code> . . . . .	A-10
445	A.4 The effect of the quality flag is explained by presenting the content of <code>TBranch number_of_hits</code> of a data file without <code>Quality_flag</code> in Figure A.4a and the content of the same <code>TBranch</code> for data corresponding to a <code>Quality_flag</code> where all TDCs were labelled as <code>GOOD</code> in Figure A.4b taken with similar conditions. It can be noted that the number of entries in Figure A.4b is slightly lower then in Figure A.4a due to the excluded events. . . . .	A-12
451	A.5 Using the same data as previously showed in Figure A.4, the effect of the quality flag is explained by presenting the reconstructed hit multiplicity of a data file without <code>Quality_flag</code> in Figure A.5a and the reconstructed content of the same RPC partition for data corresponding to a <code>Quality_flag</code> where all TDCs were labelled as <code>GOOD</code> in Figure A.5b taken with similar conditions. The artificial high content of bin 0 is completely suppressed. . . . .	A-12
457	A.6 WebDCS DAQ scan page. On this page, shifters need to choose the type of scan (Rate, Efficiency or Noise Reference scan), the gamma source configuration at the moment of data taking, the beam configuration, and the trigger mode. These information will be stored in the DAQ ROOT output. Are also given the minimal measurement time and waiting time after ramping up of the detectors is over before starting the data acquisition. Then, the list of HV points to scan and the number of triggers for each run of the scan are given in the table underneath. . . . .	A-14

464	B.1	Example of expected hit time distributions in the cases of efficiency (Figure B.1a) and noise/gamma rate per unit area (Figure B.1b) measurements as extracted from the raw ROOT files. The unit along the x-axis corresponds to ns. The fact that "the" muon peak is not well defined in Figure B.1a is due to the contribution of all the RPCs being tested at the same time that don't necessarily have the same signal arrival time. Each individual peak can have an offset with the ones of other detectors. The inconsistancy in the first 100 ns of both time distributions is an artefact of the TDCs and are systematically rejected during the analysis. . . . .	B-16
465			
466			
467			
468			
469			
470			
471			
472	B.2	The effect of the quality flag is explained by presenting the reconstructed hit multiplicity of a data file without <code>Quality_flag</code> . The artificial high content of bin 0 is the effect of corrupted data. . . . .	B-19
473			
474			
475	B.3	Display of the masking tool page on the webDCS. The window on the left allows the shifter to edit <code>ChannelsMapping.csv</code> . To mask a channel, it only is needed to set the 3rd field corresponding to the strip to mask to 0. It is not necessary for older mapping file formats to add a 1 for each strip that is not masked as the code is versatile and the default behaviour is to consider missing mask fields as active strips. The effect of the mask is directly visible for noisy channels as the corresponding bin turns red. The global effect of masking strips will be an update of the rate value showed on the histogram that will take into consideration the rejected channels. . . . .	B-24
476			
477			
478			
479			
480			
481			
482			

# List of Tables

483

484	4.1	Properties of the most used electrode materials for RPCs. . . . .	4-4
485	5.1	Total photon flux ( $E\gamma \leq 662$ keV) with statistical error predicted considering a $^{137}\text{Cs}$ activity of 740 GBq at different values of the distance $D$ to the source along the x-axis of irradiation field [61]. . . . .	5-16
486	5.2	Correction factor $c$ is computed thanks to formulae 5.5 taking as reference $D_0 = 50$ cm and the associated flux $F_0^{ABS}$ for each absorption factor available in table 5.1.	5-18
487	5.3	The data at $D_0$ in 1997 is taken from [61]. In a second step, using Equations 5.8 and 5.9, the flux at $D$ can be estimated in 1997. Then, taking into account the attenuation of the source activity, the flux at $D$ can be estimated at the time of the tests in GIF in 2014. Finally, assuming a sensitivity of the RPC to $\gamma$ $s = 2 \cdot 10^{-3}$ , an estimation of the hit rate per unit area is obtained. . . . .	5-20
495	A.1	Inter-process communication cycles in between the webDCS and the DAQ through file string signals. . . . .	A-19
496			



# List of Acronyms

## A

503 AFL

Almost Full Level

504 ALCTs

anode local charged track boards

## B

509 BARC

Bhabha Atomic Research Centre

510 BLT

Block Transfer

511 BNL

Brookhaven National Laboratory

512 BR

Branching Ratio

## C

517 CAEN

Costruzioni Apparecchiature Elettroniche Nucleari S.p.A.

518 CERN

European Organization for Nuclear Research

519 CFD

Constant Fraction Discriminator

520 CFEBs

cathode front-end boards

521 CMB

Cosmic Microwave Background

522 CMS

Compact Muon Solenoid

523 CSC

Cathode Strip Chamber

524 CuOF

copper-to-optical-fiber translators

## D

529 DAQ

Data Acquisition

530 DCS

Detector Control Software

531 DQM

Data Quality Monitoring

532 DT

Drift Tube

533		
534	<b>E</b>	
535		
536		
537	<b>ECAL</b>	electromagnetic calorimeter
538	<b>EMTF</b>	Endcap Muon Track Finder
539		
540	<b>F</b>	
541		
542		
543	<b>FCC</b>	Future Circular Collider
544	<b>FEE</b>	Front-End Electronics
545	<b>FEB</b>	Front-End Board
546		
547	<b>G</b>	
548		
549		
550	<b>GE-/-</b>	Find a good description
551	<b>GE1/1</b>	Find a good description
552	<b>GE2/1</b>	Find a good description
553	<b>GEANT</b>	GEometry ANd Tracking - a series of software toolkit platforms developed by CERN
554	<b>GEB</b>	GEM Electronics board
555	<b>GEM</b>	Gas Electron Multiplier
556	<b>GIF</b>	Gamma Irradiation Facility
557	<b>GIF++</b>	new Gamma Irradiation Facility
559		
560	<b>H</b>	
561		
562		
563	<b>HCAL</b>	hadron calorimeter
564	<b>HL-LHC</b>	High Luminosity LHC
565	<b>HPL</b>	High-pressure laminate
566	<b>HV</b>	High Voltage
567		
568	<b>I</b>	
569		
570		
571	<b>iRPC</b>	improved RPC
572	<b>IRQ</b>	Interrupt Request
573	<b>ISR</b>	Intersecting Storage Rings
574		
575		
576	<b>L</b>	
577		

578	LEIR	Low Energy Ion Ring
579	LEP	Large Electron-Positron
580	LHC	Large Hadron Collider
581	LS1	First Long Shutdown
582	LS2	Second Long Shutdown
583	LS3	Third Long Shutdown
584	LV	Low Voltage
585	LVDS	Low-Voltage Differential Signaling

586

587

**M**

589

590	MiC1	first version of Minicrate electronics
591	MC	Monte Carlo
592	MCNP	Monte Carlo N-Particle
593	ME-/	Find good description
594	ME0	Find good description
595	MRPC	Multigap RPC

596

597

**N**

599

600	NIM	Nuclear Instrumentation Module logic signals
-----	-----	--

601

602

**O**

604

605	OH	Optohybrid Board
-----	----	------------------

606

607

**P**

609

610	PMT	PhotoMultiplier Tube
611	PS	Proton Synchrotron
612	PU	pile-up

613

614

**Q**

616

617	QCD	Quantum Chromodynamics
618	QED	Quantum Electrodynamics

619

620

**R**

622

623	RE-/-	Find a good description
624	RE2/2	Find a good description
625	RE3/1	Find a good description
626	RE3/2	Find a good description
627	RE4/1	Find a good description
628	RE4/2	Find a good description
629	RE4/3	Find a good description
630	RMS	Root Mean Square
631	ROOT	a framework for data processing born at CERN
632	RPC	Resistive Plate Chamber

633

634

## S

635

636

637	SC	Synchrocyclotron
638	SLAC	Stanford Linear Accelerator Center
639	SM	Standard Model
640	SPS	Super Proton Synchrotron
641	SUSY	supersymmetry

642

643

## T

644

645

646	TDC	Time-to-Digital Converter
647	TDR	Technical Design Report
648	ToF	Time-of-flight
649	TPG	trigger primitives

650

651

## W

652

653

654	webDCS	Web Detector Control System
-----	--------	-----------------------------

655

656

## Y

657

658

659	YETS	Year End Technical Stop
-----	------	-------------------------

# 1

## Introduction

660

661

<sup>662</sup> **1.1 A story of High Energy Physics**

<sup>663</sup> **1.2 Organisation of this study**



# 2

664

665

## Investigating the TeV scale

666 „We may regard the present state of the universe as the effect of the  
667 past and the cause of the future. An intellect which at any given mo-  
668 ment knew all of the forces that animate nature and the mutual posi-  
669 tions of the beings that compose it, if this intellect were vast enough  
670 to submit the data to analysis, could condense into a single formula  
671 the movement of the greatest bodies of the universe and that of the  
672 lightest atom; for such an intellect nothing could be uncertain and  
673 the future just like the past would be present before its eyes.”

674

675 - Pierre Simon de Laplace, *A Philosophical Essay on Probabilities*, 1814

Throughout history, physics experiment became more and more powerful in order to investigate finer details of nature and helped understanding the elementary blocks of matter and the fundamental interactions that bond them in the microscopic world. Nowadays, the Standard Model (SM) of particle physics is the most accurate theory designed to explain the behaviour of particles and was able to make very precise predictions that are constantly verified, although some hints of new physics are visible as bricks are still missing to have a global comprehension of the Universe.

To highlight the limits of the SM and test the different alternative theories, ever more powerful machines are needed. This is in this context that the Large Hadron Collider (LHC) has been thought and built to accelerate and collide particles at energies exceeding anything that had been done before. Higher collision energies and high pile-up imply the use of enormous detectors to measure the properties of the interaction products. The Compact Muon Solenoid (CMS) is a multipurpose experiment that have been designed to study the proton-proton collisions of the LHC and give answers on various high energy physics scenari. Nevertheless, the luminosity delivered by the collider will in the future be increased to levels beyond the original plans to improve its discovery potential giving no choice to experiments such as CMS to upgrade their technologies to cope with the increased radiation levels and detection rates.

## 2.1 The Standard Model of Particle Physics

In this early 21<sup>st</sup> century it is now widely accepted that matter is made of elementary blocks referred to as *elementary particles*. The physics theory that classifies and describes the best the behaviour and interaction of such elementary particles is the so called Standard Model that formalizes 3 of the 4 fundamental interactions (electromagnetic, weak and strong interactions). It's development took place during the 20<sup>th</sup> century thanks to a strong collaboration in between the theoretical and experimental physicists.

### 2.1.1 A history of particle physics

The idea that nature is composed of elementary bricks, called *atomism*, is not contemporary as it was already discussed by Indian or Greek philosophers during antiquity. In Greece, atomism has been rejected by Aristotelianism as the existance of *atoms* would imply the existance of a void that would violate the physical principles of Aristotle philosophy. Aristotelianism has been considered as a reference in the european area until the 15<sup>th</sup> century and the italian *Rinascimento* where antic text and history started to be more deeply studied. The re-discovery of Platon's philosophy would allow to open the door to alternative theories and give a new approach to natural sciences where experimentation would become central. A new era of knowledge was starting. By the begining of the 17<sup>th</sup> century, atomism was re-discovered by philosophers and the very first attempt to estimate an *atom* size would be provided by Magnetus in 1646. Although his *atoms* correspond to what would nowadays be called *molecules*, Magnetus achieved feats by calculating that the number of molecules in a grain of incense would be of the order of  $10^{18}$  simply by considering the time necessary to smell it everywhere in a large church after the stick was lit on. It is now known that this number only falls short by 1 order of magnitude.

An alternative philosophy to atomism popularized by Descartes was corpuscularianism. Built on ever divisible corpuscles, contrary to atoms, it's principles would be mainly used by alchemists like Newton who would later develop a corpuscular theory of light. Boyle would combine together ideas of both atomism or corpuscularianism leading to mechanical philosophy. The 18<sup>th</sup> century have

718 seen the development of engineering providing philosophical thought experiments with repeatable  
 719 demonstration and a new point of view to explain the composition of matter and Lavoisier would  
 720 greatly contribute to chemistry and atomism by publishing in 1789 a list of 33 chemical elements  
 721 corresponding to what is now called *atoms*. In the early 19<sup>th</sup> century Dalton would summarize the  
 722 knowledge on composition of matter and Fraunhofer would invent the spectrometer and discover  
 723 the spectral lines. The rise of atomic physics, chemistry and mathematical formalism would unravel  
 724 the different atomic elements and ultimately, the 20<sup>th</sup> century would see the very first sub-atomic  
 725 particles.

726 **Discovery of the inner structure of the atom**

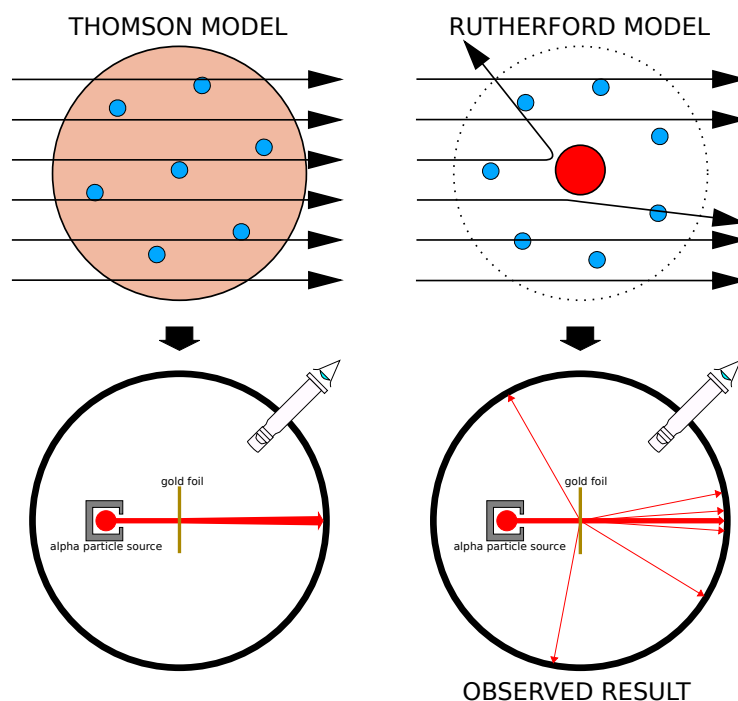


Figure 2.1: Through the gold foil experiment Rutherford could show that most of the mass of atoms was contained in a positively charged nucleus and could then propose a more accurate atomic model than that of Thomson.

727 The negative *electron* would be the first to be discovered in 1897 by Thomson after 3 decades of  
 728 research on cathode rays by proving that the electrification observed in an electroscope, as reported  
 729 by Perrin, was due to the rays themselves and that they had to be composed of electrically charged  
 730 particles. In 1900, Becquerel would show the *beta rays* emitted by radium had the same charge over  
 731 mass ratio than what measured by Thomson for cathode rays, pointing to electrons as a constituent  
 732 of atoms. In 1907, Rutherford and Royds showed that *alpha* particles, once captured in a tube  
 733 and subjected to an electric spark causing an electron avalanche, where helium ions as they could  
 734 combine with 2 electrons to form a  ${}^4\text{He}$ . This discovery was directly followed by the constraint of  
 735 the atom structure in 1909 through the gold foil experiment in which the deflection angle of alpha  
 736 particles fired at a very thin gold foil was measured and highlighted atoms where mainly empty with

737 nearly all its mass contained into a tiny positively charged *nucleus*. With these two observations,  
 738 he could formulate the Rutherford model of the atom in 1911, shown together with the Thomson  
 739 plum pudding model in Figure 2.1. The link in between atomic number and number of positive and  
 740 negative charges contained into the atoms would fast be understood and the different kind of element  
 741 transmutation appeared to be purely nuclear processes making clear that the electromagnetic nature  
 742 of chemical transformation could not possibly change nuclei. Thus a new branch in physics appeared  
 743 to study nuclei exclusively: the nuclear physics.

744 Moreover, in 1913 quantum physics would be introduced into the atomic model by Bohr based  
 745 on the assumptions of Plank to explain spectral lines, and other observed quantum effects. The same  
 746 year, Moseley would confirm Bohr's model and Debye would extend it by introducing elliptical  
 747 orbits.

748 By studying alpha emission and the product of their interaction with nitrogen gas, Rutherford  
 749 reported in 1919 the very first nuclear reaction leading to the discovery that the hydrogen nucleus was  
 750 composed of a single positively charged particle that was later baptised *proton*. This idea came from  
 751 1815 Prout's hypothesis proposing that all atoms are composed of "*protyles*" (i.e. hydrogen atoms).  
 752 By using scintillation detectors, Rutherford could highlight typical hydrogen nuclei signature and  
 753 understand that the impact of alpha particles with nitrogen would knock out an hydrogen nucleus  
 754 and produce an oxygen 17, as explicated in Formula 2.1 and would then postulate that protons are  
 755 building bricks of all elements.



756 With this assumption and the discovery of isotopes together with Aston, elements with identical  
 757 atomic number but different masses, Rutherford would propose that all elements' nuclei but hydrogen's are composed of both charged particles, protons, and of chargeless particles, which he called  
 758 *neutrons*, and that these neutral particles would help maintaining nuclei as one, as charged protons  
 759 were likely to electrostatically repulse each other, and introduced the idea of a new force, a *nuclear*  
 760 force. Though the first idea concerning neutrons was a bond state of protons and electrons as it was  
 761 known that the beta decay, emitting electrons, was taking place in the nucleus, it was then showed  
 762 that such a model would hardly be possible due to Heisenberg's uncertainty principle and by the  
 763 recently measured *spin* of both protons and electrons. The spin, discovered through the study of  
 764 the emission spectrum of alkali metals, would be understood as a "two-valued quantum degree of  
 765 freedom" and formalized by Pauli and extended by Dirac, to take the relativist case into account.  
 766 Measured to be  $\frac{1}{2}\hbar$  for both, it was impossible to arrange an odd number of half integer spins and  
 767 obtain a global nucleus spin that would be integer. Finally, in 1932, following the discovery of a new  
 768 neutral radiation, Chadwick could discover the neutron as an uncharged particle with a mass similar  
 769 to that of the proton whose half integer spin would reveal to be the solution to explain the nuclear  
 770 spin.

## 772 Development of the Quantum Electrodynamics

773 Historically, the development of the quantum theory revolved around the question of emission and  
 774 absorption of discrete amount of energy through light. Einstein used the initial intuition of Plank  
 775 about the black-body radiation to develop in 1905 a model to explain the photoelectric effect in  
 776 which light was described by discrete quanta now called *photons*. For this model, Einstein introduced  
 777 the concept of wave-particle duality as classical theory was not able to describe the phenomenon.  
 778 With the new understanding of atoms and of their structure, classical theories also proved unable

779 to explain atoms stability. Indeed, using classical mechanics, electrons orbiting around a nucleus  
 780 should radiate an energy proportional to their angular momentum and thus lose energy through  
 781 time and the spectrum of energy emission should then be continuous, but it was known since the  
 782 19<sup>th</sup> century and the discovery of spectral lines that the emission spectrum of material was discrete.

783 This was Bohr who first suggested that a quantum description of the atom was necessary in 1913.  
 784 Using the correspondence principle stating that at large enough numbers the quantum calculations  
 785 should give the same results than the classical theory, he proposed the very first quantum model  
 786 of the hydrogen atom explaining the line spectrum by introducing the principal quantum number  
 787  $n$  describing the electron shell. This model would then be improved by Sommerfeld that would  
 788 quantize the z-component of the angular momentum, leading to the second and third quantum  
 789 numbers, or azimuthal and magnetic quantum number,  $l$  and  $m$  defining for the second the orbital  
 790 angular momentum of the electrons on their shells and thus, the shape of the orbital, and for the third  
 791 the available orbital on the subshell for each electron. Nevertheless, although the model was not only  
 792 limited to spherical orbitals anymore, making the atom more realistic, the Zeeman effect couldn't be  
 793 completely explained by just using  $n$ ,  $l$  and  $m$ . A solution would be brought after the discovery of  
 794 Pauli in 1924, as Uhlenbeck, Goudsmit, and Kramers proposed in 1925 the idea of intrinsic rotation  
 795 of the electron, introducing a new angular momentum vector associated to the particle itself, and  
 796 not to the orbital, and associated to a new quantic number  $s$ , the *spin* projection quantum number  
 797 explaining the lift of degeneracy to an even number of energy levels.

798 The introduction of the *spin* happened 1 year after another attempt of improvement of the theory  
 799 was made by De Broglie in his PhD thesis. The original formulation of the quantum theory only  
 800 considered photons as energy quanta behaving as both waves and particles. De Broglie proposed  
 801 that all matter are described by waves and that their momentum is proportional to the oscillation of  
 802 quantized electromagnetic field oscillators. This interpretation was able to reproduce the previous  
 803 version of the quantum energy levels by showing that the quantum condition involves an integer  
 804 multiple of  $2\pi$ , as shown by Formula 2.2.

$$p = \hbar k \Leftrightarrow \int pdx = \hbar \int kdx = 2\pi\hbar n \quad (2.2)$$

805 Although the intuition of De Broglie about the wave-particle duality of all matter, his interpretation  
 806 was semiclassical and it's in 1926 that the first fully quantum mechanical wave-equation would  
 807 be introduced by Schrödinger to describe electron-like particles, reproducing the previous semiclassical  
 808 formulation without inconsistencies. This complexe equation describes the evolution of the  
 809 wave function  $\Psi$  of the quantum system, defined by its position vector  $\mathbf{r}$  and time  $t$  as an energy  
 810 conservation law, in which the hamiltonian of the system  $\hat{H}$  is explicit, by solving the Equation 2.3.

$$i\hbar \frac{\partial}{\partial t} |\Psi(\mathbf{r}, t)\rangle = \hat{H} |\Psi(\mathbf{r}, t)\rangle \quad (2.3)$$

811 In 1927, Dirac would go further in his paper about emission and absorption of radiation by  
 812 proposing a second quantization not only of the physical process at play but also of the electromagnetic  
 813 field, providing the ingredients to the first formulation of *Quantum Electrodynamics (QED)*  
 814 and the description of photon emission by electrons dropping into a lower energy state in which the  
 815 final number of particles is different than the initial one. To complete this model to the many-body  
 816 wave functions of identical particles, Jordan included creation and annihilation operators for fields  
 817 obeying Fermi-Dirac statistics leading to a model describing particles that would be referred to as  
 818 *fermions*. Nevertheless, in order to properly treat electromagnetism, the incorporation of the relativ-

819 ity theory developed by Einstein. Including gravity into quantum physics still is a challenge nowa-  
 820 days, but in 1928 Pauli and Jordan would show that special relativity's coordinate transformations  
 821 could be applied to quantum fields as the field commutators were Lorentz invariant. Finally derived  
 822 the same year, the Dirac equation, shown as Equation 2.4, similarly to Schrödinger's equation, is a  
 823 single-particle equation but it incorporates special relativity in addition to quantum mechanics rules.  
 824 It features the  $4 \times 4$  gamma matrices  $\gamma^\mu$  built using  $2 \times 2$  Pauli matrices and unitary matrix, the  
 825 4-gradient  $\partial_\mu$ , the rest mass  $m$  of any half integer spin massive particle described by the wave func-  
 826 tion  $\psi(x, t)$ , also called a Dirac spinor, and the speed of light  $c$ . In addition to perfectly reproduce  
 827 the results obtained with quantum mechanics so far, it also provided with *negative-energy solutions*  
 828 that would later be interpreted as a new form of matter, *antimatter* and give a theoretical justifica-  
 829 tion to the Pauli equation that was phenomenologically constructed to account for the spin as in the  
 830 non-relativistic limit, the Dirac equation is similar.

$$i\hbar\gamma^\mu\partial_\mu\psi - mc\psi = 0 \quad (2.4)$$

831 The successes of the QED was soon followed with theoretical problems as computations of any  
 832 physical process involving photons and charged particles were showed to be only reliable at the first  
 833 order of perturbation theory. At higher order of the theory, divergent contributions were appearing  
 834 giving nonsensical results. Only two effects were contributing to these infinities.

- 835 • The self-energy of the electron (or positron), the energy that the particle has due its own  
 836 interaction with its environment.
- 837 • The vacuum polarization, virtual electron–positron pairs produced by a background electro-  
 838 magnetic field in the vacuum which is not an "empty" space. These virtual pairs affect the  
 839 charge and current distributions generated by the original electromagnetic field.

840 Solving this apparent problem was done by carefully defining the concepts of each observables,  
 841 for example mass or charge, as these quantities are understood within the context of a non-interacting  
 842 field equation, and that from the experiment point of view, they are abstractions as what is measured  
 843 are "renormalized observables" shifted from there "bare" value by the interaction taking place in  
 844 the measuring process. The infinities needed to be connected to corrections of mass and charge  
 845 as those are fixed to finite values by experiment. This was the intuition of Bethe in 1947 who  
 846 successfully computed the effect of such *renormalization* in the non-relativist case. Fully covariant  
 847 formulations of QED including renormalization was achieved by 1949 by Tomonaga, Schwinger,  
 848 Feynman and Dyson and Feynman is now famous for his association of diagrams to the term of  
 849 the scattering matrix, greatly simplifying the representation and computation of interactions as the  
 850 diagrams directly corresponded the measurable physical processes and would then be used in every  
 851 quantum field theories. With the resolution of infinities, QED had mostly reached its final form,  
 852 being still today the most accurate physical theory and would serve as a model to build all other  
 853 quantum field theories.

#### 854 **Development of the quark model and Quantum Chromodynamics**

855 To explain the nuclear force that holds *nucleons* (protons and neutrons) together, Yukawa theoreti-  
 856 cally proposed in 1934 the existence of a force carrier called *meson* due to it's predicted mass in  
 857 the range in between the electron and nucleon masses. Discovered in 1936 by Anderson and Ned-  
 858 dermeyer, and confirmed using bubble chambers in 1937 by Street and Stevenson, a first meson

candidate was observed in the decay products of cosmic rays. Assuming it had the same electric charge than electrons and protons, this particle was observed to have a curvature due to magnetic field that was sharper than protons but smoother than electrons resulting in a mass in between that of electrons and protons. But its properties were not compatible with Yukawa's theory, which was emphasized by the discovery of a new candidate in 1947, again in cosmic ray products using photographic emulsions.

This new candidate, although it had a similar mass than the already believed *meson*, would rather decay into it. For distinction, the first candidate would then be renamed "*mu meson*" when the second would be the "*pi meson*". The *mu meson* was behaving like a heavy electron and didn't participate in the strong interaction whereas the pion was believed to be the carrier of the nuclear interaction. This lead to classify the *mu* in a new category of particles called *leptons* together with the electron that shared similar properties and *the neutrino*, and be renamed *muon*. The *pi meson* was finally found to be a triplet of particles: a positively charged, a negatively charged, and a neutral particle. The neutral *pi meson* has been more difficult to identify as it wouldn't leave tracks on emulsions nor on bubble chambers and needed to be studied via it's decay products. It was ultimately identified in University of California's cyclotron in 1950 through the observation of its decay into 2 photons.

Also discovered in 1947 but in cloud chamber photographs, the *K meson* as also been an important step towards the establishment of the Standard Model. A triplet of particle, 2 charged and a neutral, with a mass roughly half that of a proton, were reported. These particles were baptised *K meson* in contrast to the "light" *pi* and *mu* "L-mesons". The particularity of the *K* were there very slow decays with a typical lifetime of the order of  $10^{-10}$ s much greater than the  $10^{-23}$ s of *pi*-proton reactions. The concept of *strangeness*, a new quantum number was then introduced by Pais as an attempt to explain this phenomenon as *strange* particles appeared as a pair production of a strange and anti-strange particle.

With the development of synchrotrons, the particle *zoo* would grow to several dozens during the 1950s as higher energies were reachable through acceleration. In 1961, a first classification system, called Eightfold Way, was proposed by Gell-Mann and finding its roots in the Gell-Mann–Nishijima formula, which relates the electric charge  $Q$ , the third component of the isospin  $I_3$ , the *baryon* number  $B$  and the strangeness  $S$ , as explicitated in Formula 2.5. The isospin was a quantum number introduced in 1932 to explain symmetries of the newly discovered neutron using representation theory of SU(2). The baryon number, was introduced by Nishijima as a quantum number for baryons, i.e. particles of the same family as nucleons. The mesons were classified in an octet and baryons of spin  $\pm \frac{1}{2}$  and  $\pm \frac{3}{2}$  were respectively classified into an octet and a decuplet, as shown in Figure 2.2. To complete the baryon decuplet, Gell-Mann predicted the existance of baryon  $\Omega^-$  which would later be discovered in 1964.

$$Q = I_3 + \frac{1}{2}(B + S) \quad (2.5)$$

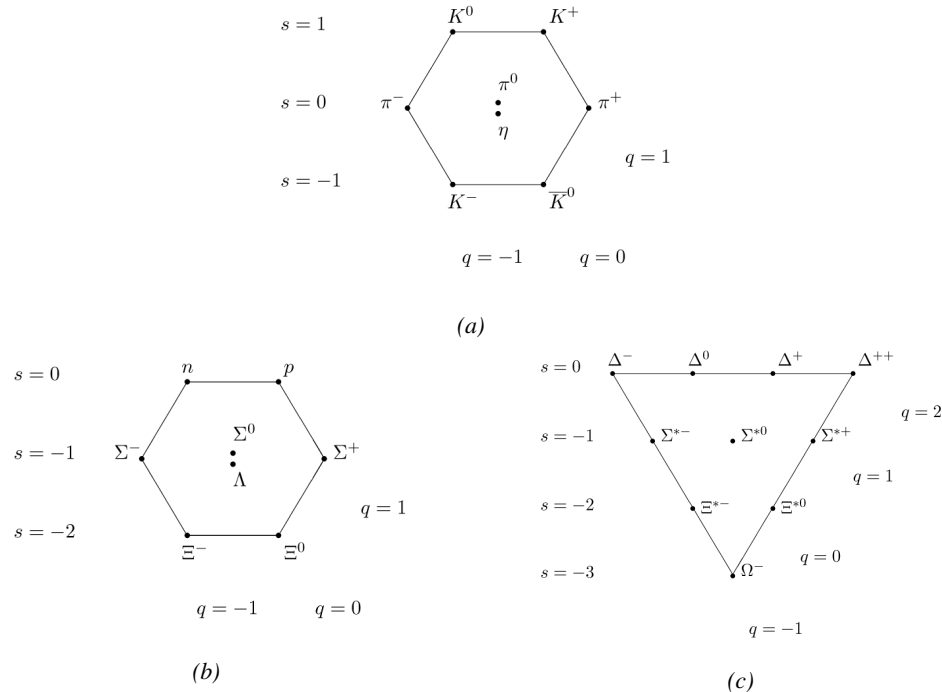


Figure 2.2: Figure 2.2a: Meson octet. Figure 2.2b: Baryon octet. Figure 2.2c: Baryon decuplet.

Strong of this classification using an SU(3) flavor symmetry, Gell-Mann, and independently Zweig, would propose a full theoretical model in which *hadrons* (strongly interacting particles, i.e. mesons and baryons) were not elementary particles anymore. They would rather be composed with 3 flavors of particles called *quarks* and there anti-particles. The 3 flavors were called *up*, *down* and *strange*. *Up* and *down* would be used to explain the nucleons and non-strange mesons, while *strange* would come into the composition of hadrons showing strangeness. *Up* and *down* flavors would be discovered in 1968 thanks to the deep inelastic scattering experiments conducted at the Stanford Linear Accelerator Center (SLAC), and *strange* could only be indirectly validated even though it provided a robust explanation to *kaon* ( $K$ ) and *pion* ( $\pi$ ). However, in the decade following the Gell-Mann-Zweig quark model proposition, several improvement to the model were brought, first by Glashow and Bjorken the same year that predicted the existence of a fourth quark flavor, the *charm*, that would equalize the then known number of quarks and leptons and finally in 1973 by Kobayashi and Maskawa that would increase the number of quarks to 6 to explain the experimental observation of CP violation. These two quarks would be referred to as *top* and *bottom* for the first time in 1975. It's only after these additions to the quark model that finally the *charm* would be discovered in 1974 at both SLAC and Brookhaven National Laboratory (BNL). A meson where the *charm* was bound with an *anti-charm*, called  $J/\psi$ , would help convince the physics community of the validity of the model. The *top* would be discovered soon after in 1977 in Fermilab and indicate the existence of the *bottom* that would resist to discovery until Fermilab's experiments CDF and D $\emptyset$  in 1995 due its very large mass and the energy needed to produce it.

As remarked by Struminsky, the original quark model proposal composed of 3 quarks should possess an additional quantum number due to mesons such as  $\Omega^-$  or  $\Delta^{++}$ . Indeed, these mesons are composed of 3 identical quarks, respectively 3 *strange* and *up* quark, with parallel spins, which

should be forbidden by the exclusion principle. Independentle, Greenberg and Han-Nambu proposed an additional SU(3) degree of freedom possessed by the quarks, that would later be refered to as *color charge gauge*, that could interact through *gluons*, the gauge boson octet corresponding to this degree of freedom. Nevertheless, as observing free quarks proved to be impossible, two visions of the quarks were argued mainly due to the failures to observe these particles free to prove their existence. On one side, Gell-Mann proposed to see quarks as mathematical construct instead of real particles, as they are always confined, implying that quantum field theory would not describe entirely the strong interaction. Opposed to this vision, Feynman on the contrary argued that quarks were real particles, that he would call *partons*, that should be described as all other particles by a distribution of position and momentum. The implications of quarks as point-like particles would be verified at SLAC and the concept of *color* would be added to the quark model in 1973 by Fritzsch and Leutwyler together with Gell-Mann to propose a description of the strong interaction through the theory of Quantum Chromodynamics (QCD). The discovery the same year of asymptotic freedom within the QCD by Groos, Politzer and Wilczek, allowed for very precise predictions thanks to the perturbation theory. Nowadays, the confinement of quarks is studied in experiments such as ALICE, through exploration of the quark-gluon plasma.

### 933 The Weak interaction, spontaneous symmetry breaking, the Higgs mechanism and the Elec- 934 troweak unification

935 The weak interaction is the process that causes radioactive decays. Thanks to the neutron discovery,  
936 Fermi could explain in 1934 the beta radiations through the beta decay process in which the neutron  
937 decays into a proton by emitting an electron. Though the missing energy observed during this  
938 process triggered a huge debate about the apparent non conservation of energy, momentum and spin  
939 of the process, Fermi, as Pauli before him, proposed that the missing energy was due to a neutral  
940 not yet discovered particle that would then be baptised *neutrino*. The impossibility to detect such  
941 a particle would leave some members of the scientific community sceptical, but hints of energy  
942 conservation and of the existence of the neutrino were provided by measuring the energy spectrum  
943 of electrons emitted through beta decay, as there was a strict limit on their energy. It's only 30 years  
944 later in 1953 that it would be discovered by the team of Cowan and Reines using the principle of  
945 inverse beta decay described through Formula 2.6. The experiment consisted in placing water tanks  
946 sandwiched in between liquid scintillators near a nuclear reactor with an estimated neutrino flux of  
947  $5 \times 10^{13} \text{ s}^{-1} \text{ cm}^{-2}$ . However, in order to explain the absence of some reactions in the experiment  
948 of Cowan and Reines, and constraint the beta decay theory of Fermi and extend it to the case of  
949 the muon, Konopinski and Mahmoud proposed in 1953 that the muon decay would eject a particle  
950 similar to the neutrino and thus predicted the existence of a muon neutrino that would be different  
951 than the one involved in the beta decay, related to the electron. With this, the idea of lepton number  
952 would arise. The muon neutrino would successfully be detected in 1962 by Lederman, Schwartz and  
953 Steinberger.

$$\bar{\nu} + p \rightarrow n + e^+ \quad (2.6)$$

954 The theory could not be valid though as the probability of interaction, called cross-section, would  
955 have been increasing without bond with the square of the energy. Fermi assumed in a two vector  
956 current coupling but Lee and Yang noted that an axial current could appear and would violate parity.  
957 The experiment of Wu in 1956 would confirm the parity violation and Gamow and Teller would try to  
958 account for it by describing Fermi's interaction through allowed (parity-violating) and superallowed

959 (parity-conserving) decays. But the success of QED as a quantum field theory would spark the  
960 development of such a theory to describe the weak interaction.

961 As previously discussed, the great success of QED was built on an underlying symmetry, inter-  
962 preted as a gauge invariance so that the effect of the force is the same in all space-time coordinates,  
963 and of the possibility to renormalize it in order to absorb the infinities. Independently in 1958,  
964 Glashow, and Salam and Ward used 1957 Schwinger ideas about vector intermediary for the decay  
965 processes, could find a way to unite both the electromagnetic and weak interaction into a gauge  
966 theory involving 4 gauge bosons, 3 of which were massive and carried out the weak interaction and  
967 a massless boson carrying the electromagnetic interaction. Among the 3 massive bosons, 2 were  
968 charged and 1 was neutral, similarly to the previously theorized *pi meson* vector of the Yukawa  
969 model and all have a mass much greater than nucleons and thus a very short life time implying a  
970 finite very short range contrary to the contact interaction originally proposed by Fermi.

971 Breakthrough in other fields of physics contributed in giving theoretical support and interpreta-  
972 tion to the unified electroweak theory. The stepping stone would be the use of spontaneous symmetry  
973 breaking that was inspired to Nambu at the end of the 1950s following the development of the BCS  
974 superconductivity mechanism in 1957. Cooper had shown that BCS pairs, pairs of electrons bound  
975 together at low temperature, could have lower energy than the Fermi energy and where responsi-  
976 ble for superconductivity. This lead to the discovery of Goldstone-Nambu bosons as a result of the  
977 spontaneous breaking of the chiral symmetry in a theory describing nucleons and mesons devel-  
978 opped by Nambu and Jona-Lasinio in 1961, and now understood as a low-energy approximation of  
979 QCD. Similarly to mechanism of energy gap appearance in superconductivity, the nucleon mass  
980 is suggested to the result of a self-energy of a fermion field and is studied through a four-fermion  
981 interaction in which, as a consequence of the symmetry, bound states of nucleon-antinucleon pairs  
982 appear and can be regarded as virtual pions. Though the symmetry is maintained in the equations,  
983 the ground state is not preserved. Goldstone would later the same year show that the bound states  
984 corresponds to spinless bosons with zero mass.

985 Although the model in itself didn't revolutionize particle physics, spontaneous symmetry break-  
986 ing would be generalized to quantum field theories. As all fundamental interactions are described  
987 using gauge theories based on underlying symmetries, processes such as the chiral symmetry break-  
988 ing would be introduced soon after the publication of Nambu and Jona-Lasinio. In 1962, Anderson,  
989 following an idea of Schwinger who suggested that zero-mass vector bosons were not necessarily  
990 required to describe the conservation of baryons contrary to the bosons emerging from chiral sym-  
991 metry breaking, discussed the implications of spontaneous symmetry breaking in particles physics.  
992 A model was finally independently built in 1964 by Brout and Englert, Higgs, and Guralnik, Hagen,  
993 and Kibble, who discovered that combining an additional field into a gauge theory in order to break  
994 the symmetry, the resulting gauge bosons acquire a nonzero mass. Moreover, Higgs stated that this  
995 implied the existence of at least one new massive, i.e. self-interacting, scalar boson, that are now  
996 known as *Higgs bosons* corresponding to this additional field. The Higgs mechanism today specific-  
997 ally refers to the process through which the gauge bosons of the weak interaction acquire mass. In  
998 1968, Weinberg could point to the Higgs mechanism to integrate a Higgs field into a new version  
999 of the electroweak theory in which the spontaneous symmetry breaking mechanism of the Higgs  
1000 field would explicitly explain the masses of the weak interaction gauge bosons and the zero-mass  
1001 of photons.

### 2.1.2 Construction and test of the model

The Standard Model of particle physics was built in the middle of the 1970s after the experimental confirmation of the existence of quarks. It is based on the assembly of the models previously introduced and describing the fundamental interactions, except for gravitation, and their gauge bosons as well as the way elementary "matter" particles interact with the fields associated with these force carriers. In this sense, the development of QED and the unification of the electroweak interaction, of the Yukawa interaction and of QCD, and of the Higgs mechanism made it possible to explain most of contemporary physics.

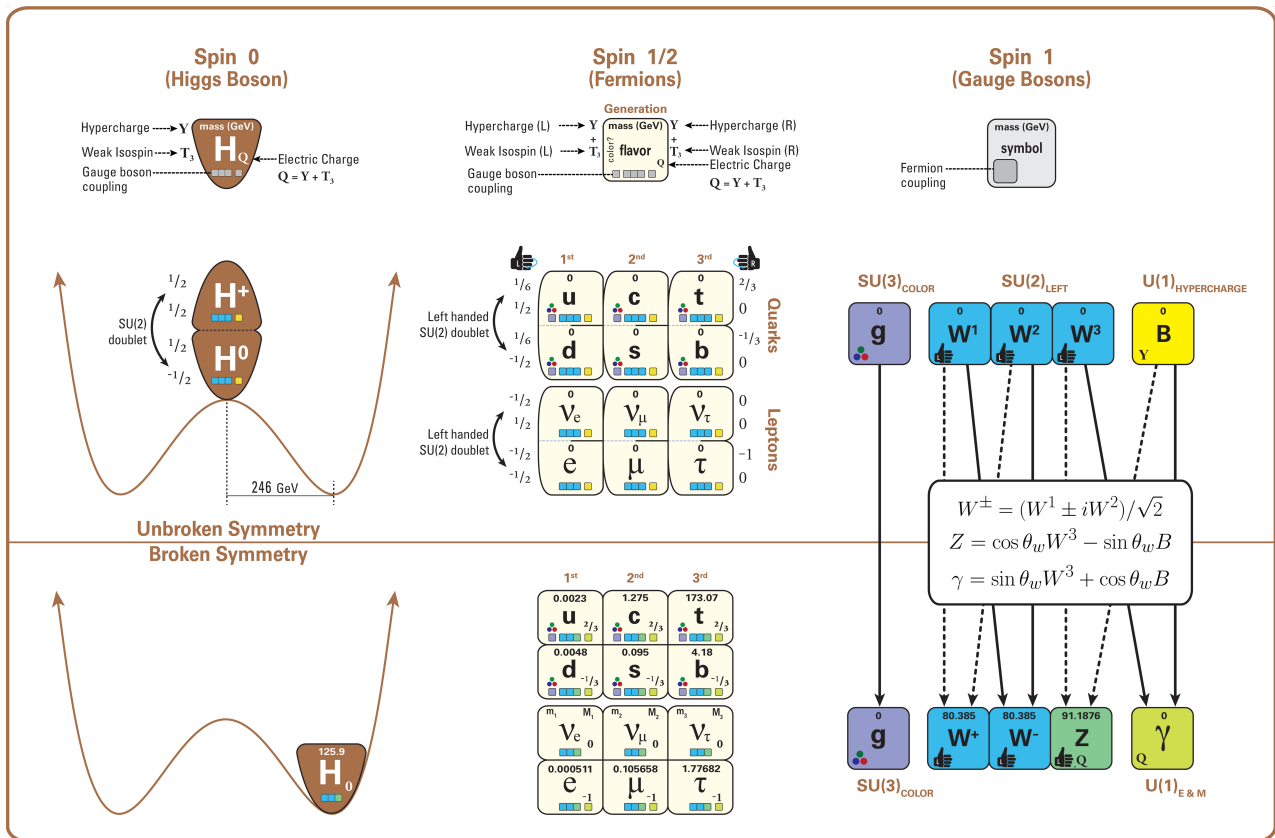


Figure 2.3: The elementary particles of the Standard Model are showed along with their names and properties. Their interactions with the strong, weak and electromagnetic forces have been explicited using color squares. In the left column, the scalar higgs boson is depicted, while the central is focused on the matter particles, the fermions, and the right on the force carriers, the gauge bosons. The role of the Higgs boson in electroweak symmetry breaking is highlighted, and the corresponding way properties of the various particles differ in the (high-energy) symmetric phase (top) and the (low-energy) broken-symmetry phase (bottom) are showed.

In the SM, "matter" particles, are described by 12 fermion fields of spin  $\frac{1}{2}$  obeying the Fermi-Dirac statistics, i.e. subjected to the Pauli exclusion principle. To each fermion is associated its corresponding antiparticle. The fermions are classified according to the way they interact and, thus, according to the charges they carry. 6 of them are classified as quarks ( $u$ ,  $d$ ,  $c$ ,  $s$ ,  $t$ , and  $b$ ) and are subjected to all interactions and the 6 others as leptons ( $e^-$ ,  $\mu^-$ ,  $\tau^-$ ,  $\nu_e$ ,  $\nu_\mu$ , and  $\nu_\tau$ ). Leptons

1015 are not subjected to the strong interaction and among them, the 3 neutrinos only interact weakly as  
 1016 they are neutral particles, which explains why they are so difficult to detect. The gauge boson fields  
 1017 are the gluons  $g$  for the strong interaction, the photon  $\gamma$  for the electromagnetic interaction and the  
 1018 weak bosons  $W^+$ ,  $W^-$ , and  $Z^0$  for the weak interaction. Finally, the Higgs field  $H^0$  is responsible,  
 1019 through the spontaneous symmetry breaking, of the mixing of the massless electroweak boson fields  
 1020  $W_1$ ,  $W_2$ ,  $W_3$ , and  $B$  leading to the observable states  $\gamma$ ,  $W^+$ ,  $W^-$ , and  $Z^0$  that can gain mass while  
 1021 interacting with the Higgs field. This picture of the SM is summarized through Figure 2.3 where the  
 1022 antifermions are not showed.

1023 When the model was first finalized, the existence of the weak gauge bosons, of the charm, of the  
 1024 third quark generation composed of top and bottom quarks to explain the observed CP violation was  
 1025 not proven but the predictions were measured with good precision in the years following. First, the  
 1026 charm quark would be discovered in 1974, followed by the bottom quark in 1977. The weak bosons  
 1027 would be discovered during the next decade in 1983. The top quark would resist until 1995 due to  
 1028 its very large mass but would offer the last piece of the elementary QCD particles. The very last  
 1029 predicted elementary particle of the model that was not observed yet would prove to be very difficult  
 1030 to observe. the Higgs boson needed the start of the LHC to finally be observed in 2012. A few years  
 1031 more of tests were necessary to measure its properties to confirm the observation of a scalar boson  
 1032 compatible with the predicted Higgs boson  $H^0$ . Eventhough only quark-antiquark (mesons) and 3  
 1033 quark states (baryons) were observed, exotic hadrons were not forbidden by QCD and no limit of  
 1034 quark is imposed by the theory. Moreover, gluons could form bond states by themselves and with  
 1035 quarks. These two types of states are called *glueballs* and *hybrid hadrons*. For decades, experi-  
 1036 ments have been conducted without confirmation of such possible states existing. Nevertheless, in  
 1037 2014, tetraquarks were observed by LHCb, one of LHC's main experiments, and in 2015, the same  
 1038 experiment reported the discovery of pentaquarks making the SM one of the best tested theories of  
 1039 physics.

### 1040 2.1.3 Investigating the TeV scale

1041 Even though the SM is a well tested theory, several hints of physics going beyond its scope have  
 1042 been observed. First of all, gravity is not explained through this model and huge difficulties are en-  
 1043 countered when trying to include gravitation. The strength of gravitational interaction is expected to  
 1044 be negligible at the scale of elementary particles, nevertheless, adding gravitation in the perspective  
 1045 of developing a "theory of everything" leads to divergent integrals that could not be fixed through  
 1046 renormalization.

1047 Moreover, the SM considers neutrinos to be massless but it was shown in the late 1960s by the  
 1048 Homestake experiment that the flux of solar neutrinos (i.e.  $\nu_e$ ) measured didn't match the predicted  
 1049 values due to neutrino oscillations, confirmed in the early 2000s by the Sudbury Neutrino Obser-  
 1050 vatory. This oscillation implies that neutrinos that can be observed are a superposition of massive  
 1051 neutrino states. The research on neutrino oscillation is already quite advanced with experiments  
 1052 looking at atmospheric, reactor or beam neutrinos in order to determine the elements of the mixing  
 1053 matrix similar to the CKM matrix describing the mixing of quarks. Nevertheless, no answer to the  
 1054 origin of neutrino mass is provided.

1055 Another intriguing fact is that the universe is dominated by matter. However, the SM predicted  
 1056 that matter and antimatter should have been created in equal amounts and no mechanism is able to  
 1057 explain this matter-antimatter asymmetry. Although this asymmetry is seen from the visible uni-  
 1058 verse, it may be possible that other unknown regions of the Universe are dominated by antimatter.

1059 Another possibility to explain the apparent asymmetry would be the existence of a electric dipole  
1060 in any fundamental particle that would permit matter and antimatter particles to decay at different  
1061 rates.

1062 The discrepancy of velocity dispersion of stars in galaxies with respect to the visible mass they  
1063 contain is known since the end of the 19<sup>th</sup> century where Kelvin proposed that this problem could  
1064 be solved if a "*great majority of [the stars] would be dark bodies*". Throughout the 20<sup>th</sup> century,  
1065 physicists like Kapteyn, Zwicky, showed the first hints of a "*dark matter*" by studying star veloc-  
1066 ities and galactic clusters, followed by robust measurements of galaxy rotation curves by Babcock  
1067 which suggested that the mass-to-luminosity ratio was different from what would be expected from  
1068 watching the visible light. Later in the 1970s, Rubin and Ford from direct light observations and  
1069 Rogstad and Shostak from radio measurements showed that the radial velocity of visible objects in  
1070 galaxies was increasing with increasing distance to the center of the galaxy. Finally observation of  
1071 lensing effect by galaxy clusters, temperature distribution of hot gas in galaxies and clusters, and  
1072 the anisotropies in the Cosmic Microwave Background (CMB) kept on pointing to a "*dark matter*".  
1073 From all the data accumulated, the visible matter would only account to no more than 5% of the total  
1074 content on the visible universe. Alternative theories have tried to investigate modified versions of  
1075 the General Relativity as this theory is only well tested at the scale of the solar system but is not suf-  
1076 ficiently tested on wider ranges or even theories in which gravitation is not a fundamental force but  
1077 rather an emergent one, but so far, such theories have difficulties to reproduce all the experimental  
1078 observations as easily as through dark matter.

1079 A possible theory to offer dark matter candidates would be supersymmetry (SUSY) which pro-  
1080 poses a relationship in between bosons and fermions. In this model, each elementary particle,  
1081 through a spontaneous spacetime symmetry breaking mechanism would have a *super partner* from  
1082 the other family of particles. On top of providing heavy dark matter candidates, supersymmetry  
1083 could also help solving the *Hierarchy problem*, the very large scale difference in between the weak  
1084 interaction and gravity, although, as mentioned before, in the case gravity is found not to be a funda-  
1085 mental force, this problem would automatically fade.

1086  
1087 All these different aspects of physics beyond the Standard Model of particle physics and the  
1088 Standard model itself can be tested through the use of very energetic and intense hadron and ion col-  
1089 liders. The LHC at CERN is a perfect tool to seek answers to these open questions except maybe for  
1090 the gravity as gravity is extremely weak at particles level. For example, one of LHCb experiment's  
1091 goal is to investigate CP-violation and thus baryonic asymmetry. In 2017, the collaboration has an-  
1092 nounced to have so far a  $3.3\sigma$  statistical significance over a CP-violation through the study of the  
1093 decays of  $\Lambda_b^0$  and  $\overline{\Lambda}_b^0$  into a proton (or antiproton) and 3 pions. Many analysis teams are also working  
1094 hard on supersymmetry both in ATLAS and CMS collaborations, the two multipurpose experiments  
1095 of LHC, even though no evidence of a supersymmetrical theory was seen, the few hint having the  
1096 tendency to confirm the standard model. These experiments also have the possibility to investigate  
1097 ways to explain Majorana neutrino mass through Yukawa interactions of scalar particles.

1098 The higher the center-of-mass energy, the smaller details the experiments will be able to see, the  
1099 heavier the potential particle creation barrier will be, the stronger the cross-section of certain rare  
1100 decay channels will be. As a comparison, with collisions happening at 14 TeV, the LHC is approxi-  
1101 mately 2 orders of magnitude more sensitive to the Higgs than the Tevatron was with its already very  
1102 powerful 2 TeV. All these advantages eventually lead to new discoveries and deeper understanding  
1103 of the models describing our Universe. But the LHC only is a step forward to gather more precise  
1104 tests of the Standard Model and new knowledge about the physics beyond it. A successful physics

<sup>1105</sup> campaign will probably serve to justify the building of new accelerators with even greater discovery  
<sup>1106</sup> potential like for example the Future Circular Collider (FCC) that would push even further the study  
<sup>1107</sup> of the unanswered questions of contemporary physics.

## <sup>1108</sup> 2.2 The Large Hadron Collider & the Compact Muon Solenoid

<sup>1109</sup> Throughout its history, CERN has played a leading role in high energy particle physics. Large re-  
<sup>1110</sup> gional facilities such as CERN were thought after the second world war in an attempt to increase  
<sup>1111</sup> international scientific collaboration and allows scientists to share the forever increasing costs of  
<sup>1112</sup> experiment facilities required due to the need for increasing the energy in the center of mass to  
<sup>1113</sup> deeper probe matter. The construction of the first accelerators at the end of the 50s, the Synchro-  
<sup>1114</sup> cyclotron (SC) and the Proton Synchrotron (PS), was directly followed by the first observation of  
<sup>1115</sup> antinuclei in 1965 [1]. Strong from the experience of the Intersecting Storage Rings (ISR), the very  
<sup>1116</sup> first proton-proton collider that showed hints that protons are not elementary particles, the Super  
<sup>1117</sup> Proton Synchrotron (SPS) was built in the 70s to investigate the structure of protons, the preference  
<sup>1118</sup> for matter over antimatter, the state of matter in the early universe or exotic particles, and lead to  
<sup>1119</sup> the discovery in 1983 of the W and Z bosons [2–5]. These newly discovered particles and the elec-  
<sup>1120</sup> troweak interaction would then be studied in details by the Large Electron-Positron (LEP) collider  
<sup>1121</sup> that will help to prove in 1989 that there only are three generations of elementary particles [6]. The  
<sup>1122</sup> LEP would then be dismantled in 2000 to allow for the LHC to be constructed in the existing tunnel.

### <sup>1123</sup> 2.2.1 LHC, the most powerful particle accelerator

<sup>1124</sup> The LHC has always been considered as an option to the future of CERN. At the moment of the  
<sup>1125</sup> construction of the LEP beneath the border between France and Switzerland, the tunnel was built in  
<sup>1126</sup> order to accomodate what would be a Large Hadron Collider with a dipole field of 10 T and a beam  
<sup>1127</sup> energy in between 8 and 9 TeV [7] directly followed in 1985 with the creation of a 'Working Group  
<sup>1128</sup> on the Scientific and Technological Future of CERN' to investigate such a collider [8]. The decision  
<sup>1129</sup> was finally taken almost 10 years later, in 1994, to construct the LHC in the LEP tunnel [9] and the  
<sup>1130</sup> approval of the 4 main experiments that would take place at the 4 interaction points would come in  
<sup>1131</sup> 1997 [10] and 1998 [11]:

- <sup>1132</sup> • ALICE [12] has been designed in the purpose of studying quark-gluon plasma that is believed  
<sup>1133</sup> to have been a state of matter that existed in the very first moment of the universe.
- <sup>1134</sup> • ATLAS [13] and CMS [14] are general purpose experiments that have been designed with  
<sup>1135</sup> the goal of continuing the exploration of the Standard Model and investigate new physics.
- <sup>1136</sup> • LHCb [15] has been designed to investigate the preference of matter over antimatter in the  
<sup>1137</sup> universe through the CP violation.

<sup>1138</sup> These large scale experiments, as well as the full CERN accelerator complex, are displayed on  
<sup>1139</sup> Figure 2.4. The LHC is a 27 km long hadron collider and the most powerful accelerator used for  
<sup>1140</sup> particle physics since 2008 [16]. The LHC was originally designed to collide protons at a center-  
<sup>1141</sup> of-mass energy of 14 TeV and luminosity of  $10^{34} \text{ cm}^{-2}\text{s}^{-1}$ , as well as Pb ions at a center-of-mass  
<sup>1142</sup> energy of 2.8 TeV/A with a peak luminosity of  $10^{27} \text{ cm}^{-2}\text{s}^{-1}$ . Run 1 of LHC, when the center-of-  
<sup>1143</sup> mass energy only was half of the nominal LHC energy, was enough for both CMS and ATLAS to

discover the Higgs boson [17] and for LHCb to discover pentaquarks [18] and confirm the existance of tetraquarks [19]. Nevertheless, after the Third Long Shutdown (LS3) (2024-2026), the accelerator will be in the so called High Luminosity LHC (HL-LHC) configuration [20], increasing its instantaneous luminosity to  $10^{35} \text{ cm}^{-2}\text{s}^{-1}$  for  $pp$  collisions and to  $4.5 \times 10^{27} \text{ cm}^{-2}\text{s}^{-1}$ , boosting the discovery potential of the LHC. The HL-LHC phase should last at least another 10 years depending on the breakthrough this machine would lead to. Already a new accelerating device, the FCC, as been proposed to prepare the future of high energy physics after the LHC.

### CERN's Accelerator Complex

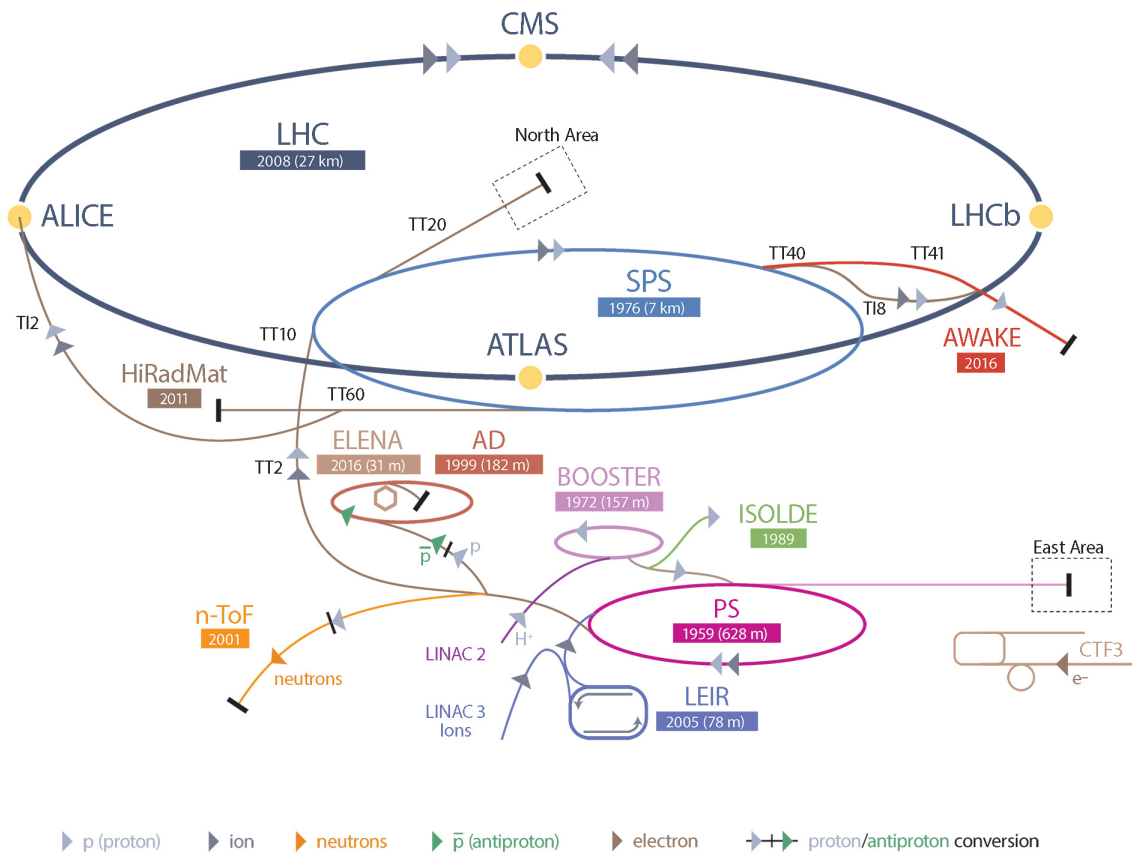


Figure 2.4: CERN accelerator complex.

#### 2.2.1.1 Particle acceleration

The LHC is the last of a long series of accelerating devices. Before being accelerated by the LHC, the particles need to pass through different acceleration stages. All these acceleration stages are visible on Figure 2.4 and pictures of the accelerators are showed in Figure 2.5.

The story of accelerated protons at CERN starts with a bottle of hydrogen gas injected into the source chamber of the linear particle accelerator *LINAC 2* in which a strong electric field strips the

1158 electron off the hydrogen molecules only to keep their nuclei, the protons. The cylindrical conductors,  
 1159 alternatively positively or negatively charged by radiofrequency cavities, accelerate protons by  
 1160 pushing them from behind and pulling them from the front and ultimately give them an energy of  
 1161 50 MeV, increasing their mass by 5% in the process.

1162

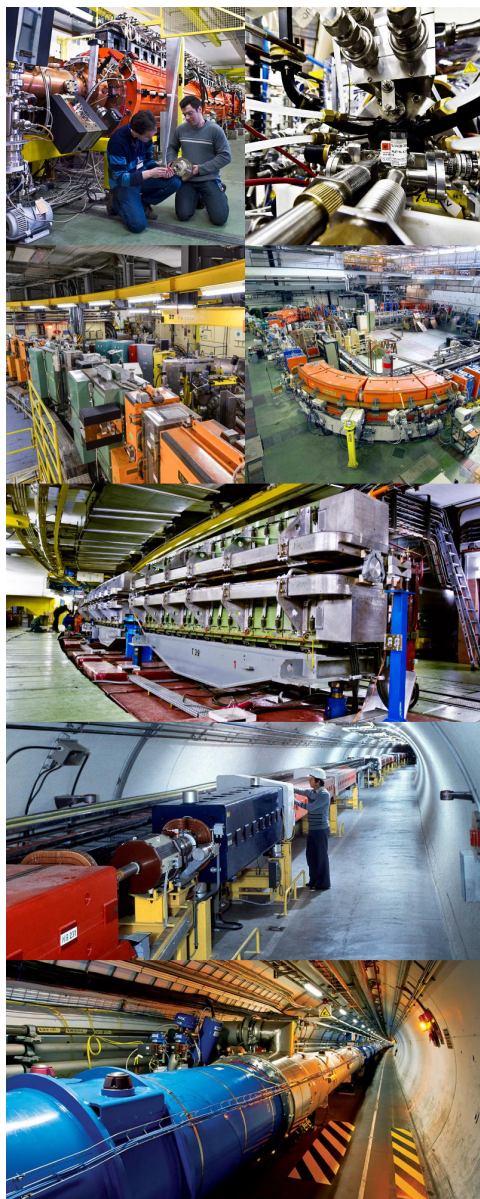


*Figure 2.5: Pictures of the different accelerators. From top to bottom: first the LINAC 2 and the Pb source of LINAC 3. Then the Booster and the LEIR. Finally, the PS, the SPS and the LHC.*

1163 When exiting the LINAC 2, the protons are divided into 4 bunches and injected into the 4 superimposed  
 1164 synchrotron rings of the *Booster* where they are then accelerated to reach an energy of

1165 1.4 GeV before being injected into the PS. Before the Booster was operational in 1972, the protons  
 1166 were directly injected into the PS from the LINAC 2 but the low injection energy limited the amount  
 1167 of protons that could be accelerated at once by the PS. With the Booster, the PS accepts approxi-  
 1168 mately 100 times more particles.

1169

1170 The 4 proton bunches are thus sent as one to the PS where their energy eventually reaches  
 1171 26 GeV. Since the 70s, the main goal of this 628 m circumference synchrotron has been to sup-  
 1172 ply other machines with accelerated particles. Nowadays, not only the PS accelerates protons, it also  
 1173 accelerates heavy ions from the *Low Energy Ion Ring (LEIR)*. Indeed, the LHC experiments are not  
 1174 only designed to study *pp*-collisions but also *Pb*-collisions. Lead is first injected into the dedicated  
 1175 linear collider *LINAC 3*, that accelerate the ions using the same principle than LINAC 2. Electrons  
 1176 are striped off the lead ions all along the acceleration process and eventually, only bare nuclei are  
 1177 injected in the LEIR whose goal is to transform the long ion pulses received into short dense bunches  
 1178 for LHC. Ions injected and stored in the PS were aceelerated by the LEIR from 4.2 MeV to 72 MeV.

1179

1180 Directly following the PS, is finally the last acceleration stage before the LHC, the 7 km long  
 1181 *SPS*. The SPS accelerates the protons to 450 GeV and inject proton in both LHC accelerator rings  
 1182 that will increase their energy up to 7 TeV. When the LHC runs with heavy lead ions for ALICE  
 1183 and LHCb, ions are injected and accelerated to reach the energy of 2.8 TeV/A.

1184

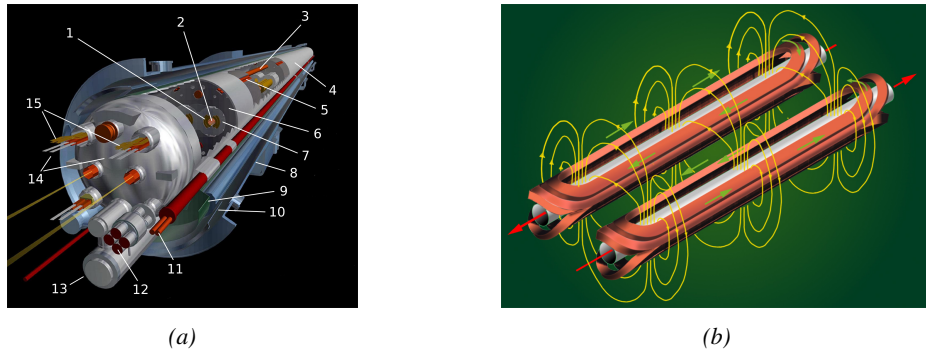
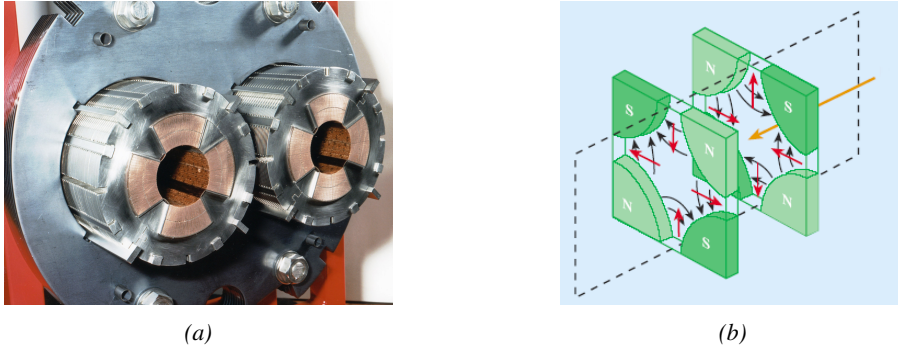


Figure 2.6: Figure 2.6a: schematics of the LHC cryodipoles. 1: Superconducting Coils, 2: Beam pipe, 3: Heat exchanger Pipe, 4: Helium-II Vessel, 5: Superconducting Bus-bar, 6: Iron Yoke, 7: Non-Magnetic Collars, 8: Vacuum Vessel, 9: Radiation Screen, 10: Thermal Shield, 11: Auxiliary Bus-bar Tube, 12: Instrumentation Feed Throughs, 13: Protection Diode, 14: Quadrupole Bus-bars, 15: Spool Piece Bus-bars. Figure 2.6b: magnetic field and resulting motion force applied on the beam particles.

1185

The LHC beams are not continuous and are rather organised in bunch of paticles. When in *pp*-  
 1186 collision mode, the beams are composed of 2808 bunches of  $1.15 \times 10^{11}$  protons separated by 25 ns.  
 1187 When in *Pb* collision mode, the 592 *Pb* bunches are on the contrary composed of  $2.2 \times 10^8$  ions  
 1188 separated by 100 ns. The two parrallel proton beams of the LHC are contained in a single twin-  
 1189 bore magnet due to the space restriction in the LEP tunnel. Indeed, building 2 completely separate  
 1190 accelerator rings next to each other was impossible. The dipoles of the 1232 twin-bore magnets are  
 1191 showed in Figure 2.6 alongside the magnetic field generated along the dipole section to accelerate the  
 1192 particles. The dipoles generate a nominal field of 8.33 T, needed to give protons and lead nucleons  
 1193 their nominal energy. Some 392 quadrupoles, presented in Figure 2.7, are also used to focus to the

<sup>1194</sup> beams, as well as other multipoles to correct smaller imperfections.



*Figure 2.7: Figure 2.7a: picture of the LHC quadrupoles. Figure 2.7b: magnetic fields and resulting focussing force applied on the beam by 2 consecutive quadrupoles.*

### <sup>1195</sup> 2.2.2 CMS, a multipurpose experiment

<sup>1196</sup> Among the four main LHC experiments is the Compact Muon Solenoid used as a multipurpose tool to  
<sup>1197</sup> investigate the SM and physics beyond its scope. Proposed through a letter of intention in 1992 [14],  
<sup>1198</sup> and as its name suggests, this very compact detector's uses the muons as a clear tag of most of SM  
<sup>1199</sup> and new physics interesting channels. In the original 1997 Technical Design Report (TDR) [21], the  
<sup>1200</sup> very first sentences were stating that "*Muons are an unmistakable signature of most of the physics*  
<sup>1201</sup> *LHC is designed to explore. The ability to trigger on and reconstruct muons at the highest lumi-*  
<sup>1202</sup> *nosities is central to the concept of CMS, the Compact Muon Solenoid.*" CMS participated in the  
<sup>1203</sup> discovery of the Higgs boson and the measurement of its properties and couplings together with  
<sup>1204</sup> ATLAS and is also actively involved in the search for SUSY and heavy ion collisions. Other exotic  
<sup>1205</sup> physics are also being investigated using the data collected by CMS.

<sup>1206</sup> The CMS apparatus in itself is the heaviest detector ever built starring a SI15m diameter and a  
<sup>1207</sup> 29 m length for a total weight of 14 kT. A thick 4 T solenoid magnet located at the beam interaction  
<sup>1208</sup> point hosts trackers and calorimeters. Extending in all directions around the magnet, heavy iron  
<sup>1209</sup> return yokes are installed to extend the magnetic field and support a muon system. The apparatus  
<sup>1210</sup> consists of a barrel, referring to the magnet and the detectors contained in it and the part of the muon  
<sup>1211</sup> system built directly in the cylinder around the magnet, and of 2 endcaps in the forward and back-  
<sup>1212</sup> ward region of the detector that closes the apparatus and complete the detection coverage along the  
<sup>1213</sup> beam line. A front view on the barrel is provided in Figure 2.8 while a detailed view of the apparatus  
<sup>1214</sup> is given in Figure 2.9.

<sup>1215</sup>  
<sup>1216</sup> In order to efficiently detect all long leaving particles and measure their properties with good  
<sup>1217</sup> precision, the CMS detector uses an onion like layout around of the interaction point in order to  
<sup>1218</sup> maximize the covered solid angle. As detailed in Figure 2.10, in the innermost region of the detector,  
<sup>1219</sup> closest to the interaction point, the silicon tracker records the trajectory of charged particles. Around  
<sup>1220</sup> it, the electromagnetic calorimeter (ECAL) stops and measure the energy deposition of electrons  
<sup>1221</sup> and photons. In the next layer, the hadron calorimeter (HCAL), hadrons are stopped and their energy  
<sup>1222</sup> measured. These layers are contained inside of the magnet of CMS, the superconducting solenoid.  
<sup>1223</sup> Outside of the magnet are the muon chambers embedded into iron return yokes used to control the

1224 magnetic field and gives muons, the only particles traveling completely through the whole detector, a  
 1225 double bending helping in reconstructing their energy and trajectory. Note that photons and neutral  
 1226 hadrons are differentiated from electrons and charged hadrons in the calorimeters by the fact that  
 1227 don't interact with the silicon tracker and that they are not influenced by the magnetic field.

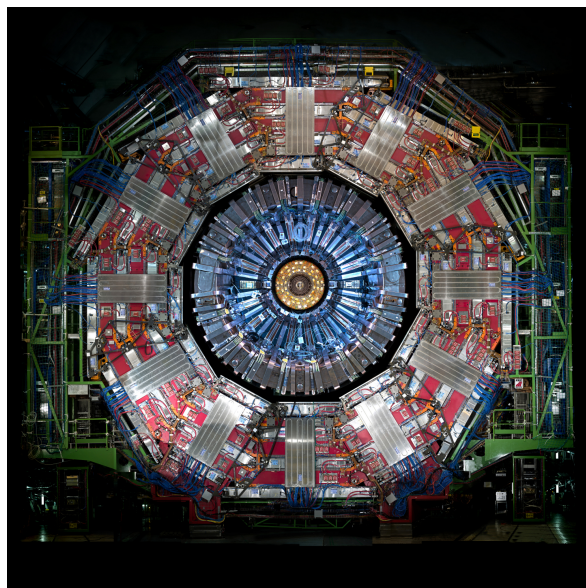


*Figure 2.8: Picture of the CMS barrel. The red outer layer is the muon system hosted into the red iron return yokes. The calorimeters are the blue cylinder inside in magnet solenoid and the tracker is the inner yellow cylinder built around the beam pipe.*

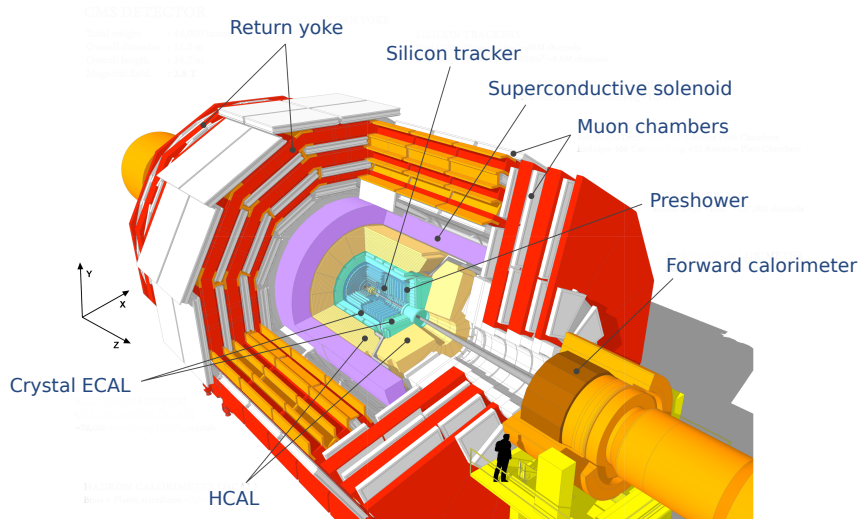


*Figure 2.9: View of the CMS apparatus and of its different components.*

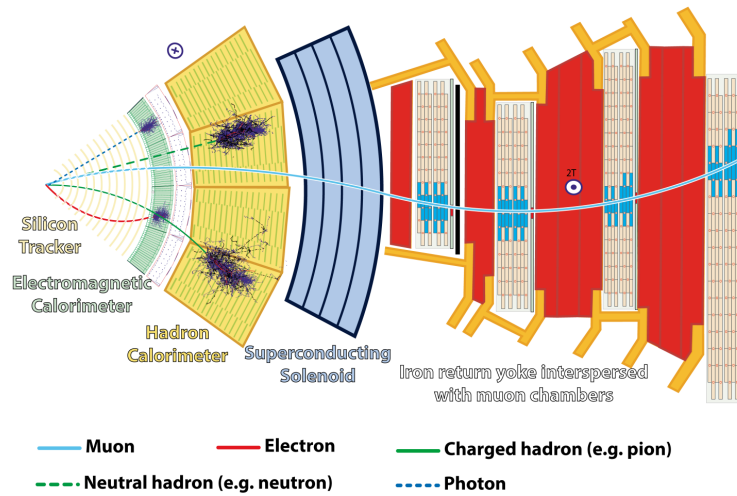


Figure 2.10: Slice showing CMS sub-detectors and how particles interact with them.

### 2.2.2.1 The silicon tracker, core of CMS

The silicon tracker visible on Figure 2.11 is divided into 2 different sub-systems: the *pixel detector* at the very core and the *microstrip detector* around it. This system is composed of 75 million individual readout channels with up to 6000 channels per squared centimeter for the pixels making it the world's biggest silicon detector. This density allows for measurements of the particle tracks with a precision of the order of  $10\ \mu\text{m}$ . This is necessary to reconstruct all the different interaction vertices with precision and have a precise measure of the curvature of the charged particles traveling through the magnetic field to estimate their charge and momentum.

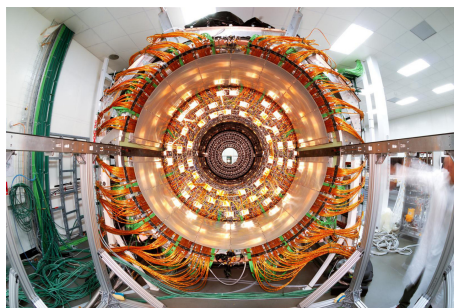
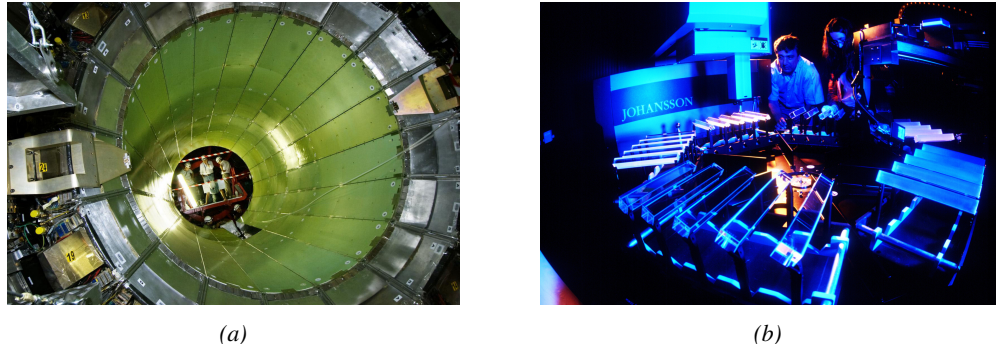


Figure 2.11: CMS tracker.

### 2.2.2.2 The calorimeters, measurement of particle's energy

The ECAL directly surrounding the tracker is composed of crystals of lead tungstate,  $\text{PbWO}_4$ , a very dense but optically transparent material used to stop high energy electrons and photons. These crystal blocks basically are extremely dense scintillators which scintillate in fast, short light bursts proportionally to the energy deposition. The light is yielded rapidly and contained at 80% in the corresponding 25 ns lasting bunch crossing. Each crystal is isolated from the other by the carbon fiber matrix they are embedded in. It is composed of a barrel containing more than 60,000 crystals

1243 and of closing endcaps containing another 15,000 crystals. In front of the ECAL endcap is installed  
 1244 a preshower detector made out of two layers of lead and silicon strip detectors to increase the spatial  
 1245 resolution close to the beam line for pion-photon and single-double photon discrimination purposes.  
 1246 Figure 2.12 shows the calorimeter inside of the magnet and the crystals.



*Figure 2.12: Figure 2.12a: picture of the ECAL. Figure 2.12b: picture of the lead tungstate crystals composing the ECAL.*

1247 The next layer is the HCAL measuring the hadrons momentum and providing indirect hints of  
 1248 non interacting neutral particles, such as neutrinos, as missing transverse momentum. Several layers  
 1249 of brass or steel are interleaved with plastic scintillators readout by photodiodes using wavelength-  
 1250 shifting fibers. The HCAL is also composed of a barrel, showed in Figure 2.13 and of endcaps. It  
 1251 also features forward calorimeters on both sides of CMS in the region very close to the beam line at  
 1252 high pseudorapidity ( $3.0 < |\eta| < 5.0$ ). The role of these forward calorimeters, made using steel and  
 1253 quartz fibers, is to measure very energetic hadrons.



*Figure 2.13: CMS hadron calorimeter barrel.*

1254 Finally, in the outer region of the apparatus, a muon system is used to trigger on potentially  
 1255 interesting event by identifying muons. Indeed, the muon system is a very important part of the  
 1256 CMS trigger infrastructure designed to efficiently select data from the enormous data flow received  
 1257 by the detectors as the LHC delivers collisions at a rate of 40 MHz with a pile-ip of 20 to 30 collisions  
 1258 per bunch crossing during Phase-I and up to 200 during Phase-II, representing billions of interactions  
 1259 per second among which a large quantity are low energy collisions that are not likely to produce new  
 1260 reactions, and which is physically impossible for nowadays technologies to cope with. Working at  
 1261 a maximum rate of 100 kHz, the trigger system is able to select the 100,000 more interesting events

by looking at the energy distribution of the interaction products and clear signatures like muons reconstructed by the muon system. the vast majority of these events will not finally be stored after physics tests are applied.

### 2.2.2.3 The muon system, corner stone of CMS

The challenge for the muon system is to provide a robust and fast measurement of muons. Three different subsystems, and soon 4 after LS2, compose the muon system as showed in Figure 2.14 in which a quadrant of the CMS detector focused on muon system. Drift Tube (DT) are found in the barrel region covering the low pseudorapidity region where particles transverse momentum is lower and Cathode Strip Chamber (CSC) are found in the endcap region covering higher pseudorapidity region closer to beam line where particles have a stronger momentum. The redundancy of the system is insured by Resistive Plate Chamber (RPC) in both the barrel and endcap region. Nevertheless, the region closest to the beam line ( $|\eta| > 1.8$ ) was not equipped with RPCs. This lack of redundancy in the high pseudo rapidity region will be solved during LS2, the following Year End Technical Stop (YETS) in 2021 and 2022, and LS3 where the necessary services, detectors and Link System, that collects the data and synchronizes them, will be installed.

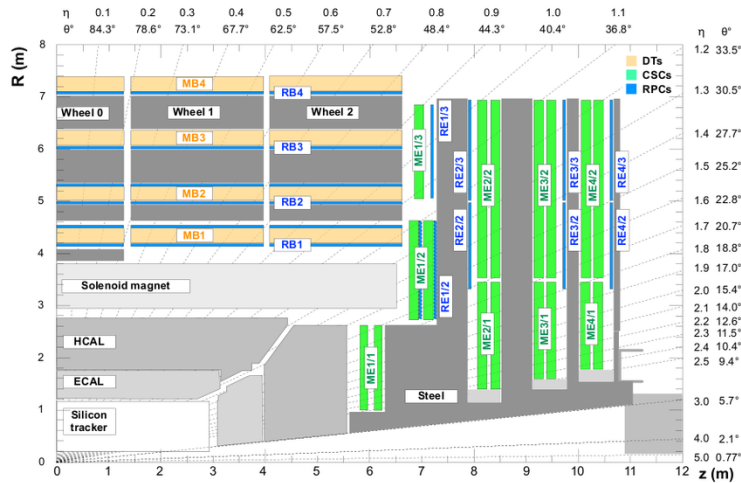
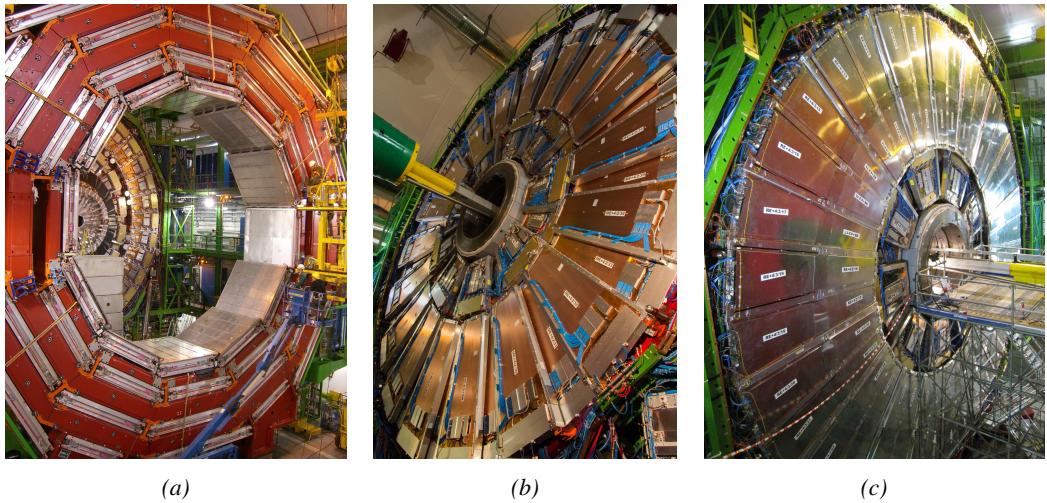


Figure 2.14: A quadrant of the muon system, showing DTs (yellow), RPCs (blue), and CSCs (green).

The barrel region is divided into 5 *wheels* made out of 4 *rings* of detectors with iron return yokes in between them whereas the endcaps are made out of 4 disks, each divided into pseudorapidity stations, 2 for CSCs (except for the first disk where 3 stations are equipped) and 3 for RPCs, although only 2 RPCs stations are equipped at present. The wheels and disks are showed in Figure 2.15. So far, each subsystem was dedicated to a particular task. DTs, in the barrel, and CSCs, in the endcaps, are used mainly for their spatial resolution. Indeed, DTs' resolution is of the order of 100  $\mu\text{m}$  along both the  $(r - \phi)$  and  $(r - z)$  components while the resolution of CSCs is similar but varies in a range from 50  $\mu\text{m}$  to 140  $\mu\text{m}$  depending on the distance to the beamline. On the other hand, RPCs are used for their time resolution as they can deliver an information on the muon tracks within 1.5 ns.

The 250 CMS DTs, found in the barrel covering the pseudorapidity region  $0 < |\eta| < 1.2$  and whose structure is shown in Figure 2.16, are composed of 3 *superlayers* of DT cells. Two of these superlayers are dedicated to measuring the  $\phi$  coordinate of the muons and while the last one

measures the  $\eta$  (or  $z$ ) coordinate. Each superlayer consists on 4 layers of 60 to 70 DT cells arranged in quincunx to allow for a precise reconstruction of the muon path through the DT layers. Each DT cell is a rectangular aluminium gas volume with a central anode wire. Cathode strips are placed on the narrow surface of the cells and electrode strips are placed on the wide surface to help shaping the electric field to ensure a consistent drift velocity of electrons in the drift volume. These detectors are operated using a 85/15 mixture of  $Ar$  and  $CO_2$ .



*Figure 2.15: Figure 2.15a: Barrel wheel with its detector rings and return yokes. Figure 2.15b: CSC endcap disk with the 2 CSC stations. The outer station is made of 10 deg detectors while the inner station is made of 20 deg detectors. Figure 2.15c: RPC endcap disk. The inner station is not equipped and the inner CSC station can be seen.*

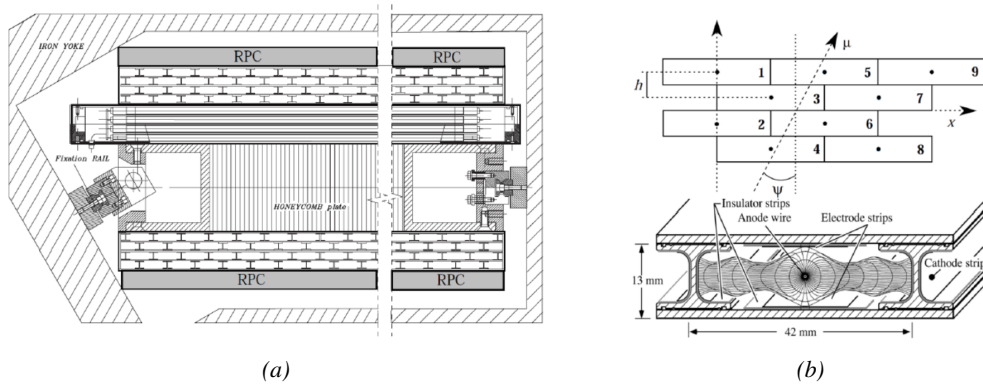


*Figure 2.16: Figure 2.16a: Cross section of a DT module showing the two superlayers measuring the  $\phi$  coordinate, perpendicular to the cross section plane, and the superlayer measuring the  $\eta$  coordinate, placed in between the two others with honeycomb and parallel to the cross section plane. The DT detector is sandwiched in between 2 RPCs whose readout strips are perpendicular to the cross section plane, measuring the  $\phi$  coordinate. Figure 2.16b: A DT cell is shown together with its electric field. The path of a muon through a superlayer is shown.*

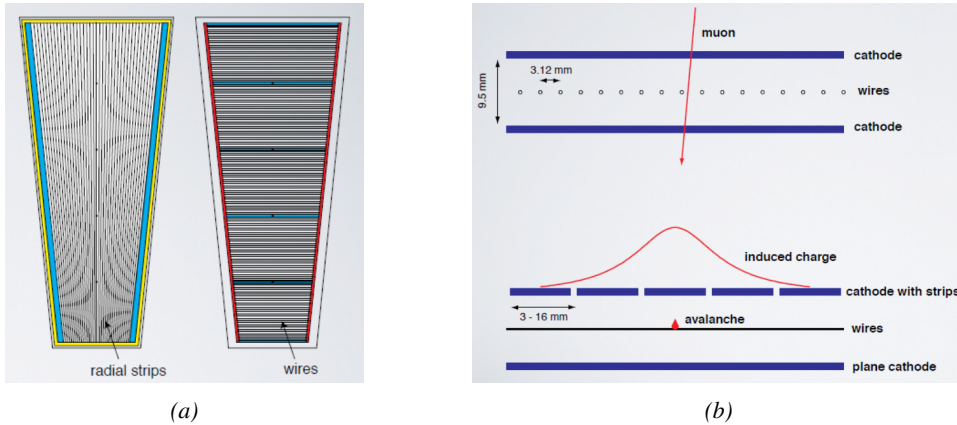


Figure 2.17: Figure 2.17a: cathode strips and anode wire layout of a CSC panel. Figure 2.17b avalanche development and charge collection by anode wires and induction on cathode strips inside of a CSC panel.

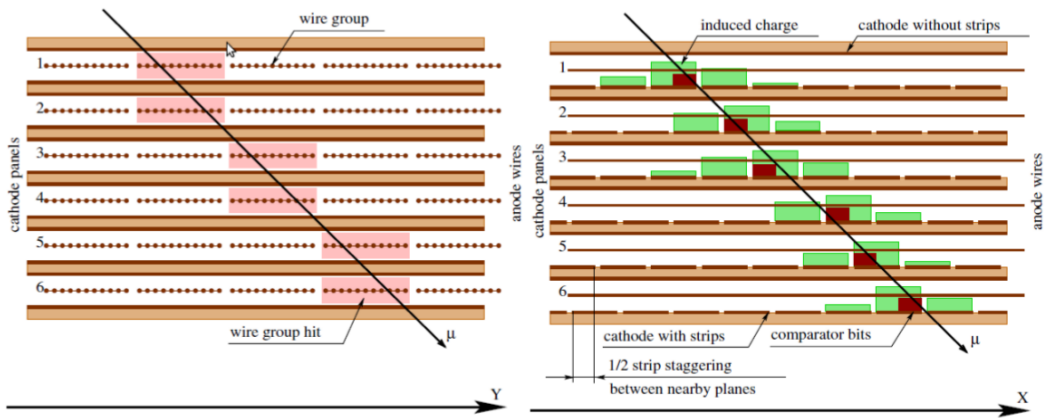


Figure 2.18: Muon track reconstruction through the 6 panels of a CMS CSC using the information of anode wire groups and cathode strip charge distribution combined with comparator bits to decide on which half strip the muon is more likely to have passed.

1295 The 540 CMS CSCs, found in the endcaps covering the pseudorapidity region  $0.9 < |\eta| < 2.5$   
 1296 and described through Figure 2.17, are composed of 6 panels of CSC, each panel consisting in  
 1297 a wide gas volume of 9.5 mm (7 mm in the case of ME1/1 station) containing anode wires and  
 1298 whose surfaces are cathodes. The top cathode is a wide copper plane of the size of the gas volume.  
 1299 The bottom cathode is divided into thin trapezoidal copper strips radially arranged to measure the  
 1300 azimuthal coordinate  $\phi$  with a pitch ranging from 8 to 16 mm. The  $0.50 \mu\text{m}$  anode wires are placed  
 1301 perpendicularly to the strips to measure radial coordinate  $r$  and are grouped by 10 to 15 with a wire  
 1302 to wire space of 3.2 mm. In the specific case of ME1/1 placed against the HCAL endcap, the  $0.30 \mu\text{m}$   
 1303 anode wires have a wire to wire distance of 2.5 mm and are not disposed perpendicularly to the strips  
 1304 but slightly tilted by an angle of 29 deg to compensate for the lorentz force due to the very strong  
 1305 local magnetic field of 4 T. These detectors are operated with a 40/50/10 mixture of Ar, CO<sub>2</sub> and  
 1306 CF<sub>4</sub>. Combining the information of the multiple CSC panels, the detectors achieve a very precise  
 1307 measurement of the muon track.

Despite their excellent spatial resolution, the wire chambers (DTs and CSCs) are limited in terms of time resolution by the fact that the charge needs to drift towards the anode wire and be collected before having the confirmation that a particle was detected as the drift volume is not used to develop avalanches. Indeed, the stronger electric field close to the anode wire triggers the avalanche and the gain of the detector. Due to the drift, the time resolution is thus limited at best to approximately 2 to 3 ns. In addition, even though the intrinsic time resolution of the tracking chambers is rather good compared to the 25 ns in between successive collisions, the processing time of the trigger system doesn't allow for very fast triggering as it provides a time precision of only 12.5 ns. Thus, detectors fully dedicated to timing measurement have been installed as a redundant system. These detectors are RPCs, also gaseous detectors but that use current induction instead of charge collection allowing for a time resolution of the order of 1.5 ns only. Theoretically, depending on the design used, RPCs could reach a time resolution of the order of 10 ps but in the context of LHC where bunch crossing happen every 25 ns, a time resolution of 1.5 ns is sufficient to accurately assign the right bunch crossing to each detected muon.

The 1056 RPCs equipping the CMS muon system both in the barrel and endcap regions and covering the pseudorapidity region  $0 < |\eta| < 1.6$  are composed of two layers of RPC *gaps* as described in Figure 2.19. Each gap consists in two resistive electrodes made out of 2 mm thick Bakelite enclosing a 2 mm thick gas volume containing a 95.2/4.5/0.3 mixture of  $C_2H_2F_4$ ,  $i - C_4H_{10}$  and  $SF_6$ . Due to this geometry, the electric field inside of a gap is homogeneous and linear at every point in the gas translating into a uniform development of avalanches in the gas volume as soon as a passing muon ionises the gas. The two gaps sandwich a readout copper strip plane. A negative voltage is applied on the outer electrodes, used as cathodes, and the inner electrodes, the anodes, are simply connected to the ground as well as the readout panel that picks up the current induced by the accumulated charge of the growing avalanches in one or both of the gas gaps. This OR system allows for a lower gain (i.e. a lower electric field) on both gaps to reach the maximal efficiency of such a detector.

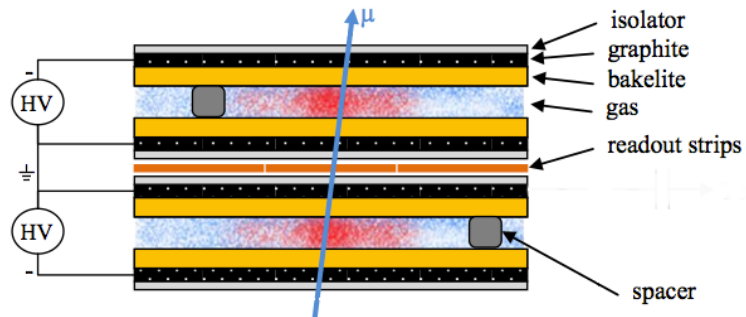


Figure 2.19: Double gap layout of CMS RPCs. Muons passing through the gas volumes will create electron-ion pairs by ionising the gas. this ionisation will immediately translate into a developing avalanche.



# 3

1334

1335

## Muon Phase-II Upgrade

1336 The very first proton beam successfully circulated in the LHC in September 2008 directly followed  
1337 by an incident leading to mechanical damage that would delay the LHC program for a year until  
1338 November 2009, the very first collisions at a center-of-mass energy of 7 TeV taking place in March  
1339 2010. The energy of the beam would be increased after a First Long Shutdown (LS1) starting early  
1340 2013 after less than 3 years of data taking. Nevertheless, this first data taking period at only 7 TeV  
1341 was sufficient to claim the discovery of a new particle compatible with the Higgs boson in July 2012.  
1342 During the 2 years of shutdown, the upgrade of the accelerator allowed for several maintainances  
1343 along the beam pipes, repair and consolidation of magnet connection and high-current splices. But  
1344 not only the LHC was upgraded. Indeed, the experiments at the 4 collision points also took the  
1345 advantage of this time to upgrade their system in prevision of the next LHC run (Run-II) until  
1346 2018 and the Second Long Shutdown (LS2) as the luminosity and energy of the beam would be  
1347 continuously increasing. By the end of Run-II, the luminosity will have reached twice its nominal  
1348 value when the center-of-mass energy has already got close to its nominal value by reaching an  
1349 historical 13 TeV for the first time in 2017.

1350 The next long shutdown will occur at the end of this year and will again be the occasion for sim-  
1351 ilar maintenance and consolidation in prevision of Run-III and the future upgrade of LS3. Still, the  
1352 main occupation of LS2 on LHC side will be the upgrade of LHC injectors. On the experiments side,  
1353 LHCb and ALICE will, in a very tight schedule, implement major upgrades while ATLAS and CMS  
1354 will wait until LS3 to upgrade their detectors in prevision of high luminosity *LHC-Phase-II*. ALICE  
1355 main challenge is an upgrade of their apparatus to cope with the 50 kHz  $Pb - Pb$  collisions. Simi-  
1356 larly, LHCb will upgrade their frontend readout electronics to cope with the full 40 MHz collisions  
1357 delivered by LHC. ATLAS will perform standard maintenance and CMS will focus on the urgent up-  
1358 grade of the pixel detector and on the installation of new muon detectors in order to take profit of LS2  
1359 time to mitigate the upgrade of detectors foreseen during LS3. Run-III will start in 2021 with the LHC  
1360 at its nominal center-of-mass energy and will bring LHC-Phase-I to an end at the end of 2023. By  
1361 then the luminosity will only increase to reach 2.5 times the nominal luminosity but during these 3  
1362 years of run, the LHC will deliver as much integrated luminosity as what what brought during the al-

most 7 years of both Run-I and II of data taking. Phase-I will end with an overall  $300 \text{ fb}^{-1}$  delivered.

1363  
1364

### 1365 3.1 High Luminosity LHC and muon system requirements

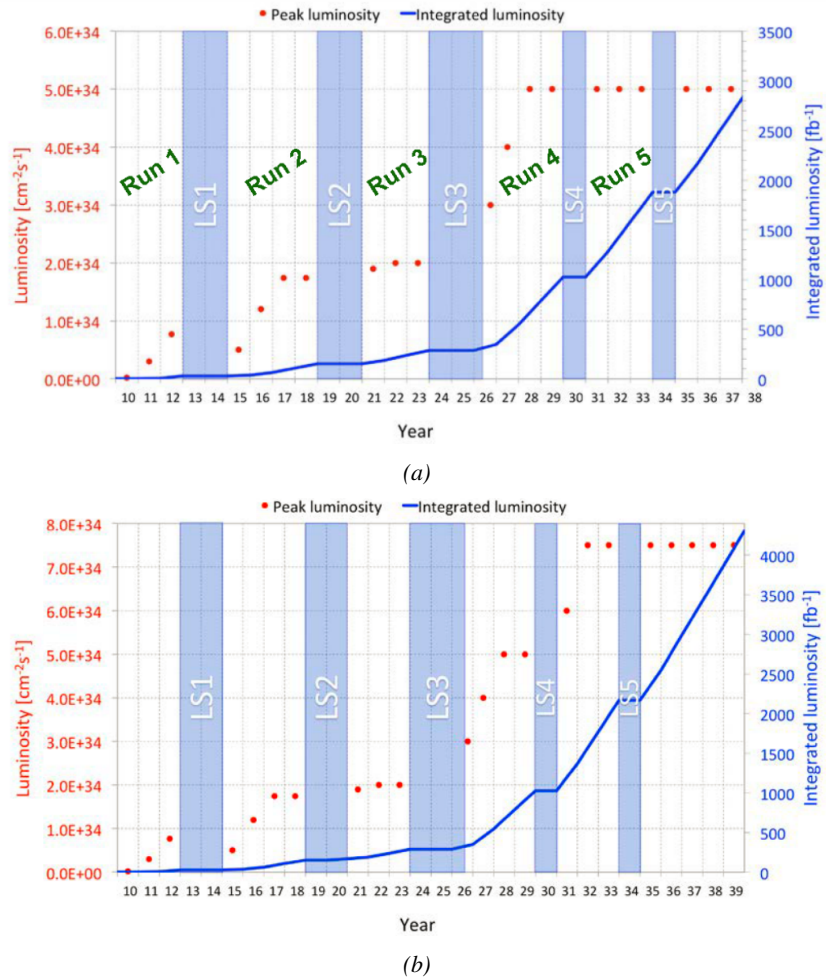


Figure 3.1: Detailed timeline projection of for LHC and HL-LHC operation until 2039 showing the evolution of the instantaneous and integrated luminosity as designed (Figure 3.1a) and in the ultimate case where the instantaneous luminosity is increased to  $7.5 \times 10^{34} \text{ cm}^{-2}\text{s}^{-1}$  (Figure 3.1b) [20, 22].

1366 After approximately 15 years of operation, the LHC will undergo a new series of upgrade during  
1367 the LS3 in order to boost its discovery potential as showed in Figure 3.1. This moment onward is  
1368 what is referred to HL-LHC or Phase-II. The goal is to aim for a luminosity 5 to 7 times stronger  
1369 than the nominal one trying to reach even 10 times this value if possible. Increasing the luminosity  
1370 means that the beam size at the collision points needs to be reduced to boost the number of collisions  
1371 per bunch crossing. For this purpose, new focusing and bending magnets, and collimators will be  
1372 installed at the collision points as well as newly developed "crab cavities" that will tilt the particle

1373 bunched just prior to the collisions by giving them transverse momentum and thus increasing their  
 1374 meeting area. In addition, the full proton injection line will be upgraded.

1375 Over its full lifetime, the HL-LHC is expected to deliver an outstanding integrated luminosity of  
 1376  $3000 \text{ fb}^{-1}$  leading, in the case of Higgs studies to measuring the couplings of the boson to a precision  
 1377 of 2 to 5% thanks to the estimated 15 millions of Higgs created every year providing a more precise  
 1378 measurement of potential deviations from the theoretical predictions. SUSY and heavy gauge boson  
 1379 studies would also see their mass range limits pushed away by at least 1 TeV and could lead to a new  
 1380 breakthrough. SUSY is a particularly important topic as it could give an answer to why the Higgs  
 1381 boson can stay so light while coupled to heavy particles by introducing the contributions of the super  
 1382 partners on top of providing dark matter candidates. Finally, the increase of luminosity will give the  
 1383 possibility to investigate "exotic" mode like for example the models introducing extra dimensions to  
 1384 explain the hierarchy problem.

1385 On the experiments side, the pile-up (PU) will be increased up to 150 to 200 interactions per  
 1386 bunch crossing in ATLAS and CMS, making necessary an strong upgrade of the trigger system and  
 1387 of the inner trackers and of the calorimeters. Both ATLAS and CMS will also need to upgrade  
 1388 the muon trigger at the level of the endcaps mainly focusing on the coverage near the beam line in  
 1389 order to increase the detection acceptance and event selection. Moreover, the increased luminosity  
 1390 will also lead to an increased background rate and a faster ageing of the detectors. This PhD work  
 1391 takes place into this very specific context of muon detector consolidation and certification for the  
 1392 HL-LHC period in order to provide the CMS experiment with robust new detectors and confirm that  
 1393 the present system will survive through the next 20 years of HL-LHC.

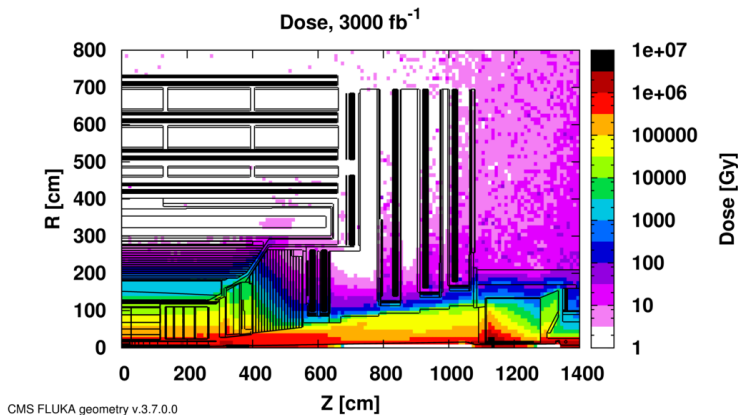


Figure 3.2: Absorbed dose in the CMS cavern after an integrated luminosity of  $3000 \text{ fb}$ . Using the interaction point as reference,  $R$  is the transverse distance from the beamline and  $Z$  is the distance along the beamline.

1394 The end of 2018 will mark the beginning of LS2 and the start of Phase-II upgrade activities.  
 1395 From the HL-LHC period onwards, i.e. past LS3, the performance degradation due to integrated  
 1396 radiation as well as the average number of inelastic collisions per bunch crossing, seen as pile-up  
 1397 into the detectors' readout that far exceeds this of the original LHC plans, will rise substantially and  
 1398 become a major challenge for all of the LHC experiments, like CMS, that were forced to address  
 1399 an upgrade program for Phase-II [23]. Dealing with the data from the muon detectors will force  
 1400 to upgrade the detectors and electronics towards the most recent technologies. Simultaneously, this  
 1401 will push new latency requirements onto the Level-1 trigger and the Data Acquisition (DAQ) that

will only be fulfilled by upgrading the system with electronics having deeper buffering and faster processing. Simulations of the expected distribution of absorbed dose in the CMS detector under HL-LHC conditions show, in Figure 3.2, that detectors placed close to the beam line will have to withstand high irradiation, the radiation dose being of the order of a few tens of Gy.

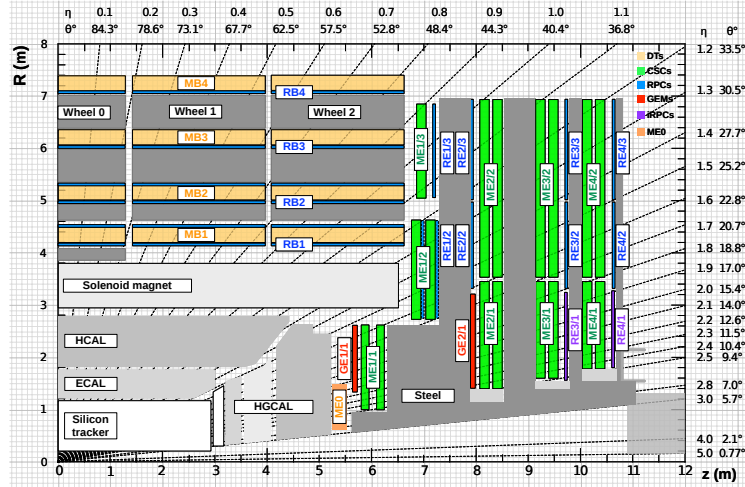


Figure 3.3: A quadrant of the muon system, showing DTs (yellow), RPCs (blue), and CSCs (green). The locations of new forward muon detectors for Phase-II are contained within the dashed box and indicated in red for GEM stations (ME0, GE1/1, and GE2/1) and dark blue for improved RPC (iRPC) stations (RE3/1 and RE4/1).

The increase of irradiation close to the beam line will affect the background rate seen by the muon detectors in this area and tracking muons will prove to be difficult as this region is not yet equipped with all the detectors that were already foreseen for Phase-I. Improving this situation will come with the increase of hit numbers recorded along the particle track to reduce the ambiguity on muon versus background detection. Moreover, the measurement of small production cross-section and/or decay branching ratio processes, such as the Higgs boson coupling to charge leptons, and in particular to muons, or the  $B_s \rightarrow \mu^+ \mu^-$  decay, is of major interest and specific upgrades in the forward regions of the detector will be required to maximize the physics acceptance to the largest possible solid angle.

To ensure proper trigger performance within the present coverage, the muon system will be completed with new chambers and the electronics of the present system will need to be upgraded to ensure an efficient triggering. Figure 3.3 shows the addition of Gas Electron Multiplier (GEM) and improved RPC (iRPC) in the pseudo-rapidity region  $1.6 < |\eta| < 2.4$  to complete the redundancy of the already existing CSCs as originally scheduled in the CMS Technical Proposal [24]. A first step into this direction will be taken by installing GEMs on the first endcap disk in position GE1/1 during LS2, during which preparations for the future installation of more GEMs and RPCs will take place by installing the needed services. During the YETS following LS2, iRPCs will be installed on the third and fourth endcap disks in position RE3/1 and RE4/1, and more GEMs will equip the second endcap in position GE2/1 and the inner layer, closest to the HCAL endcap called ME0 during LS3, finally completing the redundant coverage of the muon system and extending it a little by extending the reach to  $|\eta| = 2.8$ , the redundancy in the region  $2.4 < |\eta| < 2.8$  being maintained by the 6 GEM layers contained in each ME0 detector that provide enough tracking points to efficiently reject

<sup>1428</sup> neutron-induced background.

<sup>1429</sup> Nevertheless, the region beyond  $|\eta| > 2.8$  and extending to  $|\eta| = 5.0$  only is covered by the  
<sup>1430</sup> forward HCAL detectors and lack redundant muon detector coverage. Extensions of the tracker in  
<sup>1431</sup> the context of HL-LHC will increase its coverage up to  $|\eta| = 4.0$  but the identification of muons and  
<sup>1432</sup> measurement of their energy with reasonable precision only using the tracker is nearly impossible.  
<sup>1433</sup> Thus, this increased tracker coverage range needs to be put in parallel with a matching muon detector  
<sup>1434</sup> and will open doors to multi-lepton final states in which leptons are likely to have a low transverse  
<sup>1435</sup> momentum and to be found near the beam line.

<sup>1436</sup>

<sup>1437</sup> Finally, as the muon system is composed only of gaseous detectors, strong environmental concerns  
<sup>1438</sup> have risen over the last years as the European directives will restrict the use of fluorine based  
<sup>1439</sup> gas mixtures. Both the CSC and RPC subsystems, using  $CF_4$ ,  $C_2H_2F_4$ , or  $SF_6$ , will need to adapt  
<sup>1440</sup> their working gas in order to strongly reduce the greenhouse potential of the mixtures released into  
<sup>1441</sup> the atmosphere due to gas leaks.

## <sup>1442</sup> 3.2 Necessity for improved electronics

<sup>1443</sup> Drift Tubes and Cathode Strip Chambers are important components used to identify and measure  
<sup>1444</sup> muons, especially thanks to their spatial resolution of the order of  $100\ \mu m$ . Nevertheless, the lumi-  
<sup>1445</sup> nosity and irradiation during HL-LHC will cause serious event loss and ageing on the electronics of  
<sup>1446</sup> these subsystems that will comprise the triggering and data transferring needs of CMS. Thus, elec-  
<sup>1447</sup> tronics upgrade are foreseen to address these expected problems. While only the RPCs' electronic  
<sup>1448</sup> system is able to operate under Phase-II requirements, DTs and CSCs will need to improve their  
<sup>1449</sup> trigger accept rate and latency to ensure that Level-1 trigger threshold stays at the same level [25],  
<sup>1450</sup> and DAQ data transfer rate, that respectively need to achieve a minimum of  $500\ kHz$ , get down to  
<sup>1451</sup>  $12.5\ \mu s$  [26], and increase to  $1082\ Gbit/s$  DTs and to  $1026\ Gbit/s$  for CSCs. As of today, the Level-  
<sup>1452</sup> 1 trigger accept rate of DTs doesn't reach  $300\ kHz$  while this of CSCs is below  $250\ kHz$  but the  
<sup>1453</sup> foreseen upgrades are expected to increase the rate way beyond the requirement in the of DTs and  
<sup>1454</sup> up to  $4\ MHz$  for CSCs [23].

<sup>1455</sup> The first version of Minicrate electronics (MiC1) used by DTs don't allow for high enough  
<sup>1456</sup> trigger rate. In addition to this problem, it was showed that these electronics contain components  
<sup>1457</sup> that are not radiation hard enough to sustain HL-LHC conditions and thus, a too large number of  
<sup>1458</sup> channels may fail due to radiations. Considering the most optimistic scenario, at least 19% of the  
<sup>1459</sup> channels could have failed by LS4, as explicitated in Figure 3.4, far before the end of the HL-LHC  
<sup>1460</sup> campain. The MiC1 will be replaced on each detector by an improved version referred to as MiC2  
<sup>1461</sup> while front-end electronics and high-voltage modules will not need any replacement. On the other  
<sup>1462</sup> hand, CSCs showed that there electronics would be able to live through the 10 years of Phase-II but  
<sup>1463</sup> the limited buffer depth might cause memory overflows and readout inefficiencies with a fraction  
<sup>1464</sup> of event loss ranging from 5 to more than 10% at an instantaneous luminosity similar to which of  
<sup>1465</sup> HL-LHC depending on the expected background, as showed on Figure 3.5 through the different  
<sup>1466</sup> detector positions. Thus the replacement of CSCs' cathode front-end boards (CFEBs) by digital  
<sup>1467</sup> ones, DCFEBS, with deeper buffer would permit to make event loss negligible and satisfy HL-LHC  
<sup>1468</sup> requirements [23].

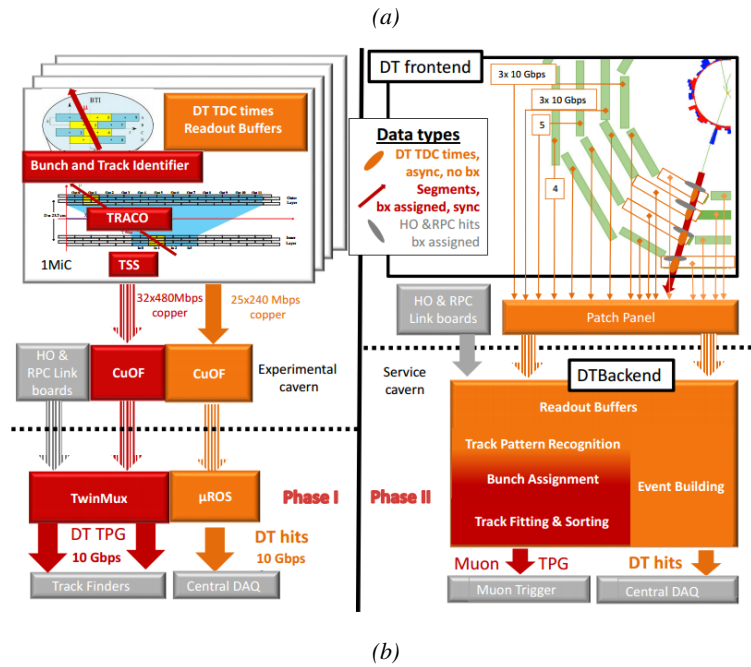
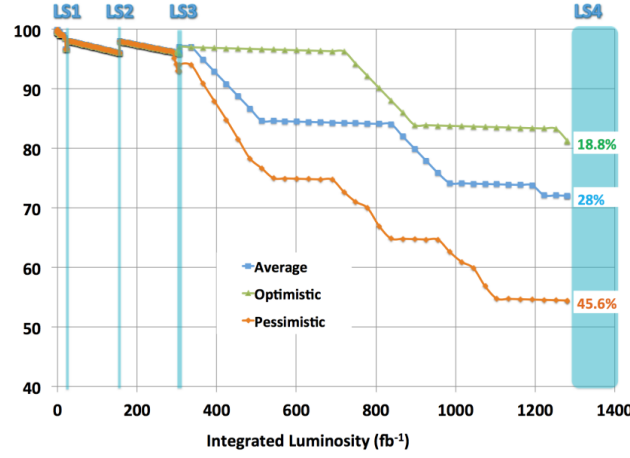


Figure 3.4: Figure 3.4a: Extrapolated fraction of failing channels of the present DT MiC1 electronics as a function of the integrated luminosity for different scenari until LS4. Figure 3.4b: Comparison of the current (left) and upgraded (right) DT data processing. So far, the data is sent to service cavern of CMS facility via copper-to-optical-fiber translators (CuOF) by each MiC1. There, data including RPCs and outer hadron calorimeter is combined into trigger primitives (TPG) and transmitted by the TwinMux system to CMS Track Finder. The time-to-digital converter (TDC) data is collected and sent to the CMS data acquisition system (DAQ) by the micro read-out server ( $\mu$ ROS). After the upgrade, the TDC data will be sent via optical links to a patch panel inside the experimental cavern by each MiC2, and transferred to the back-end, where triggering and event building will be performed.

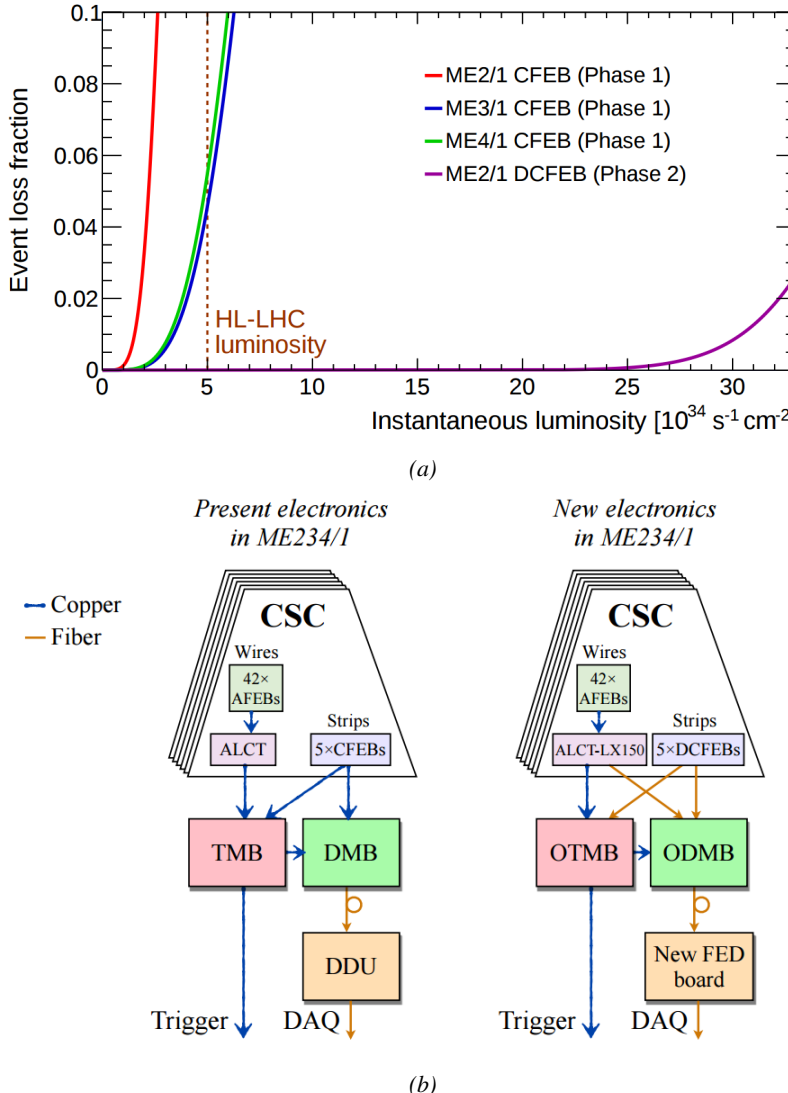
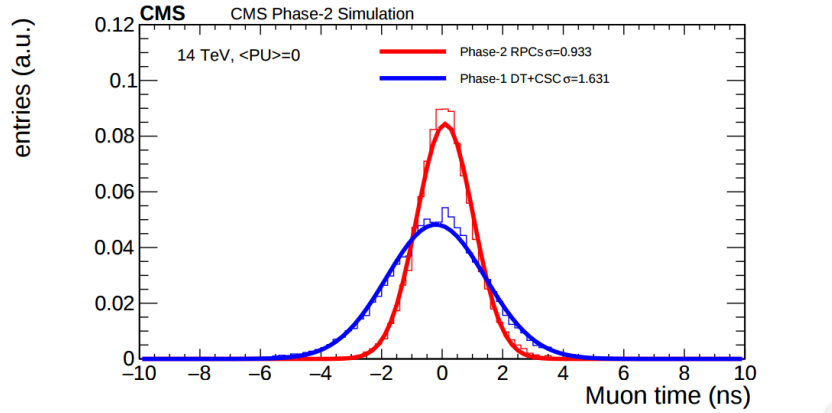


Figure 3.5: Figure 3.5a: The event loss fractions as a function of the instantaneous luminosity is compared for CFEBs (Phase-1) and DCFEBs (Phase-II) at different CSC locations. HL-LHC luminosity is marked with the dashed brown line. Figure 3.5b: Comparison of the current (left) and upgraded (right) CSC data processing. A part of the connections in between ALCTs and DCFEBs, and the trigger mother boards (TMBs) and data acquisition mother boards (DMBs) will be upgraded toward optical data transfer. The detector dependent units (DDUs) used as interface in between CSCs' front-end electronics and the CMS DAQ will be replaced by new FED boards.

All these new DT and CSC electronics will be connected to the trigger electronics via optical links to ensure a faster communication. The main change will come from the new DT minicrate modules which will not anymore be responsible for trigger and event building logic which will be transferred to the back-end electronics instead located in the service cavern via the patch pannels to which the Time-to-Digital Converter (TDC) data will be sent. The trigger and data transfer logic will barely change for CSCs. The existing copper cable connections of cathode and anode FEBs (CFEBs,

and AFEBs which data is transmitted through the ALCTs) toward the trigger and data mother boards (TMBs and DMBs) will simply be replaced by optical fibers and the TMBs and DMBs upgraded with optical versions (OTMBS and ODMBs). As a new feature, the full anode wire data from ALCTs will be sent to the ODMBs causing a lack of FPGA memory resources in these ALCT boards that will thus need replacement.



*Figure 3.6: Comparison of the simulated time residuals in between reconstructed and true muon times without (blue) and with (red) the upgraded RPC link system.*

The upgrade on the side of Resistive Plate Chambers will then not come from their on-board electronics but from the Link System located in the service cavern of CMS and that connects the front-end electronics data of RPCs into CMS trigger processors. The main motivation for such an upgrade is that the electronic board composing the link system are built using obsolete components and weak components that can easily suffer from the electromagnetic noise. These components may be the source of failing channels throughout Phase-II. Moreover, these link boards were originally designed only to match RPC digitized signals with the corresponding bunch crossing. Due to this feature, the time resolution of the full RPC chain is thus limited to 25 ns and does not exploit the full time resolution of the detectors. This would make the synchronization of the RPC system easier and allow to have a finer offline background removal within the 25 ns in between bunch crossings thanks to the order of magnitude gained in terms of time resolution.

Upgrading RPC link system will require the installation of 1376 new link boards and 216 control boards. The new boards will make use of the recent progress made with fast FPGAs and will be a great improvement to the ASICs formerly used as they will be able to process signals from several detectors in parallel. The benefit from using the full RPC time resolution thanks to the upgraded link system can be seen through Figure 3.6 where the resolution of the RPC system itself is better than that of DTs and CSCs that was used until now.

### 3.3 New detectors and increased acceptance

In the present muon system, the redundancy of was assured by RPCs used for their good timing performances. The extension of the muon system towards higher pseudo-rapidity in order to complete the redundancy in this very region and to contribute to the precision of muon momentum measurements will require muon chambers with a spatial resolution less or comparable to the contribution

muon of multiple scattering through the detector volume [21]. Most of the plausible physics is covered only considering muons with  $p_T < 100$  GeV thus, in order to match CMS requirements, a spatial resolution of  $\mathcal{O}(\text{few mm})$  will be necessary for the proposed new RPC stations while the GEMs will need a resolution better than 1 mm, as showed by the simulation in Figure 3.7.

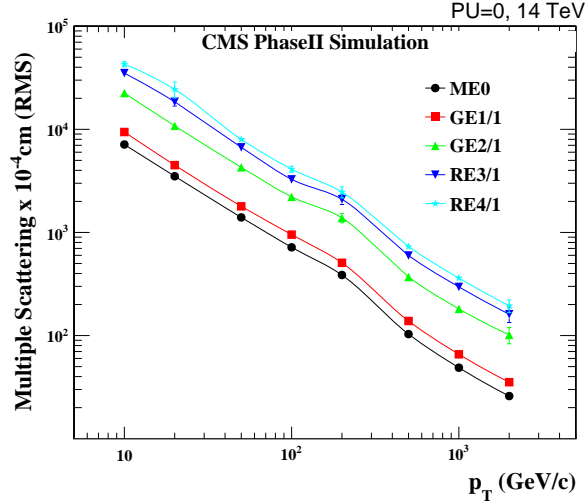


Figure 3.7: RMS of the multiple scattering displacement as a function of muon  $p_T$  for the proposed forward muon stations. All of the electromagnetic processes such as bremsstrahlung and magnetic field effect are included in the simulation.

### 3.3.1 Improved forward resistive plate chambers

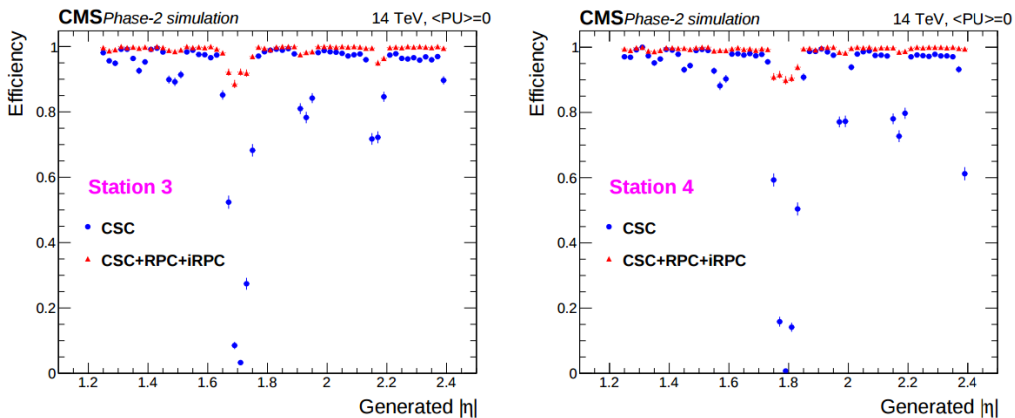


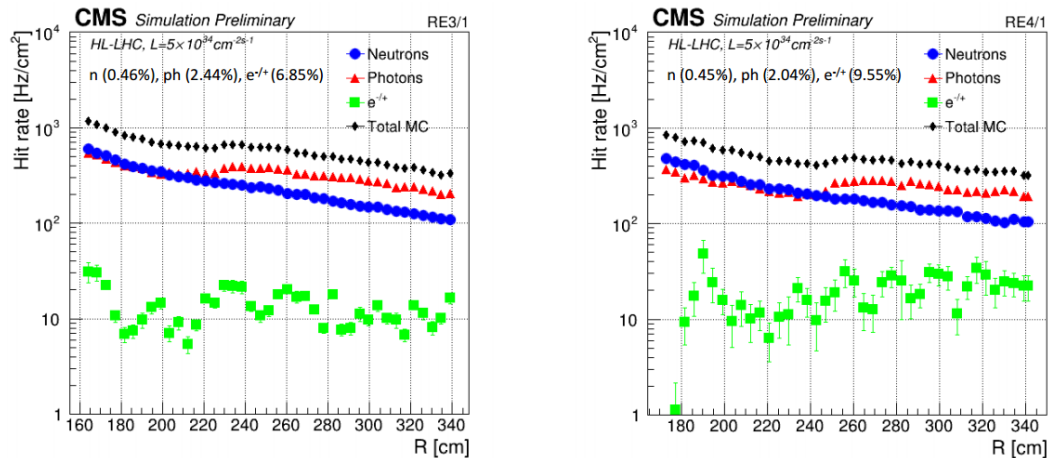
Figure 3.8: Simulation of the impact of RPC hit inclusion onto the local trigger primitive efficiency in station 3 (left) and station 4 (right). The contribution of iRPC starts above  $|\eta| = 1.8$ .

Figure 3.3 shows that the iRPCs that will equip the third and fourth endcap disks in position RE3/1 and RE4/1 will finally be the partners of the CSCs in position ME3/1 and ME4/1 and complete Phase-I plans but bringing the needed upgrades in the scope of Phase-II as the older chambers are

not suitable to equip the forward region of CMS due to HL-LHC rates and charge deposition. By completing the redundancy, more track along the muon trajectory will be available and the lever arm will be improved. The benefits from extending the redundancy of the muon system with iRPCs to the forward most region is showed in Figure 3.8 in which the trigger efficiency is showed with and without RPCs in which it is possible to see that the efficiency of CMS trigger with the complete redundancy is improved is above 95% in the region  $|\eta| > 1.8$  as the iRPCs help filling the holes in the CSC system.

1517

The detectors that will be installed in the coming years will be similar to the already existing RPC system. 18 of the new chambers, each spanning  $20^\circ$  in  $\varphi$  around the beam axis with 96 radially oriented trapezoidal read-out strips, will cover each muon endcap disk leading to the production of 72 iRPCs. The main difference with the old RPC chambers is that these detectors will not have readout strips segmented in  $\eta$  as by using fast front-end electronics the strips will be read-out on both sides allowing for a radial spatial resolution of the order of 2 cm in order to contribute to the better reconstruction of muon in the forward region where the bending of muons by the magnetic field is low. This is motivated by the fact that, in the case a  $\eta$  segmentation was used, at least 5 pseudorapidity partitions would have been necessary to reach the minimal radial spatial resolution ( $\approx 20$  cm). Having only one strip read-out from both along the chamber reduces by 60% the total number of channels and the necessary cabling and allows for a better spatial resolution. The strip pitch will range from 6.0 mm (5.9 mm) on the high pseudo-rapidity end to 12.3 mm (10.9 mm) on the low one on position RE3/1 (RE4/1). The spatial resolution in the direction perpendicular to the strips should reach approximately 3 mm, better than the minimal needed resolution (Figure 3.7), and the overall time resolution of the new installation will be equally 1.5 ns, as for the present due to the same link system being used.



*Figure 3.9: Expected hit rate due to neutrons, photons, electrons and positrons at HL-HLC instantaneous luminosity of  $5 \times 10^{34} \text{ cm}^{-2}\text{s}^{-1}$  in RE3/1 and RE4/1 chambers. The sensitivities of iRPCs used in the simulation for each particle are reported and differ from one endcap disk to another as the energies of the considered particles varies with the increasing distance from the interaction point.*

Nevertheless, having only a single strip instead of pseudo-rapidity segmentation will increase the probability of double hits in the same channel. This probability was estimated to be low enough

as it shouldn't exceed 0.7%. This estimation was made assuming an average hit rate per unit area of 600 Hz/cm<sup>2</sup> in the iRPCs (see Figure 3.9), a cluster size (average number of strips fired per muon) of 2, a strip active area of 158.4 × 0.87 cm<sup>2</sup> and a safety factor 3 leading to an estimated rate per strip of 380 kHz corresponding to an average time interval of 2600 ns in between 2 consecutive hits. The time for a signal to go through the full strip length is about 10 ns to which can be added 1 ns of dead time and 2 TDC clock cycles of 2.5 ns for a minimal time interval of 16 ns necessary to avoid ambiguities. The probability of having ambiguous double hits in a strip in then the ratio in between this minimal time interval in between 2 consecutive hits and the average time interval estimated from the rate the detectors are subjected to.

The instantaneous luminosity at HL-LHC being very high, the rates at the level of the new chambers needed to be simulated in order to understand the necessary requirements for these detectors. The simulated results for different background components (neutrons, photons, electrons and positrons) are showed in Figure 3.9 assuming known sensitivities to these particles. It is showed that on average over the iRPC areas the rates would be of the order of 600 Hz/cm<sup>2</sup> (600 Hz/cm<sup>2</sup> seen in RE3/1 and 480 Hz/cm<sup>2</sup> in RE4/1) [27]. Thus, taking into account a safety factor of about 3, it was decided that improved RPCs should at least be certified for rates reaching 2 kHz/cm<sup>2</sup> which would be achieved thanks to several improvements on the design and on the electronics. The detectors design will be based on the existing RPC design as they will be double gaps. Similarly to the existing RPC system, the electrode material will be HPL although the thickness of the electrodes and of the gas gap will be reduced to 1.4 mm as a thinner gas gap leads to a decrease of deposited charge per avalanche as showed in Figure 3.10. The smaller the gas gap, the more the detector becomes sensitive to gap non-uniformities across the electrode planes making a gap of 1.4 mm a good compromise in between these two competing factors.

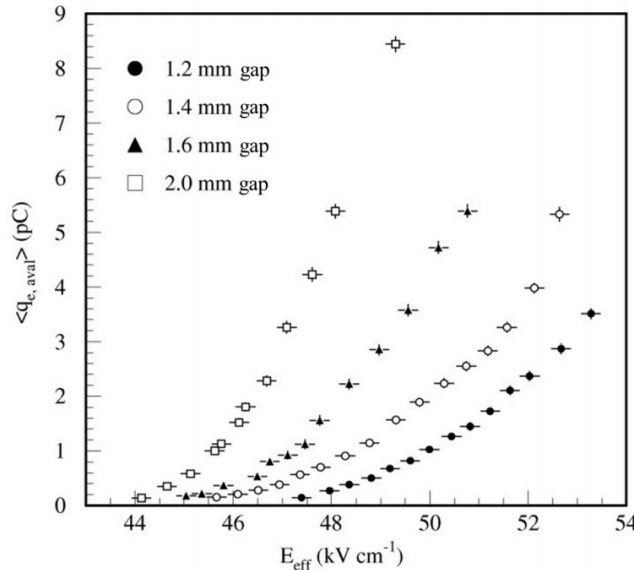


Figure 3.10: Measured average charge per avalanche as a function of the effective electric field for different gas gap thickness in double gap RPCs using HPL electrodes.

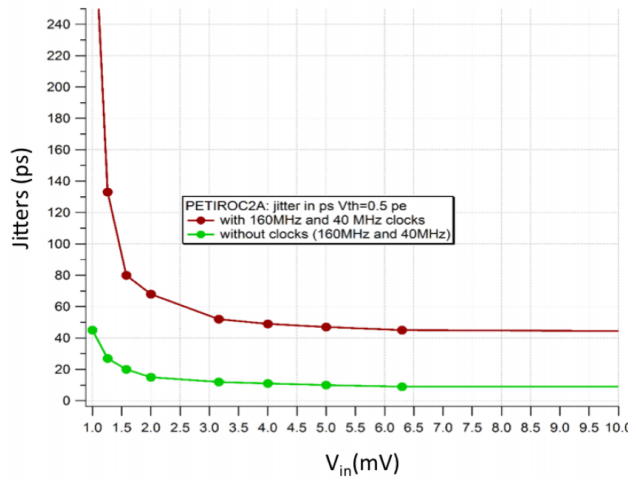


Figure 3.11: The PETIROC time jitter as a function of the input signal amplitude, measured with and without internal clocks.

A lower charge deposition inside of the detector volume means a slower ageing and a longer lifetime for detectors subjected to high irradiation. But, in order to take advantage of the lower detector gain, more sensitive electronics are required so that the part of gain that was formerly done in the gas volume can be moved to the electronics. Achieving this with the technology developed more than 10 years ago for the present system is not possible as the signal over noise ratio of such electronics doesn't allow to detect charges as low as 10 fC. Moreover, the new front-end electronics will need to be radiation hard to survive to more than 10 years of HL-LHC conditions. The new technology that has been chosen is based on the PETIROC ASIC manufactured by OMEGA and is a 64-channel ASIC called CMS RPCROC on which the original SiGe technology will be replaced by CMOS to increase its radiation hardness while keeping fast pre-amplification and discrimination with a very low jitter that can reach less than 20 ps if no internal clock is used, as can be seen from Figure 3.11. The ASIC is associated with an FPGA which purpose is to measure time thanks to a TDC with a time resolution of 50-100 ps developed by Tsinghua University and that will provide a measurement of the signal position along the strip with a precision of a few cm by measuring the signal timing on both ends of the strips. In order to read-out all 96 strips, 3 ASICs and 3 TDCs, each having 64 channels, are hosted on a front-end board attached to the chamber.

1575

1576 [Wait for the analysis of 2018 GIF++ data to add interesting information about the time and  
1577 spatial resolution measured during test beam periods.]

1578

### 1579 3.3.2 Gas electron multipliers

1580 In the region closer to the interaction point where the spatial resolution is requested to be better  
1581 than 1 mm for the new detectors (at least for GE1/1 and ME0, GE2/1 being in the same order of  
1582 requested spatial resolution than the new iRPCs that will equip the third and fourth endcaps), the  
1583 choice has been made to use triple GEMs, micro pattern gaseous detectors, in the place of RPCs.  
1584 The GE1/1 project had been the first to be approved and demonstrators had been installed in CMS

already during LS1. The rest of the detectors will be installed during LS2 while the GE2/1 and ME0 projects are still under development. ME0, GE1/1 and GE2/1 will be installed respectively next to the HCAL endcap, on the first and on the second muon endcap disks as can be seen from Figure 3.3.

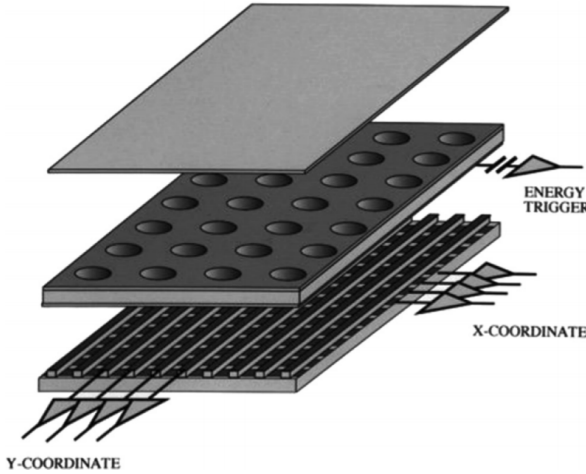


*Figure 3.12: Schematics of a GEM showing the cathode on top, the GEM foil separating the gas volume into the drift region, in between the cathode and foil, and the induction region, in between the GEM foil and the anode, and the anode on which a 2D read-out is installed. A negative voltage is applied on the cathode while the anode is connected to the ground.*

Gas Electron multipliers are gaseous detectors [28] which gas volume is confined in between 2 planar electrodes, the anode serving as read-out panel. The gas volume is divided in 2 or more regions by a single or multiple *GEM foils* as showed in Figure 3.12. These foils are very thin, of the order of a few tens of  $\mu\text{m}$ , and are pierced with holes as can be seen in Figure 3.13. Both surfaces of the GEM foils are clad with copper in order to apply a strong electric field in between each side that will generate very strong potentials in the holes. The gas region contained in between the cathode and the GEM foil is called the drift region as the electric field is not strong enough to cause avalanches and thus start an amplification. The primary electrons drift toward the foil and are accelerated and amplify by the very high potential within the holes, as showed in Figure 3.13. Then the electrons reach the second drift region in which they will induce signal on the read-out located on the anode. By restraining the amplification process at the level of the holes, the electrons can stay in a very confined space and thus induce a very localized current, providing the GEMs with a very good spatial resolution.

In order to achieve a stronger amplification, the amplification process can be repeated several times in a row. The GEMs that will be used in CMS are triple GEM detectors operated with a 70/30 gas mixture of  $\text{Ar}/\text{CO}_2$ . They contain 3 GEM foils and thus 3 electron amplifications, as can be seen in Figure 3.14. The GEM foils used in CMS are 50  $\mu\text{m}$  foils clad with 5  $\mu\text{m}$  of copper on each side. The foils are pierced with double-canonical holes which inner and outer diameters are respectively 50 and 70  $\mu\text{m}$  which are placed 140  $\mu\text{m}$  from each other in an hexagonal pattern, as showed in Figure 3.13. These detectors have a time resolution better than 10 ns and reach very good spatial resolutions of less than 200  $\mu\text{rad}$  as indeed the position of the hits is not measured along the strips but following the azimuthal angle granularity of the radially organized trapezoidal strips.

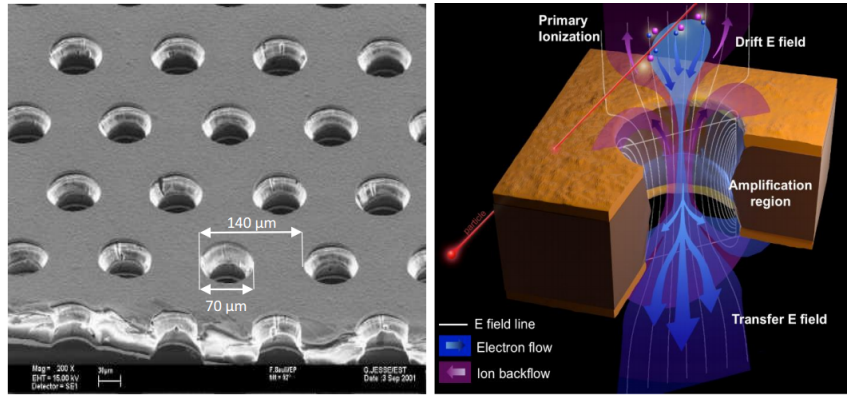


Figure 3.13: Left: Picture of a CMS GEM foil provided by a scanning electron microscope. Right: Representation of the electric field lines in a GEM hole and of the amplification that electrons and ions undergo in the hole's volume due to the very intense electric field.

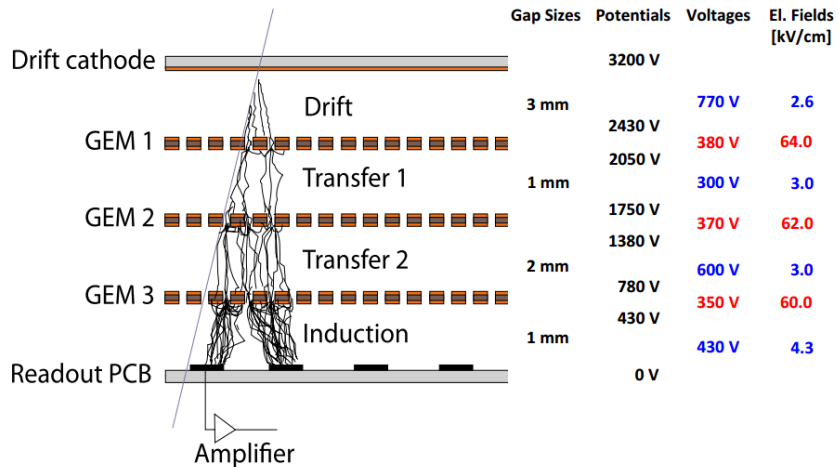


Figure 3.14: Schematic representation of CMS triple GEMs. The gas volume is divided into 4 areas. The drift area is the region where the primary electrons are created before being amplified a first time while passing through the first GEM foil. Then the process of drift and amplification is repeated twice in following two transfer areas and GEM foils. Finally, the charges have been amplified enough to induce current in the read-out strips while in the last drift area. The dimensions, potentials and electric fields are provided.

1610 The GEM Upgrade is divided into 3 subsystems as GE1/1 was the first approved project [29]  
 1611 and that the detectors will already be installed during LS2. GE2/1 and ME0, on the other hand,  
 1612 will profit of the R&D knowledge and skills developed for GE1/1 while the requirements for each  
 1613 subsystem are different as they are not placed at the same distance from the interaction point. In this  
 1614 very forward region, a different position with respect to the center of the detector can change dra-  
 1615 matically the conditions in which the detectors will have to be operated. In terms of rate capability,  
 1616 GE2/1, which is the furthest, is required to withstand 2.1 kHz/cm<sup>2</sup> while GE1/1 needs to be better  
 1617 than 10 kHz/cm<sup>2</sup> and ME0, better than 150 kHz/cm<sup>2</sup>. In terms of ageing with respect to charge  
 1618 deposition, ME0 needs to be certified to 840 mC/cm<sup>2</sup>, GE1/1 to 200 mC/cm<sup>2</sup> and GE2/1 only to

9 mC/cm<sup>2</sup>. All 3 detectors need to have a time resolution better than 10 ns and an angular resolution better than 500 µrad.

On each GE1/1 ring, 36 super chambers, consisting of 2 single GEM layers and spanning 10°, will be installed covering the pseudo-rapidity region  $1.6 < |\eta| < 2.2$  together with ME1/1 CSCs and the reach of the muon system will be improved thanks to the GE2/1 that will overlap with the GE1/1 and cover a region from  $|\eta| > 1.6$  to  $|\eta| < 2.4$  and complete the redundancy of ME2/1. The super chambers, built with 2 triple GEM layers each consisting of 4 single GEM modules due to the rather large surface of the GE2/1 chambers, that will be installed on the first ring of the second endcap will span 20° each, hence, a total of 72 chambers will be assembled to equip the muon system. Finally, the ME0 installed near the HCAL endcap will cover the region  $2.0 < |\eta| < 2.8$  and this subsystem will consist in super modules of 6 layers of triple GEM detectors covering an azimuthal angle of 20° leading to the construction of 216 single detectors.

All these new GEM detectors will be using a similar internal layout which is described in Figure 3.14. The incoming muons will create detectable electron-ion pairs in the 3 mm thick drift volume in which an electric field of 2.6 kV/cm is applied for the electrons to drift to the first GEM foil on which a very intense field of 64 kV/cm is applied over a distance of only 60 µm which allows for an average electronic gain of 20 to 25. After the first amplification stage, the electrons drift over the 1 mm separating the 2 first GEM foils thanks to an electric field of 3.0 kV/cm and are again amplified by a factor 20 to 25 while going through the second GEM foil to which is applied an electric field of 62 kV/cm. The electron drift another 2 mm towards the last GEM foil through a field of 3.0 kV/cm and are multiplied one last time from a similar factor passing through the 60 kV/cm of the last GEM foil holes. Finally, they drift along the 1 mm of the induction volume in a field of 4.3 kV/cm to reach the trapezoidal strips on the read-out PCB used as anode. The total detector gain is approximately of the order of  $10^4$  and the resulting output signal is both due to the induction of moving charges in the induction volume and of charge pick-up once they read the read-out strips.

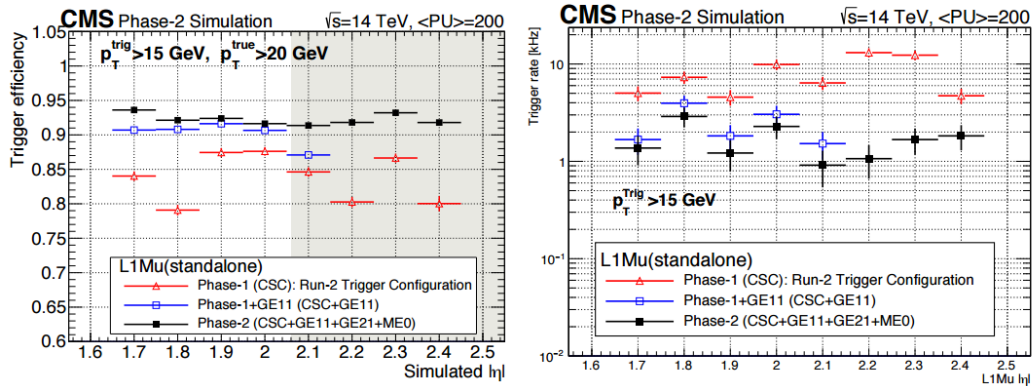


Figure 3.15: Simulated efficiency and rate of the standalone Level-1 muon trigger using tracks reconstructed in CSCs and all GEM stations compared with Phase-I values in the case where only CSCs are used or CSCs+GE1/1. The zones of inefficiency of the CSC subsystem are compensated by the addition of GEMs during Phase-II and the trigger rates is kept from increasing due to the high luminosity.

Adding the GEMs into the forward region of the muon system will allow to strongly enhance the Level-1 Trigger performance by reducing the inefficiency regions and the trigger rate as showed in Figure 3.15. Moreover, benefiting from the good spatial and angular resolution of the GEMs, the

<sup>1647</sup> precision into the muon measurement will also be greatly improved by the addition of GEMs as can  
<sup>1648</sup> be seen from the simulation presented in Figure 3.16.

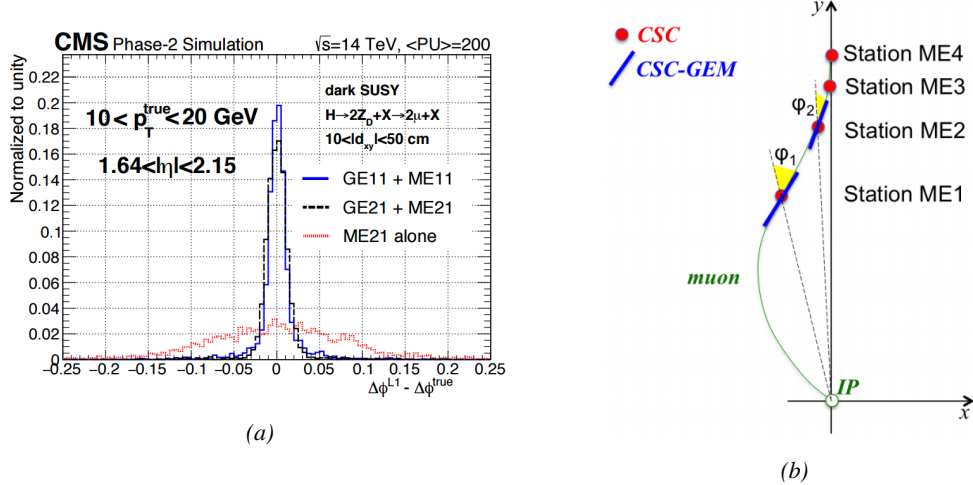


Figure 3.16: Figure 3.16a: Simulated resolution of the muon direction measurement  $\Delta\phi$  with Phase-II conditions. In the second endcap station, the resolution is compared in the case of CSCs (ME2/I) alone and CSCs+GEMs (GE2/I+ME2/I) while a similar resolution measurement is given in the case of the first station (GE1/I+ME1/I). Figure 3.16b: The addition of GEM detectors on stations 1 and 2 (ME0 is considered to contribute to station station 1) as redundant system to CSCs allows to improve the muon momentum improvement through a more accurate measurement of the local bending angles  $\phi_1$  and  $\phi_2$ .

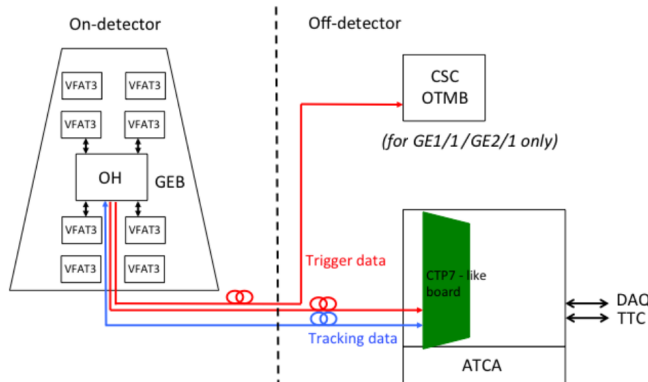


Figure 3.17: Schematics of the data communication chain for DAQ of the GEM subsystems. The sending of trigger data via optical links to the CSC OTMBs is only done for GE1/I and GE2/I to match the data with ME1/I and ME2/I.

<sup>1649</sup> The read-out of GEMs will use the same technology. The anode planes used as read-out PCBs  
<sup>1650</sup> and referred to as GEM Electronics board (GEB) host on their outer surface VFAT3 ASICs that  
<sup>1651</sup> connect to a total of 128 strips for a very fine angular granularity. Along the endcap radius, the strips are  
<sup>1652</sup> divided into 8 pseudo-rapidity partitions. In the case of GE1/I and ME0, each  $\eta$ -partition consist in  
<sup>1653</sup> 384 read-out strips connected into 3 VFAT3 ASICs and offering a while the large GE2/I partitions

1654 contain twice as many channels. Both GE1/1 and GE2/1 strips have an angular pitch of  $474\text{ }\mu\text{m}$   
 1655 while this of ME0 is twice larger due to its proximity with the interaction point. The VFAT3 ASICs  
 1656 allow for a latency better than the  $12.5\text{ }\mu\text{s}$  required by CMS Level-1 Trigger and there frequencies  
 1657 goes up to 1 MHz. They are connected into the Optohybrid Board (OH) and this full ensemble  
 1658 (GEB+VAT3+OH) constitute the on-chamber electronics. The OH is then sending the data to the  
 1659 modules constituting the DAQ of the GEM system via optical fibers. These back-end electronics  
 1660 modules are located in the service cavern of CMS and host CMS communication devices, used to  
 1661 have a common clock, and control and links to the Endcap Muon Track Finder (EMTF) system.  
 1662 Moreover, GE1/1 and GE2/1 also have links with the CSC OTMBs as the OH of these 2 subsystems  
 1663 send data into these boards. This communication chain can be seen in Figure 3.17.

1664

1665 The detectors that will placed in CMS will have to live through Phase-II without significant  
 1666 performance degradation to ensure an efficient data taking and the possibility to investigate more  
 1667 exotic physics. As the 3 GEM subsystems will be using the same detector technology, the choice  
 1668 was made to certify the GEMs in the worst of the 3 environments, i.e. the ME0 station located right  
 1669 behind the HCAL. According to FLUKA simulation, including all the latest foreseen upgrades into  
 1670 the CMS detector geometry, it was shown that the maximal hit rate expected in ME0 would be of  
 1671 the order of  $50\text{ kHz/cm}^2$  with contributions of neutrons ( $6\text{ kHz/cm}^2$ ), photons ( $35\text{ kHz/cm}^2$ ), and  
 1672 electrons and positrons ( $8\text{ kHz/cm}^2$ ) resulting in a charge deposition a little lower than  $300\text{ mC/cm}^2$   
 1673 after 10 years of HL-LHC [23]. It is necessary to understand the classical ageing effects on the GEMs  
 1674 but also premature ageing due to contaminants in the gas mixture leading to polymerization on the  
 1675 surface of the GEM foils during operation and the effect of discharges on the detector operations if  
 1676 they have to happen during their lifetime.

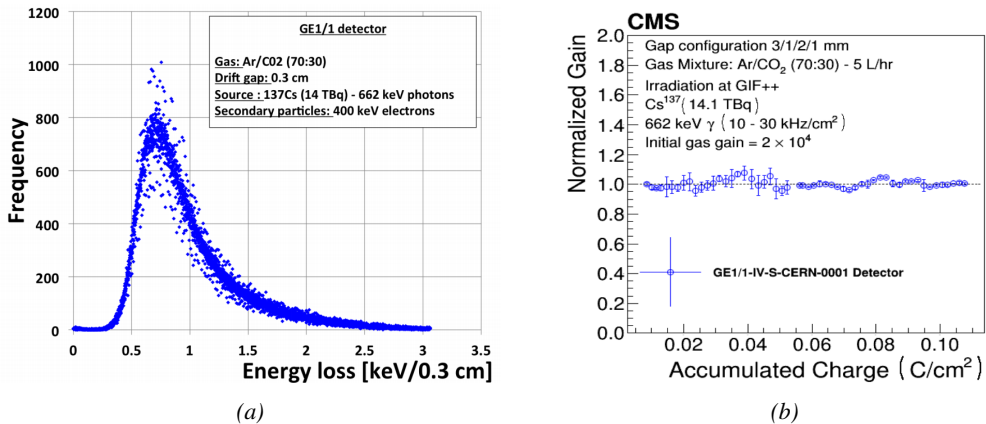


Figure 3.18: Figure 3.18a: Energy spectrum of GIF++  $^{137}\text{Cs}$  source as measured by the GE1/1 detector installed in GIF++. Figure 3.18b: Evolution of the normalized gain of the GE1/1 detector installed at in GIF++ as a function of the integrated charge per unit area. The first part of the study, up to a charge of  $55\text{ mC/cm}^2$  had been done in the former Gamma Irradiation Facility (GIF) that has now been dismantled following the construction of GIF++. No variation of the normalized gain can be observed after an accumulation of  $110\text{ mC/cm}^2$ .

1677

To characterize the classical ageing effects, a campaign is being conducted in the new Gamma Irradiation Facility (GIF++) of CERN where a GE1/1 detector operated at its nominal gain is placed 50 cm from the facility's 14 TBq  $^{137}\text{Cs}$  source which emits gammas at an energy of 662 keV. In

order to spot any ageing of the detector, the effective gain is kept monitored, as can be seen in Figure 3.18b, as its variations gives clues about different aspects of the detector such as the geometry of the holes, the electric field configuration or the gas composition. The monitoring of the gamma energy distribution, showed on Figure 3.18a, can give an idea on the evolution of the performance of the chamber and finally, the evolution of the currents through time also is a good indicator of the appearance of dark current in the detector that would be due to the emission of electrons by thin insulating layers of the detector subjected to a long lasting irradiation known as Malter effect. At the time the Technical Design Report (TDR) for the Phase-II upgrade of the muon system was written [23], the GEM group had reported a total integrated charge of  $110 \text{ mC/cm}^2$  which, if compared with 10 years of HL-LHC operation, represents a safety factor of 18 for the GE1/1 subsystem and a factor 37 for the GE2/1 subsystem but only 39% of the total expected ME0 integrated charge. It is estimated that reaching the total integrated charge necessary to certify the detectors for Phase-II operation will take another 2 to 3 years. Nevertheless, the present status of the longevity study shows no degradation of the performance of the detector installed in GIF++ as can be seen through Figure 3.18.

Aside of the classical ageing tests, outgassing of the different materials composing the GEMs have been conducted by placing the different materials to be tested into an outgassing box that consists in a stainless steel cylinder through which the CMS GEM 70/30 gas mixture of  $\text{Ar}/\text{CO}_2$  with the possible contaminants is flowed while the detector is exposed to the continuous irradiation of a radioactive source and the heat is raised to enhance the outgassing. From the detector that was placed into this outgassing box, only one component was identified to cause loss of performance due to outgassing. This component was the polyurethane *Cell-Pack* used to coat the internal frame of the GEMs and the polymerization on its surface caused a 20% decrease of the gas gain. this polyurethane was replaced with a new one for which no outgassing effect causing a loss of performance was reported.

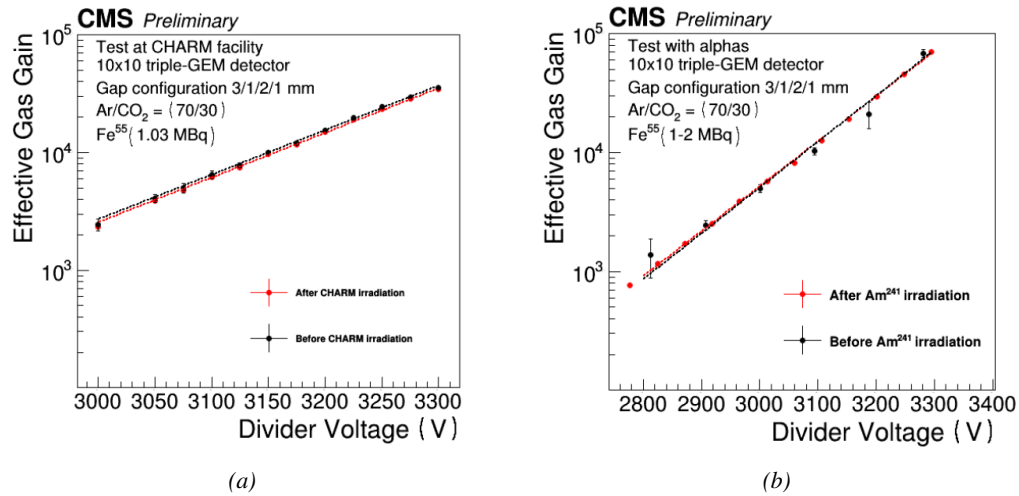


Figure 3.19: Figure 3.19a: Comparison of the gas gain as a function of the divider voltage before and after the irradiation of a triple-GEM by neutrons in CHARM. Figure 3.19b: Comparison of the gas gain as a function of the divider voltage before and after the irradiation of a triple-GEM by alpha particles.

Finally, even though the triple-GEM technology makes the detectors safe of discharges thanks to

its several amplification stages that allow to reach high gas gain using a relatively low electric field applied on the foils and to the distance separating the last foil from the read-out panel that is high enough to prevent discharging from developing all the way to the read-out, and hence, be stopped before it can cause any harm, it is important to have a good understanding of the discharge probability to ensure a safe operation over long periods. In order to further prevent discharges to develop in the detector volume, the GEM foils' power supply have been sectorized and protection resistors have been installed to limit the energy available for the discharge development. To reproduce the high-energy neutron background conditions of CMS, a GE1/1 detector have been placed in the CHARM facility of CERN. This facility allows to irradiate the detectors with a neutron fluence as high as  $2.5 \times 10^8 / \text{cm}^2$ . The detectors were operated with a slightly higher gain of  $3.5 \times 10^4$ . It was measured that the discharge probability for a GEM operated under CMS conditions was of  $2.85 \times 10^{-9}$  per heavily ionizing particle with a 95% confidence level that would correspond to 225 discharges per  $\text{cm}^2$  in ME0, 17 in GE1/1 and 12 in GE2/1 during the full HL-LHC period. According to Figure 3.19a, no degradation of the performance was observed after the irradiation at CHARM were 24 discharges per unit area were reported. Nevertheless, another test were the detector was exposed to a 5.5 MeV alpha source and were 450 discharges per unit area were reported didn't show any drop of performances either, as can be seen in Figure 3.19b.

**3.3.3 Installation schedule**

**3.4 Implications of the different upgrades on the Level-1 Trigger. Improvement of physics performance.**

**3.5 Ecofriendly gas studies**

**3.5.1 Status of the studies and potential candidates**

**3.5.2 Implications in case of no suitable ecofriendly mixture**



# 4

1729

1730

## Physics of Resistive plate chambers

1731 A Resistive Plate Chamber (RPC) is a gaseous detector using the same physical processes described  
1732 in Chapter 3. It has been developed in 1981 by Santonico and Cardarelli [30], under the name of  
1733 *Resistive Plate Counter*, as an alternative to the local-discharge spark counters proposed in 1978  
1734 by Pestov and Fedotovich [31, 32]. Working with spark chambers implied using high-pressure gas  
1735 and high mechanical precision which the RPC simplified by formerly using a gas mixture of argon  
1736 and butane flowed at atmospheric pressure and a constant and uniform electric field propagated  
1737 in between two parallel electrode plates. Moreover, a significant increase in rate capability was  
1738 introduced by the use of electrode plate material with high bulk resistivity, preventing the discharge  
1739 from growing throughout the whole gas gap. Indeed, the effect of using resistive electrodes is that  
1740 the constant electric field is locally canceled out by the development of the discharge, limiting its  
1741 growth.

1742 Through its development history, different operating modes [33–35] and new detector designs [36–  
1743 38] have been discovered, leading to further improvement of the rate capability of such a detector.  
1744 Moreover, the addition of  $SF_6$  into the gas mix improved the stability of operation of the RPC [39,  
1745 40].

1746 The low developing costs and easily achievable large detection areas offered by RPCs, as well as  
1747 the wide range of possible designs, made them a natural choice to as muon chambers and/or trigger  
1748 detectors in multipurpose experiments such as CMS [21] or ATLAS [41], time-of-flight detectors in  
1749 ALICE [42], calorimeter with CALICE [43] or even detectors for volcanic muography with ToMu-  
1750 Vol [44].

### 1751 4.1 Principle

1752 RPCs are ionisation detectors composed of two parallel resistive plate electrodes in between which  
1753 a constant electric field is set. The space in between the electrodes, referred as *gap*, is filled with a  
1754 dense gas that is used to generate primary ionization into the gas volume. The free charge carriers  
1755 (electrons and cations) created by the ionization of the gas molecules are then accelerated towards

<sup>1756</sup> the electrodes by the electric field, as shown in Figure 4.1 [45].

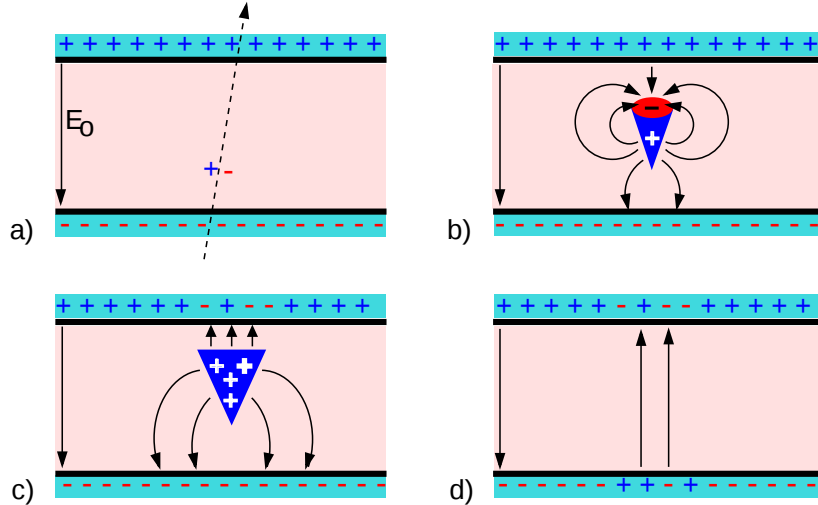


*Figure 4.1: Different phases of the avalanche development in the RPC gas volume subjected to a constant electric field  $E_0$ . a) An avalanche is initiated by the primary ionisation caused by the passage of a charged particle through the gas volume. b) Due to its growing size, the avalanche starts to locally influence the electric field. c) The electrons, lighter than the cations reach the anode first. d) The ions reach the cathode. While the charges have not recombined, the electric field in the small region around the avalanche stays affected and locally blind the detector.*

<sup>1757</sup> RPCs being passive detectors, a current on pick-up copper read-out placed outside of the gas  
<sup>1758</sup> volume is induced by the charge accumulation during the growth of the avalanche. As a result,  
<sup>1759</sup> the time resolution of the detector is substantially increased as the output signal is generated while  
<sup>1760</sup> the electrons are still in movement. The advantage of a constant electric field, over multi-wire  
<sup>1761</sup> proportional chambers, is that the electrons are being fully accelerated from the moment charge  
<sup>1762</sup> carriers are freed and feel the full strength of the electric field that doesn't depend on the distance to  
<sup>1763</sup> the readout and that the output signal doesn't need for the electrons to be physically collected.

<sup>1764</sup> The typical gas mixture RPCs are operated with is generally composed of 3 gas compounds.

- <sup>1765</sup> • Tetrafluoroethane ( $C_2F_4H_2$ ), also referred to as *Freon*, is the principal compound of the RPC  
<sup>1766</sup> gas mixtures, with a typical fraction above 90%. It is used for it's high effective Townsend  
<sup>1767</sup> coefficient and the great average fast charge that allows to operate the detector with a high  
<sup>1768</sup> threshold with respect to argon, for example, that has similar effective Townsend coefficient  
<sup>1769</sup> but suffers from a lower fast charge. To operate with similar conditions, argon would require a  
<sup>1770</sup> higher electric field leading to a higher fraction of streamers, thus limiting the rate capability  
<sup>1771</sup> of the detector [46].
- <sup>1772</sup> • Isobutane (i- $C_4H_{10}$ ), only present in a few percent in the gas mixtures, is used for its UV  
<sup>1773</sup> quenching properties [47] helping to prevent streamers due to UV photon emission during the  
<sup>1774</sup> avalanche growth.
- <sup>1775</sup> • Sulfur hexafluoride, ( $SF_6$ ), referred to simply as *SF6*, is used in very little quantities for its  
<sup>1776</sup> high electronegativity. Excess of electrons are being absorbed by the compound and streamers

1777 are suppressed [40]. Nevertheless, a fraction of  $SF_6$  higher than 1% will not bring any extra  
 1778 benefit in terms of streamer cancelation power but will lead to higher operating voltage [39],  
 1779 as can be understood through Figure 4.2.

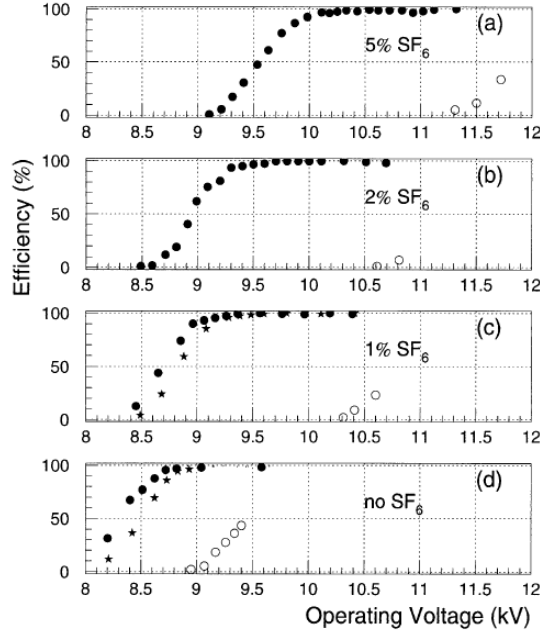


*Figure 4.2: Effeciency (circles and stars with 30 mV and 100 mV thresholds respectively) and streamer probability (opened circles) as function of the operating voltatge of a 2 mm single gap HPL RPC flushed with a gas mixture containing (a) 5%, (b) 2%, (c) 1% and (d) no  $SF_6$  [39].*

1780 After an avalanche developed in the gas, a time long compared to the development of a discharge  
 1781 is needed to recombine the charge carriers in the electrode material due to their resistivity. This  
 1782 property has the advantage of affecting the local electric field and avoiding sparks in the detector  
 1783 but, on the other hand, the rate capability is intrinsically limited by the time constant  $\tau_{RPC}$  of the  
 1784 detector. Using a quasi-static approximation of Maxwell's equations for weakly conducting media,  
 1785 it can be shown that the time constant  $\tau_{RPC}$  necessary to the charge recombination at the interface  
 1786 in between the electrode and the gas volume is given by the Formula 4.1 [48].

$$\tau_{RPC} = \frac{\epsilon_{electrode} + \epsilon_{gas}}{\sigma_{electrode} + \sigma_{gas}} \quad (4.1)$$

1787 A gas can be assimilated to vacuum, leading to  $\epsilon_{gas} = \epsilon_0$  and  $\sigma_{gas} = 0$ , and the electrodes  
 1788 permittivity and conductivity can be written as  $\epsilon_{electrode} = \epsilon_r \epsilon_0$  and  $\sigma_{electrode} = 1/\rho_{electrode}$ ,  
 1789 showing the strong dependence of the time constant to the electrodes resistivity in Formula 4.2.

$$\tau_{RPC} = (\epsilon_r + 1)\epsilon_0 \times \rho_{electrode} \quad (4.2)$$

1790 Very few materials with a low enough resistivity exist in nature. The resistivity targeted to build  
 1791 RPCs ranges from  $10^9$  to  $10^{12} \Omega \cdot \text{cm}$ . The most common RPC electrode materials are displayed in  
 1792 Table 4.1. When the doped glass and ceramics can offer short time constants of the order of 1 ms,

1793 the developing cost of such materials is quite high due to the very low demand. Thus, High-pressure  
 1794 laminate (HPL) is often the choice for high rate experiments using very large RPC detection areas.  
 1795 Other experiments working at cosmic muon fluxes can safely operate with ordinary float glass.

Material	$\rho_{electrode}$ ( $\Omega \cdot \text{cm}$ )	$\epsilon_r$	$\tau_{RPC}$ (ms)
Float glass	$10^{12}$	$\sim 7$	$\sim 700$
High-pressure laminate	$10^{10}$ to $10^{12}$	$\sim 6$	$\sim 6$ to 600
Doped glass (LR S)	$10^9$ to $10^{11}$	$\sim 10$	$\sim 1$ to 100
Doped ceramics (SiN/SiC)	$10^9$	$\sim 8.5$	$\sim 1$
Doped ceramics (Ferrite)	$10^8$ to $10^{12}$	$\sim 20$	$\sim 0.2$ to 2000

Table 4.1: Properties of the most used electrode materials for RPCs.

### 1796 4.1.1 Electron drift velocity

1797 Talk about the electron drift velocity and mention the time resolution of RPCs.

## 1798 4.2 Rate capability and time resolution of Resistive Plate Chambers

1800 As already previously discussed, the electrode material plays a key role in the max intrinsic rate  
 1801 capability of RPCs. R&D is being done to develop at always cheaper costs material with lower  
 1802 resistivity. Nevertheless, the amount of charge released, i.e. the size of the discharge, if reduced  
 1803 leads to a smaller blind area in the detector, increasing the rate capability of the detector.

### 1804 4.2.1 Operation modes

1805 RPCs where developed early 1980s. At that time it was using an operating mode now referred to  
 1806 as *streamer mode*. Streamers are large discharges that develop in between the 2 electrodes enough  
 1807 to locally discharge the electrodes. If the electric field inside of the gas volume is strong enough,  
 1808 with electrons being fast compared to ions, a large and dense cloud of positive ions will develop  
 1809 nearby the anode and extend toward the cathode while the electrons are being collected, eventually  
 1810 leading to a streamer discharge due to the increase of field seen at the cathode. the field is then strong  
 1811 enough so that electrons are pulled out of the cathode. Electrodes, though they are a unique volume  
 1812 of resistive material, can be assimilated to capacitors. At the moment an electric field is applied in  
 1813 between their outer surfaces, the charge carriers inside of the volume will start moving leading to  
 1814 a situation where there is no voltage across the electrodes and a higher density of negative charges,  
 1815 i.e. electrons, on the inner surface of the cathode. Finally, when a streamer discharge occurs, these  
 1816 electrons are partially released in the gas volume contributing to increase the discharge strength until  
 1817 the formation of a conductive plasma, the streamer. This can be understood through Figure 4.3 [33].  
 1818 Streamer signals are very convenient in terms of read-out as no amplification is required with output  
 1819 pulses amplitudes of the order of a few tens to few hundreds of mV as can be seen on Figure 4.4.

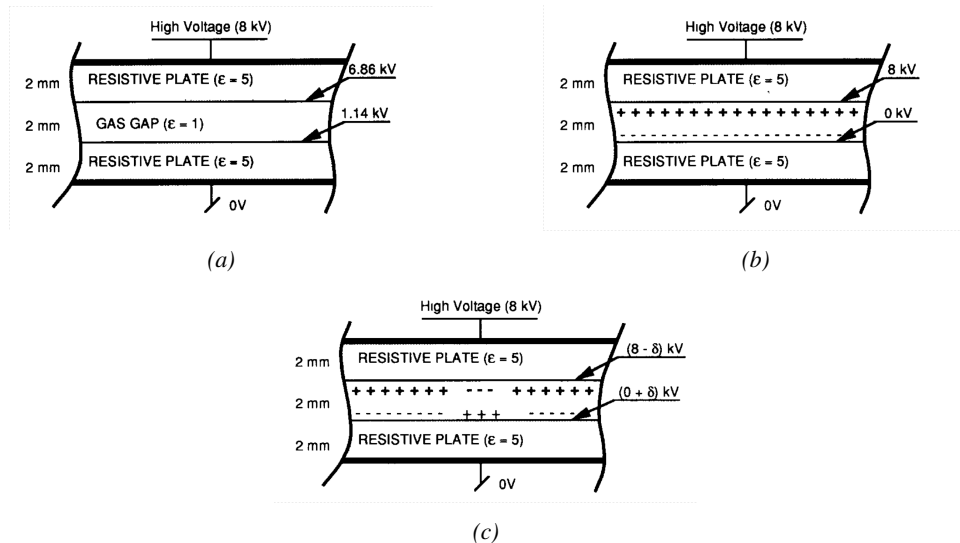


**Figure 4.3: Movement of the charge carriers in an RPC.** Figure 4.3a: Voltage across an RPC whose electrode have a relative permittivity of 5 at the moment the tension  $s$  applied. Figure 4.3b: After the charge carriers moved, the electrodes are charged and there is no voltage drop over the electrodes anymore. The full potential is applied on the gas gap only. Figure 4.3c: The streamer discharge initiated by a charged particle transports electrons and cations towards the anode and cathode respectively.

When the electric field is reduced though, the electronic gain is small until the electrons get close enough to the anode and the positive ion cloud is much smaller. The electric field cannot rise to the point a field emission of electrons on the cathode is possible. The resulting signal is weak, of the order of a few mv as shown on Figure 4.4, and requires amplification. This is the *avalanche mode* of RPC operation.

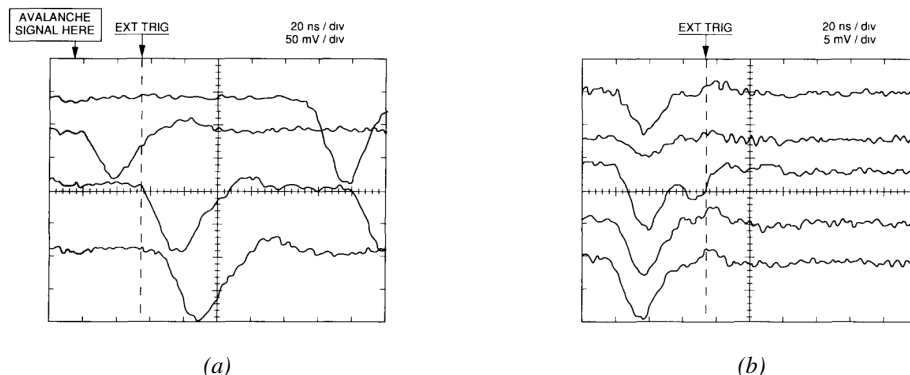


Figure 4.4: Typical oscilloscope pulses in streamer mode (Figure 4.4a) and avalanche mode (Figure 4.4b). In the case of streamer mode, the very small avalanche signal is visible.

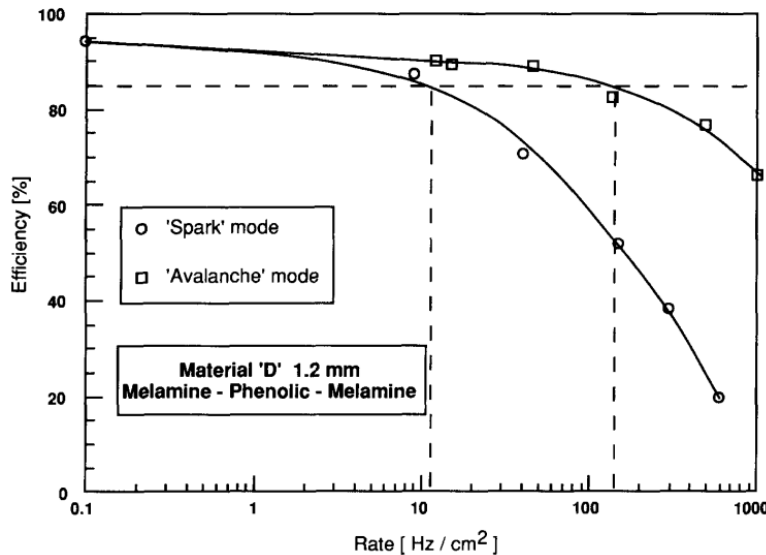


Figure 4.5: Rate capability comparison for the streamer and avalanche mode of operation. An order of magnitude in rate capability for a maximal efficiency drop of 10% is gained by using the avalanche mode over the streamer mode.

This mode offers a higher rate capability by providing smaller discharges that don't affect the electrodes charge and are more locally contained in the gas volume as was demonstrated by Crotty with Figure 4.5 [33]. The detector only stays locally blind the time the charge carriers are recombined and there is no need for electrode recharge which is a long process affecting a large portion of the detector. Another advantage of avalanche signals over streamer is the great time consistency. Figure 4.4 shows very clearly that avalanche signals have a very small time jitter. This is a natural choice for high rate experiments.

## 4.2.2 Detector designs and performance

Different RPC design have been used and each of them present its own advantages. Historically, the first type of RPC to have been developed is what is referred now to *narrow gap* RPC [30, 49]. After the avalanche mode has been discovered [33], it has been proven that increasing the width of the gas gap lead to higher rate capability, due to lower charge deposition per avalanche, and lower power dissipation [49]. Nevertheless, by increasing the gas gap width, the time resolution of the detector decreases. This is a natural result if the increase of active gas volume in the detector is taken into account. Indeed, for a given threshold, only the small fraction of gas closest to the cathode will provide enough gain to have a detectable signal. In the case of a wider gas volume, the active region is then larger and a larger time jitter is introduced with the variation of starting position of the avalanche, as discussed in [36]. To solve improve both the time resolution and the rate capability, different methods were used trying to get advantages of both narrow and wide gap RPCs.

1844 **4.2.2.1 Double-gap RPC**

1845 Double-gap RPCs are made out of 2 narrow RPC detectors. The 2 RPC gaps are stacked on top of  
 1846 each other as shown in Figure 4.6. This detector layout, popularized by the two multipurpose experiments  
 1847 CMS [21] and ATLAS [41] at LHC, can be used as an OR system in which each individual  
 1848 chamber participates in the output signal. The gain of such a detector is greatly reduced with respect  
 1849 to single-gap RPCs with an efficiency plateau reached at lower voltage, as visible on Figure 4.7.

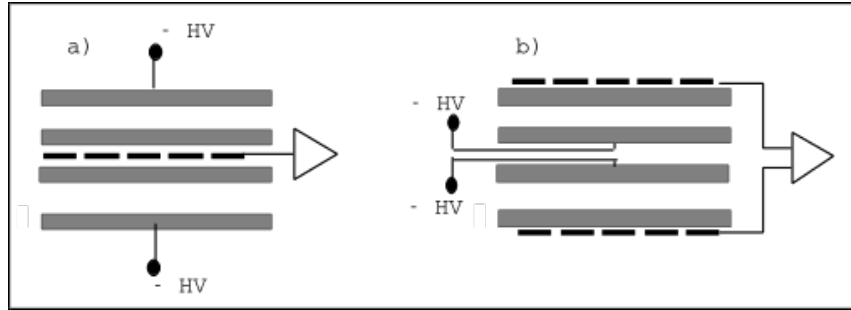


Figure 4.6: Possible double-gap RPC layouts: a) "standard" 1D double-gap RPC, as used in CMS experiment, where the anodes are facing each other and a 1D read-out plane is sandwiched in between them, b) double read-out double-gap RPC as used in ATLAS experiment, where the cathodes are facing each other and 2 read-out planes are used on the outer surfaces. This last layout can offer the possibility to use a 2D reconstruction by using orthogonal read-out planes.

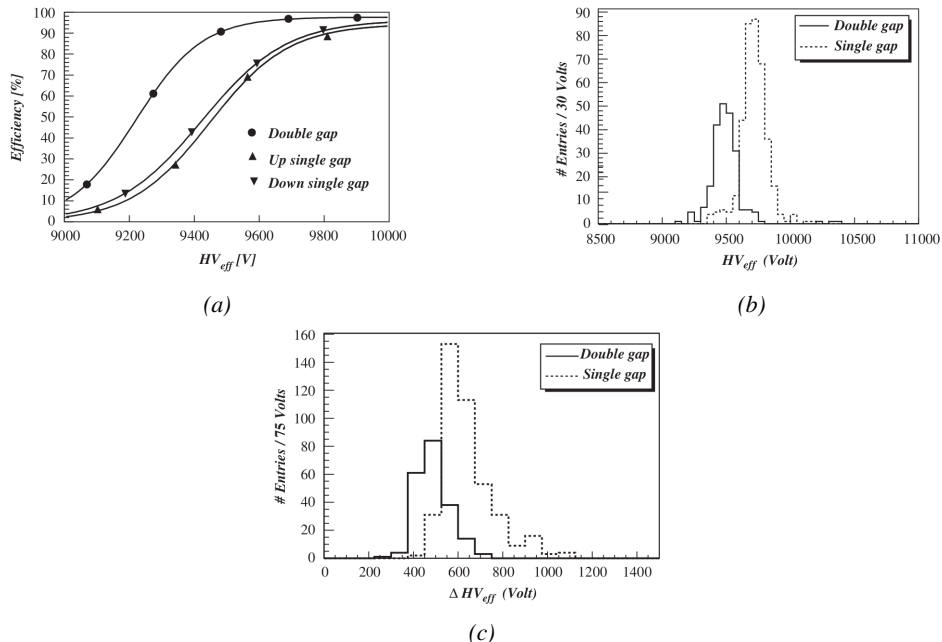


Figure 4.7: Comparison of performance of CMS double and single gap RPCs using cosmic muons [50]. Figure 4.7a: Comparison of efficiency sigmoids. Figure 4.7b: Voltage distribution at 95% of maximum efficiency. Figure 4.7c:  $\Delta_{10\%}^{90\%}$  distribution.

### 4.2.2.2 Multigap RPC (MRPC)

MRPCs are layouts in which floating sub electrode plates are placed into a wide gap RPC to divide the gas volume and create a sum of narrow gaps [36, 37]. The time resolution of such a detector can reach of few tens of ps, with gas gaps of the order of a few hundred  $\mu\text{m}$  as shown in Figure 4.8 representing ALICE Time-of-flight (ToF) MRPCs.

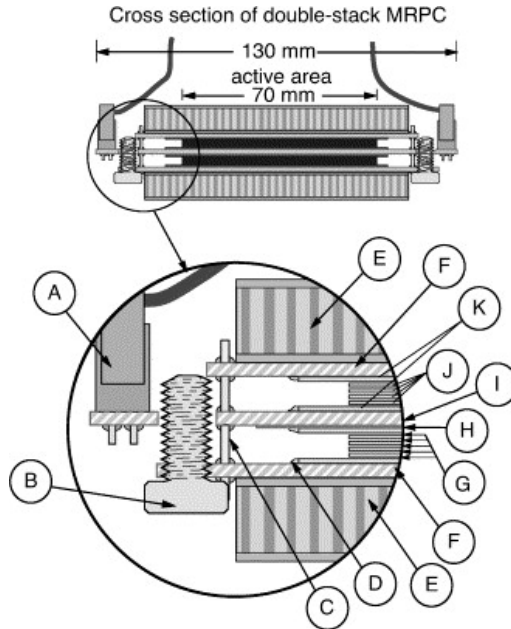


Figure 4.8: Presentation of ALICE MRPC using 250  $\mu\text{m}$  gas gaps, 620  $\mu\text{m}$  outer glass electrodes and 550  $\mu\text{m}$  inner floating electrodes. More details on the labels are given in [51].

Sometimes used as a double multigap RPC, taking advantage of the OR of double gap RPCs, the MRPC is mainly used as ToF detector [51–55] due to its excellent timing properties that allow to perform particle identification as explained by Williams in [56]. The principle of particle identification using ToF is simply the measurement of the velocity of a particle. Indeed, particles are defined by their mass (for the parameter of interest here, their electric charge being measured using the bending angle of the particles traveling through a magnetic field) and this mass can be calculated by measuring the velocity  $\beta$  and momentum of the particle:

$$\beta = \frac{p}{\sqrt{p^2 + m^2}} \quad (4.3)$$

Intuitively, it is trivial to understand that 2 different particles having the same momentum will have a different velocity due to the mass difference and thus a different flight time  $T_1$  and  $T_2$  through the detector and this is used to separate and identify particles. The better the time resolution of the ToF system used, the stronger will the separation be:

$$T = \frac{L}{v} = \frac{L}{c \cdot \beta}, \quad \Delta T = T_1 - T_2 = \frac{L}{c} \left( \sqrt{1 + m_1^2/p^2} - \sqrt{1 + m_2^2/p^2} \right) \cong (m_1^2 - m_2^2) \frac{L}{2cp^2} \quad (4.4)$$

1866 An example of particle identification is given for the case of STAR experiment in Figure 4.9.

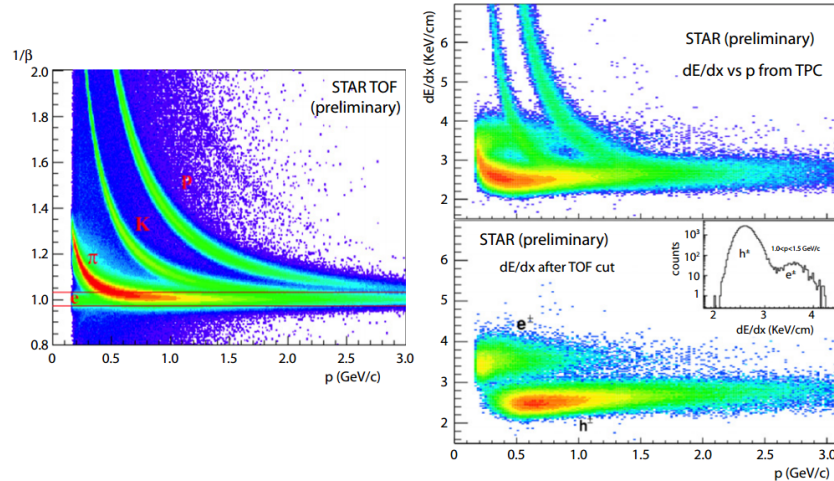


Figure 4.9: Particle identification applied to electrons in the STAR experiment. The identification is performed combining ToF and  $dE/dx$  measurements [56].

1867 Another benefice of using such small gas gaps is the strong reduction of the average avalanche  
1868 volume and thus of the blind spot on MRPCs leading to an improved rate capability. Multigaps can  
1869 sustain backgrounds of several kHz/cm<sup>2</sup> as demonstrated in Figure 4.10.

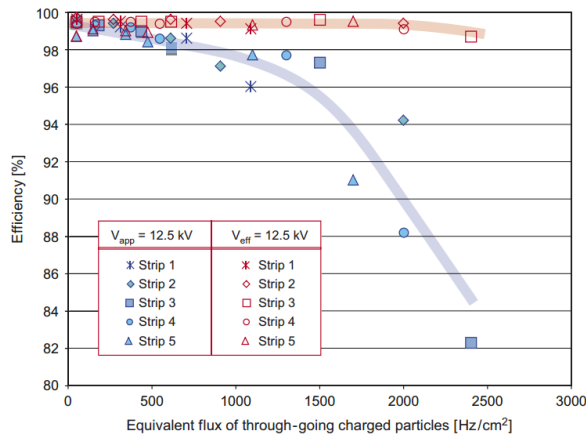


Figure 4.10: Comparison of the detector performance of ALICE ToF MRPC [57] at fixed applied voltage (in blue) and at fixed effective voltage (in red). The effective voltage is kept fixed by increasing the applied voltage accordingly to the current drawn by the detector.

#### 1870 4.2.2.3 Charge distribution and performance limitations

1871 The direct consequence of the different RPC layouts is a variation of intrinsic time resolution of the  
1872 RPC as the gap size decreases. An advantage is given to multigaps whose design use sub-millimeter  
1873 gas volumes providing very consistent signals.

1874 On the charge spectrum point of view, each layout has its own advantages. When the double-gap  
 1875 has the highest induced over drifting charge ratio, as seen in Figure 4.11, the multigap has a charge  
 1876 spectrum strongly detached from the origin, as visible in Figure 4.12. A high induced over drifting  
 1877 charge ratio means that the double gap can be safely operated at high threshold or that at similar  
 1878 threshold it can be operated with a twice smaller drifting charge, meaning a higher rate capability.  
 1879 On the other hand, the strong detachment of the charge spectrum from the origin in the MRPC case  
 1880 allows to reach a higher efficiency with increasing threshold as most of the induced charge is not low  
 1881 due to the convolution of several single gap spectra. The range of stable efficiency increases with  
 1882 the number of gap, as presented in Figure 4.13.

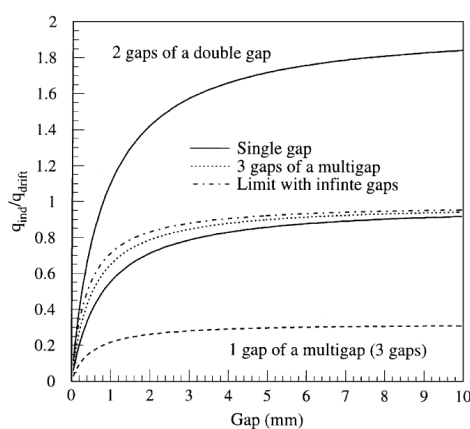


Figure 4.11: Ratio between total induced and drifting charge have been simulated for single gap, double-gap and multigap layouts [58]. The total induced charge for a double-gap RPC is a factor 2 higher than for a multigap.

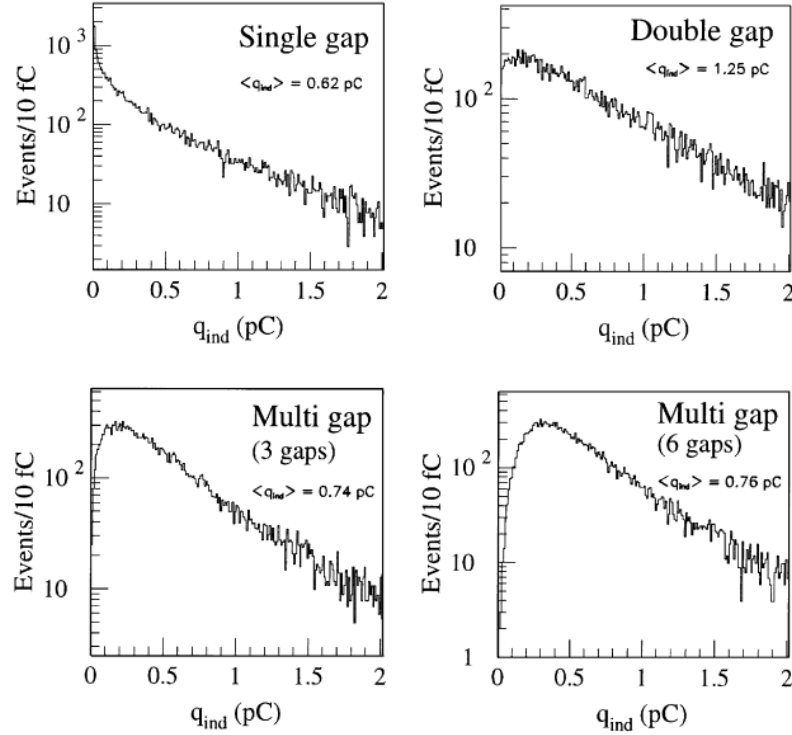


Figure 4.12: Charge spectra have been simulated for single gap, double-gap and multigap layouts [58]. It appears that when single gap shows a decreasing spectrum, double and multigap layouts exhibit a spectrum whose peak is detached from the origin. The detachment gets stronger as the number of gaps increases.

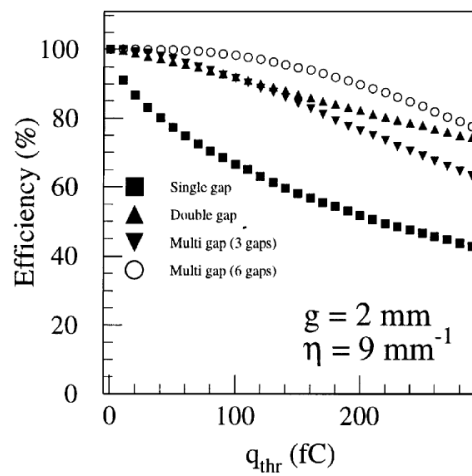


Figure 4.13: The maximal theoretical efficiency is simulated for single gap, double-gap and multigap layouts [58] at a constant gap thickness of 2 mm and using an effective Townsend coefficient of  $9 \text{ mm}^{-1}$ .

- <sup>1883</sup> **4.3 Signal formation**
- <sup>1884</sup> **4.4 Gas transport parameters**

# 5

1885

1886

1887

## Longevity studies and Consolidation of the present CMS RPC subsystem

### 5.1 Resistive Plate Chambers at CMS

#### 5.1.1 Overview

1890 The Resistive Plate Chambers (RPC) system, located in both barrel and endcap regions, provides a  
1891 fast, independent muon trigger with a looser  $p_T$  threshold over a large portion of the pseudorapidity  
1892 range ( $|\eta| < 1.6$ ) [add reconstruction].

1893

1894 During High-Luminosity LHC (HL-LHC) operations the expected conditions in terms of back-  
1895 ground and pile-up will make the identification and correct  $P_T$  assignment a challenge for the Muon  
1896 system. The goal of RPC upgrade is to provide additional hits to the Muon system with precise tim-  
1897 ing. All these informations will be elaborated by the trigger system in a global way enhancing the  
1898 performance of the trigger in terms of efficiency and rate control. The RPC Upgrade is based on two  
1899 projects: an improved Link Board System and the extension of the RPC coverage up to  $|\eta| = 2.4$ .  
1900 [FIXME 2.4 or 2.5?]

1901 The Link Board system, that will be described in section xxx, is responsible to process, syn-  
1902 chronize and zero-suppress the signals coming from the RPC front end boards. The Link Board  
1903 components have been produced between 2006 and 2007 and will be subjected to aging and failure  
1904 in the long term. The upgraded Link Board system will overcome the aging problems described in  
1905 section xxx and will allow for a more precise timing information to the RPC hits from 25 to 1 ns [ref  
1906 section xxx].

1907 The extension of the RPC system up to  $|\eta| = 2.1$  was already planned in the CMS TDR [ref  
1908 cmstdr] and staged because of budget limitations and expected background rates higher than the rate  
1909 capability of the present CMS RPCs in that region. An extensive R&D program has been done in  
1910 order to develop an improved RPC that fulfills the CMS requirements. Two new RPC layers in the  
1911 innermost ring of stations 3 and 4 will be added with benefits to the neutron-induced background

1912 reduction and efficiency improvement for both trigger and offline reconstruction.

### 1913 5.1.2 The present RPC system

1914 The RPC system is organized in 4 stations called RB1 to RB4 in the barrel region, and RE1 to RE4  
 1915 in the endcap region. The innermost barrel stations, RB1 and RB2, are instrumented with 2 layers  
 1916 of RPCs facing the innermost (RB1in and RB2in) and outermost (RB1out and RB2out) sides of the  
 1917 DT chambers. Every chamber is then divided from the read-out point of view into 2 or 3  $\eta$  partitions  
 1918 called “rolls”. The RPC system consist of 480 barrel chambers and 576 endcap chambers. Details  
 1919 on the geometry are discussed in the paper [ref to geo paper].

1920 The CMS RPC chamber is a double-gap, operated in avalanche mode to ensure reliable operation  
 1921 at high rates. Each RPC gap consists of two 2-mm-thick resistive High-Pressure Laminate (HPL)  
 1922 plates separated by a 2-mm-thick gas gap. The outer surface of the HPL plates is coated with a thin  
 1923 conductive graphite layer, and a voltage is applied. The RPCs are operated with a 3-component,  
 1924 non-flammable gas mixture consisting of 95.2% freon ( $C_2H_2F_4$ , known as R134a), 4.5% isobutane  
 1925 ( $i-C_4H_{10}$ ), and 0.3% sulphur hexafluoride ( $SF_6$ ) with a relative humidity of 40% - 50%. Readout  
 1926 strips are aligned in  $\eta$  between the 2 gas gaps. [\[Add a sentence on FEBs.\]](#)

1927 The discriminated signals coming from the Front End boards feed via twisted cables (10 to 20 m  
 1928 long) the Link Board System located in UXC on the balconies around the detector. The Link System  
 1929 consist of the 1376 Link Boards (LBs) and the 216 Control Boards (CBs), placed in 108 Link Boxes.  
 1930 The Link Box is a custom crate (6U high) with 20 slots (for two CBs and eighteen LBs). The Link  
 1931 Box contains custom backplane to which the cables from the chambers are connected, as well as the  
 1932 cables providing the LBs and CBs power supply and the cables for the RPC FEBs control with use  
 1933 of the I2C protocol (trough the CB). The backplane itself contains only connectors (and no any other  
 1934 electronic devices).

1935 The Link Board has 96 input channels (one channel corresponds to one RPC strip). The input  
 1936 signals are the  $\sim 100$  ns binary pulses which are synchronous to the RPC hits, but not to the LHC  
 1937 clock (which drives the entire CMS electronics). Thus the first step of the FEB signals processing  
 1938 is synchronization, i.e. assignment of the signals to the BXes (25 ns periods). Then the data are  
 1939 compressed with a simple zero-suppressing algorithm (the input channels are grouped into 8 bit  
 1940 partitions, only the partitions with at least one nonzero bit are selected for each BX). Next, the non-  
 1941 empty partitions are time-multiplexed i.e. if there are more than one such partition in a given BX,  
 1942 they are sent one-by-one in consecutive BXes. The data from 3 neighbouring LBs are concentrated  
 1943 by the middle LB which contains the optical transmitter for sending them to the USC over a fiber at  
 1944 1.6 Gbps.

1945 The Control Boards provide the communication of the control software with the LBs via the  
 1946 FEC/CCU system. The CBs are connected into token rings, each ring consists of 12 CBs of one  
 1947 detector tower and a FEC mezzanine board placed on the CCS board located in the VME crate in  
 1948 the USC. In total, there are 18 rings in the entire Link System. The CBs also perform automatic  
 1949 reloading of the LB's firmware which is needed in order to avoid accumulation of the radiation  
 1950 induced SEUs in the LBs firmware.

1951 Both LBs and CB are based on the Xilinx Spartan III FPGAs, the CB additionally contains  
 1952 radiation-tolerant (FLASH based) FPGA Actel ProAsicPlus.

1953 The High Voltage power system is located in USC, not exposed to radiation and easily accessible  
 1954 for any reparation. A single HV channel powers 2 RPC chambers both in the barrel and endcap  
 1955 regions. The Low Voltage boards are located in UXC on the balconies and provide the voltage to the

<sup>1956</sup> front end electronics.

### <sup>1957</sup> 5.1.3 Pulse processing of CMS RPCs

<sup>1958</sup> Signals induced by cosmic particle in the RPC strips are shaped by standard CMS RPC Front-End  
<sup>1959</sup> Electronics (FEE) following the scheme of Figure 5.1. On a first stage, analogic signals are amplified  
<sup>1960</sup> and then sent to the Constant Fraction Discriminator (CFD) described in Figure 5.2. At the end of  
<sup>1961</sup> the chain, 100 ns long pulses are sent in the LVDS output. These output signal are sent on one side to  
<sup>1962</sup> a V1190A Time-to-Digital Converter (TDC) module from CAEN and on the other to an OR module  
<sup>1963</sup> to count the number of detected signals. Trigger and hit coïncidences are monitored using scalers.  
<sup>1964</sup> The TDC is used to store the data into ROOT files. These files are thus analysed to understand the  
<sup>1965</sup> detectors performance.

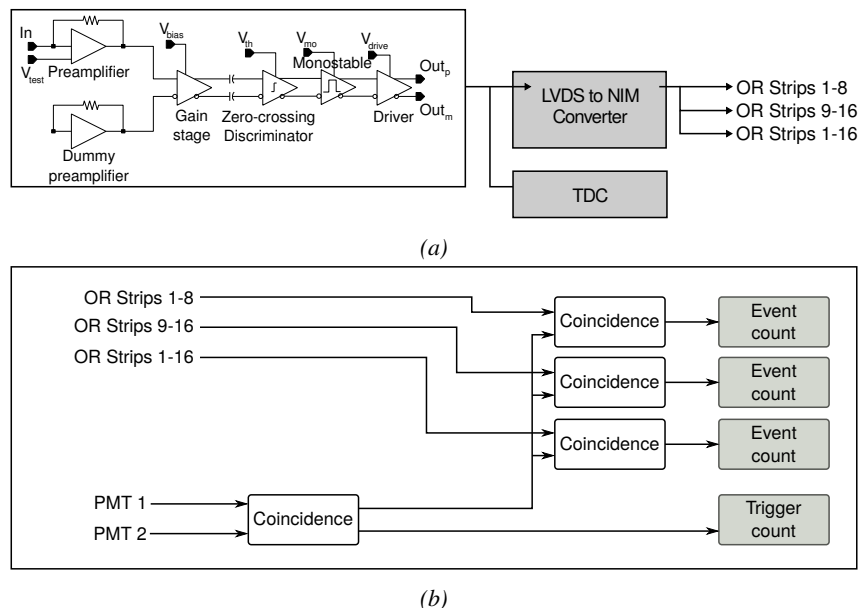
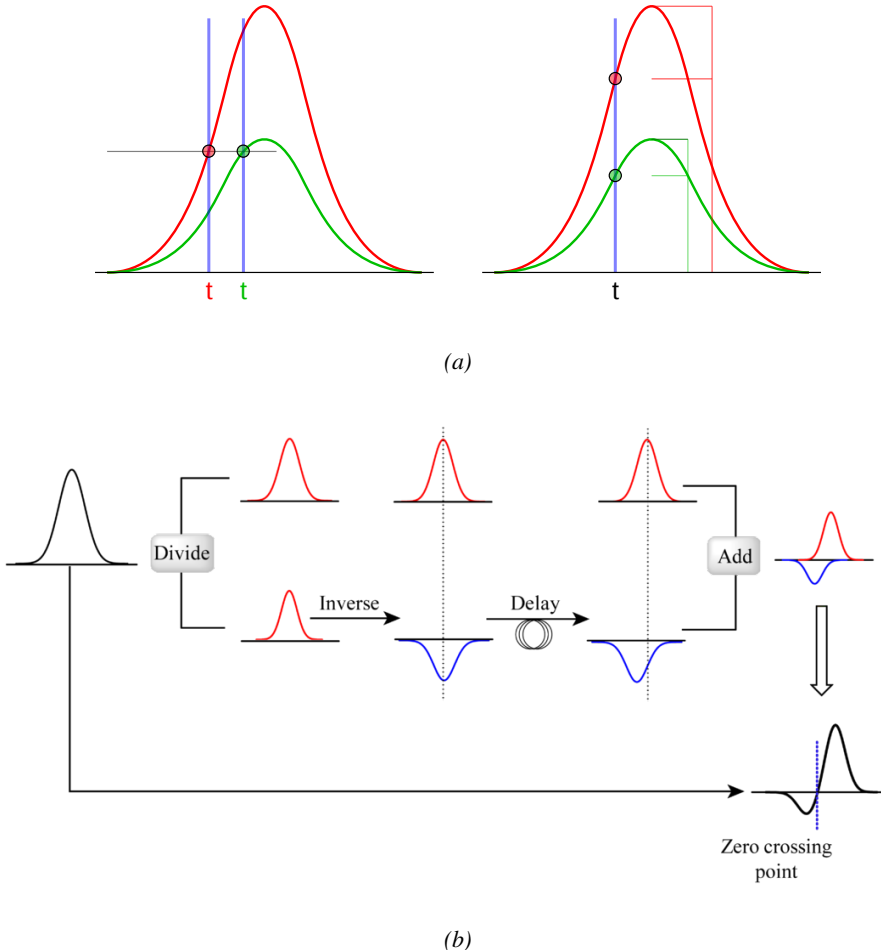


Figure 5.1: Signals from the RPC strips are shaped by the FEE described on Figure 5.1a. Output LVDS signals are then read-out by a TDC module connected to a computer or converted into NIM and sent to scalers. Figure 5.1b describes how these converted signals are put in coincidence with the trigger.



*Figure 5.2: Description of the principle of a CFD. A comparison of threshold triggering (left) and constant fraction triggering (right) is shown in Figure 5.2a. Constant fraction triggering is obtained thanks to zero-crossing technique as explained in Figure 5.2b. The signal arriving at the input of the CFD is split into three components. A first one is delayed and connected to the inverting input of a first comparator. A second component is connected to the noninverting input of this first comparator. A third component is connected to the noninverting input of another comparator along with a threshold value connected to the inverting input. Finally, the output of both comparators is fed through an AND gate.*

## 1966 5.2 Testing detectors under extreme conditions

1967 The upgrade from LHC to HL-LHC will increase the peak luminosity from  $10^{34} \text{ cm}^{-2} \text{ s}^{-1}$  to reach  
 1968  $5 \times 10^{34} \text{ cm}^{-2} \text{ s}^{-1}$ , increasing in the same way the total expected background to which the RPC  
 1969 system will be subjected to. Composed of low energy gammas and neutrons from  $p\text{-}p$  collisions, low  
 1970 momentum primary and secondary muons, puch-through hadrons from calorimeters, and particles  
 1971 produced in the interaction of the beams with collimators, the background will mostly affect the  
 1972 regions of CMS that are the closest to the beam line, i.e. the RPC detectors located in the endcaps.  
 1973 [To update.]

1974

1975 The 2016 data allowed to study the values of the background rate in all RPC system. In Figure 5.3, the distribution of the chamber background hit rate per unit area is shown at a luminosity of  $5 \times 10^{34} \text{ cm}^{-2} \cdot \text{s}^{-1}$  linearly extrapolating from data collected in 2016 [ref mentioning the linear dependency of rate vs lumi]. The maximum rate per unit area at HL-LHC conditions is expected to be of the order of  $600 \text{ Hz/cm}^2$  (including a safety factor 3). Nevertheless, Fluka simulations have conducted in order to understand the background at HL-LHC conditions. The comparison to the data has shown, in Figure 5.4, a discrepancy of a factor 2 even though the order of magnitude is consistent. [Understand mismatch.]

1983

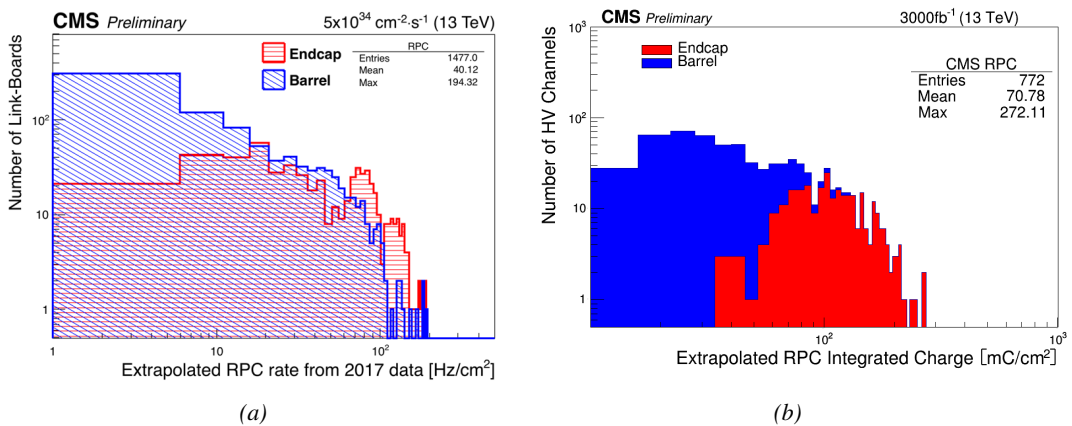


Figure 5.3: Figure 5.3a: The integrated charge per region (Barrel, Endcap) is extrapolated to HL-LHC integrated luminosity ( $3000 \text{ fb}^{-1}$ ) using the data accumulated in 2016 in every HV channels. Figure 5.3b: The hit rate per region (Barrel, Endcap) is linearly extrapolated to HL-LHC highest instantaneous luminosity ( $5 \times 10^{34} \text{ cm}^{-2} \text{s}^{-1}$ ) using the rate as a function of instantaneous luminosity recorded by RPCs in 2017 showing a linear dependence.

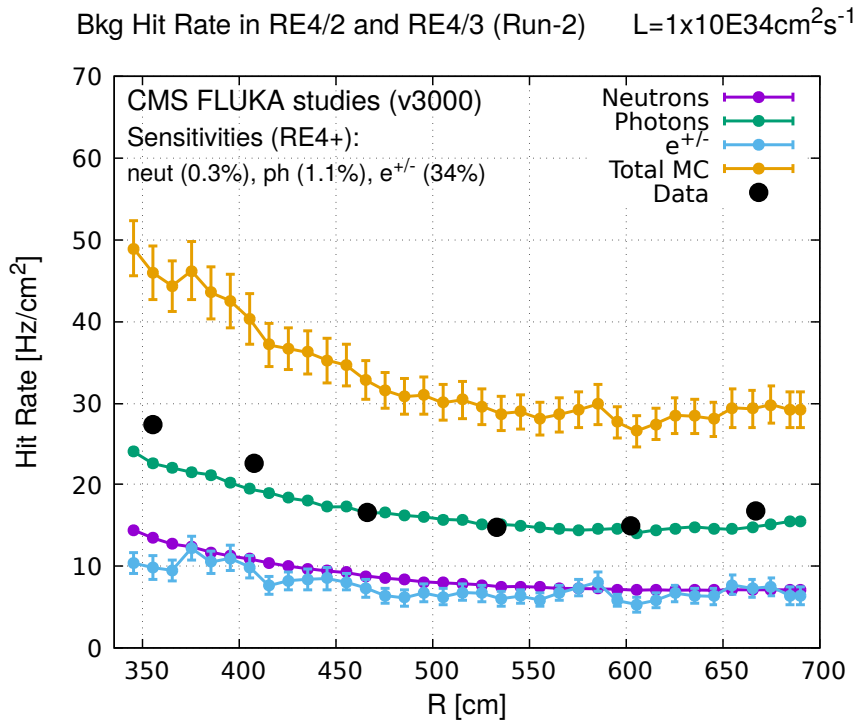


Figure 5.4: Background Fluka simulation compared to 2016 Data at  $L = 10^{34} \text{ cm}^{-2} \cdot \text{s}^{-1}$  in the fourth endcap disk region. A mismatch in between simulation and data can be observed. [\[To be understood.\]](#)

In the past, extensive long-term tests were carried out at several gamma and neutron facilities certifying the detector performance. Both full size and small prototype RPCs have been irradiated with photons up to an integrated charge of  $\sim 0.05C/\text{cm}^2$  and  $\sim 0.4C/\text{cm}^2$ , respectively [59, 60]. During Run-I, the RPC system provided stable operation and excellent performance and did not show any aging effects for integrated charge of the order of  $0.01C/\text{cm}^2$ . Projections on currents from 2016 Data, has allowed to determine that the total integrated charge, by the end of HL-LHC, would be of the order of  $1C/\text{cm}^2$  (including a safety factor 3). [\[Corresponding figure needed.\]](#)

1991

## 1992 5.2.1 The Gamma Irradiation Facilities

### 1993 5.2.1.1 GIF

1994 Located in the SPS West Area at the downstream end of the X5 test beam, the Gamma Irradiation  
 1995 Facility (GIF) was a test area in which particle detectors were exposed to a particle beam in presence  
 1996 of an adjustable gamma background [61]. Its goal was to reproduce background conditions these  
 1997 detectors would suffer in their operating environment at LHC. GIF layout is shown in Figure 5.5.  
 1998 Gamma photons are produced by a strong <sup>137</sup>Cs source installed in the upstream part of the zone  
 1999 inside a lead container. The source container includes a collimator, designed to irradiate a  $6 \times 6 \text{ m}^2$   
 2000 area at 5 m maximum to the source. A thin lens-shaped lead filter helps providing with a uniform  
 2001 outcoming flux in a vertical plane, orthogonal to the beam direction. The principal collimator hole  
 2002 provides a pyramidal aperture of  $74^\circ \times 74^\circ$  solid angle and provides a photon flux in a pyramidal vol-

ume along the beam axis. The photon rate is controled by further lead filters allowing the maximum rate to be limited and to vary within a range of four orders of magnitude. Particle detectors under test are then placed within the pyramidal volume in front of the source, perpendicularly to the beam line in order to profit from the homogeneous photon flux. Adjusting the background flux of photons can then be done by using the filters and choosing the position of the detectors with respect to the source.

2008

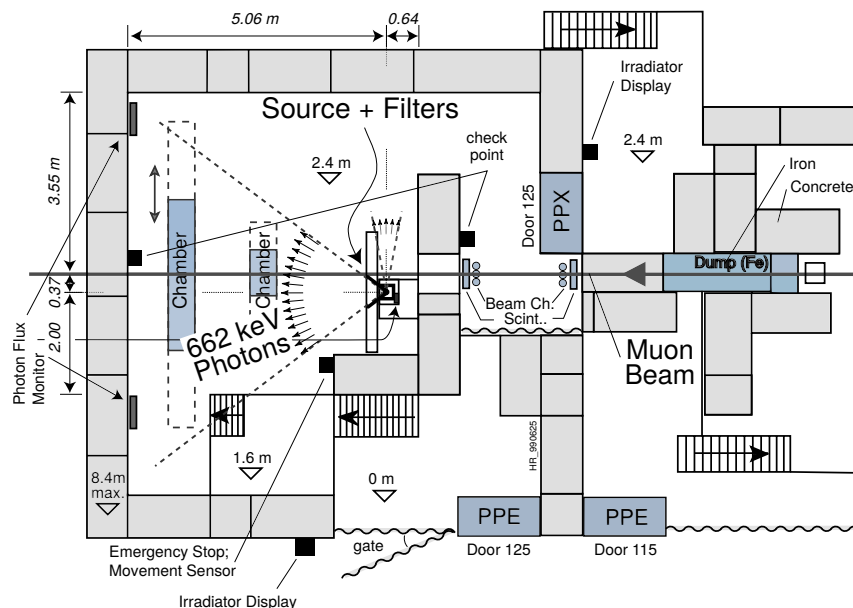


*Figure 5.5: Layout of the test beam zone called X5c GIF at CERN. Photons from the radioactive source produce a sustained high rate of random hits over the whole area. The zone is surrounded by 8 m high and 80 cm thick concrete walls. Access is possible through three entry points. Two access doors for personnel and one large gate for material. A crane allows installation of heavy equipment in the area.*

2009 As described on Figure 5.6, the  $^{137}\text{Cs}$  source emits a 662 keV photon in 85% of the decays. An  
2010 activity of 740 GBq was measured on the 5<sup>th</sup> March 1997. To estimate the strength of the flux in  
2011 2014, it is necessary to consider the nuclear decay through time assiciated to the Cesium source  
2012 whose half-life is well known ( $t_{1/2} = (30.05 \pm 0.08)$  y). The GIF tests were done in between the  
2013 20<sup>th</sup> and the 31<sup>st</sup> of August 2014, i.e. at a time  $t = (17.47 \pm 0.02)$  y resulting in an attenuation of  
2014 the activity from 740 GBq in 1997 to 494 GBq in 2014.

2015

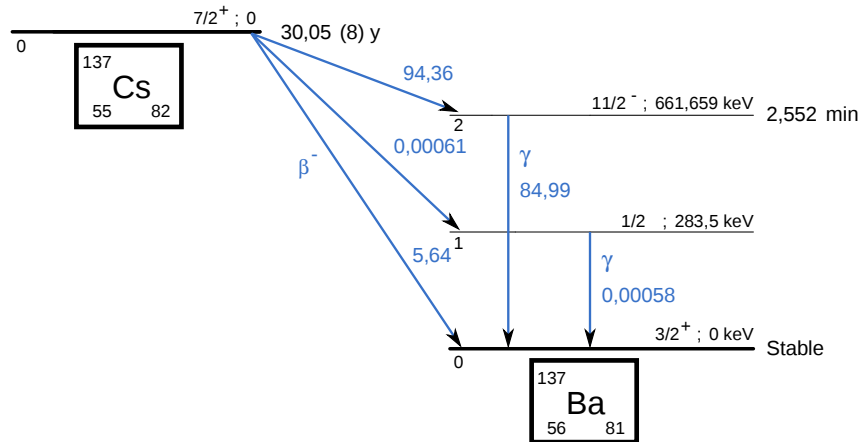


Figure 5.6:  $^{137}\text{Cs}$  decays by  $\beta^-$  emission to the ground state of  $^{137}\text{Ba}$  (BR = 5.64%) and via the 662 keV isomeric level of  $^{137}\text{Ba}$  (BR = 94.36%) whose half-life is 2.55 min.

### 2016 5.2.1.2 GIF++

2017 The new Gamma Irradiation Facility (GIF++), located in the SPS North Area at the downstream end  
 2018 of the H4 test beam, has replaced its predecessor during LS1 and has been operational since spring  
 2019 2015 [62]. Like GIF, GIF++ features a  $^{137}\text{Cs}$  source of 662 keV gamma photons, their fluence being  
 2020 controlled with a set of filters of various attenuation factors. The source provides two separated large  
 2021 irradiation areas for testing several full-size muon detectors with continuous homogeneous irradiation,  
 2022 as presented in Figure 5.7.

2023

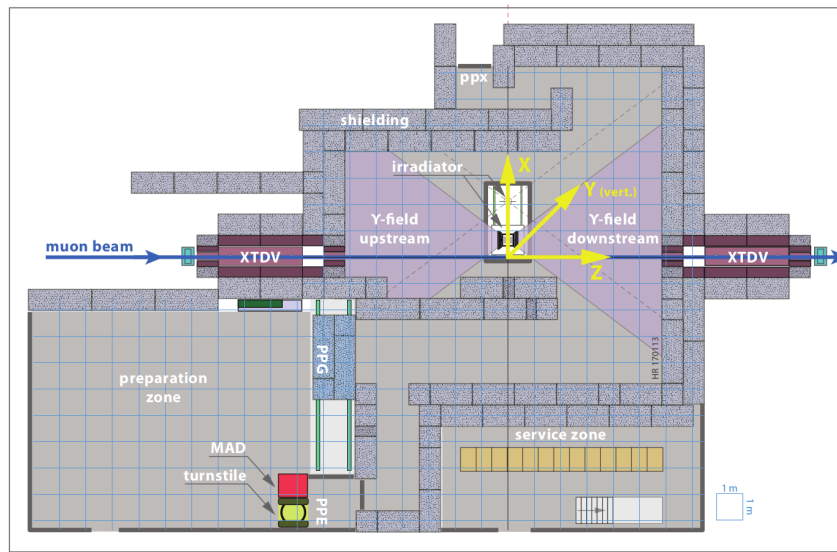
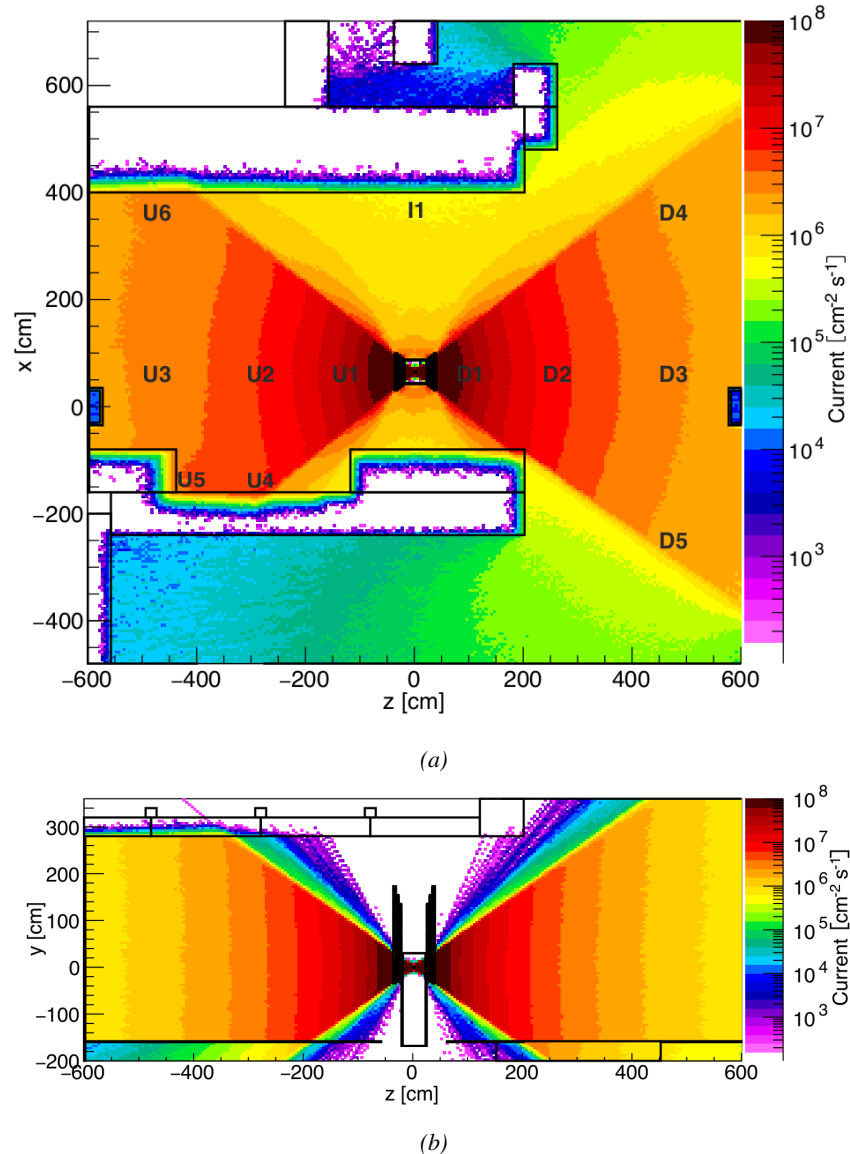


Figure 5.7: Floor plan of the GIF++ facility. When the facility downstream of the GIF++ takes electron beam, a beam pipe is installed along the beam line (z-axis). The irradiator can be displaced laterally (its center moves from  $x = 0.65 \text{ m}$  to  $2.15 \text{ m}$ ), to increase the distance to the beam pipe.

The source activity was measured to be about 13.5 TBq in March 2016. The photon flux being far greater than HL-LHC expectations, GIF++ provides an excellent facility for accelerated aging tests of muon detectors.

2027



*Figure 5.8: Simulated unattenuated current of photons in the xz plane (Figure 5.8a) and yz plane (Figure 5.8b) through the source at  $x = 0.65$  m and  $y = 0$  m. With angular correction filters, the current of 662 keV photons is made uniform in xy planes.*

2028  
2029  
2030

The source is situated in the muon beam line with the muon beam being available a few times a year. The H4 beam, composed of muons with a momentum of about 150 GeV/c, passes through the GIF++ zone and is used to study the performance of the detectors. Its flux is of 104 particles/ $\text{s cm}^2$

2031 focused in an area similar to  $10 \times 10 \text{ cm}^2$ . Therefore, with properly adjusted filters, one can imitate  
 2032 the HL-LHC background and study the performance of muon detectors with their trigger/readout  
 2033 electronics in HL-LHC environment.

2034

## 2035 5.3 Preliminary tests at GIF

### 2036 5.3.1 Resistive Plate Chamber test setup

2037 During summer 2014, preliminary tests have been conducted in the GIF area on a newly produced  
 2038 RE4/2 chamber labelled RE-4-2-BARC-161. This chamber has been placed into a trolley covered  
 2039 with a tent. The position of the RPC inside the tent and of the tent related to the source is described  
 2040 in Figure 5.9. To test this CMS RPC, three different absorber settings were used. First of all,  
 2041 measurements were done with fully opened source. Then, to complete this preliminary study, the  
 2042 gamma flux has been attenuated from a factor 2 and a factor 5. The expected gamma flux at the level  
 2043 of our detector will be discussed in subsection ??.

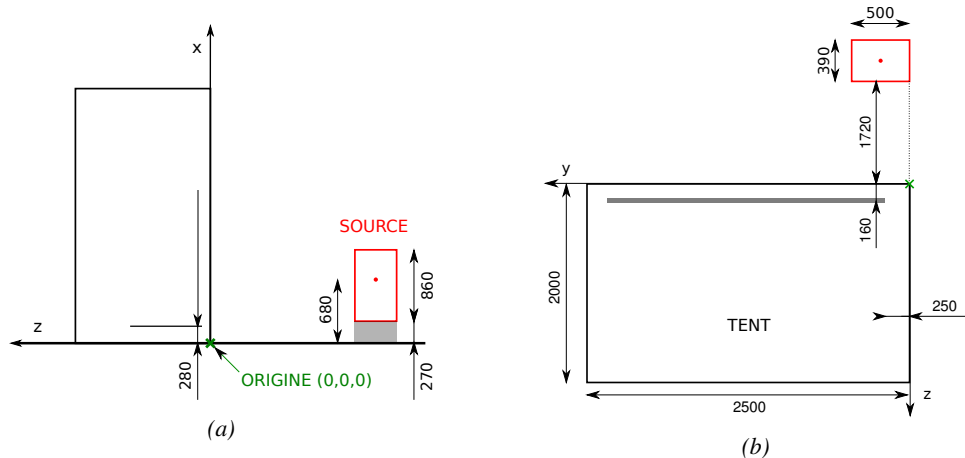
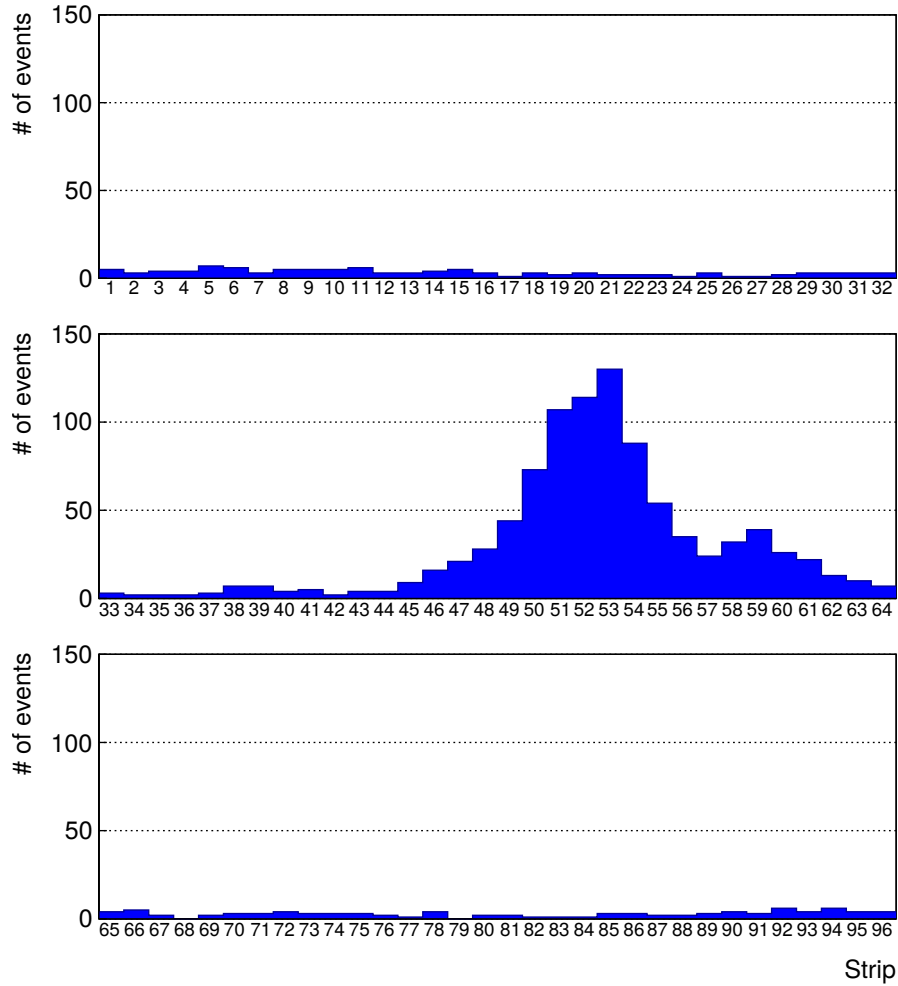


Figure 5.9: Description of the RPC setup. Dimensions are given in mm. A tent containing RPCs is placed at 1720 mm from the source container. The source is situated in the center of the container. RE-4-2-BARC-161 chamber is 160 mm inside the tent. This way, the distance between the source and the chambers plan is 2060 mm. Figure 5.9a provides a side view of the setup in the xz plane while Figure 5.9b shows a top view in the yz plane.



*Figure 5.10: RE-4-2-BARC-I61 chamber is inside the tent as described in Figure 5.9. In the top right, the two scintillators used as trigger can be seen. This trigger system has an inclination of 10° relative to horizontal and is placed above half-partition B2 of the RPCs. PMT electronics are shielded thanks to lead blocks placed in order to protect them without stopping photons from going through the scintillators and the chamber.*

2044 At the time of the tests, the beam not being operational anymore, a trigger composed of 2 plastic  
 2045 scintillators has been placed in front of the setup with an inclination of 10 deg with respect to the  
 2046 detector plane in order to look at cosmic muons. Using this particular trigger layout, shown on Fig-  
 2047 ure 5.10, leads to a cosmic muon hit distribution into the chamber similar to the one in Figure 5.11.  
 2048 Measured without gamma irradiation, two peaks can be seen on the profil of partition B, centered  
 2049 on strips 52 and 59. Section ?? will help us understand that these two peaks are due respectively to  
 2050 forward and backward coming cosmic particles where forward coming particles are first detected by  
 2051 the scintillators and then the RPC while the backward coming muons are first detected in the RPC.



*Figure 5.11: Hit distributions over all 3 partitions of RE-4-2-BARC-161 chamber is showed on these plots. Top, middle and bottom figures respectively correspond to partitions A, B, and C. These plots show that some events still occur in other half-partitions than B2, which corresponds to strips 49 to 64, in front of which the trigger is placed, contributing to the inefficiency of detection of cosmic muons. In the case of partitions A and C, the very low amount of data can be interpreted as noise. On the other hand, it is clear that a little portion of muons reach the half-partition B1, corresponding to strips 33 to 48.*

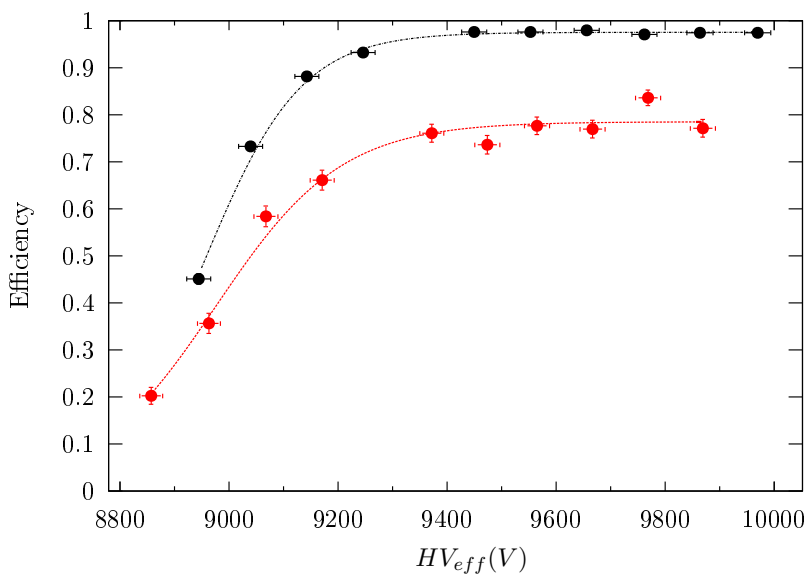
### 2052 5.3.2 Data Acquisition

### 2053 5.3.3 Geometrical acceptance of the setup layout to cosmic muons

2054 In order to profit from a constant gamma irradiation, the detectors inside of the GIF bunker need  
 2055 to be placed in a plane orthogonal to the beam line. The muon beam that used to be available was  
 2056 meant to test the performance of detectors under test. This beam not being active anymore, another  
 2057 solution to test detector performance had to be used. Thus, it has been decided to use cosmic muons  
 2058 detected through a telescope composed of two scintillators. Lead blocks were used as shielding to

2059 protect the photomultipliers from gammas as can be seen from Figure 5.10.

2060 An inclination has been given to the cosmic telescope to maximize the muon flux. A good com-  
 2061 promise had to be found between good enough muon flux and narrow enough hit distribution to  
 2062 be sure to contain all the events into only one half partitions as required from the limited available  
 2063 readout hardware. Nevertheless, a consequence of the misplaced trigger, that can be seen as a loss  
 2064 of events in half-partition B1 in Figure 5.11, is an inefficiency. Nevertheless, the inefficiency of ap-  
 2065 proximately 20 % highlighted in Figure 5.12 by comparing the performance of chamber BARC-161  
 2066 in 904 and at GIF without irradiation seems too important to be explained only by the geometri-  
 2067 cal acceptance of the setup itself. Simulations have been conducted to show how the setup brings  
 2068 inefficiency.



2069 *Figure 5.12: Results are derived from data taken on half-partition B2 only. On the 18<sup>th</sup> of June 2014, data  
 2070 has been taken on chamber RE-2-BARC-161 at building 904 (Prevessin Site) with cosmic muons providing us a  
 2071 reference efficiency plateau of  $(97.54 \pm 0.15)\%$  represented by a black curve. A similar measurement has been  
 2072 done at GIF on the 21<sup>st</sup> of July with the same chamber giving a plateau of  $(78.52 \pm 0.94)\%$  represented by a  
 2073 red curve.*

### 2069 5.3.3.1 Description of the simulation layout

2070 The layout of GIF setup has been reproduced and incorporated into a Monte Carlo (MC) simulation  
 2071 to study the influence of the disposition of the telescope on the final distribution measured by the  
 2072 RPC. A 3D view of the simulated layout is given into Figure 5.13. Muons are generated randomly  
 2073 in a horizontal plane located at a height corresponding to the lowest point of the PMTs. This way,  
 2074 the needed size of the plane in order to simulate events happening at very big azimuthal angles (i.e.  
 2075  $\theta \approx \pi$ ) can be kept relatively small. The muon flux is designed to follow the usual  $\cos^2\theta$  distribution  
 2076 for cosmic particle. The goal of the simulation is to look at muons that pass through the muon  
 2077 telescope composed of the two scintillators and define their distribution onto the RPC plane. During  
 2078 the reconstruction, the RPC plane is then divided into its strips and each muon track is assigned to a  
 2079 strip.

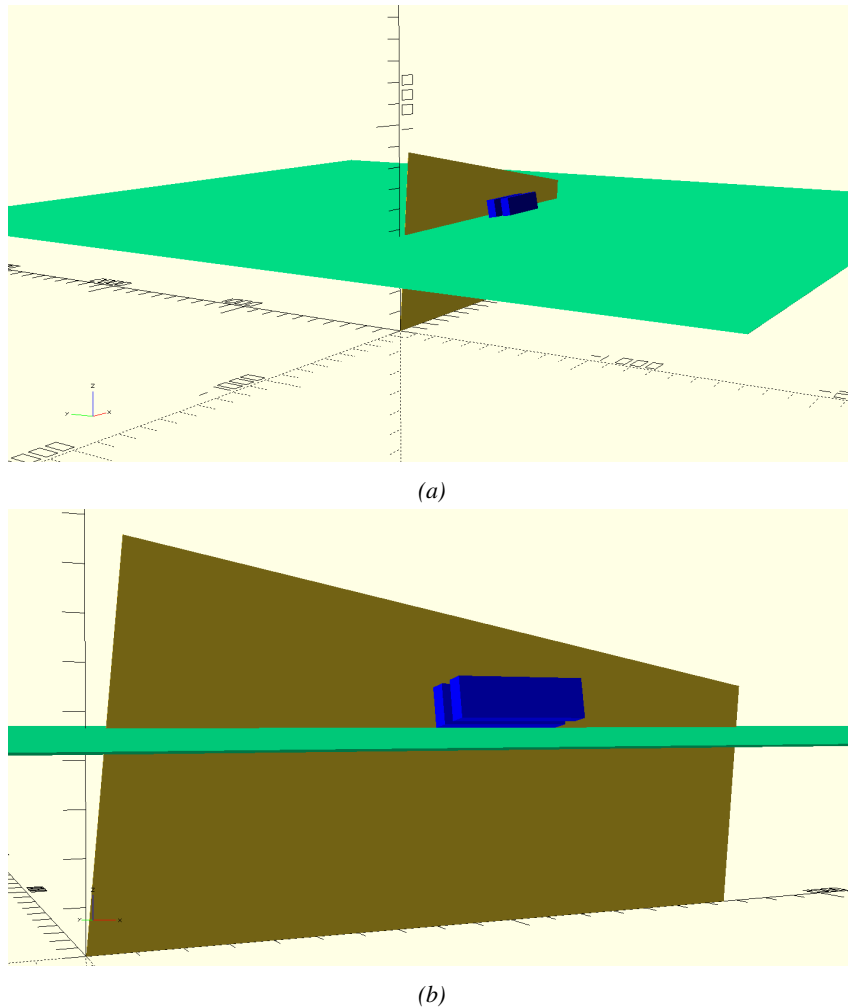


*Figure 5.13: Representation of the layout used for the simulations of the test setup. The RPC is represented as a yellow trapezoid while the two scintillators as blue cuboids looking at the sky. A green plane corresponds to the muon generation plane within the simulation. Figure 5.9a shows a global view of the simulated setup. Figure 5.9b shows a zoomed view that allows to see the 2 scintillators as well as the full RPC plane.*

2080        In order to further refine the quality of the simulation and understand deeper the results the  
 2081        dependance of the distribution has been studied for a range of telescope inclinations. Moreover,  
 2082        the threshold applied on the PMT signals has been included into the simulation in the form of a  
 2083        cut. In the approximation of uniform scintillators, it has been considered that the threshold can be  
 2084        understood as the minimum distance particles need to travel through the scintillating material to give  
 2085        a strong enough signal. Particles that travel a distance smaller than the set "threshold" are thus not  
 2086        detected by the telescope and cannot trigger the data taking. Finally, the FEE threshold also has  
 2087        been considered in a similar way. The mean momentum of horizontal cosmic rays is higher than  
 2088        those of vertical ones but the stopping power of matter for momenta ranging from 1 GeV to 1 TeV  
 2089        stays comparable. It is then possible to assume that the mean number of primary  $e^-$ /ion pairs per  
 2090        unit length will stay similar and thus, depending on the applied discriminator threshold, muons with

2091 the shortest path through the gas volume will deposit less charge and induce a smaller signal on the  
 2092 pick-up strips that could eventually not be detected. These two thresholds also restrain the overall  
 2093 geometrical acceptance of the system.

2094 **5.3.3.2 Simulation procedure**

2095 The simulation software has been designed using C++ and the output data is saved into ROOT  
 2096 histograms. Simulations start for a threshold  $T_{scint}$  varying in a range from 0 to 45 mm in steps  
 2097 of 5 mm, where  $T_{scint} = 0$  mm corresponds to the case where there isn't any threshold apply on  
 2098 the input signal while  $T_{scint} = 45$  mm, which is the scintillator thickness, is the case where muons  
 2099 cannot arrive orthogonally onto the scintillator surface. For a given  $T_{scint}$ , a set of RPC thresholds  
 2100 are considered. The RPC threshold,  $T_{RPC}$  varies from 2 mm, the thickness of the gas volume, to  
 2101 3 mm in steps of 0.25 mm. For each  $(T_{scint}; T_{RPC})$  pair,  $N_\mu = 10^8$  muons are randomly generated  
 2102 inside the muon plane described in the previous paragraph with an azimuthal angle  $\theta$  chosen to follow  
 2103 a  $\cos^2\theta$  distribution.

2104 Planes are associated to each surface of the scintillators. Knowing muon position into the muon  
 2105 plane and its direction allows us, by assuming that muons travel in a straight line, to compute the  
 2106 intersection of the muon track with these planes. Applying conditions to the limits of the surfaces  
 2107 of the scintillator faces then gives us an answer to whether or not the muon passed through the  
 2108 scintillators. In the case the muon has indeed passed through the telescope, the path through each  
 2109 scintillator is computed and muons whose path was shorter than  $T_{scint}$  are rejected and are thus  
 2110 considered as having not interacted with the setup.

2111 On the contrary, if the muon is labeled as good, its position within the RPC plane is computed  
 2112 and the corresponding strip, determined by geometrical tests in the case the distance through the  
 2113 gas volume was enough not to be rejected because of  $T_{RPC}$ , gets a hit and several histograms  
 2114 are filled in order to keep track of the generation point on the muon plane, the intersection points  
 2115 of the reconstructed muons within the telescope, or on the RPC plane, the path traveled through  
 2116 each individual scintillator or the gas volume, as well as other histograms. Moreover, muons fill  
 2117 different histograms whether they are forward or backward coming muons. They are discriminated  
 2118 according to their direction components. When a muon is generated, an  $(x, y, z)$  position is assigned  
 2119 into the muon plane as well as a  $(\theta; \phi)$  pair that gives us the direction it's coming from. This way,  
 2120 muons satisfying the condition  $0 \leq \phi < \pi$  are designated as backward coming muons while muons  
 2121 satisfying  $\pi \leq \phi < 2\pi$  as forward coming muons.

2122 This simulation is then repeated for different telescope inclinations ranging in between 4 and 20°  
 2123 and varying in steps of 2°. Due to this inclination and to the vertical position of the detector under  
 2124 test, the muon distribution reconstructed in the detector plane is asymmetrical. The choice as been  
 2125 made to chose a skew distribution formula to fit the data built as the multiplication of gaussian and  
 2126 sigmoidal curves together. A typical gaussian formula is given as 5.1 and has three free parameters  
 2127 as  $A_g$ , its amplitude,  $\bar{x}$ , its mean value and  $\sigma$ , its root mean square. Sigmoidal curves as given by  
 2128 formula 5.2 are functions converging to 0 and  $A_s$  as  $x$  diverges. The inflection point is given as  $x_i$   
 2129 and  $\lambda$  is proportional to the slope at  $x = x_i$ . In the limit where  $\lambda \rightarrow \infty$ , the sigmoid becomes a  
 2130 step function.

$$g(x) = A_g e^{-\frac{(x-\bar{x})^2}{2\sigma^2}} \quad (5.1)$$

$$s(x) = \frac{A_s}{1 + e^{-\lambda(x-x_i)}} \quad (5.2)$$

Finally, a possible representation of a skew distribution is given by formula 5.3 and is the product of 5.1 and 5.2. Naturally, here  $A_{sk} = A_g \times A_s$  and represents the theoretical maximum in the limit where the skew tends to a gaussian function.

$$sk(x) = g(x) \times s(x) = A_{sk} \frac{e^{\frac{-(x-\bar{x})^2}{2\sigma^2}}}{1 + e^{-\lambda(x-x_i)}} \quad (5.3)$$

### 5.3.3.3 Results

#### Influence of $T_{scint}$ on the muon distribution

#### Influence of $T_{RPC}$ on the muon distribution

#### Influence of the telescope inclination on the muon distribution

#### Comparison to data taken at GIF without irradiation

### 5.3.4 Photon flux at GIF

#### 5.3.4.1 Expectations from simulations

In order to understand and evaluate the  $\gamma$  flux in the GIF area, simulations had been conducted in 1999 and published by S. Agosteo et al [61]. Table 5.1 presented in this article gives us the  $\gamma$  flux for different distances  $D$  to the source. This simulation was done using GEANT and a Monte Carlo N-Particle (MCNP) transport code, and the flux  $F$  is given in number of  $\gamma$  per unit area and unit time along with the estimated error from these packages expressed in %.

Nominal ABS	Photon flux $F$ [ $s^{-1}cm^{-2}$ ]			
	at $D = 50$ cm	at $D = 155$ cm	at $D = 300$ cm	at $D = 400$ cm
1	$0.12 \cdot 10^8 \pm 0.2\%$	$0.14 \cdot 10^7 \pm 0.5\%$	$0.45 \cdot 10^6 \pm 0.5\%$	$0.28 \cdot 10^6 \pm 0.5\%$
2	$0.68 \cdot 10^7 \pm 0.3\%$	$0.80 \cdot 10^6 \pm 0.8\%$	$0.25 \cdot 10^6 \pm 0.8\%$	$0.16 \cdot 10^6 \pm 0.6\%$
5	$0.31 \cdot 10^7 \pm 0.4\%$	$0.36 \cdot 10^6 \pm 1.2\%$	$0.11 \cdot 10^6 \pm 1.2\%$	$0.70 \cdot 10^5 \pm 0.9\%$

Table 5.1: Total photon flux ( $E\gamma \leq 662$  keV) with statistical error predicted considering a  $^{137}Cs$  activity of 740 GBq at different values of the distance  $D$  to the source along the  $x$ -axis of irradiation field [61].

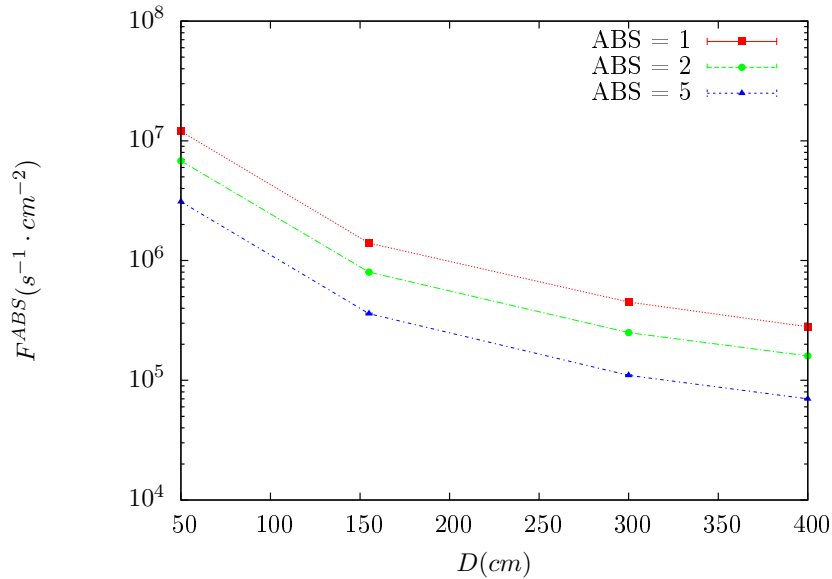


Figure 5.14:  $\gamma$  flux  $F(D)$  is plot using values from table 5.1. As expected, the plot shows similar attenuation behaviours with increasing distance for each absorption factors.

The simulation doesn't directly provides us with an estimated flux at the level of our RPC. First of all, it is needed to extract the value of the flux from the available data contained in the original paper and then to estimate the flux in 2014 at the time the experimentation took place. Figure 5.14 that contains the data from Table 5.1. In the case of a pointlike source emitting isotropic and homogeneous gamma radiations, the gamma flux  $F$  at a distance  $D$  to the source with respect to a reference point situated at  $D_0$  where a known flux  $F_0$  is measured will be expressed like in Equation 5.4, assuming that the flux decreases as  $1/D^2$ , where  $c$  is a fitting factor.

$$F^{ABS} = F_0^{ABS} \times \left( \frac{cD_0}{D} \right)^2 \quad (5.4)$$

By rewriting Equation 5.4, it comes that :

$$c = \frac{D}{D_0} \sqrt{\frac{F^{ABS}}{F_0^{ABS}}} \quad (5.5)$$

$$\Delta c = \frac{c}{2} \left( \frac{\Delta F^{ABS}}{F^{ABS}} + \frac{\Delta F_0^{ABS}}{F_0^{ABS}} \right) \quad (5.6)$$

Finally, using Equation 5.5 and the data in Table 5.1 with  $D_0 = 50$  cm as reference point, we can build Table 5.2. It is interesting to note that  $c$  for each value of  $D$  doesn't depend on the absorption factor.

Nominal ABS	Correction factor $c$		
	at $D = 155$ cm	at $D = 300$ cm	at $D = 400$ cm
1	$1.059 \pm 0.70\%$	$1.162 \pm 0.70\%$	$1.222 \pm 0.70\%$
2	$1.063 \pm 1.10\%$	$1.150 \pm 1.10\%$	$1.227 \pm 0.90\%$
5	$1.056 \pm 1.60\%$	$1.130 \pm 1.60\%$	$1.202 \pm 1.30\%$

Table 5.2: Correction factor  $c$  is computed thanks to formulae 5.5 taking as reference  $D_0 = 50$  cm and the associated flux  $F_0^{ABS}$  for each absorption factor available in table 5.1.

2157 For the range of  $D/D_0$  values available, it is possible to use a simple linear fit to get the evolution  
 2158 of  $c$ . The linear fit will then use only 2 free parameters,  $a$  and  $b$ , as written in Equation 5.7. This gives  
 2159 us the results showed in Figure 5.15. Figure 5.15b confirms that using only a linear fit to extract  $c$  is  
 2160 enough as the evolution of the rate that can be obtained superimposes well on the simulation points.

$$c \left( \frac{D}{D_0} \right) = a \frac{D}{D_0} + b \quad (5.7)$$

$$F^{ABS} = F_0^{ABS} \left( a + \frac{bD_0}{D} \right)^2 \quad (5.8)$$

$$\Delta F^{ABS} = F^{ABS} \left[ \frac{\Delta F_0^{ABS}}{F_0^{ABS}} + 2 \frac{\Delta a + \Delta b \frac{D_0}{D}}{a + \frac{bD_0}{D}} \right] \quad (5.9)$$

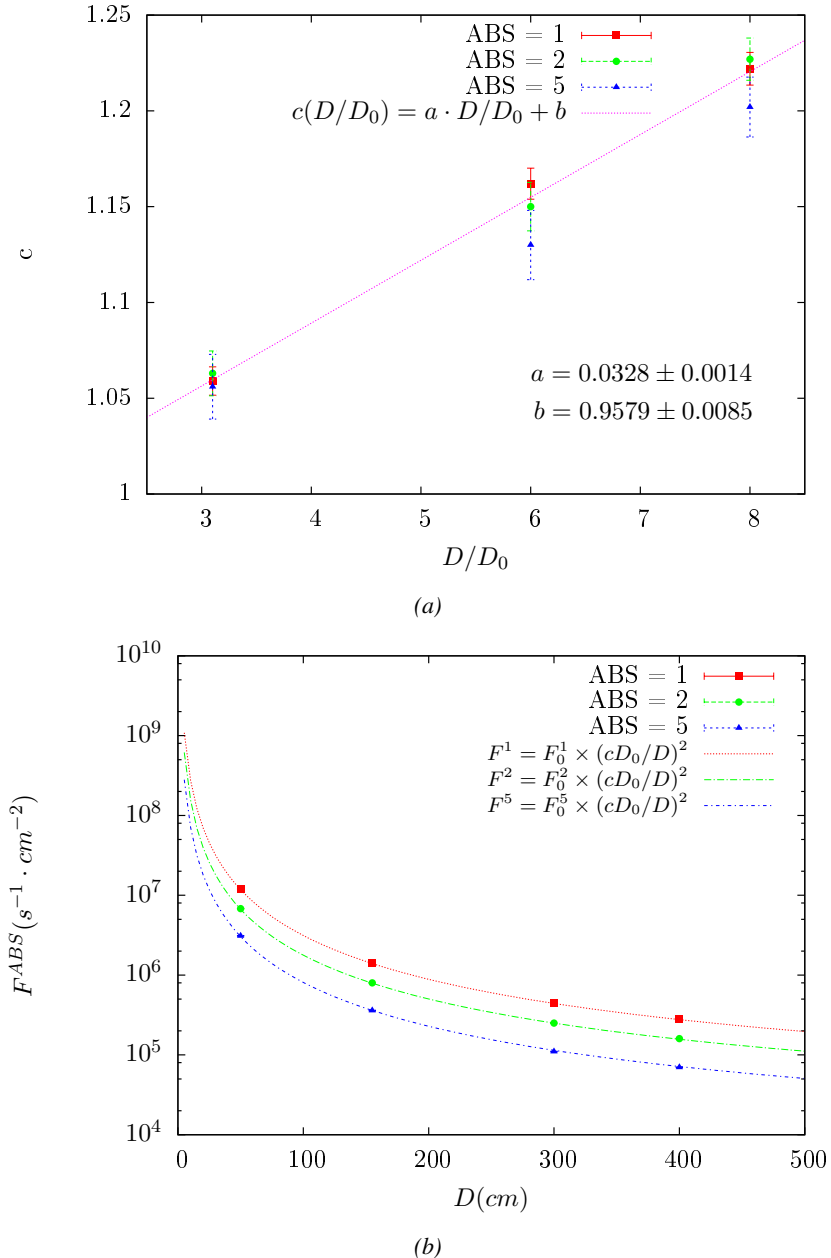


Figure 5.15: Figure 5.15a shows the linear approximation fit done via formulae 5.7 on data from table 5.2. Figure 5.15b shows a comparison of this model with the simulated flux using  $a$  and  $b$  given in figure 5.15a in formulae 5.4 and the reference value  $D_0 = 50\text{cm}$  and the associated flux for each absorption factor  $F_0^{ABS}$  from table 5.1

In the case of the 2014 GIF tests, the RPC plane is located at a distance  $D = 206\text{ cm}$  to the source. Moreover, to estimate the strength of the flux in 2014, it is necessary to consider the nuclear decay through time associated to the Cesium source whose half-life is well known ( $t_{1/2} = (30.05 \pm 0.08)\text{ y}$ ). The very first source activity measurement has been done on the 5<sup>th</sup> of March 1997 while the Gif

2165 tests were done in between the 20<sup>th</sup> and the 31<sup>st</sup> of August 2014, i.e. at a time  $t = (17.47 \pm 0.02)$  y  
 2166 resulting in an attenuation of the activity from 740 GBq in 1997 to 494 GBq in 2014. All the needed  
 2167 information to extrapolate the flux through our detector in 2014 has now been assembled, leading  
 2168 to the Table 5.3. It is interesting to note that for a common RPC sensitivity to  $\gamma$  of  $2 \cdot 10^{-3}$ , the  
 2169 order of magnitude of the estimated hit rate per unit area is of the order of the kHz for the fully  
 2170 opened source. Moreover, taking profit of the two working absorbers, it will be possible to scan  
 2171 background rates at 0 Hz,  $\sim 300$  Hz as well as  $\sim 600$  Hz. Without source, a good estimate of the  
 2172 intrinsic performance will be available. Then at 300 Hz, the goal will be to show that the detectors  
 2173 fulfill the performance certification of CMS RPCs. Then a first idea of the performance of the  
 2174 detectors at higher background will be provided with absorption factors 2 ( $\sim 600$  Hz) and 1 (no  
 2175 absorption). *[Here I will also put a reference to the plot showing the estimated background rate at  
 2176 the level of RE3/1 in the case of HL-LHC but this one being in another chapter, I will do it later.]*

Nominal ABS	Photon flux $F$ [ $s^{-1}cm^{-2}$ ]			Hit rate/unit area [ $Hz cm^{-2}$ ] at $D^{2014} = 206$ cm
	at $D_0^{1997} = 50$ cm	at $D^{1997} = 206$ cm	at $D^{2014} = 206$ cm	
1	$0.12 \cdot 10^8 \pm 0.2\%$	$0.84 \cdot 10^6 \pm 0.3\%$	$0.56 \cdot 10^6 \pm 0.3\%$	$1129 \pm 32$
2	$0.68 \cdot 10^7 \pm 0.3\%$	$0.48 \cdot 10^6 \pm 0.3\%$	$0.32 \cdot 10^6 \pm 0.3\%$	$640 \pm 19$
5	$0.31 \cdot 10^7 \pm 0.4\%$	$0.22 \cdot 10^6 \pm 0.3\%$	$0.15 \cdot 10^6 \pm 0.3\%$	$292 \pm 9$

Table 5.3: The data at  $D_0$  in 1997 is taken from [61]. In a second step, using Equations 5.8 and 5.9, the flux at  $D$  can be estimated in 1997. Then, taking into account the attenuation of the source activity, the flux at  $D$  can be estimated at the time of the tests in GIF in 2014. Finally, assuming a sensitivity of the RPC to  $\gamma$   $s = 2 \cdot 10^{-3}$ , an estimation of the hit rate per unit area is obtained.

2177 **5.3.4.2 Dose measurements**

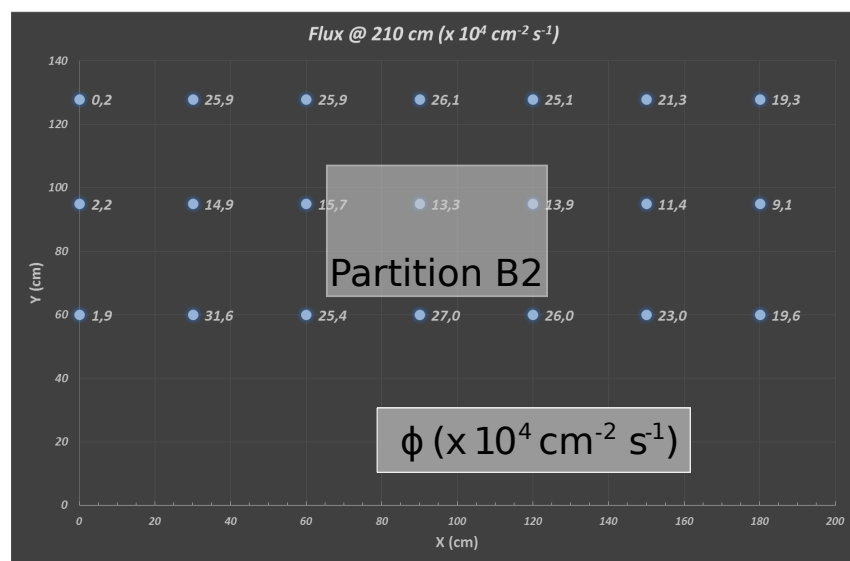


Figure 5.16: Dose measurements has been done in a plane corresponding to the tents front side. This plan is 1900 mm away from the source. As explained in the first chapter, a lens-shaped lead filter provides a uniform photon flux in the vertical plan orthogonal to the beam direction. If the second line of measured fluxes is not taken into account because of lower values due to experimental equipments in the way between the source and the tent, the uniformity of the flux is well showed by the results.

<sup>2178</sup> **5.3.5 Results and discussions**

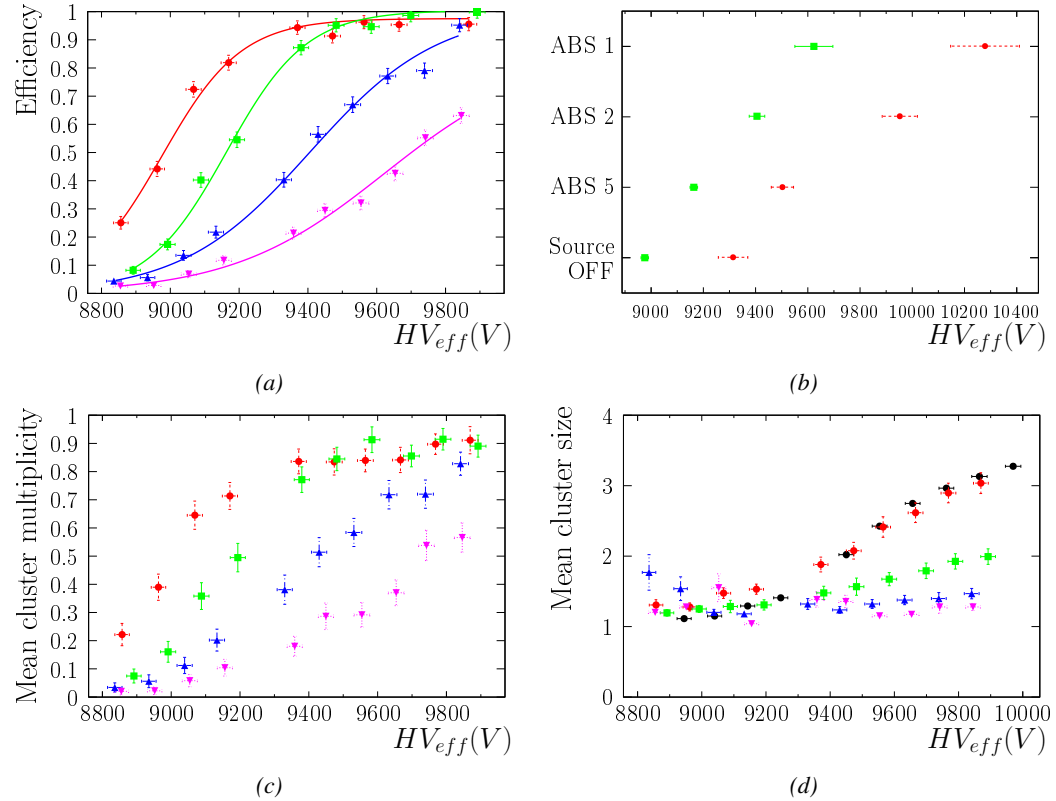


Figure 5.17

## 2179 5.4 Longevity tests at GIF++

2180 Longevity studies imply a monitoring of the performance of the detectors probed using a high inten-  
2181 sity muon beam in a irradiated environment by periodically measuring their rate capability, the dark  
2182 current running through them and the bulk resistivity of the Bakelite composing their electrodes.  
2183 GIF++, with its very intense  $^{137}\text{Cs}$  source, provides the perfect environment to perform such kind  
2184 of tests. Assuming a maximum acceleration factor of 3, it is expected to accumulate the equivalent  
2185 charge in 1.7 years.

2186 As the maximum background is found in the endcap, the choice naturally was made to focus the  
2187 GIF++ longevity studies on endcap chambers. Most of the RPC system was installed in 2007. Nev-  
2188 ertheless, the large chambers in the fourth endcap (RE4/2 and RE4/3) have been installed during  
2189 LS1 in 2014. The Bakelite of these two different productions having different properties, four spare  
2190 chambers of the present system were selected, two RE2,3/2 spares and two RE4/2 spares. Having  
2191 two chambers of each type allows to always keep one of them non irradiated as reference, the per-  
2192 formance evolution of the irradiated chamber being then compared through time to the performance  
2193 of the non irradiated one.

2194 The performance of the detectors under different level of irradiation is measured periodically dur-  
2195 ing dedicated test beam periods using the H4 muon beam. In between these test beam periods, the  
2196 two RE2,3/2 and RE4/2 chambers selected for this study are irradiated by the  $^{137}\text{Cs}$  source in order  
2197 to accumulate charge and the gamma background is monitored, as well as the currents. The two  
2198 remaining chambers are kept non-irradiated as reference detectors. Due to the limited gas flow in  
2199 GIF++, the RE4 chamber remained non-irradiated until end of November 2016 where a new mass  
2200 flow controller has been installed allowing for bigger volumes of gas to flow in the system.

2201 Figures 5.18 and 5.19 give us for different test beam periods, and thus for increasing integrated  
2202 charge through time, a comparison of the maximum efficiency, obtained using a sigmoid-like func-  
2203 tion, and of the working point of both irradiated and non irradiated chambers [50]. No aging is yet  
2204 to see from this data, the shifts in  $\gamma$  rate per unit area in between irradiated and non irradiated detec-  
2205 tors and RE2 and RE4 types being easily explained by a difference of sensitivity due to the various  
2206 Bakelite resistivities of the HPL electrodes used for the electrode production.

2207 Collecting performance data at each test beam period allows us to extrapolate the maximum effi-  
2208 ciency for a background hit rate of 300 Hz/cm<sup>2</sup> corresponding to the expected HL-LHC conditions.  
2209 Aging effects could emerge from a loss of efficiency with increasing integrated charge over time,  
2210 thus Figure 5.20 helps us understand such degradation of the performance of irradiated detectors in  
2211 comparison with non irradiated ones. The final answer for an eventual loss of efficiency is given in  
2212 Figure 5.21 by comparing for both irradiated and non irradiated detectors the efficiency sigmoids  
2213 before and after the longevity study. Moreover, to complete the performance information, the Bake-  
2214 lite resistivity is regularly measured thanks to Ag scans (Figure 5.22) and the noise rate is monitored  
2215 weekly during irradiation periods (Figure 5.23). At the end of 2016, no signs of aging were observed  
2216 and further investigation is needed to get closer to the final integrated charge requirements proposed  
2217 for the longevity study of the present CMS RPC sub-system.

2218

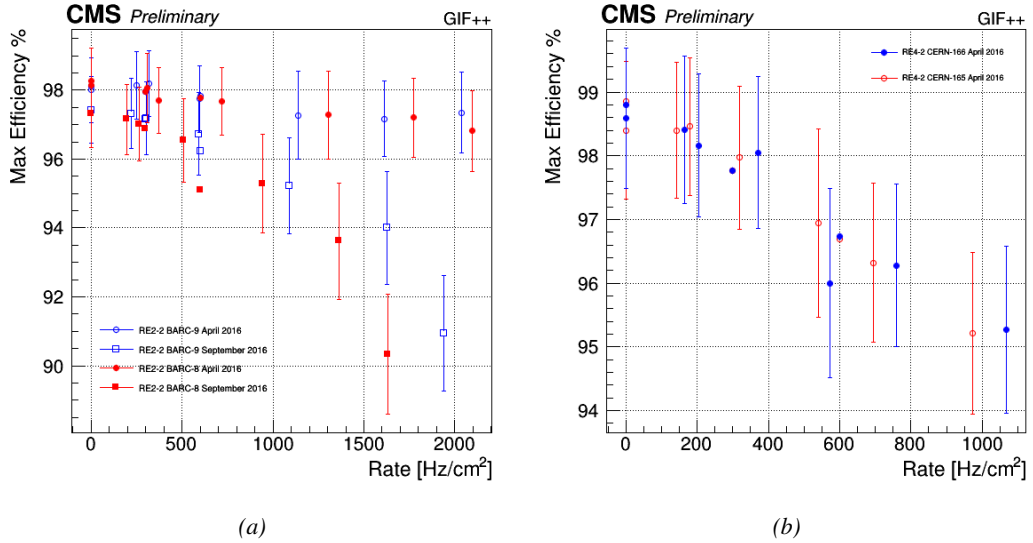


Figure 5.18: Evolution of the maximum efficiency for RE2 (5.18a) and RE4 (5.18b) chambers with increasing extrapolated  $\gamma$  rate per unit area at working point. Both irradiated (blue) and non irradiated (red) chambers are shown.

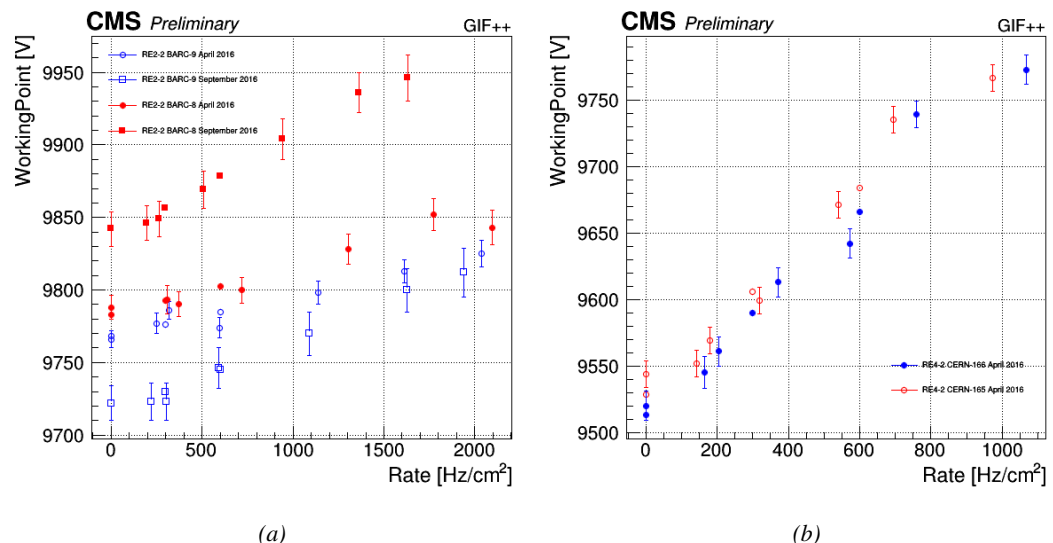
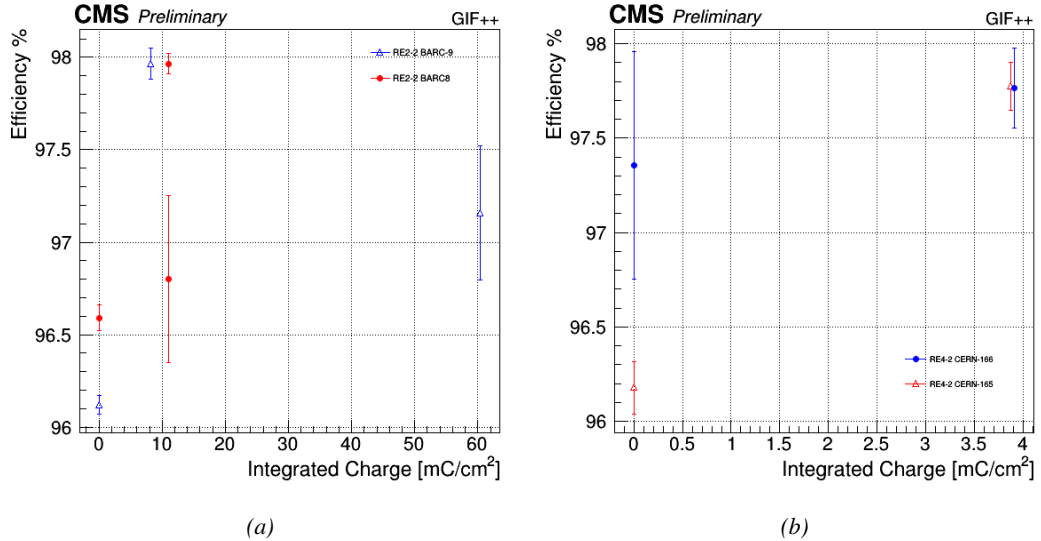
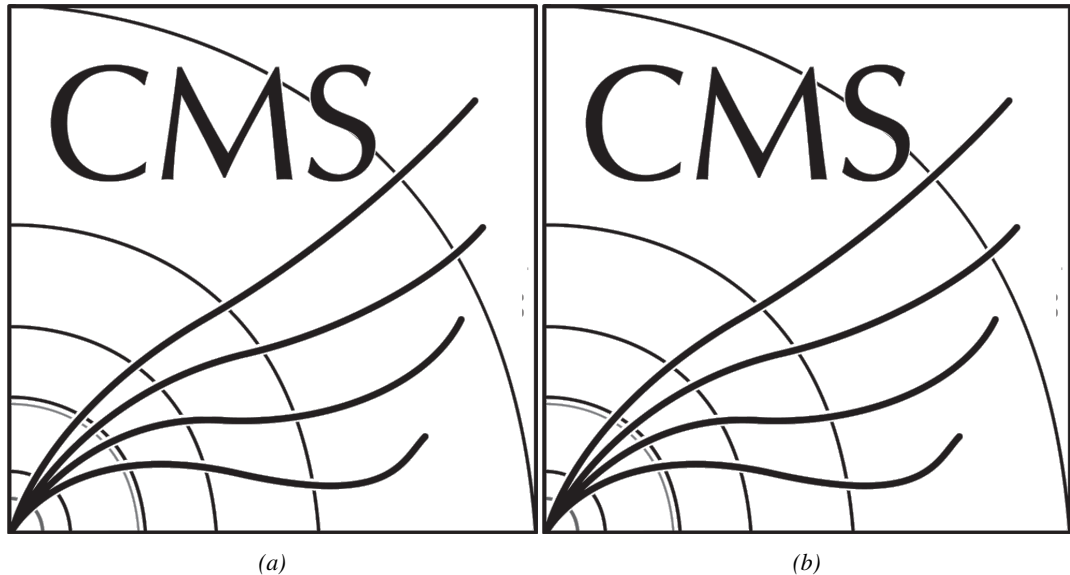


Figure 5.19: Evolution of the working point for RE2 (5.19a) and RE4 (5.19b) with increasing extrapolated  $\gamma$  rate per unit area at working point. Both irradiated (blue) and non irradiated (red) chambers are shown.



*Figure 5.20: Evolution of the maximum efficiency at HL-LHC conditions, i.e. a background hit rate per unit area of 300 Hz/cm<sup>2</sup>, with increasing integrated charge for RE2 (5.20a) and RE4 (5.20b) detectors. Both irradiated (blue) and non irradiated (red) chambers are shown. The integrated charge for non irradiated detectors is recorded during test beam periods and stays small with respect to the charge accumulated in irradiated chambers.*



*Figure 5.21: Comparison of the efficiency sigmoid before (triangles) and after (circles) irradiation for RE2 (5.21a) and RE4 (5.21b) detectors. Both irradiated (blue) and non irradiated (red) chambers are shown.*

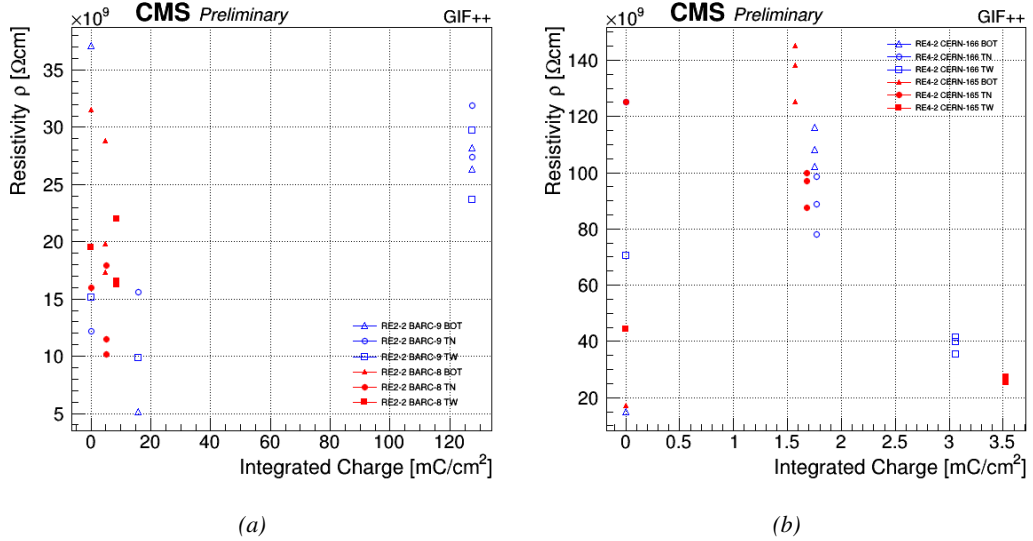


Figure 5.22: Evolution of the Bakelite resistivity for RE2 (5.22a) and RE4 (5.22b) detectors. Both irradiated (blue) and non-irradiated (red) chambers are shown.

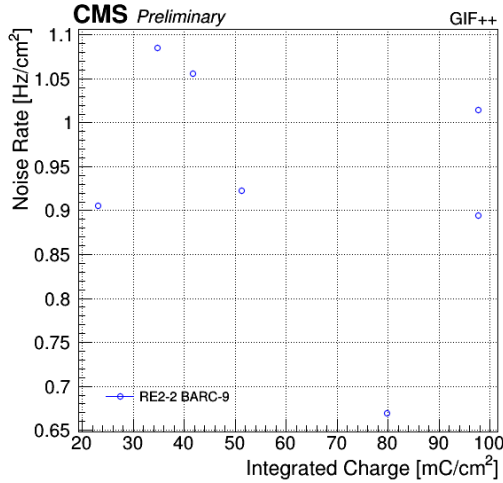


Figure 5.23: Evolution of the noise rate per unit area for the irradiated chamber RE2-2-BARC-9 only.

#### 5.4.1 Description of the Data Acquisition

For the longevity studies, four spare chambers of the present system are used. Two spare RPCs of the RE2,3 stations as well as two spare RPCs from the new RE4 stations have been mounted in a Trolley. Six RE4 gaps are also placed in the trolley. The trolley is placed inside the GIFT++ in the upstream region of the bunker, taking the cesium source as a reference. The trolley is oriented for the detection surface of the chambers to be orthogonal to the beam line. The system can be moved along the orthogonal plane in order to have the beam in all  $\eta$ -partitions. For the aging the trolley is

2226 moved outside the beam line and is placed in a distance of 5.2 m to the source, which irradiates the  
 2227 bunker using an attenuation filter of 2.2 which corresponds to a fluence of  $10^7 \text{ gamma/cm}^2$ .

2228 During GIF++ operation, the data collected can be divided into different categories as several  
 2229 parameters are monitored in addition to the usual RPC performance data. On one hand, to know  
 2230 the performance of a chamber, it is need to measure its efficiency and to know the background  
 2231 conditions in which it is operated. To do this, the hit signals from the chamber are recorded and  
 2232 stored in a ROOT file via a Data Acquisition (DAQ) software. On the other hand, it is also very  
 2233 important to monitor parameters such as environmental pressure and temperature, gas temperature  
 2234 and humidity, RPC HV, LV, and currents, or even source and beam status. This is done through the  
 2235 GIF++ web Detector Control Software (DCS) that stores this information in a database.

2236 Two different types of tests are conducted on RPCs via the DAQ. Indeed, the performance of the  
 2237 detectors is measured periodically during dedicated test beam periods using the H4 muon beam. In  
 2238 between these test beam periods, when the beam is not available, the chambers are irradiated by the  
 2239  $^{137}\text{Cs}$  in order to accumulate deposited charge and the gamma background is measured.

2240 RPCs under test are connected through LVDS cables to V1190A Time-to-Digital Converter  
 2241 (TDC) modules manufactured by CAEN. These modules, located in the rack area outside of the  
 2242 bunker, get the logic signals sent by the chambers and save them into their buffers. Due to the  
 2243 limited size of the buffers, the collected data is regularly erased and replaced. A trigger signal is  
 2244 needed for the TDC modules to send the useful data to the DAQ computer via a V1718 CAEN USB  
 2245 communication module.

2246 In the case of performance test, the trigger signal used for data acquisition is generated by the  
 2247 coincidence of three scintillators. A first one is placed upstream outside of the bunker, a second one  
 2248 is placed downstream outside of the bunker, while a third one is placed in front of the trolley, close by  
 2249 the chambers. Every time a trigger is sent to the TDCs, i.e. every time a muon is detected, knowing  
 2250 the time delay in between the trigger and the RPC signals, signals located in the right time window  
 2251 are extracted from the buffers and saved for later analysis. Signals are taken in a time window of  
 2252 400 ns centered on the muon peak (here we could show a time spectrum). On the other hand, in the  
 2253 case of background rate measurement, the trigger signal needs to be "random" not to measure muons  
 2254 but to look at gamma background. A trigger pulse is continuously generated at a rate of 300 Hz using  
 2255 a dual timer. To integrate an as great as possible time, all signals contained within a time window of  
 2256 10us prior to the random trigger signal are extracted form the buffers and saved for further analysis  
 2257 (here another time spectrum to illustrate could be useful, maybe even place both spectrum together  
 2258 as a single Figure).

2259 The signals sent to the TDCs correspond to hit collections in the RPCs. When a particle hits  
 2260 a RPC, it induce a signal in the pickup strips of the RPC readout. If this signal is higher than the  
 2261 detection threshold, a LVDS signal is sent to the TDCs. The data is then organised into 4 branches  
 2262 keeping track of the event number, the hit multiplicity for the whole setup, and the time and channel  
 2263 profile of the hits in the TDCs.

#### 2264 **5.4.2 RPC current, environmental and operation parameter monitoring**

2265 In order to take into account the variation of pressure and temperature between different data taking  
 2266 periods the applied voltage is corrected following the relationship :

$$2267 \quad HV_{eff} = HV_{app} \times \left( 0.2 + 0.8 \cdot \frac{P_0}{P} \times \frac{T}{T_0} \right) \quad (5.10)$$

2267 where  $T_0$  (=293 K) and  $P_0$  (=990 mbar) are the reference values.

2268 **5.4.3 Measurement procedure**

2269 Insert a short description of the online tools (DAQ, DCS, DQM).

2270 Insert a short description of the offline tools : tracking and efficiency algorithm.

2271 Identify long term aging effects we are monitoring the rates per strip.

2272 **5.4.4 Longevity studies results**

# 6

2273

2274

## Investigation on high rate RPCs

2275 **6.1 Rate limitations and ageing of RPCs**

2276 **6.1.1 Low resistivity electrodes**

2277 **6.1.2 Low noise front-end electronics**

2278 **6.2 Construction of prototypes**

2279 **6.3 Results and discussions**



# 7

2280

2281

## Conclusions and outlooks

2282 **7.1 Conclusions**

2283 **7.2 Outlooks**



# A

2284

2285

## A data acquisition software for CAEN VME TDCs

2286

2287 Certifying detectors in the perspective of HL-LHC required to develop tools for the GIF++ expe-  
2288 riment. Among them was the C++ Data Acquisition (DAQ) software that allows to make the com-  
2289 munications in between a computer and TDC modules in order to retrieve the RPC data [63]. In this  
2290 appendix, details about this software, as of how the software was written, how it functions and how  
2291 it can be exported to another similar setup, will be given.

### 2292 A.1 GIF++ DAQ file tree

2293 GIF++ DAQ source code is fully available on github at [https://github.com/afagot/GIF\\_](https://github.com/afagot/GIF_DAQ)  
2294 DAQ. The software requires 3 non-optional dependencies:

- 2295 • CAEN USB Driver, to mount the VME hardware,  
2296 • CAEN VME Library, to communicate with the VME hardware, and  
2297 • ROOT, to organize the collected data into a TTree.

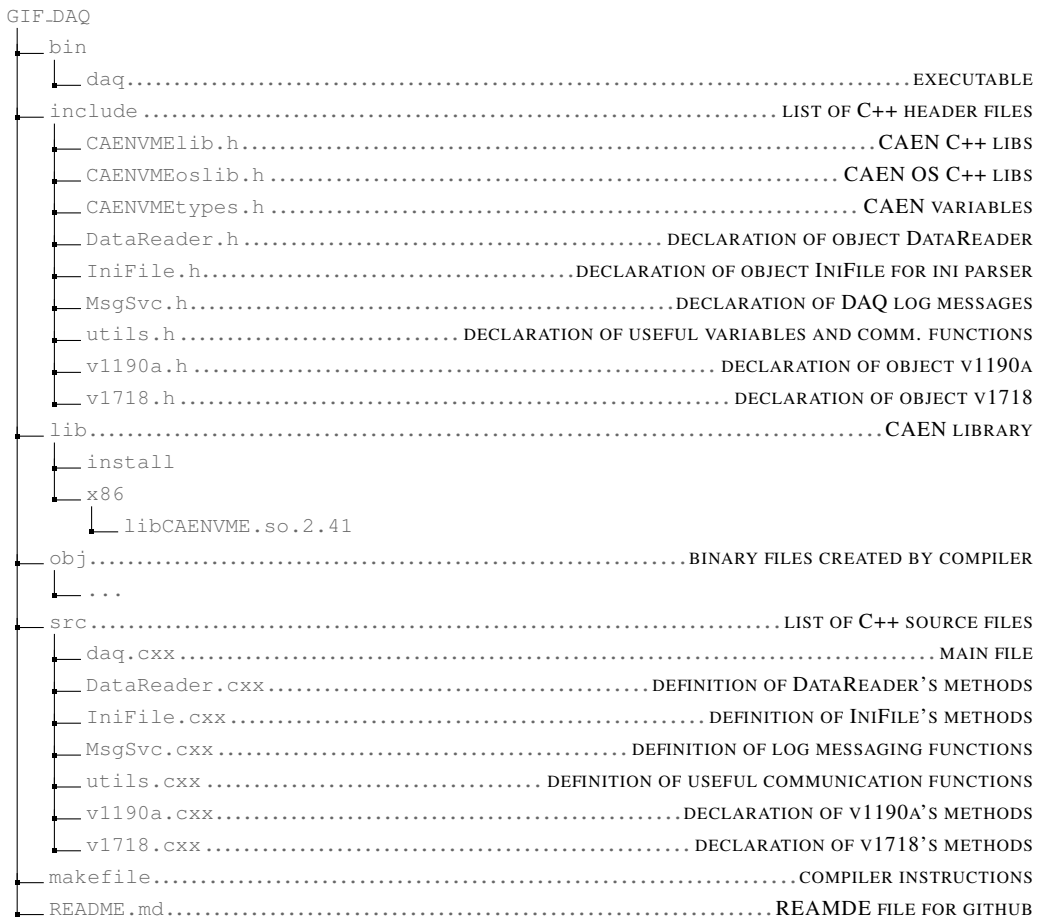
2298 The CAEN VME library will not be packaged by distributions and will need to be installed man-  
2299 ually. To compile the GIF++ DAQ project via a terminal, from the DAQ folder use the command:

2300

2301 make

2302 The source code tree is provided below along with comments to give an overview of the files' con-  
2303 tent. The different objects created for this project (`v1718`, `v1190a`, `IniFile` & `DataReader`) will be  
2304 described in details in the following sections.

2305



## 2306 A.2 Usage of the DAQ

2307     GIF++ DAQ, as used in GIF++, is not a standalone software. Indeed, the system being more com-  
 2308     plex, the DAQ only is a sub-layer of the software architecture developed to control and monitor  
 2309     the RPCs that are placed into the bunker for performance study in an irradiated environment. The top  
 2310     layer of GIF++ is a Web Detector Control System (webDCS) application. The DAQ is only called  
 2311     by the webDCS when data needs to be acquired. The webDCS operates the DAQ through command  
 2312     line. To start the DAQ, the webDCS calls:

2313

2314     bin/daq /path/to/the/log/file/in/the/output/data/folder

2315     where /path/to/the/log/file/in/the/output/data/folder is the only argument required. This  
 2316     log file is important for the webDCS as this file contains all the content of the communication of the  
 2317     webDCS and the different systems monitored by the webDCS. Its content is constantly displayed  
 2318     during data taking for the users to be able to follow the operations. The communication messages  
 2319     are normally sent to the webDCS log file via the functions declared in file `MsgSvc.h`, typically  
 2320     `MSG_INFO(string message)`.

2321

### 2322 A.3 Description of the readout setup

2323 The CMS RPC setup at GIF++ counts 5 V1190A Time-to-Digital Converter (TDC) manufactured  
 2324 by CAEN [64]. V1190A are VME units accepting 128 independent Multi-Hit/Multi-Event TDC  
 2325 channels whose signals are treated by 4 100 ps high performance TDC chips developed by CERN  
 2326 / ECP-MIC Division. The communication between the computer and the TDCs to transfer data is  
 2327 done via a V1718 VME master module also manufactured by CAEN and operated from a USB  
 2328 port [65]. These VME modules are all hosted into a 6U VME 6021 powered crate manufactured by  
 2329 W-Ie-Ne-R than can accommodate up to 21 VME bus cards [66]. These 3 components of the DAQ  
 2330 setup are shown in Figure A.1.

2331

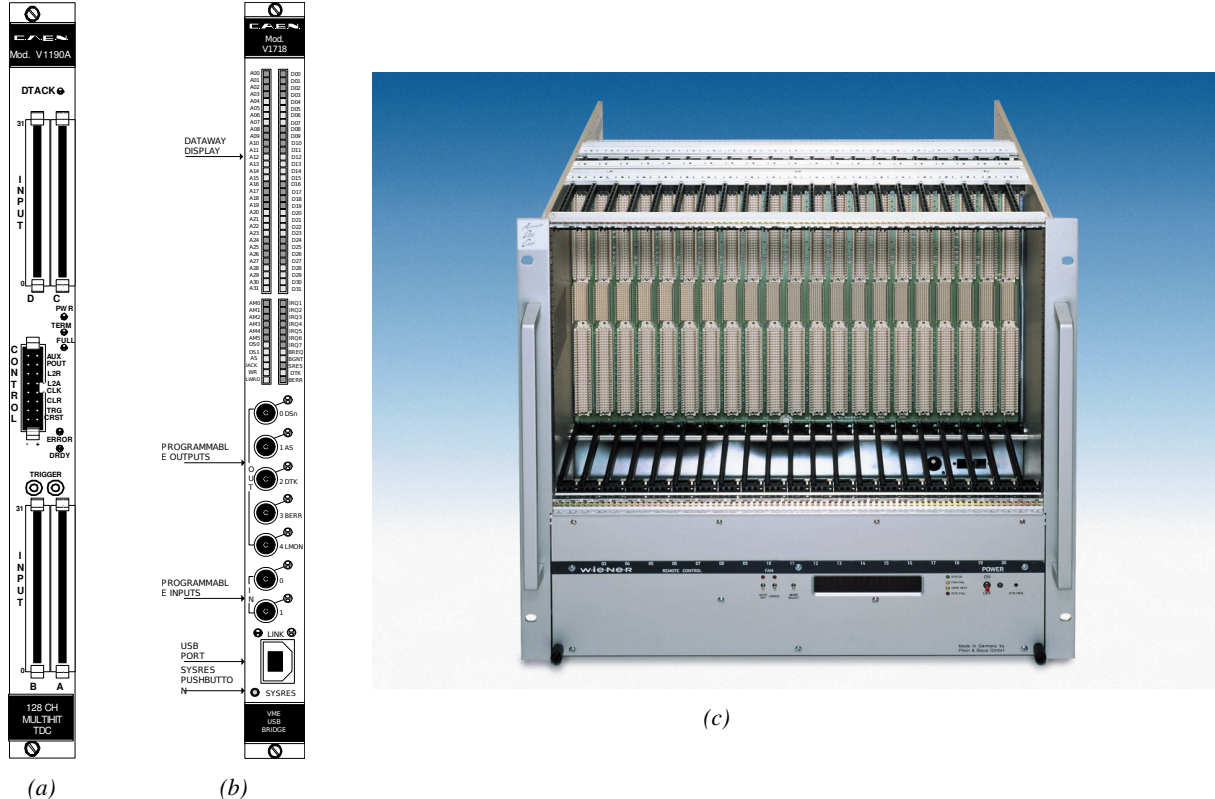


Figure A.1: (A.1a) View of the front panel of a V1190A TDC module [64]. (A.1b) View of the front panel of a V1718 Bridge module [65]. (A.1c) View of the front panel of a 6U 6021 VME crate [66].

2332

### A.4 Data read-out

2333 To efficiently perform a data readout algorithm, C++ objects to handle the VME modules (TDCs  
 2334 and VME bridge) have been created along with objects to store data and read the configuration file

2335 that comes as an input of the DAQ software.

2336

### 2337 A.4.1 V1190A TDCs

2338 The DAQ used at GIF takes profit of the *Trigger Matching Mode* offered by V1190A modules.  
 2339 This setting is enabled through the method `v1190a::SetTrigMatching (int ntdcs)` where `ntdcs`  
 2340 is the total number of TDCs in the setup this setting needs to be enabled for (Source Code A.1). A  
 2341 trigger matching is performed in between a trigger time tag, a trigger signal sent into the TRIGGER  
 2342 input of the TDC visible on Figure A.1a, and the channel time measurements, signals recorded from  
 2343 the detectors under test in our case. Control over this data acquisition mode, explained through  
 2344 Figure A.2, is offered via 4 programmable parameters:

- 2345 • **match window:** the matching between a trigger and a hit is done within a programmable time  
 2346 window. This is set via the method

2347 `void v1190a::SetTrigWindowWidth(Uint windowHeight, int ntdcs)`

- 2348 • **window offset:** temporal distance between the trigger tag and the start of the trigger matching  
 2349 window. This is set via the method

2350 `void v1190a::SetTrigWindowWidth(Uint windowHeight, int ntdcs)`

- 2351 • **extra search margin:** an extended time window is used to ensure that all matching hits are  
 2352 found. This is set via the method

2353 `void v1190a::SetTrigSearchMargin(Uint searchMargin, int ntdcs)`

- 2354 • **reject margin:** older hits are automatically rejected to prevent buffer overflows and to speed  
 2355 up the search time. This is set via the method

2356 `void v1190a::SetTrigRejectionMargin(Uint rejectMargin, int ntdcs)`

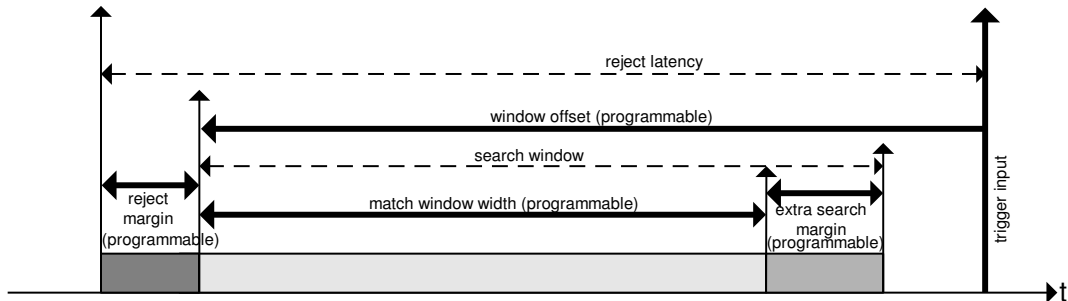


Figure A.2: Module V1190A Trigger Matching Mode timing diagram [64].

2357 Each of these 4 parameters are given in number of clocks, 1 clock being 25 ns long. It is easy to  
 2358 understand at this level that there are 3 possible functioning settings:

- 2359 • **1:** the match window is entirely contained after the trigger signal,

- 2360 • **2:** the match window overlaps the trigger signal, or

- 2361 • **3:** the match window is entirely contained before the trigger signal as displayed on Figure A.2.

2362 In both the first and second cases, the sum of the window width and of the offset can be set to  
2363 a maximum of 40 clocks, which corresponds to 1  $\mu$ s. Evidently, the offset can be negative, allowing  
2364 for a longer match window, with the constraint of having the window ending at most 1  $\mu$ s after the  
2365 trigger signal. In the third case, the maximum negative offset allowed is of 2048 clocks (12 bit) cor-  
2366 responding to 51.2  $\mu$ s, the match window being strictly smaller than the offset. In the case of GIF++,  
2367 the choice has been made to use this last setting by delaying the trigger signal. During the studies  
2368 performed in GIF++, both the efficiency of the RPCs, probed using a muon beam, and the noise or  
2369 gamma background rate are monitored. The extra search and reject margins are left unused.  
2370 To probe the efficiency of RPC detectors, the trigger time tag is provided by the coïncidence of  
2371 scintillators when a bunch of muons passes through GIF++ area is used to trigger the data acquisi-  
2372 tion. For this measurement, it is useful to reduce the match window width only to contain the muon  
2373 information. Indeed, the delay in between a trigger signal and the detection of the corresponding  
2374 muon in the RPC being very contant (typically a few tens of ns due to jitter and cable length), the  
2375 muon signals are very localised in time. Thus, due to a delay of approximalety 325 ns in between  
2376 the muons and the trigger, the settings where chosen to have a window width of 24 clocks (600 ns)  
2377 centered on the muon peak thanks to a negative offset of 29 clocks (725 ns).  
2378 On the otherhand, monitoring the rates don't require for the DAQ to look at a specific time window.  
2379 It is important to integrate enough time to have a robust measurement of the rate as the number of  
2380 hits per time unit. The triggerring signal is provided by a pulse generator at a frequency of 300 Hz  
2381 to ensure that the data taking occurs in a random way, with respect to beam physics, to probe only  
2382 the irradiation spectrum on the detectors. The match window is set to 400 clocks (10  $\mu$ s) and the  
2383 negative offset to 401 clocks as it needs to exceed the value of the match window.

```

2384
class v1190a
{
    private :
        long Handle;
        vector<Data32> Address;
        CVDataWidth DataWidth;
        CVAddressModifier AddressModifier;

    public:

        v1190a(long handle, IniFile *inifile, int ntdcs);
        ~v1190a();
        Data16 write_op_reg(Data32 address, int code, string error);
        Data16 read_op_reg(Data32 address, string error);
        void Reset(int ntdcs);
        void Clear(int ntdcs);
        void TestWR(Data16 value,int ntdcs);
        void CheckTDCStatus(int ntdcs);
        void CheckCommunication(int ntdcs);
        void SetTDCTestMode(Data16 mode,int ntdcs);
        void SetTrigMatching(int ntdcs);
        void SetTrigTimeSubtraction(Data16 mode,int ntdcs);
        void SetTrigWindowWidth(Uint windowHeight,int ntdcs);
        void SetTrigWindowOffset(Uint windowOffset,int ntdcs);
        void SetTrigSearchMargin(Uint searchMargin,int ntdcs);
        void SetTrigRejectionMargin(Uint rejectMargin,int ntdcs);
        void GetTrigConfiguration(int ntdcs);
        void SetTrigConfiguration(IniFile *inifile,int ntdcs);
        void SetTDCDetectionMode(Data16 mode,int ntdcs);
        void SetTDCResolution(Data16 lsb,int ntdcs);
        void SetTDCDeadTime(Data16 time,int ntdcs);
        void SetTDCHeadTrailer(Data16 mode,int ntdcs);
        void SetTDCEventSize(Data16 size,int ntdcs);
        void SwitchChannels(IniFile *inifile,int ntdcs);
        void SetIRQ(Data32 level, Data32 count,int ntdcs);
        void SetBlockTransferMode(Data16 mode,int ntdcs);
        void Set(IniFile *inifile,int ntdcs);
        void CheckStatus(CVErrorCodes status) const;
        int ReadBlockD32(Uint tdc, const Data16 address,
                           Data32 *data, const Uint words, bool ignore_berr);
        Uint Read(RAWData *DataList,int ntdcs);
};

2385

```

2386       *Source Code A.1: Description of C++ object v1190a.*

2387       The v1190a object, defined in the DAQ software as in Source Code A.1, offers the possibility to  
 2388       concatenate all TDCs in the readout setup into a single object containing a list of hardware addresses  
 2389       (addresses to access the TDCs' buffer through the VME crate) and each constructor and method acts  
 2390       on the list of TDCs.

2391

#### 2392     A.4.2 DataReader

2393       Enabled thanks to v1190a::SetBlockTransferMode(Data16 mode, **int** ntdcs), the data transfer  
 2394       is done via Block Transfer (BLT). Using BLT allows to tranfer a fixed number of events called a  
 2395       *block*. This is used together with an Almost Full Level (AFL) of the TDCs' output buffers, defined

2396 through `v1190a::SetIRQ(Data32 level, Data32 count, int ntdcs)`. This AFL gives the maxi-  
 2397 mum amount of 32735 words (16 bits, corresponding to the depth of a TDC output buffer) that can  
 2398 written in a buffer before an Interrupt Request (IRQ) is generated and seen by the VME Bridge,  
 2399 stopping the data acquisition to transfer the content of each TDC buffers before resuming. For each  
 2400 trigger, 6 words or more are written into the TDC buffer:

- 2401     • a **global header** providing information of the event number since the beginning of the data  
       acquisition,
- 2403     • a **TDC header**,
- 2404     • the **TDC data** (*if any*), 1 for each hit recorded during the event, providing the channel and the  
       time stamp associated to the hit,
- 2406     • a **TDC error** providing error flags,
- 2407     • a **TDC trailer**,
- 2408     • a **global trigger time tag** that provides the absolute trigger time relatively to the last reset,  
       and
- 2410     • a **global trailer** providing the total word count in the event.

2411     As previously described in Section ??, CMS RPC FEEs provide us with 100 ns long LVDS out-  
 2412 put signals that are injected into the TDCs' input. Any avalanche signal that gives a signal above the  
 2413 FEEs threshold is thus recorded by the TDCs as a hit within the match window. Each hit is assigned  
 2414 to a specific TDC channel with a time stamp, with a precision of 100 ps. The reference time,  $t_0 = 0$ ,  
 2415 is provided by the beginning of the match window. Thus for each trigger, coming from a scintillator  
 2416 coïncidence or the pulse generator, a list of hits is stored into the TDCs' buffers and will then be  
 2417 transferred into a ROOT Tree.

2418     When the BLT is used, it is easy to understand that the maximum number of words that have  
 2419 been set as ALF will not be a finite number of events or, at least, the number of events that would  
 2420 be recorded into the TDC buffers will not be a multiple of the block size. In the last BLT cycle to  
 2422 tranfer data, the number of events to transfer will most probably be lower than the block size. In that  
 2423 case, the TDC can add fillers at the end of the block but this option requires to send more data to the  
 2424 computer and is thus a little slower. Another solution is to finish the transfer after the last event by  
 2425 sending a bus error that states that the BLT reached the last event in the pile. This method has been  
 2426 chosen in GIF++.

2427     Due to irradiation, an event in GIF++ can count up to 300 words per TDC. A limit of 4096 words  
 2428 (12 bits) has been set to generate IRQ which represent from 14 to almost 700 events depending on  
 2429 the average of hits collected per event. Then the block size has been set to 100 events with enabled  
 2431 bus errors. When an AFL is reached for one of the TDCs, the VME bridge stops the acquisition by  
 2432 sending a BUSY signal.

2433

2434     The data is then transferred one TDC at a time into a structure called `RAWData` (Source Code A.2).

```
2435
2436 struct RAWData{
2437     vector<int>           *EventList;
2438     vector<int>           *NHitsList;
2439     vector<int>           *QFlagList;
2440     vector<vector<int>> >   *Channellist;
2441     vector<vector<float>> > *TimeStampList;
2442 };
```

2437                 *Source Code A.2: Description of data holding C++ structure `RAWData`.*

2438     In order to organize the data transfer and the data storage, an object called `DataReader` was  
 2439     created (Source Code A.3). On one hand, it has `v1718` and `v1190a` objects as private members for  
 2440     communication purposes, such as VME modules settings via the configuration file `*iniFile` or data  
 2441     read-out through `v1190a::Read()` and on the other hand, it contains the structure `RAWData` that allows  
 2442     to organise the data in vectors reproducing the tree structure of a ROOT file.

```
2443
2444 class DataReader
2445 {
2446     private:
2447     bool      StopFlag;
2448     IniFile *iniFile;
2449     Data32  MaxTriggers;
2450     v1718   *VME;
2451     int       nTDCs;
2452     v1190a  *TDCs;
2453     RAWData TDCData;

2454     public:
2455     DataReader();
2456     virtual ~DataReader();
2457     void      SetIniFile(string inifilename);
2458     void      SetMaxTriggers();
2459     Data32  GetMaxTriggers();
2460     void      SetVME();
2461     void      SetTDC();
2462     int       GetQFlag(Uint it);
2463     void      Init(string inifilename);
2464     void      FlushBuffer();
2465     void      Update();
2466     string  GetFileName();
2467     void      WriteRunRegistry(string filename);
2468     void      Run();
2469 };

2470 
```

2445                 *Source Code A.3: Description of C++ object `DataReader`.*

2446     Each event is transferred from `TDCData` and saved into branches of a ROOT `TTree` as 3 integers  
 2447     that represent the event ID (`EventCount`), the number of hits read from the TDCs (`nHits`), and the  
 2448     quality flag that provides information for any problem in the data transfer (`qflag`), and 2 lists of  
 2449     `nHits` elements containing the fired TDC channels (`TDCCh`) and their respective time stamps (`TDCTS`),  
 2450     as presented in Source Code A.4. The ROOT file file is named using information contained into  
 2451     the configuration file, presented in section A.5.2. The needed information is extracted using method  
 2452     `DataReader::GetFileName()` and allow to build the output filename format `ScanXXXXXX_HVX_DAQ.root`

2453 where ScanXXXXXX is a 6 digit number representing the scan number into GIFT++ database and HVX  
 2454 the HV step within the scan that can be more than a single digit. An example of ROOT data file is  
 2455 provided with Figure A.3.

```
2456
RAWData TDCData;
TFile *outputFile = new TFile(outputFileName.c_str(),"recreate");
TTree *RAWDataTree = new TTree("RAWData","RAWData");

int EventCount = -9;
int nHits = -8;
int qflag = -7;
vector<int> TDCCh;
vector<float> TDCTS;

RAWDataTree->Branch("EventNumber",&EventCount, "EventNumber/I");
RAWDataTree->Branch("number_of_hits",&nHits,"number_of_hits/I");
RAWDataTree->Branch("Quality_flag",&qflag,"Quality_flag/I");
RAWDataTree->Branch("TDC_channel",&TDCCh);
RAWDataTree->Branch("TDC_TimeStamp",&TDCTS);

2457
//...
//Here read the TDC data using v1190a::Read() and place it into
//TDCData for as long as you didn't collect the requested amount
//of data.
//...

for(Uint i=0; i<TDCData.EventList->size(); i++){
    EventCount = TDCData.EventList->at(i);
    nHits = TDCData.NHitsList->at(i);
    qflag = TDCData.QFlagList->at(i);
    TDCCh = TDCData.ChannelList->at(i);
    TDCTS = TDCData.TimeStampList->at(i);
    RAWDataTree->Fill();
}
```

2458 *Source Code A.4: Highlight of the data transfer and organisation within DataReader::Run() after the data has been collected into TDCData.*

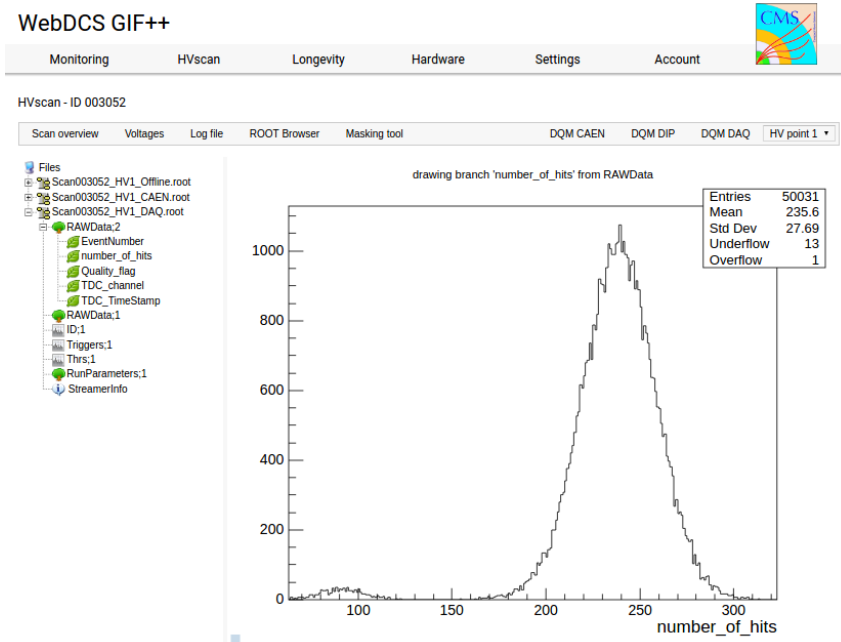


*Figure A.3: Structure of the ROOT output file generated by the DAQ. The 5 branches (EventNumber, number\_of\_hits, Quality\_flag, TDC\_channel and TDC\_TimeStamp) are visible on the left panel of the ROOT browser. On the right panel is visible the histogram corresponding to the variable nHits. In this specific example, there were approximately 50k events recorded to measure the gamma irradiation rate on the detectors. Each event is stored as a single entry in the TTree.*

#### 2459    A.4.3 Data quality flag

2460    Among the parameters that are recorded for each event, the quality flag, defined in Source Code A.5,  
 2461    is determined on the fly by checking the data recorded by every single TDC. From method `v1190a::Read()`,  
 2462    it can be understood that the content of each TDC buffer is readout one TDC at a time. Entries are  
 2463    created in the data list for the first TDC and then, when the second buffer is readout, events corre-  
 2464    sponding to entries that have already been created to store data for the previous TDC are added to  
 2465    the existing list element. On the contrary, when an event entry has not been yet created in the data  
 2466    list, a new entry is created.

```
2467
2468 typedef enum _QualityFlag {
2469     GOOD      = 1,
2470     CORRUPTED = 0
2471 } QualityFlag;
```

2469    *Source Code A.5: Definition of the quality flag `enum`.*

2470    It is possible that each TDC buffer contains a different number of events. In cases where the first  
 2471    element in the buffer list is an event for corresponds to a new entry, the difference in between the  
 2472    entry from the buffer and the last entry in the data list is recorded and checked. If it is greater than 1,  
 2473    what should never be the case, the quality flag is set to CORRUPTED for this TDC and an empty entry  
 2474    is created in the place of the missing ones. Missing entries are believe to be the result of a bad hold

2475 on the TDC buffers at the moment of the readout. Indeed, the software hold is effective only on 1  
 2476 TDC at a time and no solution as been found yet to completely block the writting in the buffers when  
 2477 an IRQ is received.

2478 At the end of each BLT cycle, the ID of the last entry stored for each TDC buffer is not recorded.  
 2479 When starting the next cycle, if the first entry in the pile corresponds to an event already existing  
 2480 in the list, the readout will start from this list element and will not be able to check the difference  
 2481 in between this entry's ID and the one of the last entry that was recorded for this TDC buffer in  
 2482 the previous cycle. In the case events were missing, the flag stays at its initial value of 0, which is  
 2483 similar to CORRUPTED and it is assumed that then this TDC will not contribute to `number_of_hits`,  
 2484 `TDC_channel` or `TDC_TimeStamp`.

2485 Finally, since there will be 1 `RAWData` entry per TDC for each event (meaning `nTDCs` entries,  
 2486 referring to `DataReader` private attribute), the individual flags of each TDC will be added together.  
 2487 The final format is an integer composed `nTDCs` digits where each digit is the flag of a specific TDC.  
 2488 This is constructed using powers of 10 like follows:

```
2489 TDC 0: QFlag = 100 × _QualityFlag
2490 TDC 1: QFlag = 101 × _QualityFlag
2491 ...
2492 TDC N: QFlag = 10N × _QualityFlag
```

2493 and the final flag to be with N digits:

```
2494 QFlag = n....3210
```

2495 each digit being 1 or 0. Below is given an example with a 4 TDCs setup.

2496 If all TDCs were good : `QFlag = 1111`,

2497 but if TDC 2 was corrupted : `QFlag = 1011`.

2498 When data taking is over and the data contained in the dynamical `RAWData` structure is transferred  
 2499 to the ROOT file, all the 0s are changed into 2s by calling the method `DataReader::GetQFlag()`.  
 2500 This will help translating the flag without knowing the number of TDCs beforehand. Indeed, a flag  
 2501 111 could be due to a 3 TDC setup with 3 good individual TDC flags or to a more than 3 TDC setup  
 2502 with TDCs those ID is greater than 2 being CORRUPTED, thus giving a 0.

2503 The quality flag has been introduced quite late, in October 2017 only, to the list of GIFT++ DAQ  
 2504 parameters to be recorded into the output ROOT file. Before this addition, the missing data, corrupting  
 2505 the quality for the offline analysis, was contributing to artificially fill data with lower multiplicity.  
 2506 Looking at `TBranch number_of_hits` provides an information about the data of the full GIFT++  
 2507 setup. When a TDC is not able to transfer data for a specific event, the effect is a reduction of the  
 2508 total number of hits recorded in the full setup, this is what can be seen from Figure A.4. After offline  
 2509 reconstruction detector by detector, the effect of missing events can be seen in the artificially filled  
 2510 bin at multiplicity 0 shown in Figure A.5. Nonetheless, for data with high irradiation levels, as it is  
 2511 the case for Figure A.5a, discarding the fake multiplicity 0 data can be done easily during the offline  
 2512 analysis. At lower radiation, the missing events contribution becomes more problematic as the mul-  
 2513 tiplicity distribution overlaps the multiplicity 0 and that in the same time the proportion of missing

2514 events decreases. Attempts to fit the distribution with a Poisson or skew distribution function were  
 2515 not conclusive and this very problem has been at the origin of the quality flag that allows to give a  
 2516 non ambiguous information about each event quality.

2517

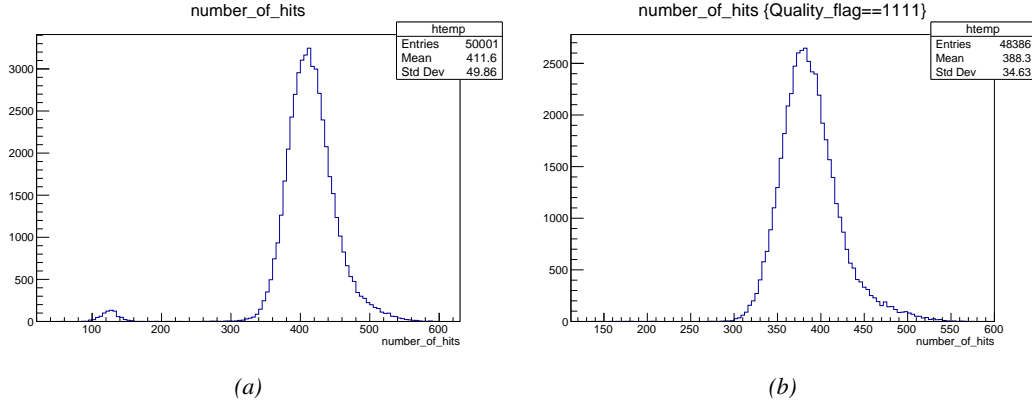


*Figure A.4: The effect of the quality flag is explained by presenting the content of TBranch `number_of_hits` of a data file without `Quality_flag` in Figure A.4a and the content of the same TBranch for data corresponding to a `Quality_flag` where all TDCs were labelled as `GOOD` in Figure A.4b taken with similar conditions. It can be noted that the number of entries in Figure A.4b is slightly lower than in Figure A.4a due to the excluded events.*

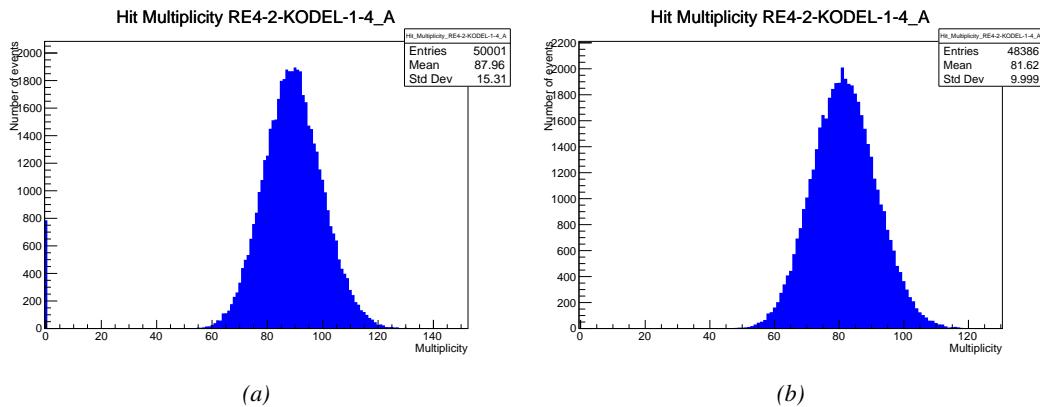


*Figure A.5: Using the same data as previously showed in Figure A.4, the effect of the quality flag is explained by presenting the reconstructed hit multiplicity of a data file without `Quality_flag` in Figure A.5a and the reconstructed content of the same RPC partition for data corresponding to a `Quality_flag` where all TDCs were labelled as `GOOD` in Figure A.5b taken with similar conditions. The artificial high content of bin 0 is completely suppressed.*

## A.5 Communications

2518 To ensure data readout and dialog in between the machine and the TDCs or in between the webDCS  
 2519 and the DAQ, different communication solutions were used. First of all, it is important to have a

2521 module to allow the communication in between the TDCs and the computer from which the DAQ  
 2522 operates. When this communication is effective, shifters using the webDCS to control data taking  
 2523 can thus send instructions to the DAQ.

2524

### 2525 A.5.1 V1718 USB Bridge

2526 In the previous section, the data transfer has been discussed. The importance of the `v1718` object  
 2527 (Source Code A.6), used as private member of `DataReader`, was not explicated. VME master  
 2528 modules are used for communication purposes as they host the USB port that connects the pow-  
 2529 ered crate buffer to the computer where the DAQ is installed. From the source code point of view,  
 2530 this object is used to control the communication status, by reading the returned error codes with  
 2531 `v1718::CheckStatus()`, or to check for IRQs coming from the TDCs through `v1718::CheckIRQ()`.  
 2532 Finally, to ensure that triggers are blocked at the hardware level, a NIM pulse is sent out of one of the  
 2533 5 programmable outputs (`v1718::SendBUSY()`) to the VETO of the coincidence module where the  
 2534 trigger signals originate from. As long as this signal is ON, no trigger can reach the TDCs anymore.  
 2535

```
2536 class v1718{
2537     private:
2538         int Handle;
2539         Data32 Data;           // Data
2540         CVIRQLevels Level;    // Interrupt level
2541         CVAddressModifier AM;   // Addressing Mode
2542         CVDataWidth dataSize;  // Data Format
2543         Data32 BaseAddress;    // Base Address
2544
2545     public:
2546         v1718(IniFile *inifile);
2547         ~v1718();
2548         long GetHandle(void) const;
2549         int SetData(Data16 data);
2550         Data16 GetData(void);
2551         int SetLevel(CVIRQLevels level);
2552         CVIRQLevels GetLevel(void);
2553         int SetAM(CVAddressModifier am);
2554         CVAddressModifier GetAM(void);
2555         int SetDatasize(CVDataWidth datasize);
2556         CVDataWidth GetDataSize(void);
2557         int SetBaseAddress(Data16 baseaddress);
2558         Data16 GetBaseAddress(void);
2559         void CheckStatus(CVErrorCodes status) const;
2560         void CheckIRQ();
2561         void SetPulsers();
2562         void SendBUSY(BusyLevel level);
2563     };

```

2537 *Source Code A.6: Description of C++ object v1718.*

### 2538 A.5.2 Configuration file

2539 The DAQ software takes as input a configuration file written using INI standard [67]. This file is  
 2540 partly filled with the information provided by the shifters when starting data acquisition using the  
 2541 webDCS, as shown by Figure A.6. This information is written in section [`General`] and will later

2542 be stored in the ROOT file that contains the DAQ data as can be seen from Figure A.3. Indeed,  
 2543 another `TTree` called `RunParameters` as well as the 2 histograms `ID`, containing the scan number,  
 2544 start and stop time stamps, and `Triggers`, containing the number of triggers requested by the shifter,  
 2545 are available in the data files. Moreover, `ScanID` and `HV` are then used to construct the file name  
 2546 thanks to the method `DataReader::GetFileName()`.

**WebDCS GIF++**

Monitoring HVscan Longevity Hardware Settings Account 

DAQ High Voltage Scan

Type scan: Rate Scan Comments:

Source configuration: Source OFF U 333 D 333 HV after scan: Turn off

Beam configuration: Beam OFF

Waiting time: 1 (min)

Trigger mode: External Internal Random

Minimal measure time: 10 (min)

Chamber	RE2-2-NPD-BARC-8	RE4-2-CERN-106	RE2-3-NPD-BARC-9	RE4-2-CERN-165	RE4-2-KODEL-1-4	Max triggers
HV <sub>eff</sub> 1	8600	8500	8600	8500	6500	
HV <sub>eff</sub> 2	8700	8600	8700	8600	6600	
HV <sub>eff</sub> 3	8800	8700	8800	8700	6700	
HV <sub>eff</sub> 4	8900	8800	8900	8800	6800	
HV <sub>eff</sub> 5	9000	8900	9000	8900	6900	
HV <sub>eff</sub> 6	9100	9000	9100	9000	7000	
HV <sub>eff</sub> 7	9200	9100	9200	9100	7100	
HV <sub>eff</sub> 8	9300	9200	9300	9200	7200	
HV <sub>eff</sub> 9	9400	9300	9400	9300	7300	
HV <sub>eff</sub> 10	9500	9400	9500	9400	7400	

**Start HV scan**

Figure A.6: WebDCS DAQ scan page. On this page, shifters need to choose the type of scan (Rate, Efficiency or Noise Reference scan), the gamma source configuration at the moment of data taking, the beam configuration, and the trigger mode. These information will be stored in the DAQ ROOT output. Are also given the minimal measurement time and waiting time after ramping up of the detectors is over before starting the data acquisition. Then, the list of HV points to scan and the number of triggers for each run of the scan are given in the table underneath.

2547 The rest of the information is written beforehand in the configuration file template, as explicated  
 2548 in Source Code A.7, and contains the hardware addresses to the different VME modules in the  
 2549 setup as well as settings for the TDCs. As the TDC settings available in the configuration file are not  
 2550 supposed to be modified, an improvement would be to remove them from the configuration file and  
 2551 to hardcode them inside of the DAQ code itself or to place them into a different INI file that would  
 2552 host only the TDC settings to lower the probability for a bad manipulation of the configuration file  
 2553 that can be modified from one of webDCS' menus.

2554

```
[General]
TdcS=4
ScanID=$scanid
HV=$HV
RunType=$runtype
MaxTriggers=$maxtriggers
Beam=$beam
[VMEInterface]
Type=V1718
BaseAddress=0xFF0000
Name=VmeInterface
[TDC0]
Type=V1190A
BaseAddress=0x00000000
Name=Tdc0
StatusA00-15=1
StatusA16-31=1
StatusB00-15=1
StatusB16-31=1
StatusC00-15=1
StatusC16-31=1
StatusD00-15=1
StatusD16-31=1
[TDC1]
Type=V1190A
BaseAddress=0x11110000
Name=Tdc1
StatusA00-15=1
StatusA16-31=1
StatusB00-15=1
StatusB16-31=1
StatusC00-15=1
StatusC16-31=1
StatusD00-15=1
StatusD16-31=1
[TDC2]
Type=V1190A
BaseAddress=0x22220000
Name=Tdc2
StatusA00-15=1
StatusA16-31=1
StatusB00-15=1
StatusB16-31=1
StatusC00-15=1
StatusC16-31=1
StatusD00-15=1
StatusD16-31=1
[TDC3]
Type=V1190A
BaseAddress=0x44440000
Name=Tdc3
StatusA00-15=1
StatusA16-31=1
StatusB00-15=1
StatusB16-31=1
StatusC00-15=1
StatusC16-31=1
StatusD00-15=1
StatusD16-31=1
[TDCSettings]
TriggerExtraSearchMargin=0
TriggerRejectMargin=0
TriggerTimeSubtraction=0b1
TdcDetectionMode=0b01
TdcResolution=0b10
TdcDeadTime=0b00
TdcHeadTrailer=0b1
TdcEventSize=0b1001
TdcTestMode=0b0
BLTMode=1
```

Source Code A.7: *INI configuration file template for 4 TDCs.* In section [**General**], the number of TDCs is explicitated and information about the ongoing run is given. Then, there are sections for each and every VME modules. There buffer addresses are given and for the TDCs, the list of channels to enable is given. Finally, in section [**TDCSettings**], a part of the TDC settings are given.

In order to retrieve the information of the configuration file, the object `IniFile` has been developed to provide an INI parser, presented in Source Code A.8. It contains private methods returning a boolean to check the type of line written in the file, whether a comment, a group header or a key line (`IniFile::CheckIfComment()`, `IniFile::CheckIfGroup()` and `IniFile::CheckIfToken()`). The key may sometimes be referred to as *token* in the source code. Moreover, the private element `FileData` is a map of `const string` to `string` that allows to store the data contained inside the configuration file via the public method `IniFile::GetFileData()` following the formatting (see method `IniFile::Read()`):

```
2557     string group, token, value;
2558     // Get the field values for the 3 strings.
2559     // Then concatenate group and token together as a single string
2560     // with a dot separation.
2561     token = group + "." + token;
2562     FileData[token] = value;
```

More methods have been written to translate the different keys into the right variable format when used by the DAQ. For example, to get a `float` value out of the configuration file data, knowing the group and the key needed, the method `IniFile::floatType()` can be used. It takes 3 arguments being the group name and key name (both `string`), and a default `float` value used as exception in the case the expected combination of group and key cannot be found in the configuration file. This default value is then used and the DAQ continues on working after sending an alert in the log file for further debugging.

```

2574
typedef map< const string, string > IniFileData;

class IniFile{
private:
    bool      CheckIfComment(string line);
    bool      CheckIfGroup(string line, string& group);
    bool      CheckIfToken(string line, string& key, string& value);
    string    FileName;
    IniFileData FileData;
    int       Error;

public:
    IniFile();
    IniFile(string filename);
    virtual ~IniFile();

    // Basic file operations
    void      SetFileName(string filename);
    int       Read();
    int       Write();
    IniFileData GetFileData();

    // Data readout methods
    Data32    addressType (string groupname, string keyname, Data32
2575    defaultValue);
    long      intType     (string groupname, string keyname, long
    defaultValue);
    long long  longType   (string groupname, string keyname, long long
    defaultValue );
    string    stringType  (string groupname, string keyname, string
    defaultValue );
    float     floatType   (string groupname, string keyname, float
    defaultValue );

    // Error methods
    string    GetErrorMsg();
};

}

```

2576       *Source Code A.8: Description of C++ object `IniFile` used as a parser for INI file format.*

### 2577   A.5.3 WebDCS/DAQ intercommunication

2578   When shifters send instructions to the DAQ via the configuration file, it is the webDCS itself that  
 2579   gives the start command to the DAQ and then the 2 softwares use inter-process communication  
 2580   through file to synchronise themselves. This communication file is represented by the variable `const`  
 2581   string \_\_runstatuspath.

2582   On one side, the webDCS sends commands or status that are readout by the DAQ:

- 2583     ● INIT, status sent when launching a scan and read via function `CtrlRunStatus(...)`,
- 2584     ● START, command to start data taking and read via function `CheckSTART()`,
- 2585     ● STOP, command to stop data taking at the end of the scan and read via function `CheckSTOP()`,  
 2586       and
- 2587     ● KILL, command to kill data taking sent by user and read via function `CheckKILL()`

2588 and on the other, the DAQ sends status that are controled by the webDCS:

- 2589     ● `DAQ_RDY`, sent with `SendDAQReady()` to signify that the DAQ is ready to receive commands  
2590       from the webDCS,
- 2591     ● `RUNNING`, sent with `SendDAQRunning()` to signify that the DAQ is taking data,
- 2592     ● `DAQ_ERR`, sent with `SendDAQError()` to signify that the DAQ didn't receive the expected com-  
2593       mand from the webDCS or that the launch command didn't have the right number of argu-  
2594       ments,
- 2595     ● `RD_ERR`, sent when the DAQ wasn't able to read the communication file, and
- 2596     ● `WR_ERR`, sent when the DAQ wasn't able to write into the communication file.

#### 2597     **A.5.4 Example of inter-process communication cycle**

2598 Under normal conditions, the webDCS and the DAQ processes exchange commands and status via  
2599 the file hosted at the address `__runstatuspath`, as explained in subsection A.5.3. An example of  
2600 cycle is given in Table A.1. In this example, the steps 3 to 5 are repeated as long as the webDCS tells  
2601 the DAQ to take data. A data taking cycle is the equivalent as what is called a *Scan* in GIFT++ jargon,  
2602 referring to a set a runs with several HV steps. Each repetition of steps 3 to 5 is then equivalent to a  
2603 single *Run*.

2604

2605 At any moment during the data taking, for any reason, the shifter can decide that the data taking  
2606 needs to be stopped before it reached the end of the scheduled cycle. Thus at any moment on the  
2607 cycle, the content of the inter-process communication file will be changed to `KILL` and the DAQ will  
2608 shut down right away. The DAQ checks for `KILL` signals every 5s after the TDCs configuration is  
2609 over. So far, the function `CheckKILL()` has been used only inside of the data taking loop of method  
2610 `DataReader::Run()` and thus, if the shifter decides to KILL the data taking during the TDC con-  
2611 figuration phase or the HV ramping in between 2 HV steps, the DAQ will not be stopped smoothly  
2612 and a *force kill* command will be sent to stop the DAQ process that is still awake on the computer.  
2613 Improvements can be brought on this part of the software to make sure that the DAQ can safely  
2614 shutdown at any moment.

2615

#### 2616     **A.6 Software export**

2617 In section A.2 was discussed the fact that the DAQ as written in its last version is not a standalone  
2618 software. It is possible to make it a standalone program that could be adapted to any VME setup  
2619 using V1190A and V1718 modules by creating a GUI for the software or by printing the log mes-  
2620 sages that are normally printed in the webDCS through the log file, directly into the terminal. This  
2621 method was used by the DAQ up to version 3.0 moment where the webDCS was completed. Also, it  
2622 is possible to check branches of DAQ v2.X to have example of communication through a terminal.

2623

2624 DAQ v2.X is nonetheless limited in it's possibilities and requires a lot of offline manual interven-  
2625 tions from the users. Indeed, there is no communication of the software with the detectors' power  
2626 supply system that would allow for a user a predefine a list of voltages to operate the detectors at

step	actions of webDCS	status of DAQ	<code>__runstatuspath</code>
1	launch DAQ ramp voltages ramping over wait for currents stabilization	readout of IniFile configuration of TDCs	INIT
2		configuration done send DAQ ready wait for START signal	DAQ_RDY
3	waiting time over send START		START
4	wait for run to end monitor DAQ run status	data taking ongoing check for KILL signal	RUNNING
5		run over send DAQ_RDY wait for next DCS signal	DAQ_RDY
6	ramp voltages ramping over wait for currents stabilization		DAQ_RDY
3	waiting time over send START		START
4	wait for run to end monitor DAQ run status	update IniFile information data taking ongoing check for KILL signal	RUNNING
5		run over send DAQ_RDY wait for next DCS signal	DAQ_RDY
7	send command STOP	DAQ shuts down	STOP

Table A.1: Inter-process communication cycles in between the webDCS and the DAQ through file string signals.

2627 and loop over to take data without any further manual intervention. In v2.X, the data is taken for a  
2628 single detector setting and at the end of each run, the softwares asks the user if he intends on taking  
2629 more runs. If so, the software invites the user to set the operating voltages accordingly to what is  
2630 necessary and to manual update the configuration file in consequence. This working mode can be a  
2631 very first approach before an evolution and has been successfully used by colleagues from different  
2632 collaborations.

2633  
2634 For a more robust operation, it is recommended to develop a GUI or a web application to inter-  
2635 face the DAQ. Moreover, to limit the amount of manual interventions, and thus the probability to  
2636 make mistakes, it is also recommended to add an extra feature into the DAQ by installing the HV  
2637 Wrapper library provided by CAEN of which an example of use in a similar DAQ software devel-  
2638 opped by a master student of UGent, and called TinyDAQ, is provided on UGent's github. Then, this  
2639 HV Wrapper will help you communicating with and give instructions to a CAEN HV powered crate  
2640 and can be added into the DAQ at the same level where the communication with the user was made  
2641 in DAQ v2.X. In case you are using another kind of power system for your detectors, it is stringly  
2642 adviced to use HV modules or crates that can be remotely controled via a using C++ libraries.  
2643

# B

2644

2645

## Details on the offline analysis package

2646 The data collected in GIF++ thanks to the DAQ described in Appendix A is difficult to interpret by  
2647 a human user that doesn't have a clear idea of the raw data architecture of the ROOT data files. In  
2648 order to render the data human readable, a C++ offline analysis tool was designed to provide users  
2649 with detector by detector histograms that give a clear overview of the parameters monitored during  
2650 the data acquisition [68]. In this appendix, details about this software in the context of GIF++, as of  
2651 how the software was written and how it functions will be given.

### 2652 **B.1 GIF++ Offline Analysis file tree**

2653 GIF++ Offline Analysis source code is fully available on github at [https://github.com/aafagot/GIF\\_OfflineAnalysis](https://github.com/aafagot/GIF_OfflineAnalysis). The software requires ROOT as non-optionnal dependency  
2654 as it takes ROOT files in input and write an output ROOT file containing histograms. To compile the  
2655 GIF++ Offline Analysis project is compiled with cmake. To compile, first a build/ directory must  
2656 be created to compile from there:

```
2658 mkdir build
2659 cd build
2660 cmake ..
2661 make
2662 make install
```

2660 To clean the directory and create a new build directory, the bash script cleandir.sh can be used:

```
2661
2662 ./cleandir.sh
```

2663 The source code tree is provided below along with comments to give an overview of the files' con-  
2664 tent. The different objects created for this project (`Infrastructure`, `Trolley`, `RPC`, `Mapping`, `RPCHit`,  
2665 `RPCCluster` and `Inifile`) will be described in details in the following sections.

2666

```

GIF_OfflineAnalysis
├── bin
│   └── offlineanalysis ..... EXECUTABLE
├── build..... CMAKE COMPILATION DIRECTORY
└── ...
    ├── include..... LIST OF C++ HEADER FILES
    │   ├── Cluster.h..... DECLARATION OF OBJECT RPCCLUSTER
    │   ├── Current.h..... DECLARATION OF GETCURRENT ANALYSIS MACRO
    │   ├── GIFTrolley.h..... DECLARATION OF OBJECT TROLLEY
    │   ├── Infrastructure.h..... DECLARATION OF OBJECT INFRASTRUCTURE
    │   ├── IniFile.h..... DECLARATION OF OBJECT INI FILE FORINI PARSER
    │   ├── Mapping.h..... DECLARATION OF OBJECT MAPPING
    │   ├── MsgSvc.h..... DECLARATION OF OFFLINE LOG MESSAGES
    │   ├── OfflineAnalysis.h..... DECLARATION OF DATA ANALYSIS MACRO
    │   ├── RPCDetector.h..... DECLARATION OF OBJECT RPC
    │   ├── RPCHit.h..... DECLARARION OF OBJECT RPCHIT
    │   ├── types.h..... DEFINITION OF USEFUL VARIABLE TYPES
    │   └── utils.h..... DECLARATION OF USEFUL FUNCTIONS
    ├── obj..... BINARY FILES CREATED BY COMPILER
    └── ...
        ├── src..... LIST OF C++ SOURCE FILES
        │   ├── Cluster.cc..... DEFINITION OF OBJECT RPCCLUSTER
        │   ├── Current.cc ..... DEFINITION OF GETCURRENT ANALYSIS MACRO
        │   ├── GIFTrolley.cc..... DEFINITION OF OBJECT TROLLEY
        │   ├── Infrastructure.cc..... DEFINITION OF OBJECT INFRASTRUCTURE
        │   ├── IniFile.cc..... DEFINITION OF OBJECT INI FILE FORINI PARSER
        │   ├── main.cc..... MAIN FILE
        │   ├── Mapping.cc..... DEFINITION OF OBJECT MAPPING
        │   ├── MsgSvc.cc..... DEFINITION OF OFFLINE LOG MESSAGES
        │   ├── OfflineAnalysis.cc..... DEFINITION OF DATA ANALYSIS MACRO
        │   ├── RPCDetector.cc..... DEFINITION OF OBJECT RPC
        │   ├── RPCHit.cc..... DEFINITION OF OBJECT RPCHIT
        │   └── utils.cc..... DEFINITION OF USEFUL FUNCTIONS
        ├── cleandir.sh..... BASH SCRIPT TO CLEAN BUILD DIRECTORY
        ├── CMakeLists.txt..... SET OF INSTRUCTIONS FOR CMAKE
        ├── config.h.in..... DEFINITION OF VERSION NUMBER
        └── README.md..... REAMDE FILE FOR GITHUB

```

2667

## B.2 Usage of the Offline Analysis

2668

In order to use the Offline Analysis tool, it is necessary to know the Scan number and the HV Step of the run that needs to be analysed. This information needs to be written in the following format:

2670

2671

```
Scan00XXXX_HVY
```

2672

where xxxx is the scan ID and y is the high voltage step (in case of a high voltage scan, data will be taken for several HV steps). This format corresponds to the base name of data files in the database

2673

2674 of the GIF++ webDCS. Usually, the offline analysis tool is automatically called by the webDCS at  
 2675 the end of data taking or by a user from the webDCS panel if an update of the tool was brought.  
 2676 Nonetheless, an expert can locally launch the analysis for tests on the GIF++ computer, or a user can  
 2677 get the code on its local machine from github and download data from the webDCS for its own anal-  
 2678 ysis. To launch the code, the following command can be used from the `GIF_OfflineAnalysis` folder:

2679  
 2680     `bin/offlineanalysis /path/to/Scan00XXXX_HVY`

2681 where, `/path/to/Scan00XXXX_HVY` refers to the local data files. Then, the offline tool will by itself  
 2682 take care of finding all available ROOT data files present in the folder, as listed below:

- 2683
  - 2684         ● `Scan00XXXX_HVY_DAQ.root` containing the TDC data as described in Appendix ?? (events, hit  
     and timestamp lists), and
  - 2685         ● `Scan00XXXX_HVY_CAEN.root` containing the CAEN mainframe data recorded by the monitor-  
     ing tool webDCS during data taking (HVs and currents of every HV channels). This file is  
     created independently of the DAQ.

## 2688     **B.2.1 Output of the offline tool**

### 2689         **B.2.1.1 ROOT file**

2690 The analysis gives in output ROOT datafiles that are saved into the data folder and called using the  
 2691 naming convention `Scan00XXXX_HVY_Offline.root`. Inside those, a list of `TH1` histograms can be  
 2692 found. Its size will vary as a function of the number of detectors in the setup as each set of histograms  
 2693 is produced detector by detector. For each partition of each chamber, can be found:

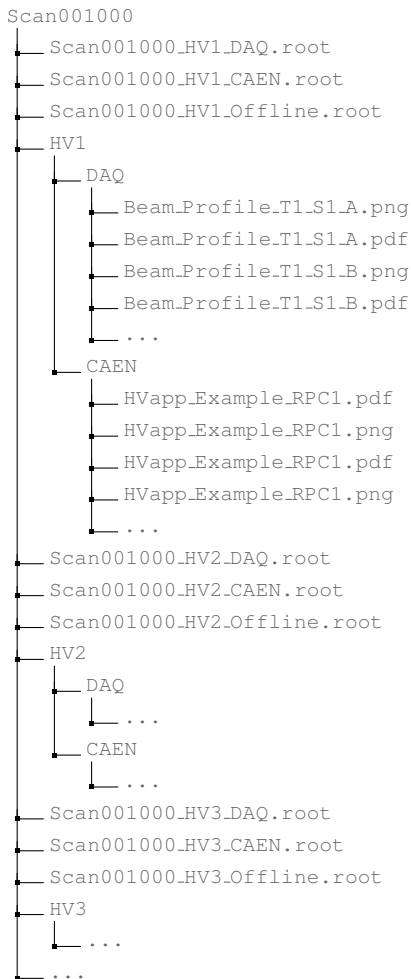
- 2694
  - 2695         ● `Time_Profile_Tt_Sc_p` shows the time profile of all recorded events (number of events per  
     time bin),
  - 2696         ● `Hit_Profile_Tt_Sc_p` shows the hit profile of all recorded events (number of events per chan-  
     nel),
  - 2698         ● `Hit_Multiplicity_Tt_Sc_p` shows the hit multiplicity (number of hits per event) of all recorded  
     events (number of occurrences per multiplicity bin),
  - 2700         ● `Strip_Mean_Noise_Tt_Sc_p` shows noise/gamma rate per unit area for each strip in a se-  
     lected time range. After filters are applied on `Time_Profile_Tt_Sc_p`, the filtered version  
     of `Hit_Profile_Tt_Sc_p` is normalised to the total integrated time and active detection area  
     of a single channel,
  - 2704         ● `Strip_Activity_Tt_Sc_p` shows noise/gamma activity for each strip (normalised version of  
     previous histogram - strip activity = strip rate / average partition rate),
  - 2706         ● `Strip_Homogeneity_Tt_Sc_p` shows the *homogeneity* of a given partition ( $\text{homogeneity} = \exp(-\text{strip rates standard deviation(strip rates in partition/average partition rate)})$ ),
  - 2708         ● `mask_Strip_Mean_Noise_Tt_Sc_p` shows noise/gamma rate per unit area for each masked  
     strip in a selected time range. Offline, the user can control the noise/gamma rate and decide to  
     mask the strips that are judged to be noisy or dead. This is done via the *Masking Tool* provided  
     by the webDCS,

- 2712     ● `mask_Strip_Activity_Tt_Sc_p` shows noise/gamma activity per unit area for each masked  
2713       strip with respect to the average rate of active strips,
- 2714     ● `NoiseCSize_H_Tt_Sc_p` shows noise/gamma cluster size, a cluster being constructed out of  
2715       adjacent strips giving a signal at the *same time* (hits within a time window of 25 ns),
- 2716     ● `NoiseCMult_H_Tt_Sc_p` shows noise/gamma cluster multiplicity (number of reconstructed  
2717       clusters per event),
- 2718     ● `Chip_Mean_Noise_Tt_Sc_p` shows the same information than `Strip_Mean_Noise_Tt_Scp` us-  
2719       ing a different binning (1 chip corresponds to 8 strips),
- 2720     ● `Chip_Activity_Tt_Sc_p` shows the same information than `Strip_Activity_Tt_Scp` using  
2721       chip binning,
- 2722     ● `Chip_Homogeneity_Tt_Sc_p` shows the homogeneity of a given partition using chip binning,
- 2723     ● `Beam_Profile_Tt_Sc_p` shows the estimated beam profile when taking efficiency scan. This  
2724       is obtained by filtering `Time_Profile_Tt_Sc_p` to only consider the muon peak where the  
2725       noise/gamma background has been subtracted. The resulting hit profile corresponds to the  
2726       beam profile on the detector channels,
- 2727     ● `L0_Efficiency_Tt_Sc_p` shows the level 0 efficiency that was estimated **without** muon track-  
2728       ing,
- 2729     ● `MuonCSize_H_Tt_Sc_p` shows the level 0 muon cluster size that was estimated **without** muon  
2730       tracking, and
- 2731     ● `MuonCMult_H_Tt_Sc_p` shows the level 0 muon cluster multiplicity that was estimated **without**  
2732       muon tracking.

2733     In the histogram labels,  $t$  stands for the trolley number (1 or 3),  $c$  for the chamber slot label in  
2734     trolley  $t$  and  $p$  for the partition label (A, B, C or D depending on the chamber layout) as explained  
2735     in Chapter 5.4.

2736     In the context of GIF++, an extra script called by the webDCS is called to extract the histograms  
2737     from the ROOT files. The histograms are then stored in PNG and PDF formats into the correspond-  
2738     ing folder (a single folder per HV step, so per ROOT file). the goal is to then display the histograms  
2739     on the Data Quality Monitoring (DQM) page of the webDCS in order for the users to control the  
2740     quality of the data taking at the end of data taking. An example of histogram organisation is given  
2741     below:

2742



2744       *Here can put some screens from the webDCS to show the DQM and the plots available to users.*  
 2745

### 2746       **B.2.1.2 CSV files**

2747       Moreover, up to 3 CSV files can be created depending on which ones of the 3 input files were in the  
 2748       data folder:

- 2749       ● `Offline-Corrupted.csv` , is used to keep track of the amount of data that was corrupted and  
 2750       removed from old data format files that don't contain any data quality flag.
- 2751       ● `Offline-Current.csv` , contains the summary of the currents and voltages applied on each  
 2752       RPC HV channel.
- 2753       ● `Offline-L0-EffC1.csv` , is used to write the efficiencies, cluster size and cluster multiplicity  
 2754       of efficiency runs. Note that `L0` refers here to *Level 0* and means that the results of efficiency and  
 2755       clusterization are a first approximation calculated without performing any muon tracking in

2756 between the different detectors. This offline tool provides the user with a preliminar calculation  
 2757 of the efficiency and of the muon event parameters. Another analysis software especially  
 2758 dedicated to muon tracking is called on selected data to retrieve the results of efficiency and  
 2759 muon clusterization using a tracking algorithm to discriminate noise or gamma from muons  
 2760 as muons are the only particles that pass through the full setup, leaving hits than can be used  
 2761 to reconstruct their tracks.

- 2762 • `Offline-Rate.csv`, is used to write the noise or gamma rates measured in the detector readout  
 2763 partitions.

2764 Note that these 4 CSV files are created along with their *headers* (`Offline-[...]-Header.csv`  
 2765 containing the names of each data columns) and are automatically merged together when the offline  
 2766 analysis tool is called from the webDCS, contrary to the case where the tool is runned locally from  
 2767 the terminal as the merging bash script is then not called. Thus, the resulting files, used to make  
 2768 official plots, are:

- 2769 • `Corrupted.csv`,  
 2770 • `Current.csv`,  
 2771 • `L0-EffCl.csv`.  
 2772 • `Rate.csv`.

### 2773 B.3 Analysis inputs and information handling

2774 The usage of the Offline Analysis tool as well as its output have been presented in the previous section.  
 2775 It is now important to dig further and start looking at the source code and the inputs necessary  
 2776 for the tool to work. Indeed, other than the raw ROOT data files that are analysed, more information  
 2777 needs to be imported inside of the program to perform the analysis such as the description of the  
 2778 setup inside of GIFT++ at the time of data taking (number of trolleys, of RPCs, dimensions of the  
 2779 detectors, etc...) or the mapping that links the TDC channels to the coresponding RPC channels in  
 2780 order to translate the TDC information into human readable data. 2 files are used to transmit all this  
 2781 information:  
 2782

- 2783 • `Dimensions.ini`, that provides the necessary setup and RPC information, and  
 2784 • `ChannelsMapping.csv`, that gives the link between the TDC and RPC channels as well as the  
 2785 *mask* for each channel (masked or not?).

#### 2786 B.3.1 Dimensions file and InFile parser

2787 This input file, present in every data folder, allows the analysis tool to know of the number of active  
 2788 trolleys, the number of active RPCs in those trolleys, and the details about each RPCs such as  
 2789 the number of RPC gaps, the number of pseudo-rapidity partitions (for CMS-like prototypes), the  
 2790 number of strips per partion or the dimensions. To do so, there are 3 types of groups in the INI file  
 2791 architecture. A first general group, appearing only once at the head of the document, gives information  
 2792 about the number of active trolleys as well as their IDs, as presented in Source Code B.1. For

2793 each active trolley, a group similar to Source Code B.2 can be found containing information about  
 2794 the number of active detectors in the trolley and their IDs. Each trolley group as a `Tt` name format,  
 2795 where `t` is the trolley ID. Finally, for each detector stored in slots of an active trolley, there is a group  
 2796 providing information about their names and dimensions, as shown in Source Code B.3. Each slot  
 2797 group as a `TtSs` name format, where `s` is the slot ID of trolley `t` where the active RPC is hosted.

```
2798 [General]
2799 nTrolleys=2
  TrolleysID=13
```

2800 *Source Code B.1: Example of `[General]` group as might be found in `Dimensions.ini`. In Gif++, only 2 trolleys are available to hold RPCs and place them inside of the bunker for irradiation. The IDs of the trolleys are written in a single string as "13" and then read character by character by the program.*

```
2801 [T1]
  nSlots=4
  SlotsID=1234
```

2802 *Source Code B.2: Example of trolley group as might be found in `Dimensions.ini`. In this example, the file tells that there are 4 detectors placed in the holding slots of the trolley `T1` and that their IDs, written as a single string variable, are 1, 2, 3 and 4.*

```
2803 [T1S1]
  Name=RE2-2-NPD-BARC-8
  Partitions=3
  Gaps=3
  Gap1=BOT
  Gap2=TN
  Gap3=TW
  AreaGap1=11694.25
  AreaGap2=6432
  AreaGap3=4582.82
  Strips=32
  ActiveArea-A=157.8
  ActiveArea-B=121.69
  ActiveArea-C=93.03
```

2804 *Source Code B.3: Example of slot group as might be found in `Dimensions.ini`. In this example, the file provides information about a detector named `RE2-2-NPD-BARC-8`, having 3 pseudo-rapidity readout partitions and stored in slot `S1` of trolley `T1`. This is a CMS RE2-2 type of detector. This information will then be used for example to compute the rate per unit area calculation.*

2805 This information is readout and stored in a C++ object called `IniFile`, that parses the information  
 2806 in the INI input file and stores it into a local buffer for later use. This INI parser is the exact same  
 2807 one that was previously developed for the Gif++ DAQ and described in Appendix A.5.2.

### 2808 B.3.2 TDC to RPC link file and Mapping

2809 The same way the INI dimension file information is stored using `map`, the channel mapping and mask  
 2810 information is stored and accessed through `map`. First of all, the mapping CSV file is organised into  
 2811 3 columns separated by tabulations (and not by commas, as expected for CSV files as it is easier using  
 2812 streams to read tab or space separated data using C++):

2813

2814       RPC\_channel           TDC\_channel           mask

2815       using as formatting for each field:

2816

2817	TSCCC	TCCC	M
------	-------	------	---

2818 TSCCC is a 5-digit integer where  $\tau$  is the trolley ID,  $s$  the slot ID in which the RPC is held insite  
 2819       the trolley  $\tau$  and ccc is the RPC channel number, or *strip* number, that can take values up to  
 2820       3-digits depending on the detector,

2821 TCCC is a 4 digit integer where  $\tau$  is the TDC ID, ccc is the TDC channel number that can take values  
 2822       in between 0 and 127, and

2823 M is a 1-digit integer indicating if the channel should be considered ( $M = 1$ ) or discarded ( $M = 0$ )  
 2824       during analysis.

2825       This mapping and masking information is readout and stored thanks to the object `Mapping`, pre-  
 2826       sented in Source Code B.4. Similarly to `IniFile` objects, this class has private methods. The first  
 2827       one, `Mapping::CheckIfNewLine()` is used to find the newline character '`\n`' or return character  
 2828       '`\r`' (depending on which kind of operating system interacted with the file). This is used for the  
 2829       simple reason that the masking information has been introduced only during the year 2017 but the  
 2830       channel mapping files exist since 2015 and the very beginning of data taking at GIF++. This means  
 2831       that in the older data folders, before the upgrade, the channel mapping file only had 2 columns, the  
 2832       RPC channel and the TDC channel. For compatibility reasons, this method helps controling the  
 2833       character following the readout of the 2 first fields of a line. In case any end of line character is  
 2834       found, no mask information is present in the file and the default  $M = 1$  is used. On the contrary, if  
 2835       the next character was a tabulation or a space, the mask information is present.

2836       Once the 3 fields have been readout, the second private method `Mapping::CheckIfTDCCh()` is  
 2837       used to control that the TDC channel is an existing TDC channel. Finally, the information is stored  
 2838       into 3 different maps (`Link`, `ReverseLink` and `Mask`) thanks to the public method `Mapping::Read()`.  
 2839       `Link` allows to get the RPC channel by knowing the TDC channel while `ReverseLink` does the op-  
 2840       posite by returning the TDC channel by knowing the RPC channel. Finally, `Mask` returns the mask  
 2841       associated to a given RPC channel.

```

2842 typedef map<Uint,Uint> MappingData;

2843 class Mapping {
    private:
        bool          CheckIfNewLine(char next);
        bool          CheckIfTDCCh(Uint channel);
        string         FileName;
        MappingData   Link;
        MappingData   ReverseLink;
        MappingData   Mask;
        int           Error;

    public:
        Mapping();
        Mapping(string baseName);
        ~Mapping();

        void SetFileName(const string filename);
        int Read();
        Uint GetLink(Uint tdcchannel);
        Uint GetReverse(Uint rpcchannel);
        Uint GetMask(Uint rpcchannel);
};


```

2844 *Source Code B.4: Description of C++ object Mapping used as a parser for the channel mapping and mask file.*

## 2845 **B.4 Description of GIF++ setup within the Offline Analysis tool**

2846 In the previous section, the tool input files have been discussed. The dimension file information is  
 2847 stored in a map hosted by the `IniFile` object. But this information is then used to create a series of  
 2848 new objects that helps defining the GIF++ infrastructure directly into the Offline Analysis. Indeed,  
 2849 from the `RPC`, to the more general `Infrastructure`, every element of the GIF++ infrastrucutre is  
 2850 recreated for each data analysis based on the information provided in input. All this information  
 2851 about the infrastructure will be used to assign each hit signal to a specific strip channel of a specific  
 2852 detector, and having a specific active area. This way, rate per unit area calculation is possible.  
 2853

### 2854 **B.4.1 RPC objects**

2855 `RPC` objects have been developped to represent physical active detectors in GIF++ at the moment  
 2856 of data taking. Thus, there are as many `RPC` objects created during the analysis than there were  
 2857 active RPCs tested during a run. Each `RPC` hosts the information present in the corresponding INI  
 2858 slot group, as shown in B.3, and organises it using a similar architecture. This can be seen from  
 2859 Source Code B.5.

2860 To make the object more compact, the lists of gap labels, of gap active areas and strip active  
 2861 areas are stored into `vector` dynamical containers. `RPC` objects are always contructed thanks to the  
 2862 dimension file information stored into the `IniFILE` and their ID, using the format `TtSs`. Using the  
 2863 `RPC` ID, the constructor calls the methods of `IniFILE` to initialise the `RPC`. The other constructors  
 2864 are not used but exist in case of need. Finally, some getters have been written to access the different  
 2865 private parameters storing the detector information.

```

2866
class RPC{
    private:
        string      name;           //RPC name as in webDCS database
        Uint        nGaps;          //Number of gaps in the RPC
        Uint        nPartitions;    //Number of partitions in the RPC
        Uint        nStrips;         //Number of strips per partition
        vector<string> gaps;       //List of gap labels (BOT, TOP, etc...)
        vector<float>  gapGeo;        //List of gap active areas
        vector<float>  stripGeo;      //List of strip active areas

    public:
        RPC();
        RPC(string ID, IniFile* geofile);
        RPC(const RPC& other);
        ~RPC();
        RPC& operator=(const RPC& other);

        string GetName();
        Uint GetNGaps();
        Uint GetNPartitions();
        Uint GetNStrips();
        string GetGap(Uint g);
        float GetGapGeo(Uint g);
        float GetStripGeo(Uint p);
};

2867

```

2868 *Source Code B.5: Description of C++ objects RPC that describe each active detectors used during data taking.*

## 2869 B.4.2 Trolley objects

2870 Trolley objects have been developped to represent physical active trolleys in GIFT++ at the moment  
 2871 of data taking. Thus, there are as many trolley objects created during the analysis than there were  
 2872 active trolleys hosting tested RPCs during a run. Each Trolley hosts the information present in the  
 2873 corresponding INI trolley group, as shown in B.2, and organises it using a similar architecture. In  
 2874 addition to the information hosted in the INI file, these object have a dynamical container of RPC  
 2875 objects, representing the active detectors the active trolley was hosting at the time of data taking.  
 2876 This can been seen from Source Code B.6.

2877 Trolley objects are always contructed thanks to the dimension file information stored into the  
 2878 IniFILE and their ID, using the format Tt. Using the Trolley ID, the constructor calls the methods  
 2879 of IniFILE to initialise the Trolley. Retrieving the information of the RPC IDs via SlotsID, a new  
 2880 RPC is constructed and added to the container RPCs for each character in the ID string. The other  
 2881 constructors are not used but exist in case of need. Finally, some getters have been written to access  
 2882 the different private parameters storing the trolley and detectors information.

```

2883
class Trolley{
    private:
        Uint          nSlots; //Number of active RPCs in the considered trolley
        string        SlotsID; //Active RPC IDs written into a string
        vector<RPC*> RPCs;   //List of active RPCs

    public:
        //Constructors, destructor and operator =
        Trolley();
        Trolley(string ID, IniFile* geofile);
        Trolley(const Trolley& other);
        ~Trolley();
        Trolley& operator=(const Trolley& other);

        //Get GIFTrolley members
        Uint  GetNSlots();
        string GetSlotsID();
        Uint   GetSlotID(Uint s);

        //Manage RPC list
        RPC*  GetRPC(Uint r);
        void  DeleteRPC(Uint r);

        //Methods to get members of RPC objects stored in RPCs
        string GetName(Uint r);
        Uint   GetNGaps(Uint r);
        Uint   GetNPartitions(Uint r);
        Uint   GetNStrips(Uint r);
        string GetGap(Uint r, Uint g);
        float  GetGapGeo(Uint r, Uint g);
        float  GetStripGeo(Uint r, Uint p);
    };

```

*Source Code B.6: Description of C++ objects `Trolley` that describe each active trolley used during data taking.*

### 2886    B.4.3 Infrastructure object

2887 The `Infrastructure` object has been developped to represent the GIFT++ bunker area dedicated to  
 2888 CMS RPC experiments. With this very specific object, all the information about the CMS RPC  
 2889 setup within GIFT++ at the moment of data taking is stored. It hosts the information present in the  
 2890 corresponding INI general group, as shown in B.1, and organises it using a similar architecture. In  
 2891 addition to the information hosted in the INI file, this object have a dynamical container of `Trolley`  
 2892 objects, representing the active tolleys in GIFT++ area. This can be seen from Source Code B.7.

2893 The `Infrastructure` object is always contructed thanks to the dimension file information stored  
 2894 into the `IniFILE`. Retrieving the information of the trolley IDs via `TrolleysID`, a new `Trolley` is  
 2895 constructed and added to the container `Trolleys` for each character in the ID `string`. By extension,  
 2896 it is easy to understand that the process described in Section B.4.2 for the construction of RPCs  
 2897 takes place when a trolley is constructed. The other constructors are not used but exist in case of  
 2898 need. Finally, some getters have been written to access the different private parameters storing the  
 2899 infrastructure, tolleys and detectors information.

```

2900
class Infrastructure {
    private:
        Uint             nTrolleys;   //Number of active Trolleys in the run
        string          TrolleysID; //Active trolley IDs written into a string
        vector<Trolley*> Trolleys; //List of active Trolleys (struct)

    public:
        //Constructors and destructor
        Infrastructure();
        Infrastructure(IniFile* geofile);
        Infrastructure(const Infrastructure& other);
        ~Infrastructure();
        Infrastructure& operator=(const Infrastructure& other);

        //Get Infrastructure members
        Uint  GetNTrolleys();
        string GetTrolleysID();
        Uint  GetTrolleyID(Uint t);

2901
        //Manage Trolleys
        Trolley* GetTrolley(Uint t);
        void     DeleteTrolley(Uint t);

        //Methods to get members of GIFTrolley objects stored in Trolleys
        Uint  GetNSlots(Uint t);
        string GetSlotsID(Uint t);
        Uint  GetSlotID(Uint t, Uint s);
        RPC*  GetRPC(Uint t, Uint r);

        //Methods to get members of RPC objects stored in RPCs
        string GetName(Uint t, Uint r);
        Uint  GetNGaps(Uint t, Uint r);
        Uint  GetNPartitions(Uint t, Uint r);
        Uint  GetNStrips(Uint t, Uint r);
        string GetGap(Uint t, Uint r, Uint g);
        float  GetGapGeo(Uint t, Uint r, Uint g);
        float  GetStripGeo(Uint t, Uint r, Uint p);
    };

```

*Source Code B.7: Description of C++ object Infrastructure that contains the full information about CMS RPC experiment in GIF++.*

## 2903 B.5 Handeling of data

2904 As discussed in Appendix A.4.2, the raw data as a `TTree` architecture where every entry is related to  
 2905 a trigger signal provided by a muon or a random pulse, whether the goal of the data taking was to  
 2906 measure the performance of the detector or the noise/gamma background respectively. Each of these  
 2907 entries, referred also as events, contain a more or less full list of hits in the TDC channels to which  
 2908 the detectors are connected. To this list of hits corresponds a list of time stamps, marking the arrival  
 2909 of the hits within the TDC channel.

2910 The infrastructure of the CMS RPC experiment within `GIF++` being defined, combining the  
 2911 information about the raw data with the information provided by both the mapping/mask file and the  
 2912 dimension file allows to build new physical objects that will help in computing efficiency or rates.

### 2913 B.5.1 RPC hits

2914 The raw data stored in the ROOT file as output of the GIFT++ DAQ, is readout by the analysis tool  
 2915 using the structure `RAWData` presented in Source Code B.9 that differs from the structure presented  
 2916 in Appendix A.4.2 as it is not meant to hold all of the data contained in the ROOT file. In this sense,  
 2917 this structure is in the case of the offline analysis tool not a dynamical object and will only be storing  
 2918 a single event contained in a single entry of the `TTree`.

```
2919
2920 class RPCHit {
2921     private:
2922         Uint Channel;      //RPC channel according to mapping (5 digits)
2923         Uint Trolley;      //0, 1 or 3 (1st digit of the RPC channel)
2924         Uint Station;      //Slot where is held the RPC in Trolley (2nd digit)
2925         Uint Strip;        //Physical RPC strip where the hit occurred (last 3
2926         →   digits)
2927         Uint Partition;    //Readout partition along eta segmentation
2928         float TimeStamp;   //Time stamp of the arrival in TDC
2929
2930     public:
2931         //Constructors, destructor & operator =
2932         RPCHit();
2933         RPCHit(Uint channel, float time, Infrastructure* Infra);
2934         RPCHit(const RPCHit& other);
2935         ~RPCHit();
2936         RPCHit& operator=(const RPCHit& other);
2937
2938         //Get RPCHit members
2939         Uint GetChannel();
2940         Uint GetTrolley();
2941         Uint GetStation();
2942         Uint GetStrip();
2943         Uint GetPartition();
2944         float GetTime();
2945     };
2946
2947     typedef vector<RPCHit> HitList;
2948     typedef struct GIFHitList { HitList rpc[NTROLLEYS][NSLOTS][NPARTITIONS]; } →
2949     →   GIFHitList;
2950
2951     bool SortHitbyStrip(RPCHit h1, RPCHit h2);
2952     bool SortHitbyTime(RPCHit h1, RPCHit h2);
2953 }
```

2921           *Source Code B.8: Description of C++ object RPCHit.*

```
2922 struct RAWData{
2923     int          iEvent;      //Event i
2924     int          TDCNHits;   //Number of hits in event i
2925     int          QFlag;       //Quality flag list (1 flag digit per TDC)
2926     vector<Uint> *TDCCh;    //List of channels giving hits per event
2927     vector<float> *TDCTS;     //List of the corresponding time stamps
2928 };
```

2923           *Source Code B.9: Description of C++ structure RAWData.*

2924     Each member of the structure is then linked to the corresponding branch of the ROOT data tree,  
 2925 as shown in the example of Source Code B.10, and using the method `GetEntry(int i)` of the ROOT  
 2926 class `TTree` will update the state of the members of `RAWData`.

```

2927   TTree* dataTree = (TTree*)dataFile.Get("RAWData");
2928   RAWData data;
2929
2930   dataTree->SetBranchAddress("EventNumber", &data.iEvent);
2931   dataTree->SetBranchAddress("number_of_hits", &data.TDCNHits);
2932   dataTree->SetBranchAddress("Quality_flag", &data.QFlag);
2933   dataTree->SetBranchAddress("TDC_channel", &data.TDCCh);
2934   dataTree->SetBranchAddress("TDC_TimeStamp", &data.TDCTS);

```

2929       *Source Code B.10: Example of link in between RAWData and TTree.*

2930       The data is then analysed entry by entry and to each element of the TDC channel list, a `RPCHit` is  
 2931       constructed by linking each TDC channel to the corresponding RPC channel thanks to the `Mapping`  
 2932       object. The information carried by the RPC channel format allows to easily retrieve the trolley and  
 2933       slot from which the hit was recorded (see section B.3.2). Using these 2 values, the readout partition  
 2934       can be found by knowing the strip channel and comparing it with the number of partitions and strips  
 2935       per partition stored into the `Infrastructure` object.

2936       Thus `RPCHit` objects are then stored into 3D dynamical list called `GIFHitList` (Source Code B.9)  
 2937       where the 3 dimensions refer to the 3 layers of the readout in `GIF++` : in the bunker there are *trolleys*  
 2938       ( $\tau$ ) holding detectors in *slots* ( $s$ ) and each detector readout is divided into 1 or more pseudo-rapidity  
 2939       *partitions* ( $p$ ). Using these 3 information allows to assign an address to each readout partition and  
 2940       this address will point to a specific hit list.

2941

## 2942     **B.5.2 Clusters of hits**

2943       All the hits contained in the ROOT file have been sorted into the different hit lists through the  
 2944       `GIFHitList`. At this point, it is possible to start looking for clusters. A cluster is a group of adjacent  
 2945       strips getting hits within a time window of 25 ns. These strips are then assumed to be part of the same  
 2946       physical avalanche signal generated by a muon passing through the chamber or by the interaction of  
 2947       a gamma stopping into the electrodes of the RPCs.

2948       To keep the cluster information, `RPCCluster` objects have been defined as shown in Source  
 2949       Code B.11. Using the information of each individual `RPCHit` taken out of the hit list, it stores  
 2950       the cluster size (number of adjacent strips composing the cluster), the first and last hit, the center for  
 2951       spatial reconstruction and finally the start and stop time stamps as well as te time spread in between  
 2952       the first and last hit.

```

2953
class RPCCluster{
    private:
        Uint ClusterSize; //Size of cluster #ID
        Uint FirstStrip; //First strip of cluster #ID
        Uint LastStrip; //Last strip of cluster #ID
        float Center; //Center of cluster #ID ((first+last)/2)
        float StartStamp; //Time stamp of the earliest hit of cluster #ID
        float StopStamp; //Time stamp of the latest hit of cluster #ID
        float TimeSpread; //Time difference between earliest and latest hits
                           //of cluster #ID

    public:
        //Constructors, destructor & operator =
        RPCCluster();
        RPCCluster(HitList List, Uint cID, Uint cSize, Uint first, Uint firstID);
        RPCCluster(const RPCCluster& other);
        ~RPCCluster();
        RPCCluster& operator=(const RPCCluster& other);

        //Get Cluster members
        Uint GetID();
        Uint GetSize();
        Uint GetFirstStrip();
        Uint GetLastStrip();
        float GetCenter();
        float GetStart();
        float GetStop();
        float GetSpread();
};

typedef vector<RPCCluster> ClusterList;

//Other functions to build cluster lists out of hit lists
void BuildClusters(HitList &cluster, ClusterList &clusterList);
void Clusterization(HitList &hits, TH1 *hcSize, TH1 *hcMult);

```

*Source Code B.11: Description of C++ object cluster.*

To investigate the hit list of a given detector partition, the function `Clusterization()` defined in `include/Cluster.h` needs the hits in the list to be time sorted. This is achieved by calling function `sort()` of library `<algorithm>` using the comparator `SortHitbyTime(RPCHit h1, RPCHit h2)` defined in `include/RPCHit.h` that returns `true` if the time stamp of hit `h1` is lower than that of `h2`. A first isolation of strips is made only based on time information. All the hits within the 25 ns window are taken separately from the rest. Then, this sub-list of hits is sorted this time by ascending strip number, using this time the comparator `SortHitbyStrip(RPCHit h1, RPCHit h2)`. Finally, the groups of adjacent strips are used to construct `RPCcluster` objects that are then stored in a temporary list of clusters that is at the end of the process used to know how many clusters were reconstructed and to fill their sizes into an histogram that will allows to know the mean size of muon or gamma clusters.

## **2968 B.6 DAQ data Analysis**

All the ingredients to analyse GIF++ data have been defined. This section will focus on the different part of the analysis performed on the data, from determining the type of data the tool is dealing with

2971 to calculating the rate in each detector or reconstructing muon or gamma clusters.

### 2972 B.6.1 Determination of the run type

2973 In GIF++, both the performance of the detectors in detecting muons in an irradiated environment and  
 2974 the gamma background can be independantly measured. These corresponds to different run types  
 2975 and thus, to different TDC settings giving different data to look at.

2976     In the case of performance measurements, the trigger for data taking is provided by the coïncidence  
 2977 of several scintillators when muons from the beam passing through the area are detected. Data  
 2978 is collected in a 600 ns wide window around the arrival of muons in the RPCs. The expected time  
 2980 distribution of hits is shown in Figure B.1a. The muon peak is clearly visible in the center of the  
 2981 distribution and is to be extracted from the gamma background that composes the flat part of the  
 2982 distribution.

2983     On the other hand, gamma background or noise measurements are focussed on the non muon  
 2984 related physics and the trigger needs to be independant from the muons to give a good measurement  
 2985 of the gamma/noise distribution as seen by the detectors. The trigger is then provided by a pulse  
 2986 generator at a frequency of 300 Hz whose pulse is not likely to be on time with a muon. In order  
 2987 to increase the integrated time without increasing the acquisition time too much, the width of the  
 2988 acquisition windows are increased to 10  $\mu$ s. The time distribution of the hits is expected to be flat, as  
 2989 shown by Figure B.1b.

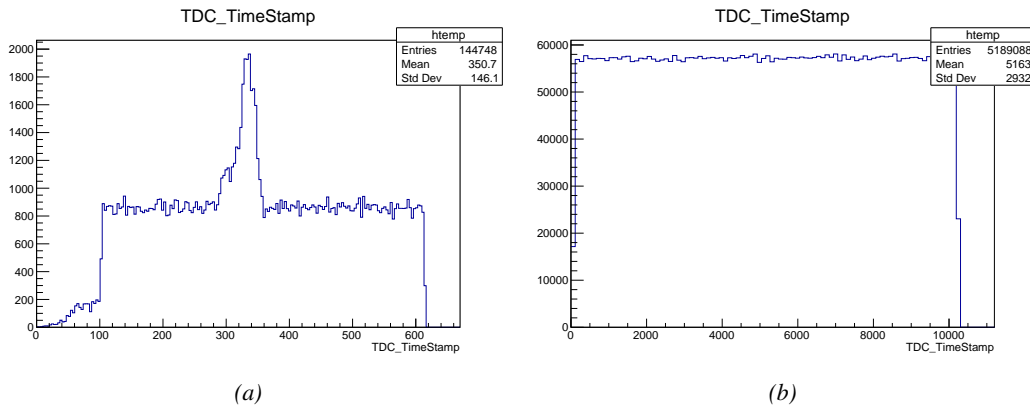


Figure B.1: Example of expected hit time distributions in the cases of efficiency (Figure B.1a) and noise/gamma rate per unit area (Figure B.1b) measurements as extracted from the raw ROOT files. The unit along the x-axis corresponds to ns. The fact that "the" muon peak is not well defined in Figure B.1a is due to the contribution of all the RPCs being tested at the same time that don't necessarily have the same signal arrival time. Each individual peak can have an offset with the ones of other detectors. The inconsistency in the first 100 ns of both time distributions is an artefact of the TDCs and are systematically rejected during the analysis.

2990     The ROOT files include a TTree called RunParameters containing, among other things, the in-  
 2991 formation related to the type of run. The run type can then be accessed as described by Source  
 2992 Code B.12 and the function IsEfficiencyRun() is then used to determine if the run file is an effi-  
 2993 ciency run or, on the contrary, another type of run (noise or gamma measurement).

```

2994     TTree* RunParameters = (TTree*)dataFile.Get("RunParameters");
2995     TString* RunType = new TString();
2996     RunParameters->SetBranchAddress("RunType", &RunType);
2997     RunParameters->GetEntry(0);

```

2996       *Source Code B.12: Access to the run type contained in TTree\* RunParameters.*

2997       Finally, the data files will have a slightly different content whether it was collected before or after  
 2998       October 2017 and the upgrade of the DAQ software that brought a new information into the ROOT  
 2999       output. This is discussed in Appendix A.4.3 and implies that the analysis will differ a little depending  
 3000       on the data format. Indeed, as no information on the data quality is stored, in older data files, the cor-  
 3001       rections for missing events has to be done at the end of the analysis. The information about the type  
 3002       of data format is stored in the variable **bool** `isNewFormat` by checking the list of branches contained  
 3003       in the data tree via the methods `TTree::GetListOfBranches()` and `TCollection::Contains()`.

### 3004       **B.6.2 Beam time window calculation for efficiency runs**

3005       Knowing the run type is important first of all to know the width of the acquisition window to be used  
 3006       for the rate calculation and finally to be able to seek for muons. Indeed, the peak that appears in the  
 3007       time distribution for each detectors is then fitted to extract the most probable time window in which  
 3008       the tool should look for muon hits. The data outside of this time window is then used to evaluate the  
 3009       noise or gamma background the detector was subjected to during the data taking. Computing the  
 3010       position of the peak is done calling the function `SetBeamWindow()` defined in file `src/RPCHit.cc` that  
 3011       loops a first time on the data. The data is first sorted in a 3D array of 1D histograms (`GIFH1Array`, see  
 3012       include/types.h). Then the location of the highest bin is determined using `TH1::GetMaximumBin()`  
 3013       and is used to define a window in which a gaussian fit will be applied to compute the peak width.  
 3014       This window is a 80 ns defined by Formula B.1 around the central bin.

$$t_{center}(ns) = bin \times width_{bin}(ns) \quad (\text{B.1a})$$

$$[t_{low}; t_{high}] = [t_{center} - 40; t_{center} + 40] \quad (\text{B.1b})$$

3015       Before the fit is performed, the average number of noise/gamma hits per bin is evaluated using  
 3016       the data outside of the fit window. Excluding the first 100 ns, the average number of hits per bin  
 3017       due to the noise or gamma is defined by Formula B.2 after extracting the amount of hits in the time  
 3018       windows  $[100; t_{low}]$  and  $[t_{high}; 600]$  thanks to the method `TH1::Integral()`. This average number  
 3019       of hits is then subtracted to every bin of the 1D histogram, in order to *clean* it from the noise or  
 3020       gamma contribution as much as possible to improve the fit quality. Bins where  $\langle n_{hits} \rangle$  is greater  
 3021       than the actual bin content are set to 0.

$$\Delta t_{noise}(ns) = 600 \overbrace{-t_{high} + t_{low}}^{-80ns} - 100 = 420ns \quad (\text{B.2a})$$

$$\langle n_{hits} \rangle = width_{bin}(ns) \times \frac{\sum_{t=100}^{t_{low}} + \sum_{t=t_{high}}^{600}}{\Delta t_{noise}(ns)} \quad (\text{B.2b})$$

3022       Finally, the fit parameters are extracted and saved for each detector in 3D arrays of **float**  
 3023       (`muonPeak`, see include/types.h), a first one for the mean arrival time of the muons, `PeakTime`,

3024 and a second one for the width of the peak, `PeakWidth`. The width is defined as  $6\sigma$  of the gaussian  
 3025 fit. The same settings are applied to every partitions of the same detector. To determine which one  
 3026 of the detector's partitions is directly illuminated by the beam, the peak height of each partition is  
 3027 compared and the highest one is then used to define the peak settings.

### 3028    B.6.3 Data loop and histogram filling

3029 3D arrays of histogram are created to store the data and display it on the DQM of G4F++ webDCS  
 3030 for the use of shifters. These histograms, presented in section B.2.1.1, are filled while looping on  
 3031 the data. Before starting the analysis loop, it is necessary to control the entry quality for the new  
 3032 file formats featuring `QFlag`. If the `QFlag` value for this entry shows that 1 TDC or more have a  
 3033 `CORRUPTED` flag, then this event is discarded. The loss of statistics is low enough to be neglected.  
 3034 `QFlag` is controlled using the function `IsCorruptedEvent()` defined in `src/utils.cc`. As explained  
 3035 in Appendix A.4.3, each digit of this integer represents a TDC flag that can be 1 or 2. Each 2 is  
 3036 the sign of a `CORRUPTED` state. Then, the data is accessed entry by entry in the ROOT `TTree` using  
 3037 `RAWData` and each hit in the hit list is assigned to a detector channel and saved in the corresponding  
 3038 histograms. In the first part of the analysis, in which the loop over the ROOT file's content is  
 3039 performed, the different steps are:

3040 **1- RPC channel assignment and control:** a check is done on the RPC channel extracted thanks  
 3041 to the mapping via the method `Mapping::GetLink()`. If the channel is not initialised and is 0, or if  
 3042 the TDC channel was greater than 5127, the hit is discarded. This means there was a problem in the  
 3043 mapping. Often a mapping problem leads to the crash of the offline tool.

3044 **2- Creation of a `RPCHit` object:** to easily get the trolley, slot and partition in which the hit has  
 3045 been assigned, this object is particularly helpful.

3046 **3- General histograms are filled:** the hit is filled into the time distribution and the general hit  
 3047 distribution histograms, and if the arrival time is within the first 100 ns, it is discarded and nothing  
 3048 else happens and the loop proceeds with the next hit in the list.

3049 **4- Multiplicity counter:** the hit multiplicity counter of the corresponding detectors incremented.

3050 **5-a- Efficiency runs - Is the hit within the peak window? :** if the peak is contained in the peak  
 3051 window previously defined in section B.6.2, the hit is filled into the beam hit profile histogram of  
 3052 the corresponding chamber, added into the list of muon hits and increments the counter of *in time*  
 3053 hits. The term *in time* here refers to the hits that are likely to be muons by arriving in the expected  
 3054 time window. If the hit is outside of the peak window, it is filled into the noise profile histogram  
 3055 of the corresponding detector, added into the list of noise/gamma hits and increments the counter of  
 3056 noise/gamma hits.

3057 **5-b- Noise/gamma rate runs - Noise histograms are filled:** the hit is filled into the noise profile  
 3058 histogram of the corresponding detector, added into the list of noise/gamma hits and increments the  
 3059 counter of noise/gamma hits.

3060

After the loop on the hit list of the entry is over, the next step is to clusterize the 3D lists filled in the previous steps. A 3D loop is then started over the active trolley, slot and RPC partitions to access these objects. Each `NoiseHitList` and `MuonHitList`, in case of efficiency run, are clusterized as described in section B.5.2. There corresponding cluster size and multiplicity histograms are filled at the end of the clustering process. Then, the efficiency histogram is filled in case of efficiency run. The selection is simply made by checking whether the RPC detected signals in the peak window during this event. Nevertheless, it is useful to highlight that at this level, it is not possible yet to discriminate in between a muon hit and noise or gamma hit. Thus, `MuonCSize_H`, `MuonCMult_H` and `Efficiency0_H` are subjected to noise and gamma contamination. This contamination will be estimated and corrected at the moment the results will be written into output CSV files. Finally, the loop ends on the filling of the general hit multiplicity histogram.

#### B.6.4 Results calculation

As mentioned in section B.2.1, the analysis of DAQ data provides the user with 3 CSV files and a ROOT file associated to each and every ROOT data file. The fourth CSV file is provided by the extraction of the CEAN main frame data monitored during data taking and will be discussed later. After looping on the data in the previous part of the analysis macro, the output files are created and a 3D loop on each RPC readout partitions is started to extract the histograms parameters and compute the final results.

3079

##### B.6.4.1 Rate normalisation

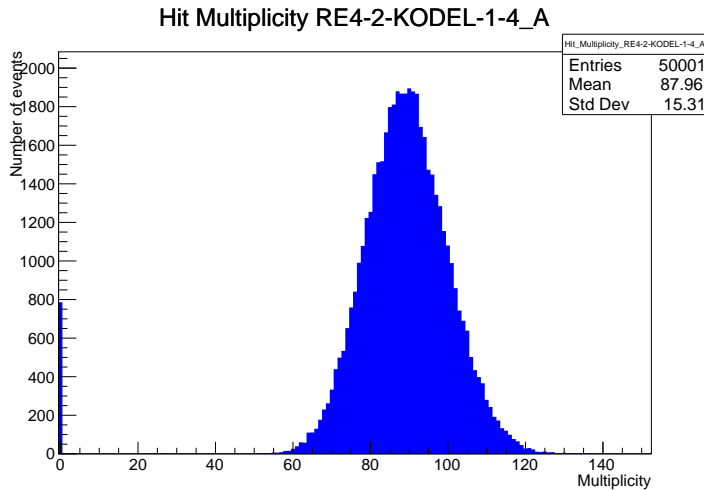


*Figure B.2: The effect of the quality flag is explained by presenting the reconstructed hit multiplicity of a data file without `Quality_flag`. The artificial high content of bin 0 is the effect of corrupted data.*

To analyse old data format files, not containing any quality flag, it is needed to estimate the amount of corrupted data via a fit as the corrupted data will always fill events with a fake "0 multiplicity". Indeed, as no hits were stored in the DAQ ROOT files, these events artificially contribute to fill the bin corresponding to a null multiplicity, as shown in Figure B.2. In the case the mean of the

3081

3082

3083

3084

3085 hit multiplicity distribution is high, the contribution of the corrupted data can easily be evaluated  
 3086 for later correction by comparing the level of the bin at multiplicity 0 and of a skew fit curve that  
 3087 should indicate a value consistent with 0. A skew fit has been chosen over a Poisson fit as it was  
 3088 giving better results for lower mean multiplicity values. Nevertheless, for low irradiation cases,  
 3089 as explained in Appendix A.4.3, the hit multiplicity distribution mean is, on the contrary, rather  
 3090 small and the probability to record events without hits can't be considered small anymore, leading  
 3091 to a difficult and non-reliable estimation of the corruption. As can be seen in Source Code B.13,  
 3092 conditions have been applied to prevent bad fits and wrong corruption estimation in cases where :

3093 • The difference in between the data for multiplicity 1 and the corresponding fit value should be  
 3094 lower than 1% of the total amount of data :  $\frac{|n_{m=1} - sk(1)|}{N_{tot}} < 0.01$  where  $n_{m=1}$  is the number  
 3095 of entries with multiplicity 1,  $sk(1)$  the value of the skew fit, as defined by Formula 5.3, for  
 3096 multiplicity 1 and  $N_{tot}$  the total number of entries.

3097 • The amount of data contained in the multiplicity 0 bin should not exceed 40% :  $\frac{n_{m=0}}{N_{tot}} \leq 0.4$   
 3098 where  $n_{m=0}$  is the number of entries with multiplicity 0. This number has been determined  
 3099 to be the maximum to be able to separate the excess of data due to corruption from the hit  
 3100 multiplicity distribution.

3101 Those 2 conditions need to be fulfilled to estimate the corruption of old data format files. If the  
 3102 fit was successful, the level of corruption is written in `Offline-Corrupted.csv` and the number of  
 3103 corrupted entries, refered as the integer `nEmptyEvent`, is subtracted from the total number of entries  
 3104 when the rate normalisation factor is computed as explicit in Source Code B.13. Note that for new  
 3105 data format files, the number of corrupted entries being set to 0, the definition of `rate_norm` stays  
 3106 valid.

```

3107
if(!isNewFormat){
    TF1* GaussFit = new TF1("gaussfit","[0]*exp(-0.5*((x-[1])/[2])**2)",0,Xmax);
    GaussFit->SetParameter(0,100);
    GaussFit->SetParameter(1,10);
    GaussFit->SetParameter(2,1);
    HitMultiplicity_H.rpc[T][S][p]->Fit(GaussFit,"LIQR","",0.5,Xmax);

    TF1* SkewFit = new TF1("skewfit","[0]*exp(-0.5*((x-[1])/[2])**2) / (1 +
→ exp(-[3]*(x-[4])))",0,Xmax);
    SkewFit->SetParameter(0,GaussFit->GetParameter(0));
    SkewFit->SetParameter(1,GaussFit->GetParameter(1));
    SkewFit->SetParameter(2,GaussFit->GetParameter(2));
    SkewFit->SetParameter(3,1);
    SkewFit->SetParameter(4,1);
    HitMultiplicity_H.rpc[T][S][p]->Fit(SkewFit,"LIQR","",0.5,Xmax);

    double fitValue = SkewFit->Eval(1,0,0,0);
    double dataValue = (double)HitMultiplicity_H.rpc[T][S][p]->GetBinContent(2);
    double difference = TMath::Abs(dataValue - fitValue);
    double fitTOdataVSentries_ratio = difference / (double)nEntries;
    bool isFitGOOD = fitTOdataVSentries_ratio < 0.01;

3108
    double nSinglehit = (double)HitMultiplicity_H.rpc[T][S][p]->GetBinContent(1);
    double lowMultRatio = nSinglehit / (double)nEntries;
    bool isMultLOW = lowMultRatio > 0.4;

    if(isFitGOOD && !isMultLOW){
        nEmptyEvent = HitMultiplicity_H.rpc[T][S][p]->GetBinContent(1);
        nPhysics = (int)SkewFit->Eval(0,0,0,0);
        if(nPhysics < nEmptyEvent)
            nEmptyEvent = nEmptyEvent-nPhysics;
    }
}

double corrupt_ratio = 100.*(double)nEmptyEvent / (double)nEntries;
outputCorrCSV << corrupt_ratio << '\t';

float rate_norm = 0.;
float stripArea = GIFIInfra->GetStripGeo(tr,sl,p);

if(IsEfficiencyRun(RunType)){
    float noiseWindow = BMTDCWINDOW - TIMEREJECT - 2*PeakWidth.rpc[T][S][p];
    rate_norm = (nEntries-nEmptyEvent)*noiseWindow*1e-9*stripArea;
} else
    rate_norm = (nEntries-nEmptyEvent)*RDMNOISEWDW*1e-9*stripArea;

```

*Source Code B.13: Definition of the rate normalisation variable. It takes into account the number of non corrupted entries and the time window used for noise calculation, to estimate the total integrated time, and the strip active area to express the result as rate per unit area.*

#### 3110 B.6.4.2 Rate and activity

3111 At this point, the strip rate histograms, StripNoiseProfile\_H.rpc[T][S][p], only contain an in-
3112 formation about the total number of noise or rate hits each channel received during the data taking.
3113 As described in Source Code B.14, a loop on the strip channels will be used to normalise the content
3114 of the rate distribution histogram for each detector partitions. The initial number of hits recorded for
3115 a given bin will be extracted and 2 values will be computed:

- 3116     ● the strip rate, defined as the number of hits recorded in the bin normalised like described in  
 3117               the previous section, using the variable `rate_norm`, and

- 3118     ● the strip activity, defined as the number of hits recorded in the bin normalised to the average  
 3119               number of hits per bin contained in the partition histogram, using the variable `averageNhit`.  
 3120               This value provides an information on the homogeneity of the detector response to the gamma  
 3121               background or of the detector noise. An activity of 1 corresponds to an average response.  
 3122               Above 1, the channel is more active than the average and bellow 1, the channel is less active.

```

int nNoise = StripNoiseProfile_H.rpc[T][S][p]->GetEntries();
float averageNhit = (nNoise>0) ? (float)(nNoise/nStripsPart) : 1.;

for(Uint st = 1; st <= nStripsPart; st++){
    float stripRate =
        StripNoiseProfile_H.rpc[T][S][p]->GetBinContent(st)/rate_norm;
    float stripAct =
        StripNoiseProfile_H.rpc[T][S][p]->GetBinContent(st)/averageNhit;

    StripNoiseProfile_H.rpc[T][S][p]->SetBinContent(st,stripRate);
    StripActivity_H.rpc[T][S][p]->SetBinContent(st,stripAct);
}

```

3124     *Source Code B.14: Description of the loop that allows to set the content of each strip rate and strip activity  
 channel for each detector partition.*

3125     On each detector partitions, which are readout by a single FEE, all the channels are not processed  
 3126       by the same chip. Each chip can give a different noise response and thus, histograms using a chip  
 3127       binning are used to investigate chip related noise behaviours. The average values of the strip rate  
 3128       or activity grouped into a given chip are extracted using the using the function `GetChipBin()` and  
 3129       stored in dedicated histograms as described in Source Codes B.15 and B.16 respectively.

```

float GetChipBin(TH1* H, Uint chip){
    Uint start = 1 + chip*NSTRIPSCHIP;
    int nActive = NSTRIPSCHIP;
    float mean = 0.;

    for(Uint b = start; b <= (chip+1)*NSTRIPSCHIP; b++){
        float value = H->GetBinContent(b);
        mean += value;
        if(value == 0.) nActive--;
    }

    if(nActive != 0) mean /= (float)nActive;
    else mean = 0.;

    return mean;
}

```

3132     *Source Code B.15: Function used to compute the content of a bin for an histogram using chip binning.*

```

3133     for(UInt ch = 0; ch < (nStripsPart/NSTRIPSCHIP); ch++) {
3134         ChipMeanNoiseProf_H.rpc[T][S][p]->
3135             SetBinContent(ch+1,GetChipBin(StripNoiseProfile_H.rpc[T][S][p],ch));
3136         ChipActivity_H.rpc[T][S][p]->
3137             SetBinContent(ch+1,GetChipBin(StripActivity_H.rpc[T][S][p],ch));
3138     }

```

*Source Code B.16: Description of the loop that allows to set the content of each chip rate and chip activity bins for each detector partition knowing the information contained in the corresponding strip distribution histograms.*

The activity variable is used to evaluate the homogeneity of the detector response to background or of the detector noise. The homogeneity  $h_p$  of each detector partition can be evaluated using the formula  $h_p = \exp(-\sigma_p^R / \langle R \rangle_p)$ , where  $\langle R \rangle_p$  is the partition mean rate and  $\sigma_p^R$  is the rate standard deviation calculated over the partition channels. The more homogeneously the rates are distributed and the smaller will  $\sigma_p^R$  be, and the closer to 1 will  $h_p$  get. On the contrary, if the standard deviation of the channel's rates is large,  $h_p$  will rapidly get to 0. This value is saved into histograms as shown in Source Code B.17 and could in the future be used to monitor through time, once extracted, the evolution of every partition homogeneity. This could be of great help to understand the apparition of eventual hot spots due to ageing of the chambers subjected to high radiation levels. The monitored homogeneity information could then be combined with a monitoring of the activity of each individual channel in order to have a finer information. Monitoring tools have been suggested and need to be developed for this purpose.

```

3147     float MeanPartSDev = GetTH1StdDev(StripNoiseProfile_H.rpc[T][S][p]);
3148     float strip_homog = (MeanPartRate==0)
3149         ? 0.
3150         : exp(-MeanPartSDev/MeanPartRate);
3151     StripHomogeneity_H.rpc[T][S][p]->Fill("exp -#left(#frac{\#sigma_{Strip}
3152         \rightarrow Rate}{\#mu_{Strip Rate}}\#right)",strip_homog);
3153     StripHomogeneity_H.rpc[T][S][p]->GetYaxis()->SetRangeUser(0.,1.);

3154     float ChipStDevMean = GetTH1StdDev(ChipMeanNoiseProf_H.rpc[T][S][p]);
3155     float chip_homog = (MeanPartRate==0)
3156         ? 0.
3157         : exp(-ChipStDevMean/MeanPartRate);
3158     ChipHomogeneity_H.rpc[T][S][p]->Fill("exp -#left(#frac{\#sigma_{Chip}
3159         \rightarrow Rate}{\#mu_{Chip Rate}}\#right)",chip_homog);
3160     ChipHomogeneity_H.rpc[T][S][p]->GetYaxis()->SetRangeUser(0.,1.);

3161 
```

*Source Code B.17: Storage of the homogeneity into dedicated histograms.*

### B.6.4.3 Strip masking tool

The offline tool is automatically called at the end of each data taking to analyse the data and offer the shifter DQM histograms to control the data quality. After the histograms have been published online in the DQM page, the shifter can decide to mask noisy or dead channels that will contribute to bias the final rate calculation by editing the mask column of `ChannelsMapping.csv` as can be seen in Figure B.3.

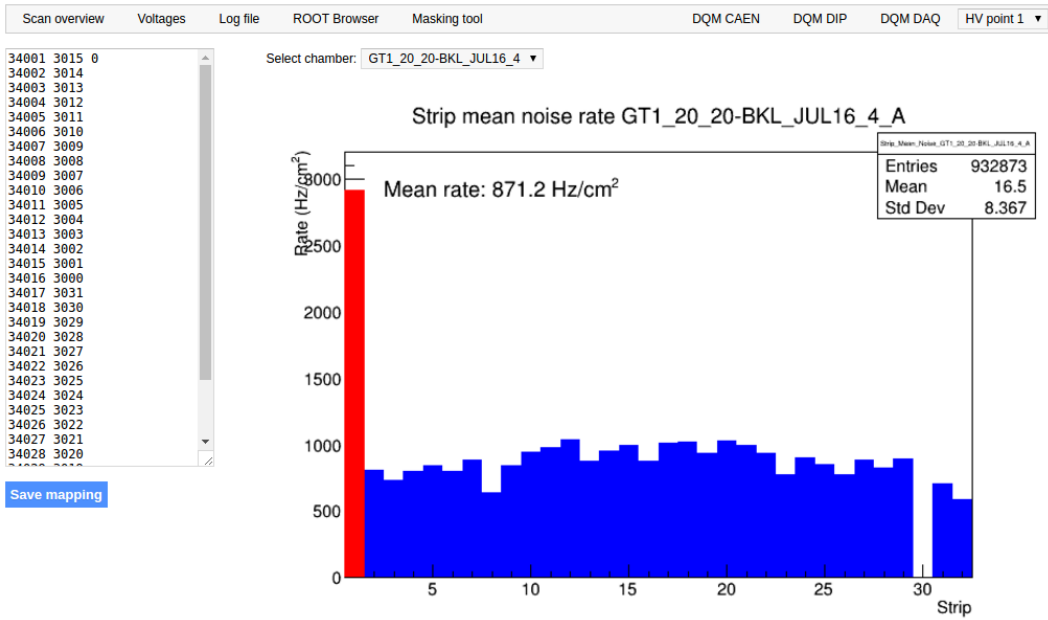


*Figure B.3: Display of the masking tool page on the webDCS. The window on the left allows the shifter to edit ChannelsMapping.csv. To mask a channel, it only is needed to set the 3rd field corresponding to the strip to mask to 0. It is not necessary for older mapping file formats to add a 1 for each strip that is not masked as the code is versatile and the default behaviour is to consider missing mask fields as active strips. The effect of the mask is directly visible for noisy channels as the corresponding bin turns red. The global effect of masking strips will be an update of the rate value showed on the histogram that will take into consideration the rejected channels.*

3156        From the code point of view, the function `GetTH1Mean()` is used to retrieve the mean rate par-  
 3157        tition by partition after the rates have been calculated strip by strip and filled into the histograms  
 3158        `StripNoiseProfile_H.rpc[T][S][p]`, as described through Source Code B.18.

3159        Once the mask for each rejected channel has been updated, the shifter can manually run the of-  
 3160        fline tool again to update the DQM plots, now including the masked strips, as well the rate results  
 3161        written in the output CSV file `Offline-Rate.csv`. If not done during the shifts, the strip masking  
 3162        procedure needs to be carefully done by the person in charge of data analysis on the scans that were  
 3163        selected to produce the final results.

```

3164
float GetTH1Mean(TH1* H) {
    int nBins = H->GetNbinsX();
    int nActive = nBins;
    float mean = 0.;

    for(int b = 1; b <= nBins; b++) {
        float value = H->GetBinContent(b);
        mean += value;
        if(value == 0.) nActive--;
    }

    if(nActive != 0) mean /= (float)nActive;
    else mean = 0.;

    return mean;
}

```

*Source Code B.18: The function `GetTH1Mean()` is used to return the mean along the y-axis of TH1 histograms containing rate information. In order to take into account masked strips whose rate is set to 0, the function looks for masked channels and decrement the number of active channels for each null value found.*

#### 3167 B.6.4.4 Output CSV files filling

3168 All the histograms have been filled. Parameters will then be extracted from them to compute the  
 3169 final results that will later be used to produce plots. Once the results have been computed, the very  
 3170 last step of the offline macro is to write these values into the corresponding CSV outputs. Aside of  
 3171 the file `Offline-Corrupted.csv`, 2 CSV files are being written by the macro `offlineAnalysis()`,  
 3172 `Offline-Rates.csv` and `Offline-L0-EffCl.csv` that respectively contain information about noise  
 3173 or gamma rates, cluster size and multiplicity, and about level 0 reconstruction of the detector effi-  
 3174 ciency, muon cluster size and multiplicity. Details on the computation and file writing are respec-  
 3175 tively given in Sources Codes B.19 and B.20.

3176 **Noise/gamma background variables** are computed and written in the output file for each detector  
 3177 partitions. A detector average of the hit and cluster rate is also provided, as shown through Sources  
 3178 Code B.19. The variables that are written for each partition are:

- 3179 • The mean partition hit rate per unit area, `MeanPartRate`, that is extracted from the histogram  
   3180   `StripNoiseProfile_H` as the mean value along the y-axis, as described in section B.6.4.3. No  
   3181   error is recorded for the hit rate as this is considered a single measurement. No statistical error  
   3182   can be associated to it and the systematics are unknown.
- 3183 • The mean cluster size, `cSizePart`, is extracted from the histogram `NoiseCSize_H` and it's  
   3184   statistical error, `cSizePartErr`, is taken to be  $2\sigma$  of the total distribution.
- 3185 • The mean cluster multiplicity per trigger, `cMultPart`, is extracted from the histogram `NoiseCMult_H`  
   3186   and it's statistical error, `cMultPartErr`, is taken to be  $2\sigma$  of the total distribution. It is impor-  
   3187   tant to point to the fact that this variable gives an information that is dependent on the buffer  
   3188   window width used for each trigger for the calculation.
- 3189 • The mean cluster rate per unit area, `ClustPartRate`, is defined as the mean hit rate normalised

3190 to the mean cluster size and it's statistical error, `ClustPartRateErr`, is then obtained using the  
 3191 relative statistical error on the mean cluster size.

```

for (UInt tr = 0; tr < GIFInfra->GetNTrolleys(); tr++) {
  UInt T = GIFInfra->GetTrolleyID(tr);

  for (UInt sl = 0; sl < GIFInfra->GetNSlots(tr); sl++) {
    UInt S = GIFInfra->GetSlotID(tr,sl) - 1;

    float MeanNoiseRate = 0.;
    float ClusterRate = 0.;
    float ClusterSDev = 0.;

    for (UInt p = 0; p < GIFInfra->GetNPartitions(tr,sl); p++) {
      float MeanPartRate = GetTH1Mean(StripNoiseProfile_H.rpc[T][S][p]);
      float cSizePart = NoiseCSIZE_H.rpc[T][S][p]->GetMean();
      float cSizePartErr = (NoiseCSIZE_H.rpc[T][S][p]->GetEntries()==0)
        ? 0.
        : 2*NoiseCSIZE_H.rpc[T][S][p]->GetStdDev() /
          sqrt(NoiseCSIZE_H.rpc[T][S][p]->GetEntries());
      float cMultPart = NoiseCMult_H.rpc[T][S][p]->GetMean();
      float cMultPartErr = (NoiseCMult_H.rpc[T][S][p]->GetEntries()==0)
        ? 0.
        : 2*NoiseCMult_H.rpc[T][S][p]->GetStdDev() /
          sqrt(NoiseCMult_H.rpc[T][S][p]->GetEntries());
      float ClustPartRate = (cSizePart==0) ? 0.
        : MeanPartRate/cSizePart;
      float ClustPartRateErr = (cSizePart==0) ? 0.
        : ClustPartRate * cSizePartErr/cSizePart;

      outputRateCSV << MeanPartRate << '\t'
        << cSizePart << '\t' << cSizePartErr << '\t'
        << cMultPart << '\t' << cMultPartErr << '\t'
        << ClustPartRate << '\t' << ClustPartRateErr << '\t';

      RPCarea += stripArea * nStripsPart;
      MeanNoiseRate += MeanPartRate * stripArea * nStripsPart;
      ClusterRate += ClustPartRate * stripArea * nStripsPart;
      ClusterSDev += (cSizePart==0)
        ? 0.
        : ClusterRate*cSizePartErr/cSizePart;
    }

    MeanNoiseRate /= RPCarea;
    ClusterRate /= RPCarea;
    ClusterSDev /= RPCarea;

    outputRateCSV << MeanNoiseRate << '\t'
      << ClusterRate << '\t' << ClusterSDev << '\t';
  }
}

```

Source Code B.19: Description of rate result calculation and writing into the CSV output `Offline-Rate.csv`. Are saved into the file for each detector, the mean partition rate, cluster size and cluster mutiplicity, along with their errors, for each partition and as well as a detector average.

3194 **Muon performance variables** are computed and written in the output file for each detector parti-  
 3195 tions as shown through Sources Code B.20. The variables that are written for each partition are:

- 3196     ● The muon efficiency, `eff`, extracted from the histogram `Efficiency0_H`. It is reminded that  
3197       this offline tool doesn't include any tracking algorithm to identify muons from the beam and  
3198       only relies on the hits arriving in the time window corresponding to the beam time. The con-  
3199       tent of the efficiency histogram is thus biased by the noise/gamma background contribution  
3200       into this window and is thus corrected by estimating the muon data content in the peak re-  
3201       gion knowing the noise/gamma content in the rate calculation region. Both time windows  
3202       being different, the choice was made to normalise the noise/gamma background calculation  
3203       window to it's equivalent beam window in order to have comparable values using the variable  
3204       `windowRatio`. Finally, to estimate the data ratio in the peak region, the variable `DataRatio`  
3205       is defined as the ratio in between the estimated mean cluster multiplicity of the muons in the  
3206       peak region, `MuonCM`, and of the total mean cluster multiplicity in the peak region, `PeakCM`.  
3207       `MuonCM` is itself defined as the difference in between the total mean cluster multiplicity in the  
3208       peak region and the normalised mean noise/gamma cluster multiplicity calculated outside of  
3209       the peak region. The statistical error related to the efficiency, `eff_err`, is computed using a  
3210       binomial distribution, as the efficiency measure the probability of "success" and "failure" to  
3211       detect muons.
- 3212     ● The mean muon cluster size, `MuonCS`, is calculated using the total mean cluster size and multi-  
3213       plicity in the peak region, respectively extracted from histograms `MuonCSize_H` and `MuonCMult_H`,  
3214       the noise/gamma background mean cluster size and normalised multiplicity, extracted from  
3215       `NoiseCSize_H` and `NoiseCMult_H`, and of the estimated muon cluster multiplicity `MuonCM` pre-  
3216       viously explicated. The associated statistical error, `MuonCM_err`, is calculated using the propa-  
3217       gation of errors of the mentioned variables.
- 3218     ● The mean muon cluster multiplicity in the peak region, `MuonCM`, explicated above whose sta-  
3219       tistical error, `MuonCM_err`, is the sum of statistical error associated to the total mean clus-  
3220       ter multiplicity in the peak reagion, `PeakCM_err`, and of the mean noise/gamma cluster size,  
3221       `NoiseCM_err`.

3222       In addition to these 2 CSV files, the histograms are saved in ROOT file `Scan00XXXX_HVY_Offline.root`  
3223       as explained in section B.2.1.1.

3224

```

for (UInt tr = 0; tr < GIFInfra->GetNTrolleys(); tr++) {
    UInt T = GIFInfra->GetTrolleyID(tr);
    for (UInt sl = 0; sl < GIFInfra->GetNSlots(tr); sl++) {
        UInt S = GIFInfra->GetSlotID(tr,sl) - 1;
        for (UInt p = 0; p < GIFInfra->GetNPartitions(tr,sl); p++) {
            float noiseWindow =
                BMTDCWINDOW - TIMEREJECT - 2*PeakWidth.rpc[T][S][p];
            float peakWindow = 2*PeakWidth.rpc[T][S][p];
            float windowRatio = peakWindow/noiseWindow;

            float PeakCM = MuonCMult_H.rpc[T][S][p]->GetMean();
            float PeakCS = MuonCSize_H.rpc[T][S][p]->GetMean();
            float NoiseCM = NoiseCMult_H.rpc[T][S][p]->GetMean() *windowRatio;
            float NoiseCS = NoiseCSize_H.rpc[T][S][p]->GetMean();
            float MuonCM = (PeakCM<NoiseCM) ? 0. : PeakCM-NoiseCM;
            float MuonCS = (MuonCM==0 || PeakCM*PeakCS<NoiseCM*NoiseCS)
                ? 0.
                : (PeakCM*PeakCS-NoiseCM*NoiseCS) / MuonCM;
            float PeakCM_err = (MuonCMult_H.rpc[T][S][p]->GetEntries()==0.)
                ? 0.
                : 2*MuonCMult_H.rpc[T][S][p]->GetStdDev() /
                    sqrt(MuonCMult_H.rpc[T][S][p]->GetEntries());
            float PeakCS_err = (MuonCSize_H.rpc[T][S][p]->GetEntries()==0.)
                ? 0.
                : 2*MuonCSize_H.rpc[T][S][p]->GetStdDev() /
                    sqrt(MuonCSize_H.rpc[T][S][p]->GetEntries());
            float NoiseCM_err = (NoiseCMult_H.rpc[T][S][p]->GetEntries()==0.)
                ? 0.
                : windowRatio*2*NoiseCMult_H.rpc[T][S][p]->GetStdDev() /
                    sqrt(NoiseCMult_H.rpc[T][S][p]->GetEntries());
            float NoiseCS_err = (NoiseCSize_H.rpc[T][S][p]->GetEntries()==0.)
                ? 0.
                : 2*NoiseCSize_H.rpc[T][S][p]->GetStdDev() /
                    sqrt(NoiseCSize_H.rpc[T][S][p]->GetEntries());
            float MuonCM_err = (MuonCM==0) ? 0. : PeakCM_err+NoiseCM_err;
            float MuonCS_err = (MuonCS==0 || MuonCM==0) ? 0.
                : (PeakCS*PeakCM_err + PeakCM*PeakCS_err +
                    NoiseCS*NoiseCM_err + NoiseCM*NoiseCS_err +
                    MuonCS*MuonCM_err) / MuonCM;

            float DataRatio = MuonCM/PeakCM;
            float DataRatio_err = (MuonCM==0) ? 0.
                : DataRatio*(MuonCM_err/MuonCM + PeakCM_err/PeakCM);
            float eff = DataRatio*Efficiency0_H.rpc[T][S][p]->GetMean();
            float eff_err = DataRatio*2*Efficiency0_H.rpc[T][S][p]->GetStdDev() /
                sqrt(Efficiency0_H.rpc[T][S][p]->GetEntries()) +
                Efficiency0_H.rpc[T][S][p]->GetMean()*DataRatio_err;

            outputEffCSV << eff << '\t' << eff_err << '\t'
                << MuonCS << '\t' << MuonCS_err << '\t'
                << MuonCM << '\t' << MuonCM_err << '\t';
        }
    }
}

```

3225

*Source Code B.20: Description of efficiency result calculation and writing into the CSV output Offline-L0-EffCl.csv. Are saved into the file for each detector, the efficiency, corrected taking into account the background in the peak window of the time profile, muon cluster size and muon cluster multiplicity, along with their errors, for each partition and as well as a detector average.*

3226

## 3227 B.7 Current data Analysis

3228 Detectors under test at GIF++ are connected both to a CAEN HV power supply and to a CAEN  
3229 ADC that reads the currents inside of the RPC gaps bypassing the supply cable. During data tak-  
3230 ing, the webDCS records into a ROOT file called `Scan00XXXX_HVY_CAEN.root` histograms with the  
3231 monitored parameters of both CAEN devices. Are recorded for each RPC channels (in most cases,  
3232 a channel corresponds to an RPC gap):

- 3233 • the effective voltage,  $HV_{eff}$ , set by the webDCS using the PT correction on the CAEN power  
3234 supply,
- 3235 • the applied voltage,  $HV_{app}$ , monitored by the CAEN power supply, and the statistical error  
3236 related to the variations of this value through time to follow the variation of the environmental  
3237 parameters defined as the RMS of the histogram divided by the square root of the number of  
3238 recorded points,
- 3239 • the monitored current,  $I_{mon}$ , monitored by the CAEN power supply, and the statistical error  
3240 related to the variations of this value through time to follow the variation of the environmental  
3241 parameters defined as the RMS of the histogram divided by the square root of the number of  
3242 recorded points,
- 3243 • the corresponding current density,  $J_{mon}$ , defined as the monitored current per unit area,  
3244  $J_{mon} = I_{mon}/A$ , where  $A$  is the active area of the corresponding gap,
- 3245 • the ADC current,  $I_{ADC}$ , recorded through the CAEN ADC module that monitors the dark  
3246 current in the gap itself. First of all, the resolution of such a module is better than that of  
3247 CAEN power supplies and moreover, the current is not read-out through the HV supply line  
3248 but directly at the chamber level giving the real current inside of the detector. The statistical  
3249 error is defined as the RMS of the histogram distribution divided by the square root of the  
3250 number of recorded points.

3251 Once extracted through a loop over the element of GIF++ infrastructure via the C++ macro  
3252 `GetCurrent()`, these parameters, organised in 9 columns per detector HV supply line, are written in  
3253 the output CSV file `Offline-Current.csv`. The macro can be found in the file `Current.cc`.

## References

3254

- 3255 [1] T. Massam et al. “Experimental observation of antideuteron production”. In: *Il Nuovo Cimento A* 63 (1965), pp. 10–14.
- 3256
- 3257 [2] UA1 Collaboration. “Experimental observation of isolated large transverse energy electrons with associated missing energy at  $s = 540 \text{ GeV}$ ”. In: *Physics Letters B* 122 (1983), pp. 103–116.
- 3258
- 3259
- 3260 [3] UA2 Collaboration. “Observation of single isolated electrons of high transverse momentum in events with missing transverse energy at the CERN pp collider”. In: *Physics Letters B* 122 (1983), pp. 476–485.
- 3261
- 3262
- 3263 [4] UA1 Collaboration. “Experimental observation of lepton pairs of invariant mass around  $95 \text{ GeV}/c^2$  at the CERN SPS collider”. In: *Physics Letters B* 126 (1983), pp. 398–410.
- 3264
- 3265 [5] UA2 Collaboration. “Evidence for  $Z_0 \rightarrow e^+e^-$  at the CERN pp collider”. In: *Physics Letters B* 129 (1983), pp. 130–140.
- 3266
- 3267 [6] ALEPH Collaboration. “Determination of the number of light neutrino species”. In: *Physics Letters B* 231 (1989), pp. 519–529.
- 3268
- 3269 [7] CERN, ed. (1985).
- 3270 [8] CERN, ed. (1986).
- 3271 [9] CERN, ed. (1994).
- 3272 [10] CERN, ed. (1998).
- 3273 [11] CERN, ed. (1999).
- 3274 [12] CERN. Geneva. LHC Experiments Committee. *Letter of Intent for A Large Ion Collider Experiment [ALICE]*, note = CERN-LHCC-93-016. Tech. rep. ALICE Collaboration, 1993.
- 3275
- 3276 [13] CERN. Geneva. LHC Experiments Committee. *ATLAS : technical proposal for a general-purpose pp experiment at the Large Hadron Collider at CERN*, note = CERN-LHCC-94-43. Tech. rep. ATLAS Collaboration, 1994.
- 3277
- 3278
- 3279 [14] CERN. Geneva. LHC Experiments Committee. *CMS : letter of intent by the CMS Collaboration for a general purpose detector at LHC*, note = CERN-LHCC-92-003. Tech. rep. CMS Collaboration, 1992.
- 3280
- 3281
- 3282 [15] CERN. Geneva. LHC Experiments Committee. *LHCb : letter of intent*. Tech. rep. CERN-LHCC-95-5. LHCb Collaboration, 1995.
- 3283
- 3284 [16] L. Evans and P. Bryant. “LHC Machine”. In: *JINST* 3 (2008). S08001.
- 3285
- 3286 [17] CMS Collaboration ATLAS Collaboration. “Combined Measurement of the Higgs Boson Mass in  $pp$  Collisions at  $\sqrt{s} = 7$  and  $8 \text{ TeV}$  with the ATLAS and CMS Experiments”. In: *Physical Review Letters* 114 (2015). 191803.
- 3287
- 3288 [18] LHCb Collaboration. “Observation of  $J/\psi p$  Resonances Consistent with Pentaquark States in  $\Lambda_b^0 \rightarrow J/\psi K^- p$  Decays”. In: *Physical Review Letters* 115 (2015). 072001.
- 3289

- 3290 [19] LHCb Collaboration. “Observation of  $J/\psi\phi$  Structures Consistent with Exotic States from  
3291 Amplitude Analysis of  $B^+ \rightarrow J/\psi\phi K^+$  Decays”. In: *Physical Review Letters* 118 (2017).  
3292 022003.
- 3293 [20] CERN. Geneva. *High-Luminosity Large Hadron Collider (HL-LHC) Technical Design Re-*  
3294 *port V. 0.1*. Tech. rep. CERN-2017-007-M. 2017.
- 3295 [21] CERN. Geneva. LHC Experiments Committee. *The CMS muon project : Technical Design*  
3296 *Report*. Tech. rep. CERN-LHCC-97-032. CMS Collaboration, 1997.
- 3297 [22] CERN. Geneva. LHC Experiments Committee. *CMS, the Compact Muon Solenoid : technical*  
3298 *proposal*. Tech. rep. CERN-2015-005. 2015.
- 3299 [23] CERN. Geneva. LHC Experiments Committee. *The Phase-2 Upgrade of the CMS Muon*  
3300 *Detectors*. Tech. rep. CERN-LHCC-2017-012, CMS-TDR-016. CMS Collaboration, 2017.
- 3301 [24] CERN. Geneva. LHC Experiments Committee. *High-Luminosity Large Hadron Collider*  
3302 *(HL-LHC) Preliminary Design Report*. Tech. rep. CERN-LHCC-94-38. CMS Collaboration,  
3303 1994.
- 3304 [25] CERN. Geneva. LHC Experiments Committee. *The Phase-2 Upgrade of the CMS Level-1*  
3305 *Trigger - Interim Report to the LHCC*. Tech. rep. CERN-LHCC-2017-013, CMS-TDR-017.  
3306 CMS Collaboration, 2017.
- 3307 [26] CERN. Geneva. LHC Experiments Committee. *Technical Proposal for the Phase-II Upgrade*  
3308 *of the CMS Detector*. Tech. rep. CERN-LHCC-2015-010, CMS-TDR-15-02. CMS Collabo-  
3309 ration, 2015.
- 3310 [27] A. Gelmi. *CMS iRPC at HL-LHC: background study*. 2018. URL: [https://indico.cern.ch/event/732794/contributions/3021836/attachments/1657792/2654574/iRPC\\_bkg\\_study\\_Upgrade29\\_05\\_18.pdf](https://indico.cern.ch/event/732794/contributions/3021836/attachments/1657792/2654574/iRPC_bkg_study_Upgrade29_05_18.pdf).
- 3313 [28] F.Sauli. “GEM: A new concept for electron amplification in gas detectors”. In: *Nucl. Instr.*  
3314 *Meth. Phys. Res.* 386 (1997), pp. 531–534.
- 3315 [29] CERN. Geneva. LHC Experiments Committee. *CMS Technical Design Report for the Muon*  
3316 *Endcap GEM Upgrade*. Tech. rep. CERN-LHCC-2015-012, CMS-TDR-013. CMS Collabo-  
3317 ration, 2015.
- 3318 [30] R. Santonico and R. Cardarelli. “Development of resistive plate counters”. In: *Nucl. Instr.*  
3319 *Meth. Phys. Res.* 187 (1981), pp. 377–380.
- 3320 [31] Yu.N. Pestov and G.V. Fedotovich. *A picosecond time-of-flight spectrometer fot eh VEPP-2M*  
3321 *based on local-discharge spark counter*. Tech. rep. SLAC-TRANS-0184. SLAC, 1978.
- 3322 [32] W.W. Ash, ed. *Spark Counter With A Localized Discharge*. Vol. SLAC-R-250. 1982, pp. 127–  
3323 131.
- 3324 [33] I. Crotty et al. “The non-spark mode and high rate operation of resistive parallel plate cham-  
3325 bers”. In: *NIMA* 337 (1993), pp. 370–381.
- 3326 [34] I. Crotty et al. “Further studies of avalanche mode operation of resistive parallel plate cham-  
3327 bers”. In: *NIMA* 346 (1994), pp. 107–113.
- 3328 [35] R. Cardarelli et al. “Avalanche and streamer mode operation of resistive plate chambers”. In:  
3329 *NIMA* 382 (1996), pp. 470–474.
- 3330 [36] E. Cerron Zeballos et al. “A new type of resistive plate chamber: The multigap RPC”. In:  
3331 *NIMA* 374 (1996), pp. 132–135.
- 3332 [37] M.C.S. Williams. “The development of the multigap resistive plate chamber”. In: *Nucl. Phys.*  
3333 *B* 61 (1998), pp. 250–257.

## BIBLIOGRAPHY

---

- 3334 [38] H. Czyrkowski et al. “New developments on resistive plate chambers for high rate operation”.  
3335 In: *NIMA* 419 (1998), pp. 490–496.
- 3336 [39] P. Camarri et al. “Streamer suppression with SF<sub>6</sub> in RPCs operated in avalanche mode”. In: *NIMA* 414 (1998), pp. 317–324.
- 3338 [40] E. Cerron Zeballos et al. “Effect of adding SF<sub>6</sub> to the gas mixture in a multigap resistive plate  
3339 chamber”. In: *NIMA* 419 (1998), pp. 475–478.
- 3340 [41] CERN. Geneva. LHC Experiments Committee. *ATLAS muon spectrometer: Technical design  
3341 report*. Tech. rep. CERN-LHCC-97-22. ATLAS Collaboration, 1997.
- 3342 [42] CERN. Geneva. LHC Experiments Committee. *ALICE Time-Of-Flight system (TOF) : Tech-  
3343 nical Design Report*. Tech. rep. CERN-LHCC-2000-012. ALICE Collaboration, 2000.
- 3344 [43] The CALICE collaboration. “First results of the CALICE SDHCAL technological proto-  
3345 type”. In: *JINST* 11 (2016).
- 3346 [44] PoS, ed. *Density Imaging of Volcanoes with Atmospheric Muons using GRPCs*. International  
3347 Europhysics Conference on High Energy Physics - HEP 2011. 2011.
- 3348 [45] C. Lippmann. “Detector Physics of Resistive Plate Chambers”. PhD thesis. Johann Wolfgang  
3349 Goethe-Universität, 2003.
- 3350 [46] M. Abbrescia et al. “Properties of C<sub>2</sub>H<sub>2</sub>F<sub>4</sub>-based gas mixture for avalanche mode operation  
3351 of resistive plate chambers”. In: *NIMA* 398 (1997), pp. 173–179.
- 3352 [47] G. Battistoni et al. “Sensitivity of streamer mode to single ionization electrons”. In: *NIMA*  
3353 235 (1985), pp. 91–97.
- 3354 [48] W. Riegler. “Induced signals in resistive plate chambers”. In: *NIMA* 491 (2002), pp. 258–271.
- 3355 [49] E. Cerron Zeballos et al. “A comparison of the wide gap and narrow gap resistive plate  
3356 chamber”. In: *NIMA* 373 (1996), pp. 35–42.
- 3357 [50] M. Abbrescia et al. “Cosmic ray tests of double-gap resistive plate chambers for the CMS  
3358 experiment”. In: *NIMA* 550 (2005), pp. 116–126.
- 3359 [51] ALICE Collaboration. “A study of the multigap RPC at the gamma irradiation facility at  
3360 CERN”. In: *NIMA* 490 (2002), pp. 58–70.
- 3361 [52] B. Bonner et al. “A multigap resistive plate chamber prototype for time-of-flight for the STAR  
3362 experiment at RHIC”. In: *NIMA* 478 (2002), pp. 176–179.
- 3363 [53] S. Yang et al. “Test of high time resolution MRPC with different readout modes for the  
3364 BESIII upgrade”. In: *NIMA* 763 (2014), pp. 190–196.
- 3365 [54] A. Akindinov et al. “RPC with low-resistive phosphate glass electrodes as a candidate for  
3366 the CBM TOF”. In: *NIMA* 572 (2007), pp. 676–681.
- 3367 [55] JINST, ed. *Development of the MRPC for the TOF system of the MultiPurpose Detector*.  
3368 RPC2016: XII Workshop on Resistive Plate Chambers and Related Detectors. 2016.
- 3369 [56] M.C.S. Williams. “Particle identification using time of flight”. In: *Journal of Physics G* 39  
3370 (2012).
- 3371 [57] A. Alici et al. “Aging and rate effects of the Multigap RPC studied at the Gamma Irradiation  
3372 Facility at CERN”. In: *NIMA* 579 (2007), pp. 979–988.
- 3373 [58] M. Abbrescia et al. “The simulation of resistive plate chambers in avalanche mode: charge  
3374 spectra and efficiency”. In: *NIMA* 431 (1999), pp. 413–427.
- 3375 [59] M. Abbrescia et al. “Study of long-term performance of CMS RPC under irradiation at the  
3376 CERN GIF”. In: *NIMA* 533 (2004), pp. 102–106.

- 3377 [60] H.C. Kim et al. “Quantitative aging study with intense irradiation tests for the CMS forward  
3378 RPCs”. In: *NIMA* 602 (2009), pp. 771–774.
- 3379 [61] S. Agosteo et al. “A facility for the test of large-area muon chambers at high rates”. In: *NIMA*  
3380 452 (2000), pp. 94–104.
- 3381 [62] PoS, ed. *CERN GIF ++ : A new irradiation facility to test large-area particle detectors for*  
3382 *the high-luminosity LHC program*. Vol. TIPP2014. 2014, pp. 102–109.
- 3383 [63] A. Fagot. *GIF++ DAQ v4.0*. 2017. URL: [https://github.com/afagot/GIF\\_DAQ](https://github.com/afagot/GIF_DAQ).
- 3384 [64] CAEN. *Mod. V1190-VX1190 A/B, 128/64 Ch Multihit TDC*. 14th ed. 2016.
- 3385 [65] CAEN. *Mod. V1718 VME USB Bridge*. 9th ed. 2009.
- 3386 [66] W-Ie-Ne-R. *VME 6021-23 VXI*. 5th ed. 2016.
- 3387 [67] Wikipedia. *INI file*. 2017. URL: [https://en.wikipedia.org/wiki/INI\\_file](https://en.wikipedia.org/wiki/INI_file).
- 3388 [68] S. Carrillo A. Fagot. *GIF++ Offline Analysis v6*. 2017. URL: <https://github.com/>  
3389 [afagot/GIF\\_OfflineAnalysis](https://github.com/afagot/GIF_OfflineAnalysis).